Towards a

# Continuous active optical clock

Based on superradiant lasing

Using strontium

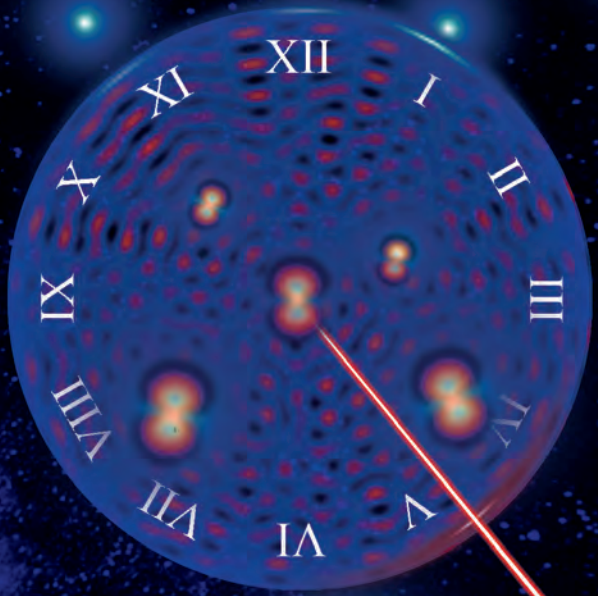


Sheng Zhou 周晟

# Towards a continuous active optical clock based on superradiant lasing using strontium

ACADEMISCH PROEFSCHRIFT

ter verkrijging van de graad van doctor
aan de Universiteit van Amsterdam
op gezag van de Rector Magnificus
prof. dr. ir. P. P. C. C. Verbeek
ten overstaan van een door het College voor Promoties ingestelde commissie,
in het openbaar te verdedigen in de Agnietenkapel
op maandag 2 december 2024, te 10:00 uur

door

Sheng Zhou

geboren te Sichuan

***Promotiecommissie***

| | | | |
|---|---|---|---|
| *Promotor:* | prof. dr. | F. E. Schreck | Universiteit van Amsterdam |
| *Copromotor:* | dr. | S. P. Bennetts | Universiteit van Amsterdam |
| *Overige leden:* | prof. dr. | J. Chen | Peking University |
| | prof. dr. | S. Hoekstra | University of Groningen |
| | prof. dr. | A. Polman | Universiteit van Amsterdam |
| | dr. | E. van Heumen | Universiteit van Amsterdam |
| | dr. | R. J. C. Spreeuw | Universiteit van Amsterdam |

Faculteit der Natuurwetenschappen, Wiskunde en Informatica

Chapter 1 cover: *Time*. It was created by Sheng using Leonardo AI https://leonardo.ai/.

ChatGPTv3.5 was used (https://chatgpt.com/) to polish passages to improve clarity.

ISBN: 978-94-6473-609-0

The author can be reached at:
zhous_pku@163.com or szhouworld@outlook.com

The research for this doctoral thesis received financial assistance from the European Union's Horizon 2020 research and innovation programme [grant agreement No 820404 (iqClock project www.iqclock.eu) and No 860579 (MoSaiQ project www.mosaiqc.eu)] and from the Dutch National Growth Fund (NGF), as part of the Quantum Delta NL programme (https://quantumdelta.nl/). The research was carried out at the Van der Waals Zeeman Institute, Institute of Physics, University of Amsterdam.

# Summary

Clocks are one of the oldest and most important inventions of human beings. The development of clocks has spanned 2000 years and for nearly 30 years optical clocks have doubled in performance every year. Today's best clocks are passive optical clocks, which will lose less than one second over the age of the universe. Achieving such accuracy is technically challenging. It requires an ultra-stable optical cavity to provide short-term stability for the clock laser, as well as atomic samples with a highly forbidden atomic transition in the optical domain for long-term stability and accuracy. The stability of optical cavities that provide the short-term reference is a remarkable scientific and engineering achievement. With length variations kept much smaller than the size of an atom, the performance of a clock laser locked to such a cavity can exceed $6.5 \times 10^{-17}$ stability averaged over 1 s [1].

There are however, always new proposals. An alternative that could dramatically reduce the extreme engineering challenges of ultra-stable cavities is to construct a clock laser directly using an ultra-narrow atomic transition. This approach faces its own challenges: the narrower the atomic transition, the lower the emission rate. For instance, our strontium clock transition has a 1.35 mHz natural linewidth, meaning an atom typically takes over 1000 seconds to emit a photon. Superradiance, a form of coherent emission, can enhance the emission rate for this long-lived state quadratically with the number of emitters making such a concept viable even for extremely narrow transitions. Additionally, such a superradiant laser can operate in the bad cavity regime, where the cavity linewidth is much broader than the atomic transition. This makes the laser output much less sensitive to cavity fluctuations and noise.

This thesis builds on the work of previous researchers. In 2016, pulsed superradiant lasers were first demonstrated using a non-continuous ultracold strontium source. A clock laser must however produce a continuous output. In 2017, our group demonstrated a steady-state ultracold high phase-space density (PSD) strontium source and in 2019 a guided high PSD strontium beam that could be ideal for pumping a continuous superradiant clock laser. These achievements set the stage for the development of a continuous active optical clock.

This thesis details the development of a continuous active optical clock based on superradiant lasing with strontium. It describes the basic quantum theory including the

conditions needed for continuous superradiance. It describes the experimental designs for the vacuum system, optics, electronics, and control software as well as our debugging process. This thesis aims to assist future researchers by passing on what I learned in the same generous tradition of the theses I learned so much from.

In the last five years, we have developed two types of machines to achieve continuous superradiance using different methods. The first is a straightforward hot atomic beam superradiance machine, based on a theoretical proposal from 2020 [2]. It utilizes the $^1S_0$ - $^3P_1$ 7.5 kHz-wide transition in strontium to target a laser with a linewidth of 7 Hz. We employed frequency modulation spectroscopy to measure the atoms in the cavity and heterodyne detection to analyze atoms in the excited state. This clock offers potential industrial applications as a compact, low-cost, and rugged frequency reference, especially suited for harsh environments, avoiding the cost and complexity associated with ultracold beam approaches.

The other machine is an ultracold strontium superradiant laser. We designed and built this unique machine to demonstrate continuous superradiance on the mHz-wide $^1S_0$ - $^3P_0$ clock transition. This setup promises to significantly enhance the stability, portability and bandwidth of optical clocks and related sensors by utilizing the ultra-narrow atomic transition.

Using this platform, we have demonstrated a compact steady-state $^{88}$Sr MOT on the 7.5 kHz-wide $^1S_0$ - $^3P_1$ transition. We have cooled $3 \times 10^8$ atoms with modulated, broadband 689 nm red lasers to approximately 10 µK, with a loading rate of $1 \times 10^8$ atoms/s, achieving performance similar to our atom laser machine. Further time-sequential cooling with single-frequency 689 nm lasers produces nearly recoil-limited ultracold atoms with temperatures as low as 800 nK. The next step is to load atoms into the cavity and to achieve the first continuous superradiant laser on the clock transition.

# Samenvatting

Klokken behoren tot de oudste en belangrijkste uitvindingen van de mensheid. De ontwikkeling van klokken beslaat 2000 jaar en optische klokken hebben de afgelopen 30 jaar elk jaar hun prestaties verdubbeld. De beste klokken van vandaag zijn passieve optische klokken, die minder dan een seconde zullen scheef lopen over de leeftijd van het universum. Het bereiken van dergelijke nauwkeurigheid is technisch uitdagend. Het vereist een ultrastabiele optische holte om de korte-termijn stabiliteit van de kloklaser te bieden, evenals specifieke atomaire samenstellingen met een zeer verboden atomaire overgang in het optische domein voor lange-termijn stabiliteit en nauwkeurigheid.

De stabiliteit van optische holtes die de korte-termijn frequentie referentie bieden, is een opmerkelijke wetenschappelijke en technische prestatie. Met lengteverandering die veel kleiner worden gehouden dan de grootte van een atoom, kan de prestatie van een klokkenlaser die aan een dergelijke caviteit is vergrendeld, een stabiliteit van $6.5 \times 10^{-17}$ bereiken, gemiddeld over 1 s [1].

Er zijn echter altijd nieuwe voorstellen. Een alternatief dat de extreme technische uitdagingen van ultrastabiele holtes dramatisch zou kunnen verminderen, is het direct bouwen van een kloklaser met behulp van een ultranauwkeurige atomaire overgang. Deze benadering heeft zijn eigen uitdagingen: hoe smaller de atomaire overgang, hoe lager de emissiesnelheid. Onze strontiumklokovergang heeft bijvoorbeeld een natuurlijke lijnbreedte van 1.35 mHz, wat betekent dat een atoom meestal meer dan 1000 seconden nodig heeft om een foton uit te zenden. Superradiantie, een vorm van coherente emissie, kan de emissiesnelheid voor deze langlevende toestand kwadratisch vergroten met het aantal emittoren, waardoor een dergelijk concept zelfs voor extreem smalle overgangen haalbaar is. Bovendien kan een dergelijke superstralingslaser werken in het slechte holteregime, waar de holte lijnbreedte veel breder is dan de atomaire overgang. Dit maakt de laseruitgang veel minder gevoelig voor holtefluctuaties en ruis.

Dit proefschrift bouwt voort op het werk van eerdere onderzoekers. In 2016 werden gepulseerde superstralingslasers voor het eerst gedemonstreerd met een niet-continue ultrakoude strontiumbron. Een kloklaser moet echter een continue output produceren. In 2017 demonstreerde onze groep een stationaire ultrakoude strontiumbron met hoge faseruimtedichtheid (PSD) en in 2019 een geleid strontiumstraal met hoge PSD die ideaal

zou kunnen zijn voor het pompen van een continue superstralingskloklaser. Deze prestaties legden de basis voor de ontwikkeling van een continue actieve optische klok.

Dit proefschrift beschrijft de ontwikkeling van een continue actieve optische klok gebaseerd op superstralingslasering met strontium. Het beschrijft de fundamentele kwantumtheorie inclusief de voorwaarden die nodig zijn voor continue superstralings. Het beschrijft de experimentele ontwerpen voor het vacuümsysteem, optica, elektronica en besturingssoftware evenals ons debugproces. Dit proefschrift heeft tot doel toekomstige onderzoekers te helpen door door te geven wat ik heb geleerd in dezelfde genereuze traditie van de proefschriften waarvan ik zoveel heb geleerd.

In de afgelopen vijf jaar hebben we twee soorten machines ontwikkeld om continue superstralings te bereiken met verschillende methoden. De eerste is een eenvoudige superstralingsmachine met hete atoomstraal, gebaseerd op een theoretisch voorstel uit 2020 [2]. Het maakt gebruik van de $^1S_0$ - $^3P_1$ 7.5 kHz brede overgang in strontium om een laser met een lijnbreedte van 7 Hz te richten. We hebben frequentiemodulatiespectroscopie gebruikt om de atomen in de holte te meten en heterodyne detectie om de atomen in de aangeslagen toestand te analyseren. Deze klok biedt potentiële industriële toepassingen als een compacte, goedkope en robuuste frequentiereferentie, vooral geschikt voor veranderende en uitdagende omgevingen, waarbij de kosten en complexiteit van ultrakoude straalbenaderingen worden vermeden.

De andere machine is een ultrakoude strontium superstralingslaser. We hebben deze unieke machine ontworpen en gebouwd om continue superstralings op de $^1S_0$ - $^3P_0$ mHz brede klokovergang te demonstreren. Deze opstelling belooft de stabiliteit, draagbaarheid en bandbreedte van optische klokken en gerelateerde sensoren aanzienlijk te verbeteren door gebruik te maken van de ultranauwkeurige atomaire overgang.

Met behulp van deze machine hebben we een compacte stationaire $^{88}$Sr MOT gedemonstreerd op de 7.5 kHz brede $^1S_0$ - $^3P_1$ overgang. We hebben $3 \times 10^8$ atomen gekoeld met gemoduleerde, breedbandige 689 nm rode lasers tot ongeveer 10 µK, met een laadsnelheid van $1 \times 10^8$ atomen/s, wat vergelijkbaar prestaties met onze atoomlasermachine oplevert. Verdere koeling met enkel-frequentie afstemming van de 689 nm lasers produceert bijna recoillimited ultrakoude atomen met temperaturen zo laag als 800 nK. De volgende stap is om atomen in de holte te laden en de eerste continue superstralingslaser op de klokovergang te bereiken.

# Contents

Chapter 1

# Introduction

# Chapter 1

# Introduction

Time has left its indelible mark on the fabric of everyone's daily existence, serving as the cornerstone upon which we construct and coordinate our activities. Even the slightest one-minute deviation can disrupt finely tuned schedules, resulting in missed trains and delayed plans. Furthermore, time is a valuable resource. The accuracy of Global Positioning System (GPS) positioning relies on precise time measurement. In summary, in our rapidly advancing modern society, there is a heavy reliance on accurate and precise timekeeping systems.

Thus, an accurate and precise clock is essential to maintain such timekeeping standards. Given the recurrent utilization of the terms "accuracy" and "precision" in characterizing clocks, it becomes imperative to explain these concepts. In Figure 1.1, the upper row illustrates these concepts through bullet holes: (a) bullets accurately and precisely hitting the target, (b) bullets hitting with precision but lacking accuracy, (c) bullets hitting accurately but lacking precision, and (d) bullets failing both accuracy and precision criteria. The lower row correspondingly illustrates the different performances of frequency measurements.

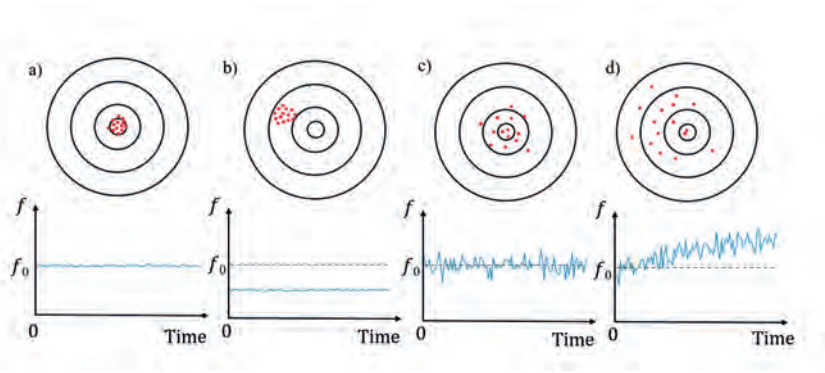


FIGURE 1.1: **The concept of accuracy and precision.** Each column represents a distinct condition reflecting these qualities.

The clock is one of the oldest inventions in human history, boasting a developmental history spanning approximately two millennia. To this day, time remains the most accurately measurable physical quantity. The rich tapestry of clock-related narratives is replete with fascinating anecdotes. However, given the focus and page constraints of this thesis, we shall limit ourselves to a very brief exploration of clock history. For a more comprehensive treatment, interested readers are directed to the many books on this topic [3–8].

## 1.1 Brief history of frequency and time measurement

The inherent periodic movement of our Earth and Sun allowed the creation of the sundial, a simple and ancient clock. Our modern Universal Time is still based on the rotation of the Earth. However, relying on the Earth's periodic movements as a time standard poses challenges. Firstly, the low frequency of these movements results in time intervals that are impractical for precise technical applications. Secondly, the accuracy of a sundial is constrained to around 100 s/d [1]. Lastly, the Earth's periodic movements undergo temporal changes. These are evident in astronomical findings such as those from the International Earth Rotation and Reference Systems Service (IERS) [9], which indicates daily variations in the length of a day shown in Figure 1.2. Likewise, historical chronometric records [10] reveal that one year in the Jurassic era, around 135 million years ago, comprised approximately 377 days instead of 365 days.

Innovative methods for measuring elapsed time emerged to address these challenges, incorporating the utilization of candles, water clocks, hourglasses, and eventually mechanical clocks. A pivotal moment transpired in 1656 when Christian Huygens in the Netherlands had the groundbreaking insight of utilizing a simple periodic object, the pendulum, to quantify time. The introduction of the pendulum clock marked a significant leap forward, achieving an accuracy surpassing 10 s/d, as illustrated in Figure 1.3. John Harrison further refined the pendulum clock, expanding its application to measure sea time and enhancing the precision of longitudinal measurements. This breakthrough revolutionized maritime navigation, rendering it more accurate and, consequently, safer.

Pendulum clocks maintained their status as the global standard for precise timekeeping for an impressive span of 270 years, until the advent of the quartz clock in 1927. The crystal oscillator within a quartz clock generated a signal with an exceedingly high and precise frequency, making quartz clocks and watches at least an order of magnitude more accurate than their mechanical counterparts. Notably, the relative stability of the quartz resonator

[1] This limitation arises due to the apparent diameter of the Sun as observed from Earth, which is approximately 0.5 deg. This implies that the shadow of even the thinnest sundial stick has a width corresponding to at least two minutes, given that there are 15 deg of longitude per hour.

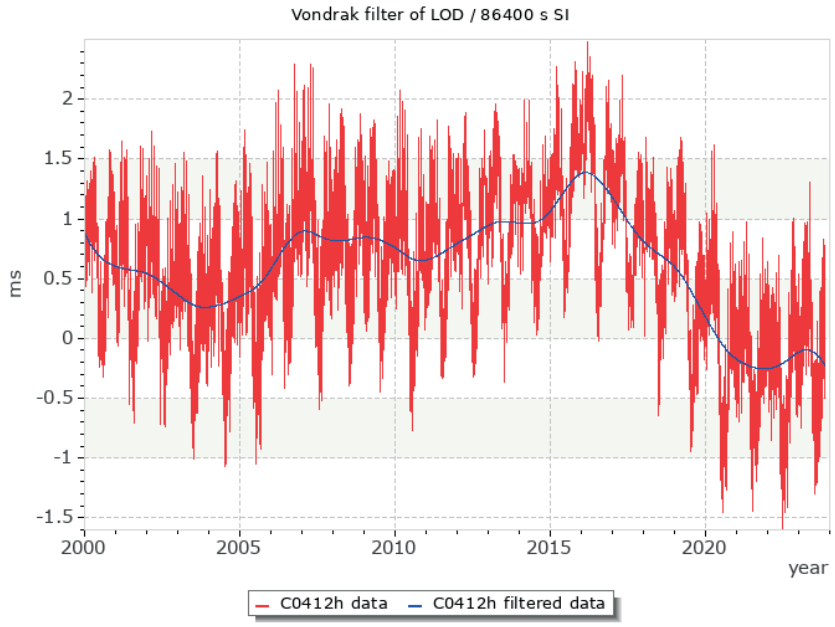


FIGURE 1.2: **The duration of each day changed in the last 24 years.** It fluctuates as evidenced by measurements from the International Earth Rotation and Reference Systems Service.

and its driving circuit surpasses its absolute accuracy. Even inexpensive, standard-quality 32 768 Hz resonators of this type exhibit a long-term accuracy of just a few parts per million (ppm). Additionally, quartz clocks possess the advantage of rather low-frequency variations with temperature fluctuation about $-1.2 \times 10^{-9}\,^{\circ}\mathrm{C}^{-1}$ [11].

So far, all these man-made clocks have overlooked another crucial aspect of creating a time standard: repeatability. Repeatability entails ensuring that two clocks are precisely identical. Achieving identical ticking rates in two pendulum clocks, for instance, requires their lengths to be meticulously identical. On the other hand, the frequency of quartz clocks is contingent on the period of a suitably elastic oscillation of a carefully cut and prepared quartz crystal. Moreover, quartz oscillators tend to drift in frequency by about 1 ms/d, rendering them unsuitable as a frequency standard unless calibrated.

Fortuitously, nature provides us with a solution.

Atoms possess quantized energy levels and therefore transitions between these levels can only be driven by electromagnetic radiation at specific frequencies. Furthermore, any two atoms of the same isotope are perfectly identical. Consequently, these inherently reproducible atomic transitions offer an ideal frequency standard.

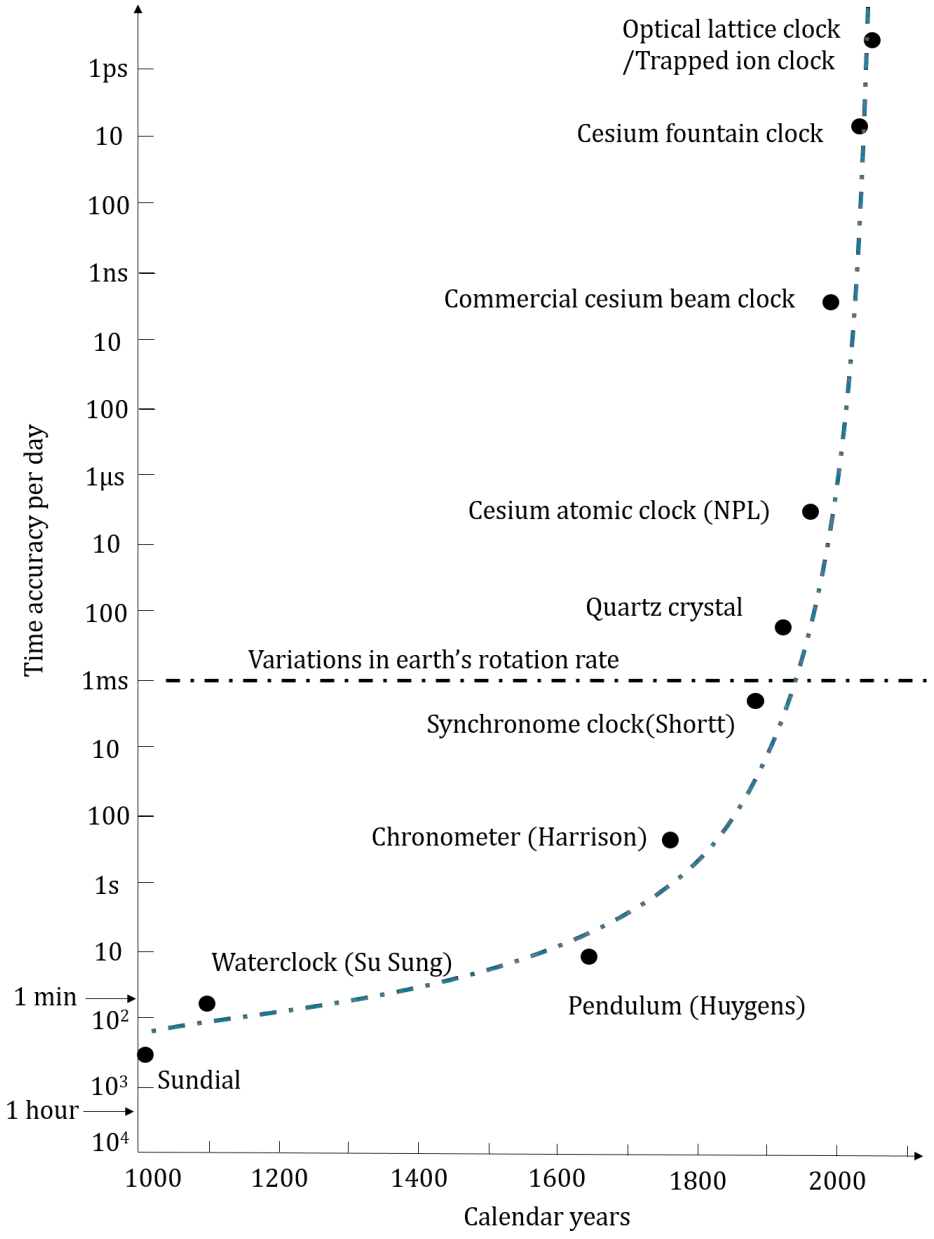


FIGURE 1.3: **Progress in the accuracy of clocks.** The progression of clock accuracy over the last 2000 years has been remarkable. The improvements in timekeeping accuracy have increased by 13 orders of magnitude.

The advent of atomic clocks utilizing microwave transitions in cesium atoms marked another revolution in timekeeping. The first atomic clock boasted an accuracy of $10^{-9}$, underscoring the need to redefine our approach to measuring time. In 1967, the second was redefined as the duration of 9,192,631,770 periods of radiation between the two hyperfine levels of the ground state of cesium-133. Moreover, frequency can be measured with greater resolution and less uncertainty than any other physical quantity. Consequently, almost all SI units are now derived from the second.

The advancement in precision within clock technology has been remarkable, as illustrated in Figure 1.4. The precision attainable with pendulum clocks, on average, doubled every 25 years. By contrast, cesium atomic clocks [12–15] have consistently doubled their performance every three years, sustaining this rapid pace for nearly six decades.

The advent of laser cooling techniques with the technology of high-quality coatings on mirrors has opened up the possibility of using optical transitions to make atomic clocks. This development is significantly reshaping the landscape of precision measurement and quantum physics.

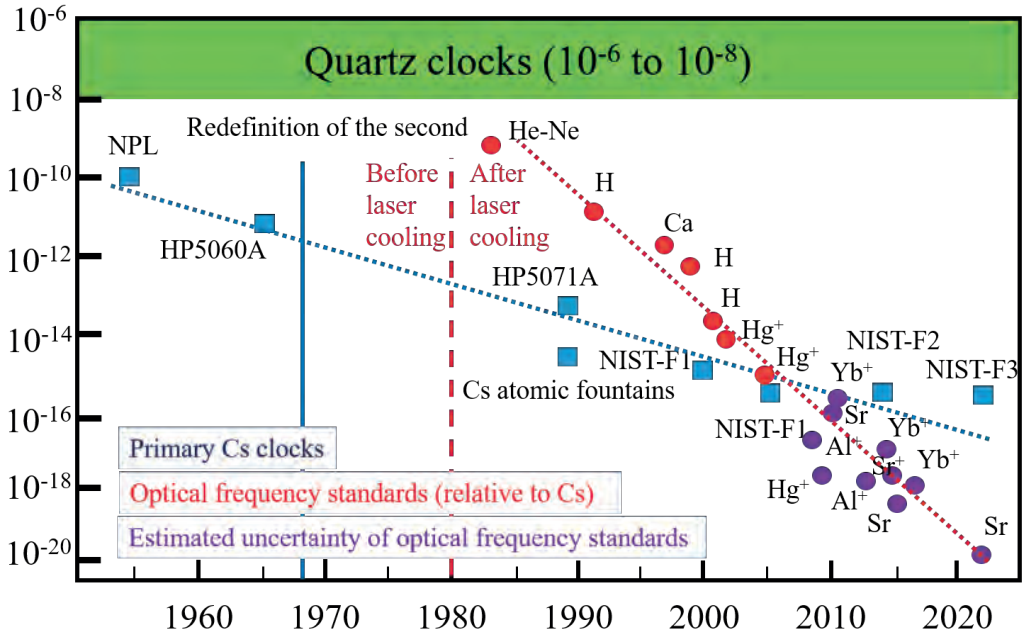


FIGURE 1.4: **The progress of improving the precision of clocks.** The precision attainable from pendulum clocks on average doubled every 25 years. By contrast, the performance of cesium atomic clocks has doubled every three years and has kept up this pace for nearly 60 years.

## 1.2 Optical lattice clocks

The inherent advantage that drives the adoption of optical frequencies in atomic clocks is that higher frequencies offer a higher resolution ruler to measure time. The accuracy of optical clocks has achieved $2 \times 10^{-18}$ [16], equivalent to approximately 1 s over the age of the universe. Moreover, optical clocks have demonstrated an unprecedented pace of performance growth [17–19] as shown in Figure 1.4 over the last three decades. On average, the precision of optical clocks is doubling every single year, surpassing even the renowned Moore's Law.

The development of laser cooling techniques has been crucial for the development of optical atomic clocks. Laser cooling reduces atomic motion and the associated Doppler linewidth broadening. Doppler effects can be further minimized by trapping cold atoms in an optical lattice. A deep optical lattice in the "Lamb-Dicke" regime allows spectroscopic resolution of the transition with motional effects reduced to resolvable sidebands. Furthermore, lattice trapping offers precise control over atomic collisions, essentially eliminating the density shift by maintaining atoms in a deep lattice with an atom-filling factor on the order of unity.

In an optical atomic lattice clock, samples of cold atoms are prepared and trapped, and the atomic transition frequency is compared to the frequency of the clock laser. The preparation of a cold atomic sample typically takes hundreds of milliseconds. Once prepared, the sample is interrogated by a clock laser using a Ramsey interferometer pulse sequence [20], a process that destroys the sample due to heating. The resulting measurement is then employed to steer and maintain the clock laser to the correct frequency. The atomic transition is passively used as a reference, so this optical lattice clock is also called a passive optical clock.

Maintaining the stability of the clock laser's frequency between measurements is crucial. In a passive optical lattice clock, shown in Figure 1.5, this is achieved using an ultra-stable resonator, essentially composed of two mirrors held at a precise distance by a glass tube. This optical cavity is meticulously engineered with an ultra-low expansion glass spacer and high-quality mirror coatings. By locking the clock laser to this ultra-stable cavity, the clock laser frequency noise at timescales within the locking bandwidth matches the noise spectrum of the reference cavity, while a slow lock to the atomic transition stabilizes the laser frequency at longer timescales. However, the periodic referencing of the clock laser to the atomic transition can introduce frequency instability, known as the Dick effect [21]. Due to the periodic interrogation of the atomic transition by the clock laser, high-frequency noise in the clock laser is aliased down to lower frequencies. This effect contributes to the inherent statistical instability of the clock.

The precision of a measurement, particularly in the absence of drift, improves significantly with increased averaging. During atomic clock characterization, stability is assessed across various timescales, ranging from short-term stability over a few seconds to long-term averaging spanning tens of thousands of seconds. The current stability record for strontium lattice clocks is a precision of $5 \times 10^{-19}$ after an hour of averaging, but this precision is reduced to $5 \times 10^{-17}$ [22] with only a second of averaging, largely reflecting the noise floor of the ultrastable reference cavity. Despite ongoing advancements in long-term averaging performance, short-term precision remains constrained by the residual thermal noise within the ultra-stable optical resonator.

Although photodetectors are not sufficiently fast to directly measure an optical frequency, the stability of the clock laser can be transferred to other wavelengths and into the microwave domain using an optical frequency comb. The frequency comb, generated by a modelocked femtosecond pulsed laser, creates a broad spectral comb comprising harmonics of the repetition rate. By locking one of these comb lines to the clock laser and by locking the second harmonic of a comb to itself [23], the frequency of all comb lines and thus the repetition rate can be precisely established. The repetition rate typically operates around 200 MHz where electronics is well-established.

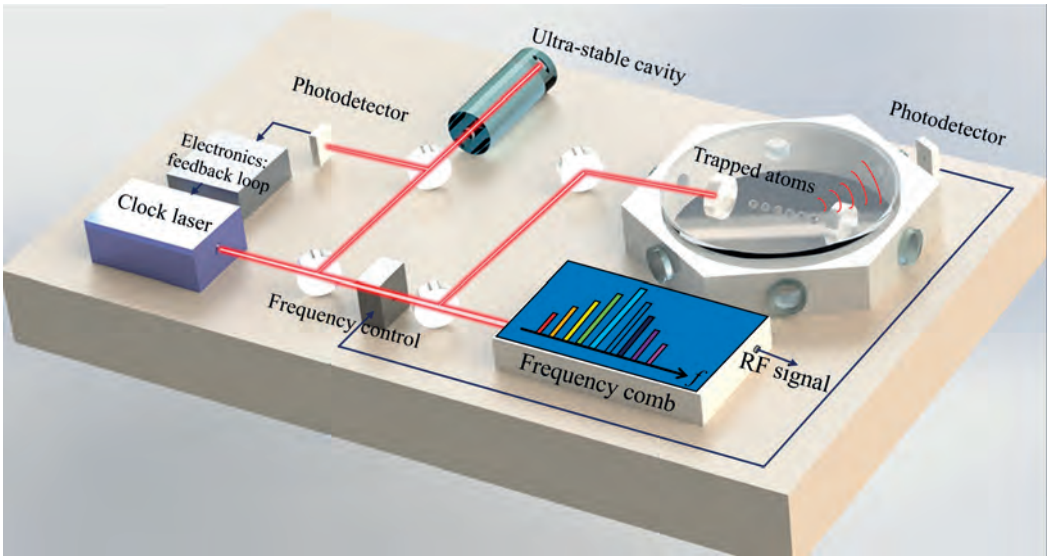


FIGURE 1.5: **The schematic of a passive optical lattice clock.** An ultra-stable optical cavity ensures the clock laser's stability within the timescale corresponding to the locking bandwidth, while a periodic interrogation of the atomic transition stabilizes the laser frequency over longer durations. The stability of the clock laser is transferred into the microwave domain using an optical frequency comb.

### 1.2.1 Improving the short-term stability

Given that the ultra-stable cavity significantly influences short-term stability, most efforts to improve short-term stability have focused on enhancing the cavity itself. Since any variation of the optical path length between the mirrors results in a variation of the frequency of the stabilized clock laser, meticulous methods are undertaken to place the optical cavity in a vacuum environment and shield it from variations arising from airflow, temperature changes, and mechanical vibrations.

Today's most advanced reference cavities, which feature relative stabilities around $5 \times 10^{-17}$ [1, 24, 25], are constructed using monocrystalline silicon spacers operating at around 4 K within a vacuum, and positioned atop an optical table equipped with active vibration cancellation mechanisms. However, even under these controlled conditions, the ultra-stable cavity's performance is constrained by thermal fluctuations, particularly attributed to Brownian motion within the mirror coatings.

Another proposed method to reduce a particular type of thermo-mechanical noise, Brownian noise, in the mirror coatings is the use of crystalline mirror coatings. At room temperature, a thermally limited noise floor was observed for crystalline-coated mirrors, indicating a tenfold reduction [26] compared to traditional dielectric coatings. However, follow-on work found anomalies [27], and most labs are sticking to traditional dielectric mirrors until this has been better understood.

Since implementing a monocrystalline cavity as well as a cryogenic system comes at the cost of significant expense and complexity, alternative strategies to enhance short-term stability are being pursued. These strategies encompass extending the length and mode volume of the cavity [22, 28] as well as investigating novel materials for the mirror substrate and cavity spacer. These include the use of cryogenic sapphire cavity spacers [29] already widely used for precision microwave oscillators [30].

The stability of optical cavities represents a remarkable achievement of science and engineering, maintaining a length variation much smaller than the size of an atom. It is a feat that is very challenging to improve upon.

### 1.2.2 Improving the long-term stability

The long-term stability of a clock is typically constrained by the drift of the atomic transition frequency caused by environmental impacts. If any of these factors change over time, the clock's long-term stability will diminish. One approach to address this issue is either to isolate atoms from the environment or to establish feedback loops to stabilize environmental factors that cause frequency drifts [16, 31]. For instance, in my previous work on Cs

clocks [32], it was crucial to stabilize the magnetic field and the power of microwave radiation used to interrogate the atoms to improve the clock's long-term stability.

The periodic interrogation of the atomic transition also undermines the long-term stability of the clock due to the Dick effect [21]. In the operation of most lattice clocks, the measurement of the atomic transition probability results in a complete loss of the atoms. Consequently, a significant portion of the atomic clock cycle time is consumed by loading atoms into the optical lattice at the beginning of each cycle, resulting in dead time. Non-destructive detection methods [33] have been devised to address this issue. Additionally, alternative approaches such as zero-dead-time measurement [34], continuous double Ramsey spectroscopy [35], and steady-state spectral hole burning [36] have been proposed to conduct continuous atomic spectroscopy, which is then used to lock the clock laser. Continuous measurement and control of the probe laser lead to improvements in Allan deviation as $\tau$ instead of $\sqrt{\tau}$ for an averaging time $\tau$, until reaching the quantum projection noise limit.

## 1.3 Active optical clocks

The hydrogen maser is today often used as a microwave frequency reference because of its excellent short-term stability (better than $5 \times 10^{-14}/\sqrt{\tau}$ scaling for times > 1 s [37]). The hydrogen maser relies on direct emission from a very narrow transition in hydrogen at 1.42 GHz to create a highly stable output with the stability of an atomic clock.

Drawing inspiration from the success of the hydrogen maser in the realm of microwave atomic clocks, a similar approach has been proposed to create a highly stable optical frequency reference. This approach, known as an *active optical clock* [38, 39], proposes to directly collect emission from a narrow optical atomic clock transition. Given the low output power of these emissions, one method to transfer their stability to a useful reference is employing them to lock a clock laser. Using the clock transition to provide gain for a laser could produce a linewidth that is much narrower than the transition linewidth. In a typical "good cavity" laser, the linewidth of the resonating cavity is much narrower than the linewidth of the gain medium. This produces an output frequency that follows the cavity resonance and thus the noise of the cavity. In order to overcome this challenge, active optical clocks operate in a "bad cavity" regime, where the cavity linewidth is much broader than the atomic transition linewidth. This scheme produces a frequency reference that is significantly immune ($1 \times 10^{-6}$) to cavity noise, which would otherwise greatly limit short-term stability. It is this immunity to environmental noise that perhaps offers one of the most significant attractive properties of active optical clocks, because it potentially

greatly simplifies the challenge of decoupling the impact of environmental noise in devices like transportable optical clocks.

An active optical clock requires continuous operation, as the phase reference is stored in the atoms rather than the field of a reference cavity. Its output is inherently locked to the atomic transition, which provides a high degree of long-term accuracy and stability, resulting in an excellent continuous clock that also eliminates the Dick effect. However, it is likely that state-of-the-art performance active optical clocks will still need to be paired with a passive reference clock at least in the near term, shown in Figure 1.6. This is due to the comparative difficulty of both stabilizing and accounting for the shifts in an active clock due to blackbody radiation, light or magnetic fields. In this sense the active clock can be considered an upgrade of the clock laser reference cavity.

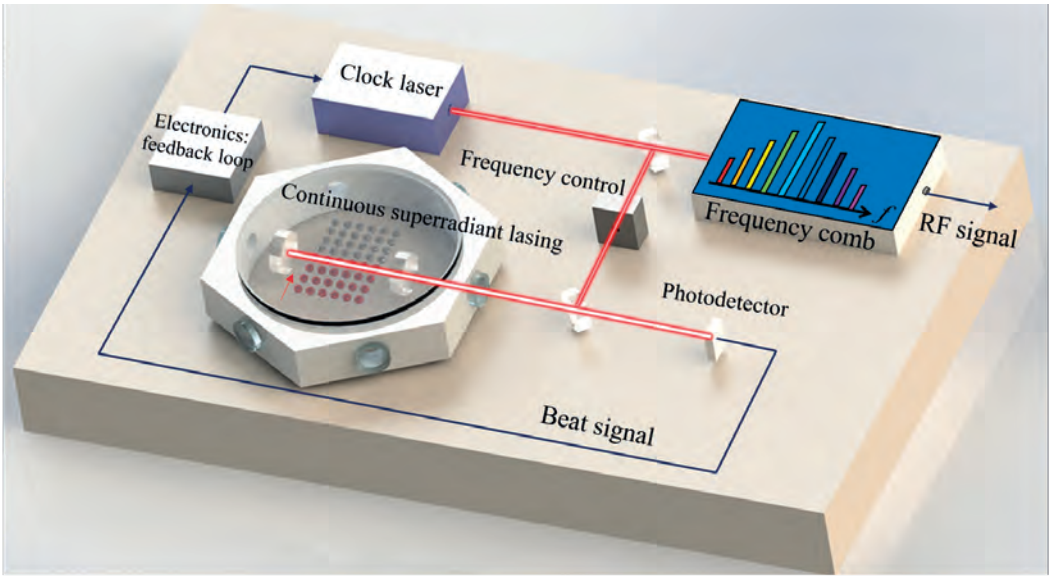


FIGURE 1.6: **The schematic of an active optical clock.** Continuously excited atoms are loaded into a cavity, which assists the atoms to build a collective emission known as superradiance. This continuous superradiant lasing on the atomic clock transition inherently has a ultra-narrow linewidth due to the property of the atomic clock transition. Besides, working in the "bad cavity regime" makes the lasing frequency less sensitive to the cavity noise. As analyzed in Chapter 2, since the superradiant lasing power may be low, a clock laser can be locked onto the superradiant signal using a heterodyne method. Optionally, this clock laser can also be pre-locked to a passive optical reference clock. Lastly, the stability of the clock laser is transferred into the microwave domain using an optical frequency comb.

Constructing a high-performance active optical clock poses numerous experimental

challenges. For example, the natural linewidth of the clock transition of $^{87}$Sr is only 1.35 mHz, so each strontium atom will spontaneously emit only one photon every 15 min. Such a weak transition can provide very little power and gain. Secondly, ultracold and trapped atoms are preferred to allow sufficient time for photon emission. Lastly without a laser cavity spontaneous emission is isotropic, further reducing the ability to collect sufficient photons with which to lock a laser. Using superradiance [38–40] can address these challenges.

A simple way to view superradiance is as an analogy to a classical phased-array transmitter. When emitters at the same frequency but with a random phase are present, the far-field signal is proportional to their number, $N$ (similar to spontaneous emission). However, if the emitters are phase-locked, they constructively interfere in one direction. As a result, the combined electric field strength is amplified by a factor of $N$ compared to that of a single emitter. Consequently, the emitted power scales proportionally to $N^2$. In the atomic equivalent, an ensemble of atoms phase-lock their dipole oscillations, resulting in an enhanced emission rate that can be much faster than spontaneous emission.

The key question is: How can we phase-lock atoms? Quantum mechanically, superradiant enhancement relies on not precisely knowing which atom emitted a photon. One way to achieve this condition is by closely packing atoms within a wavelength of the electromagnetic field. However, this may lead to chemical reactions destroying the sample and a high probability of collisions between atoms leading to density shifts. Another approach is to couple many excited-state atoms to the same optical field mode of an optical cavity [41–45] or a fiber [46, 47].

### 1.3.1 Pulsed or quasi-continuous superradiant clocks

Both optical cavities [41–45] and hollow core [47] optical fiber platforms have been used to trap and phase-lock samples of atoms to produce pulsed superradiant emission. Hollow-core platforms offer the advantage of extremely small mode volumes, allowing for closely spaced atoms and high superradiant gains. However, challenges arise in loading atoms into such fibers and achieving significant cavity finesse, such as through inscribing fiber Bragg gratings. These obstacles present difficulties in envisioning a pathway towards continuous superradiance, essential for state-of-the-art clocks.

Our research instead primarily focuses on loading atoms into optical cavities, which offers us several practical advantages. Firstly, optical cavities can accommodate cavity mode length extending to centimeters, enabling many options for high flux loading and trapping of many atoms within the cavity mode. Secondly, optical cavities can be easily offset-locked

to the atomic clock spectral line. Thirdly, our laboratory has already established fabrication techniques for in-vacuum high-finesse (∼10,000) optical cavities.

This approach has been used to demonstrate pulsed or quasi-continuous superradiance in several groups, such as JILA [41, 42], Hamburg university [48] and the University of Copenhagen [45]. The work at JILA demonstrated pulsed superradiance using Rubidium [41], the 7.5 kHz linewidth $^1S_0$ - $^3P_1$ transition of $^{88}$Sr [49] and impressively the 1.35 mHz linewidth $^1S_0$ - $^3P_0$ transition of $^{87}$Sr [42]. In this last work an ensemble of cold $^{87}$Sr atoms is laser-cooled and loaded into a high-finesse optical cavity. Atoms collectively emitted photons 10,000 times faster than would be possible by independent spontaneous decay. The pulse length of the superradiance lasted about 50 ms after which new excited-state atoms needed time to be prepared. The frequency stability of the pulsed superradiant output using the clock transition of strontium was measured at $6.7(1) \times 10^{-16}$ and is limited only by the Fourier width of the finite pulse length [50]. While this is still ten times lower than the best reference cavities and optical lattice clocks, which have a short-term stability of $5 \times 10^{-17}$ at 1 s, it looks very promising. If one would be able to sustain such superradiant emission continuously, the Fourier limit would be overcome and dramatically improved stabilities should be possible, up until drifts become significant.

### 1.3.2 Continuous superradiant clocks

Two methods can be employed to extend the superradiant pulse length. One approach involves repumping, which entails returning atoms that have emitted a photon back to the excited state. Previous studies have demonstrated the effectiveness of this technique [41, 45]. However, repumping typically heats the atoms, eventually rendering them too hot to be trapped. Repumping also does nothing to address the need to replace atoms lost due to heating and collisions with background gas. Perhaps a better approach is to continually introduce fresh excited-state atoms to the optical cavity and repumping or discarding atoms that have decayed to the ground state. A continuous high phase space density cold atom source is essential for implementing this second approach. In the past, our group has dedicated significant effort [51–54] to the development of this capability. The steady-state supply of atoms necessitates a different experimental architecture compared to typical atomic physics experiments. Typical cold atom experiments proceed in a time-sequential cooling manner, during which atoms largely maintain their spatial position as different optical or electromagnetic fields are activated and deactivated to cool a cloud over time. Decoupling those fields and cooling sequences to operate at different locations in space at the same time requires tackling a different set of challenges compared with conventional architectures. This was illustrated in our group's continuous Bose-Einstein

Condensation [54] experiment which explored a number of unsuccessful architectures as it evolved and where even the successful final architecture was by no means certain [55, 56].

We are not the only ones working on the development of continuous superradiant clocks. Other research groups, including those at JILA [57], FEMTO-ST [58], and Nicolaus Copernicus University in Toruń [59], are all exploring ways to create a continuous superradiant output on the millihertz clock transitions of $^{87}$Sr or $^{171}$Yb. Meanwhile, work at University of Copenhagen [45], Laboratoire de Physique des Lasers [60], Peking University [61, 62], and Tokyo University [47, 63], is exploring avenues to create continuous active optical clocks using broader linewidth transitions like the $^1S_0$ - $^3P_1$ transition of calcium and strontium or cesium.

## 1.4 Why do we want better clocks?

The measurement of frequency or time stands as one of the most precise and vital accomplishments of humanity, underpinning various aspects of modern society. For instance, the Global Navigation Satellite System (GNSS) relies on precise time measurements to gauge the delay time from signal transmission satellites to receivers. This enables distance measurements with an accuracy of better than 1 m using atomic clocks. However, the drift on these satellite-based cesium/rubidium clocks means they must be regularly re-synchronized by ground stations to maintain the network performance. Many aspects of modern life rely on synchronization, which is often implemented using GNSS signals. This includes applications from communication networks to high-speed trading and even to power grids. Precision clocks can detect GNSS anomalies to counter spoofing and jamming attempts. Some special applications, like submarines, which cannot access GPS signals underwater, rely on clocks and inertial sensors for navigation. Sensor networks equipped with clocks can detect gravitational signatures, map mineral deposits, heights and monitor volcanic activity. For these applications and many others, there is a growing need from the industry to move optical clocks out of the lab so that we may benefit from the impressive performances now possible.

For research, the most advanced clocks can detect frequency variations corresponding to changes in height as small as 1 mm [19, 64]. If this sensitivity can be further improved to 1 µm, we could potentially measure gravitational shifts on the scale of ultracold atom matter-waves. This prospect is particularly intriguing as it presents an opportunity to explore the intersection of quantum physics and general relativity, two theories that remain ununified. Clocks offer opportunities to explore some of the most significant questions in physics that remain unanswered, including inquiries about the nature of dark matter and dark energy, the matter/antimatter imbalance, and physics beyond the standard model.

Precision measurements using networks of clocks offer one of the few tools available to tackle these profound questions.

In summary, clocks play a crucial role in various scientific, technological, and societal domains, and their continued advancement holds the key to addressing many fundamental questions and enabling new possibilities across multiple disciplines.

## 1.5 Outline of thesis

I will present two active optical clock apparatuses that I have worked to develop. One aims to achieve continuous superradiance using the clock transition $^1S_0$ to $^3P_0$ of cold strontium, which in the long-term can enhance the performance of state-of-the-art optical clocks. The other machine aims to rapidly demonstrate a simplified continuous superradiant laser on the $^1S_0$ to $^3P_1$ transition using a hot strontium beam.

The remainder of this thesis is structured as follows.

Chapter 2 provides an in-depth examination of the theory of the steady-state superradiant laser. Utilizing the mean-field method, I will tackle the Dicke model and explore the conditions under which superradiance occurs. Additionally, I will investigate key characteristics of superradiance such as output power and linewidth. These theoretical insights will inform the design of our experiments for continuous cold atom superradiance and hot atomic beam superradiance, and I will evaluate the projected apparatus performance based on simplified conceptual designs.

Chapter 3 focuses on the apparatus aiming for the experimental demonstration of hot atomic beam superradiance. I will outline the experimental setup and construction process and present some preliminary results obtained before I moved to lead the development of a second “millihertz” clock apparatus.

Chapter 4 describes the design and construction of our continuous cold atom superradiant clock apparatus. This chapter also highlights many of the insights and lessons learned throughout the development process.

Finally, in Chapter 5, I present the initial results obtained from this continuous cold atom superradiant clock machine, with a particular focus on achieving a steady-state “red magneto-optical trap (MOT)”.

Chapter 2

# Theory of the steady-state superradiant clock

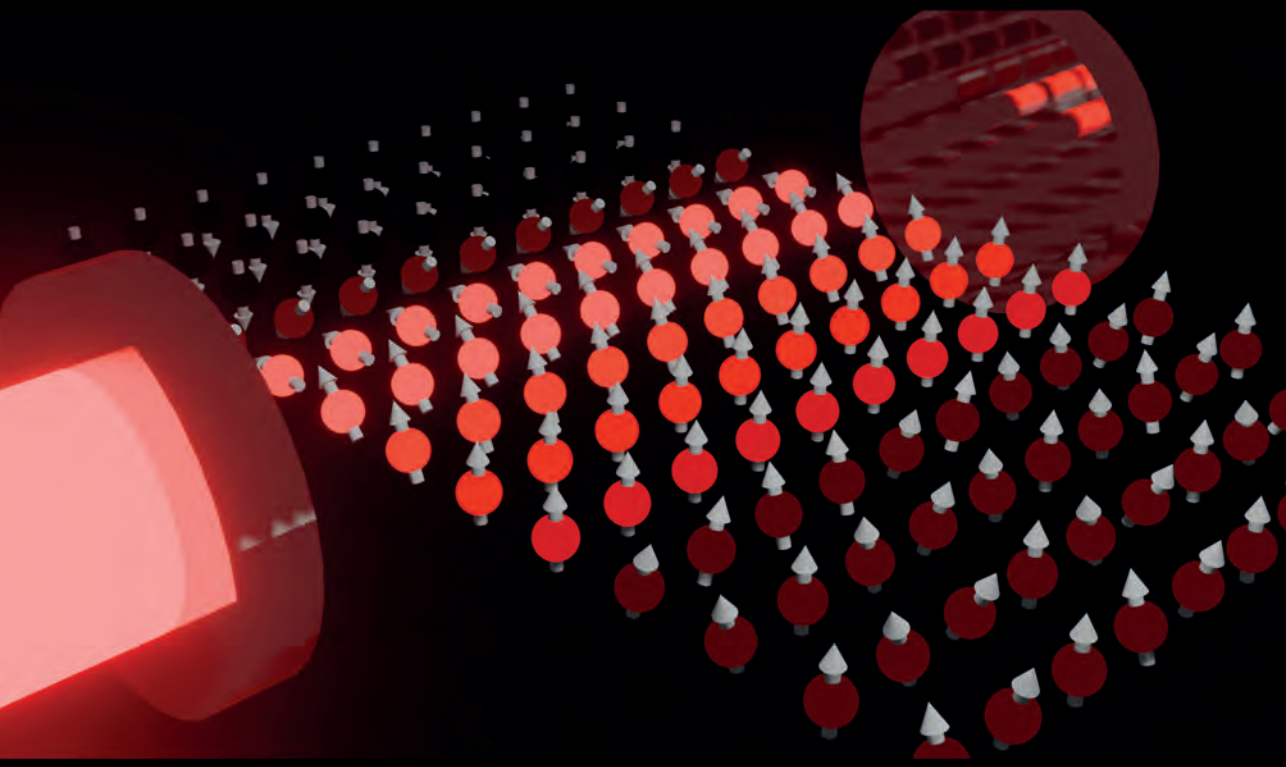

# Chapter 2

# Theory of the steady-state superradiant clock

Superradiance, first conceptualized by Robert H. Dicke [40] within the context of spontaneous emission, challenges the conventional understanding of photon emission from multiple emitters. In traditional analyses, each atom's radiation is considered independent due to the considerable distances between them and the resulting weak interactions. However, this approach fails to capture coherent spontaneous radiation, where atoms are coupled together with a shared radiation field. Such coupling, occurring when atoms are close to each other within a wavelength of the field or when atoms are in the same optical cavity field, can lead to either increased radiation, termed superradiance, or decreased radiation, known as subradiance.

A classic way to consider the coherent spontaneous radiation of many emitters is from a wave perspective, as mentioned in Section 1.3. In this chapter, we explore a quantum perspective to understand the prerequisites for achieving superradiance and its potential applications, particularly in constructing frequency references. Despite nearly seven decades of research in this field, significant challenges and opportunities remain. Interested readers can consult the extensive literature [38–40, 65–69] for more detailed investigations.

I begin by presenting the mean-field solution of the Dicke model to elucidate the conditions for steady-state superradiance, as well as the resulting output power and linewidth in Section 2.1. Furthermore, we delve into the practical aspects of realizing continuous superradiance experimentally in Section 2.2. This chapter aims to provide a comprehensive understanding of superradiance from both theoretical and experimental perspectives.

## 2.1 Mean field solutions of steady-state superradiance

In the realm of quantum optics, the Jaynes-Cummings model [70] serves as a foundational framework for describing systems featuring a two-level atom interacting with a quantized field mode within an optical cavity. Expanding upon this model to encompass multiple two-state atoms interacting with a single quantum field mode, as depicted in Figure 2.1, leads to the Dicke model [71] or the Tavis-Cummings model [72]. The distinction between these models lies in the inclusion of counter-rotating terms; the Dicke model incorporates these terms, whereas the Tavis-Cummings model does not. Superradiance, a phenomenon involving N two-level atoms interacting with a single-mode cavity field via dipole interactions, finds its description within the Dicke model.

Let us begin by describing the theoretical framework that underpins superradiance. Here I will follow the treatment given in Minghui Xu's thesis [67, 73] from Murray Holland's group in JILA.

The Hamiltonian governing such a system is expressed as follows [71]:

$$\hat{\mathcal{H}} = \frac{\hbar\omega_a}{2}\sum_{j=1}^{N}\hat{\sigma}_j^z + \hbar\omega_c\hat{a}^\dagger\hat{a} + \frac{\hbar\Omega}{2}\sum_{j=1}^{N}(\hat{a}^\dagger\hat{\sigma}_j^- + \hat{\sigma}_j^+\hat{a}), \tag{2.1}$$

where $\omega_a$ is the frequency corresponding to the atomic transition, $\omega_c$ is the frequency of the cavity mode, $\hat{\sigma}_j^z$ are Pauli matrices of the $j^{\text{th}}$ atom, and $\hat{\sigma}_j^+$, $\hat{\sigma}_j^-$ are raising and lowering operators for the $j^{\text{th}}$ atom. The operators $\hat{a}^\dagger$ and $\hat{a}$ represent the bosonic creation and annihilation operators for the photons in the laser mode. The coupling strength $\Omega$ is

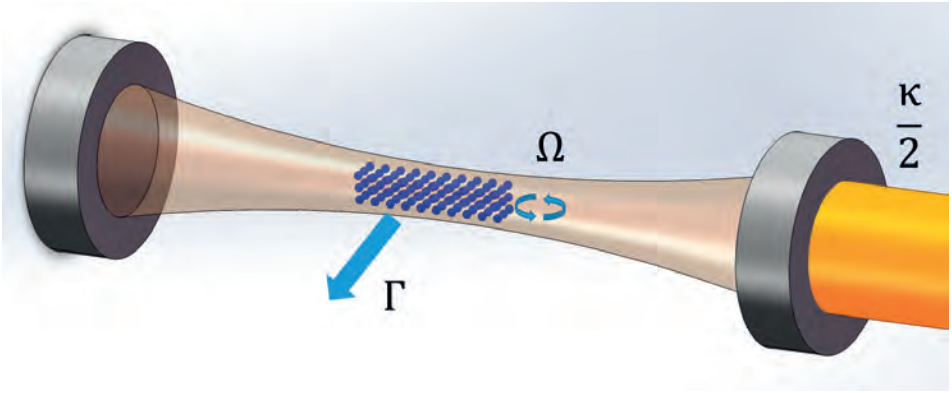


FIGURE 2.1: **Cavity quantum electrodynamics.** Atoms can emit photons into or absorb photons from the cavity mode at a rate $\Omega$, and they can emit photons into other modes of the electromagnetic field at a rate $\Gamma$. The cavity emits photons into the environment with rate $\kappa/2$.

determined by the atomic dipole moment ($\vec{d}$) and the electric field of a single photon in the cavity mode [67], as defined by Eq. 2.2,

$$\Omega = \vec{\epsilon}\vec{d}\sqrt{\frac{\omega_c}{(2\epsilon_0\hbar V_{eff})}}. \tag{2.2}$$

The effective mode volume $V_{eff}$ is given by $V_{eff} = \pi\omega_{waist}^2 L$, where $\omega_{waist}$ is determined by the cavity waist and $L$ is the length of the region where the atoms are situated. $\vec{\epsilon}$ is the polarization of the cavity field, and $\vec{d}$ represents the dipole matrix element of the atomic transition. $\epsilon_0$ is the vacuum permittivity. The term $\hbar\Omega$ physically represents the energy associated with the interaction between the atomic dipole moment ($\vec{d}$) and the electric field ($\vec{E}$) of a single photon in the cavity mode.

The Hamiltonian (Eq. 2.1) delineates the closed dynamics of the atom-field system. However, to incorporate decay processes such as spontaneous emission, a master equation derived within the Born-Markov approximation is employed [73]. Operating on the reduced atom-cavity density matrix $\hat{\rho}$, this equation accounts for dissipative effects, encapsulating both coherent evolution and dissipative processes, as depicted in Eq. 2.3.

$$\frac{d}{dt}\hat{\rho} = \frac{1}{i\hbar}[\hat{\mathcal{H}}, \hat{\rho}] + \hat{\mathcal{L}}[\hat{\rho}] \tag{2.3}$$

The $\hat{\mathcal{L}}$ operator describes the dissipative processes, including cavity decay, spontaneous decay, repumping, and inhomogeneous dephasing. These processes are non-Hermitian and encompass various mechanisms that can influence the dynamics of the atom-cavity system. Cavity decay pertains to photon loss from the optical cavity, while spontaneous emission involves the emission of photons due to atomic transitions. Repumping processes aim to restore population imbalances, and inhomogeneous dephasing accounts for variations in atomic transition frequencies.

$$\begin{aligned}
\hat{\mathcal{L}}[\hat{\rho}] = &-\frac{\kappa}{2}(\hat{a}^\dagger\hat{a}\hat{\rho} + \hat{\rho}\hat{a}^\dagger\hat{a} - 2\hat{a}\hat{\rho}\hat{a}^\dagger) \\
&-\frac{\gamma}{2}\sum_{j=1}^{N}(\hat{\sigma}_j^+\hat{\sigma}_j^-\hat{\rho} + \hat{\rho}\hat{\sigma}_j^+\hat{\sigma}_j^- - 2\hat{\sigma}_j^-\hat{\rho}\hat{\sigma}_j^+) \\
&-\frac{w}{2}\sum_{j=1}^{N}(\hat{\sigma}_j^+\hat{\sigma}_j^-\hat{\rho} + \hat{\rho}\hat{\sigma}_j^+\hat{\sigma}_j^- - 2\hat{\sigma}_j^-\hat{\rho}\hat{\sigma}_j^+) \\
&+\frac{1}{2T_2}\sum_{j=1}^{N}(\hat{\sigma}_j^z\hat{\rho}\hat{\sigma}_j^z - \hat{\rho}),
\end{aligned} \tag{2.4}$$

where $\kappa$ is the decay rate of the cavity, $\gamma$ is the free space spontaneous emission rate of the atoms, $w$ is the repumping rate, and $1/T_2$ is the rate of inhomogeneous dephasing.

To derive the steady-state solution, collective operators are introduced [73], given by:

$$\hat{S}^{\pm} = \frac{1}{N}\sum_{j=1}^{N}\hat{\sigma}_j^{\pm}, \tag{2.5}$$

$$\hat{S}^{z} = \frac{1}{N}\sum_{j=1}^{N}\hat{\sigma}_j^{z}. \tag{2.6}$$

To derive Eq. 2.3, it is straightforward to work in the Heisenberg picture. The resulting equations are the quantum Langevin equations.

$$\frac{d}{dt}\hat{a} = -\frac{1}{2}(\kappa + 2i\omega_c)\hat{a} - \frac{iN\Omega}{2}\hat{S}^{-} + \hat{F}^{a}, \tag{2.7}$$

$$\frac{d}{dt}\hat{S}^{-} = -\frac{1}{2}(\Gamma + 2i\omega_a)\hat{S}^{-} + \frac{i\Omega}{2}\hat{a}\hat{S}^{z} + \hat{F}^{-}, \tag{2.8}$$

$$\frac{d}{dt}\hat{S}^{z} = -(w+\gamma)(\hat{S}^{z} - d_0) + i\Omega(\hat{a}^{\dagger}\hat{S}^{-} - \hat{a}\hat{S}^{+}) + \hat{F}^{z}. \tag{2.9}$$

$\Gamma = w + \gamma + \frac{2}{T_2}$ is the generalized single-atom decoherence rate, and $d_0 = \frac{w-\gamma}{w+\gamma}$ characterizes the atomic inversion that would be obtained for a single atom in the absence of the cavity. $\hat{F}^{\nu}$ represents the quantum noise operators, which have zero mean and second-order correlations given by

$$\langle \hat{F}^{\mu}(t)\hat{F}^{\nu}(t')\rangle = 2D^{\mu\nu}\delta(t-t'). \tag{2.10}$$

And the diffusion matrix elements $D^{\mu\nu}$ are presented as follows [73]:

$$\begin{aligned}
D^{aa^\dagger} &= \frac{\kappa}{2}, \\
D^{zz} &= \frac{\gamma}{N}(1+\langle\hat{S}^z\rangle) + \frac{\omega}{N}(1-\langle\hat{S}^z\rangle), \\
D^{+-} &= \frac{1}{2N}\left(\omega + \frac{1}{T_2}(1+\langle\hat{S}^z\rangle)\right), \\
D^{-+} &= \frac{1}{2N}\left(\gamma + \frac{1}{T_2}(1-\langle\hat{S}^z\rangle)\right), \\
D^{+z} &= -\frac{\omega}{N}\langle\hat{S}^+\rangle, \\
D^{z+} &= \frac{\gamma}{N}\langle\hat{S}^+\rangle, \\
D^{-z} &= \frac{\gamma}{N}\langle\hat{S}^-\rangle, \\
D^{z-} &= -\frac{\omega}{N}\langle\hat{S}^-\rangle.
\end{aligned} \tag{2.11}$$

From Eq. 2.11, the noise is $1/\sqrt{N}$ smaller than the deterministic terms in the quantum Langevin equation.

$\hat{a}$, $\hat{S}^-$, and $\hat{S}^z$ are operators or matrices. To find the steady-state solution, those operators could be replaced with complex numbers $a = \langle\hat{a}\rangle$, $S^- = \langle\hat{S}^-\rangle$, $S^z = \langle\hat{S}^z\rangle$ [68, 73, 74], and the noise term becomes zero.

$$\frac{d}{dt}a = -\frac{1}{2}(\kappa + 2i\omega_c)a - \frac{iN\Omega}{2}S^-, \tag{2.12}$$

$$\frac{d}{dt}S^- = -\frac{1}{2}(\Gamma + 2i\omega_a)S^- + \frac{i\Omega}{2}aS^z, \tag{2.13}$$

$$\frac{d}{dt}S^z = -(w+\gamma)(S^z - d_0) + i\Omega(a^*S^- - aS^+). \tag{2.14}$$

By taking expectation values of the semi-classical equations, we obtain the mean-field equations written in the reference frame rotating at frequency $\omega_{\text{ref}}$:

$$\frac{d}{dt}a = -\frac{1}{2}(\kappa + 2i(\omega_c - \omega_{\text{ref}}))a - \frac{iN\Omega}{2}S^-, \tag{2.15}$$

$$\frac{d}{dt}S^- = -\frac{1}{2}(\Gamma + 2i(\omega_a - \omega_{\text{ref}}))S^- + \frac{i\Omega}{2}aS^z, \tag{2.16}$$

$$\frac{d}{dt}S^z = -(w+\gamma)(S^z - d_0) + i\Omega(a^*S^- - aS^+). \tag{2.17}$$

A solution in a steady-state situation can be found by setting the left-hand sides to zero. Then, with Eq. 2.15 and Eq. 2.16, we have

$$S^z = \frac{(\kappa + 2i(\omega_c - \omega_{\text{ref}}))(\Gamma + 2i(\omega_a - \omega_{\text{ref}}))}{N\Omega^2}. \tag{2.18}$$

For the steady-state inversion, the oscillation frequency of the atom-cavity coupled system $\omega_{\text{ref}}$ can be determined by using the condition that $S_z$ must be real, giving

$$\omega_{\text{ref}} = \frac{\kappa\omega_a + \Gamma\omega_c}{\kappa + \Gamma}. \tag{2.19}$$

This reference frequency $\omega_{\text{ref}}$ is also the output laser frequency, which is the weighted average of the cavity frequency and atomic frequency.

Now $S^z$ is given by

$$S^z = \frac{\kappa\Gamma}{N\Omega^2}(1 + 4(\omega_a - \omega_c)^2) \approx \frac{\kappa\Gamma}{N\Omega^2}, \tag{2.20}$$

where the approximation is made because of the limit $\omega_a - \omega_c \ll \Gamma, \kappa$, which can experimentally be achieved by locking the cavity frequency to the atomic spectroscopy.

Next, the photon number is derived as

$$|a|^2 \approx \frac{N(w + \gamma)}{2\kappa}(d_0 - S_z). \tag{2.21}$$

With steady-state atom-atom correlation, we have

$$S^+S^- = \frac{\kappa^2 + 4(\omega_c - \omega_{\text{ref}})^2}{N^2\Omega^2}\,|a|^2\,. \tag{2.22}$$

In summary, we established the theoretical foundation for analyzing the dynamics of atom-cavity systems. By transitioning to mean-field equations (Eqs. 2.20, 2.21, 2.22), we simplified the analysis and identified steady-state solutions, which we will use for discussing the requirements and performance of continuous superradiant lasing in Section 2.1.1. This theoretical framework provides a basis for understanding the intricate behavior of atom-cavity systems, setting the stage for further exploration.

### 2.1.1 Conditions for continuous superradiance

Alkaline earth(-like) atoms or ions (Mg, Ca, Sr, Yb, Hg, $Al^+$, ...) possess ultranarrow optical transitions, making them ideal candidates for superradiant clocks. With two valence electrons, these atoms feature a rich energy level structure, as illustrated in Figure 2.2. This richness enables a variety of applications, each with distinct characteristics.

The two valence electrons' spin can align parallel or anti-parallel, resulting in singlet and triplet states. Strong optical transitions occur between singlet-singlet states or triplet-triplet states. Much weaker spin-forbidden transitions between singlet and triplet states also exist, called intercombination transitions. For instance, the strong $^1S_0$ - $^1P_1$ cycling transition is commonly employed for laser cooling to mK temperatures, trapping, and precise state detection, whereas the spin-forbidden $^1S_0$ - $^3P_1$ transition facilitates second-stage laser cooling to $\mu$K temperatures. Moreover, transitions from $^3P_J$ states to $^3S_1$ or $^3D_J$ are valuable for repumping or laser cooling. Of special interest is the doubly forbidden $^1S_0$ - $^3P_0$ transition, notable for its ultra-narrow linewidth, making it highly suitable as the frequency reference of an optical clock.

I will utilize strontium as an illustrative example to delve into the conditions and performance of steady-state superradiant lasing. The analysis of other species will be presented in Section 2.2.3. The key parameters governing the onset of superradiant lasing can be discerned from the equations (Eqs.2.20, 2.21, 2.22). These parameters encompass atom-related factors, including the atom number ($N$), spontaneous decay rate ($\gamma$), pump rate ($w$), and the generalized single-atom decoherence rate ($\Gamma = w + \gamma + 2/T_2$), as well as cavity-related parameters such as cavity linewidth ($\kappa$) and atom-cavity interaction parameter ($\Omega$).

Concerning the atom-related parameters specific to $^{87}$Sr, our experimental observations suggest that the cavity can accommodate and trap up to $1 \times 10^6$ atoms [51–53]. The natural linewidth, $\gamma$, of the clock transition ($^1S_0$ to $^3P_0$) is $(2\pi)1.35$ mHz. Atoms can be efficiently repumped at a rate $\omega$ ranging from 0 to $1 \times 10^4$ Hz. And recent experiments on lattice clocks have demonstrated an inhomogeneous lifetime $T_2$ of approximately 1 s [75].

Regarding cavity parameters, a cavity design characterized by a $1/e^2$ waist radius of 100 µm and a length 10 mm long, allows for an effective mode volume $V_{eff} = \pi(100\,\mu m)^2 \times 10\,mm$, resulting in a vacuum Rabi frequency of $\Omega \approx (2\pi)4.3$ Hz. The cavity linewidth $\kappa$ is contingent upon the total reflectivity of the mirrors and the cavity length. Opting for a cavity length of 10 cm with a total reflectivity of 99.98%, yields a finesse of approximately 40,000 and $\kappa \approx (2\pi)35$ kHz.

With the parameters above, the steady-state lasing output power is calculated using Eq. 2.21 and presented in Figure 2.3 as the function of atom number and pump rate. The blue area indicates minimal photon emission, while the colorful region represents the superradiant lasing region, allowing the determination of the conditions for achieving steady-state superradiance.

First and foremost, the pump rate $w$ must exceed the threshold rate of $\gamma$, irrespective of the number of atoms stored in the cavity mode. This threshold rate can be derived in the

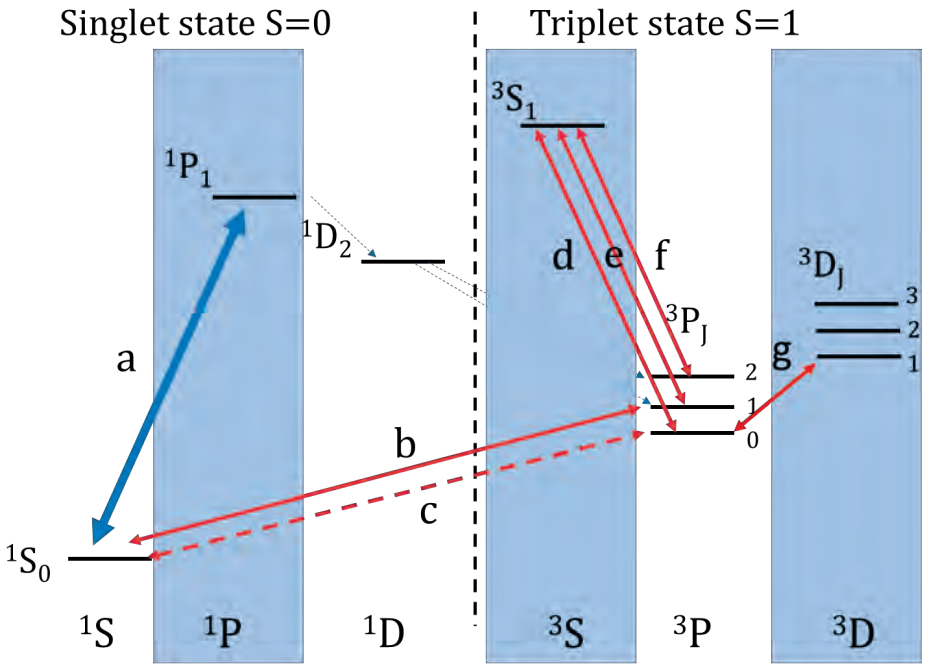


| | Wavelength (nm) | Mg | Ca | Sr | Yb | Hg |
|---|---|---|---|---|---|---|
| a | Strong cooling | 285 (79 MHz) | 423 (34 MHz) | 461 (32 MHz) | 399 (29 MHz) | 185 (120 MHz) |
| b | Narrow cooling | 475 (36 Hz) | 657 (400 Hz) | 689 (7.5 kHz) | 556 (180 kHz) | 254 (1.3 MHz) |
| c | Clock | 209 (2.7 Hz) | - | 698 (1.35 mHz) | 578 (10 mHz) | 265.6 (100 mHz) |
| d-f | Repump lasers | | 610,612, 616 | 679, 688, 707 | 649, 680, 770 | 405, 546 |
| g | Optional cooling or repumpers | 390 | 1931 | 2603 | 1388 | 297 |
| | Optional Magic wavelength | 432 | | 813 | 759 | 363 |

FIGURE 2.2: **Energy level diagram of alkaline earth atoms.** The $^1S_0$ - $^1P_1$ transition is a broad, cycling transition ideally suited for slowing of atomic beams, first-stage laser cooling and probing due to its tens of MHz linewidth. The $^1S_0$ - $^3P_1$ transition, narrower than the former, is used to cool atoms further. The $^1S_0$ - $^3P_0$ transition is exceptionally narrow, boasting a quality factor (Q) of $10^{16}$, making it an ideal choice for frequency standards. Other transitions can serve for pumping or optional cooling. The table on the bottom illustrates the properties of each transition for different elements.

limit $N \to$ a large number. In this limit, the average photon number can be approximated as:

$$|a|^2 \approx \frac{N(w+\gamma)}{2\kappa}\left(d_0 - \frac{\kappa\Gamma}{N\Omega^2}\right) \approx \frac{N(w+\gamma)}{2\kappa} d_0 = \frac{N(w+\gamma)}{2\kappa}\frac{w-\gamma}{w+\gamma} > 0. \tag{2.23}$$

Since the average photon number must be greater than zero for lasing to occur, the pump rate $w$ must exceed $\gamma$. This signifies that above the threshold, pumping compensates

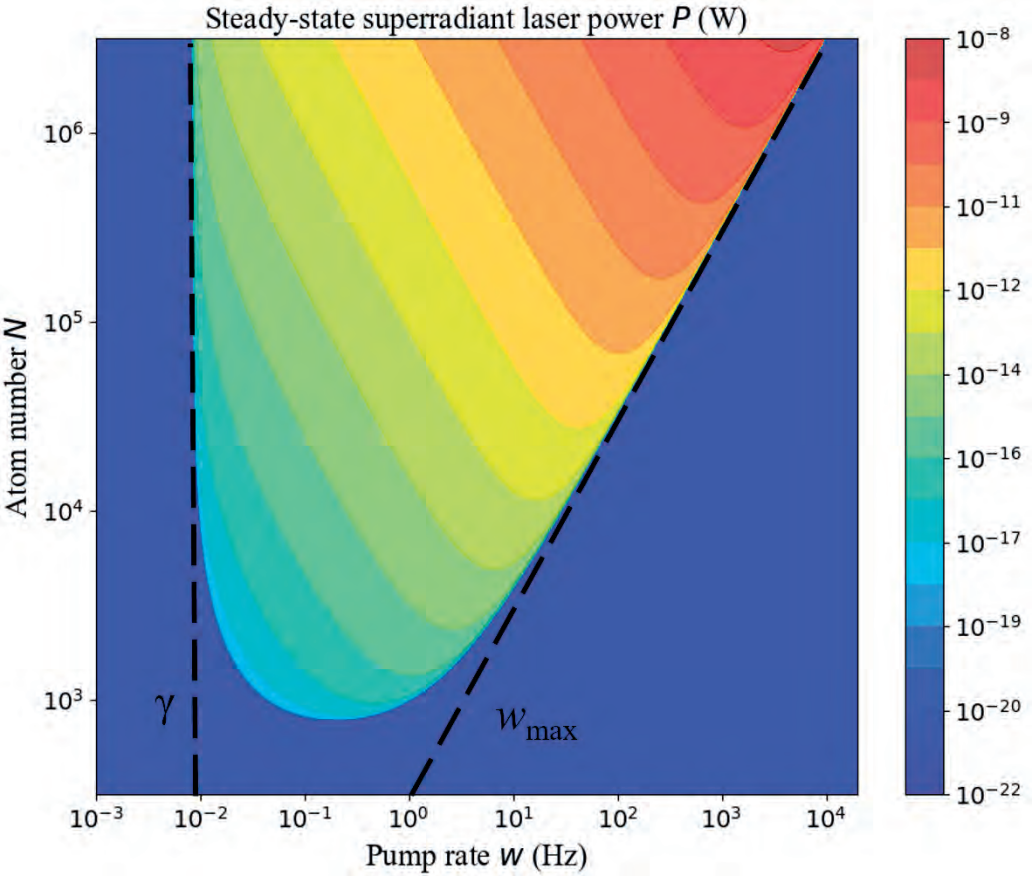


FIGURE 2.3: **Steady-state superradiant lasing power for varying atom number and pump rate.** The figure illustrates the calculated steady-state laser power for different atom numbers and pump rates. The analysis focuses on $^{87}$Sr to determine the conditions for continuous superradiant lasing, with parameters set to $\Omega = (2\pi)4.3\,\text{Hz}$, $\gamma = (2\pi)1.35\,\text{mHz}$, $T_2 = 1\,\text{s}$, and $\kappa = (2\pi)35\,\text{kHz}$. The dashed lines show the minimum and the maximum pump rates for superradiant lasing.

for atom losses, achieving population inversion.

More interestingly, at a pumping rate beyond a certain $w_{\max}$, the collective emission vanishes, indicating that a too high pumping rate can disrupt coherence between the atoms. The reason is that atoms get pumped faster than they can build up a collective spin through interactions mediated by the cavity field. Under this condition, the atoms get fully inverted and the coherence between them is lost. The maximum pump rate can be determined by setting $S_z = (\kappa(w+\gamma+2/T_2)/(N\Omega^2))$ close to unity, and assuming that the collective decay rate $N\Omega^2/\kappa$ is also much larger than the single atom relaxation rate $\gamma$ and the inverse of the coherent time $1/T_2$. These considerations lead to

$$w_{\max} = NC\gamma, \tag{2.24}$$

where $C$, the single-atom cooperativity, is defined by,

$$C = \Omega^2/(\kappa\gamma). \tag{2.25}$$

Given that the average photon number $|a|^2$ is a quadratic function of $w$, the maximum output photon flux can be achieved at $d|a|^2/dw = 0$, resulting in:

$$w_{opt} = \frac{N\Omega^2}{2\kappa} - \gamma - \frac{1}{T_2} \approx \frac{N\Omega^2}{2\kappa}. \tag{2.26}$$

Using $w$ from Eq. 2.26 and taking into account the energy of each photon $\hbar\omega_a$, we obtain the maximum output power which is determined by:

$$P_{max} = \hbar\omega_a N^2 C\gamma/8. \tag{2.27}$$

Figure 2.3 illustrates the output power obtained with $1\times10^6$ atoms in the cavity and a pump rate of 1 Hz. The steady-state power is about 1 pW, which is insufficient for laser injection.

Furthermore, it's noteworthy to mention that when the atom-cavity system emits the maximum output power, the population inversion of atoms $S_z \approx 1/2$, which signifies that each atom is in an equal superposition of ground and excited state. The phase of the emitted light is mainly stored in the phase of this superposition, which is equal for all atoms.

Another threshold worth mentioning is the minimum number of atoms needed to achieve collective superradiant lasing, which is determined by:

$$N_{min} = \frac{2}{C\gamma T_2}. \tag{2.28}$$

### 2.1.2 Linewidth of continuous superradiant laser

An essential feature we need to determine is the linewidth achieved by steady-state superradiant lasing. To calculate this linewidth, we employ Haken's phase diffusion method to derive a closed-form solution. Differentiating Eq. 2.12 with respect to time and substituting Eqs. 2.12-2.14, we obtain:

$$\frac{d^2}{dt^2}\hat{a} = -\frac{1}{2}(\kappa+\Gamma)\frac{d}{dt}\hat{a} - \frac{\kappa\Gamma}{4}\hat{a} + \frac{N\Omega^2}{4}\hat{a}\hat{S}^z + \hat{F}, \tag{2.29}$$

where

$$\hat{S}^z = \int_0^t dt' e^{-(w+\gamma)(t-t')}\left\{(w+\gamma) + \hat{F}^z - \frac{2}{N}\left(\frac{d}{dt}(\hat{a}^\dagger a) + \kappa\hat{a}^\dagger a - \hat{a}^\dagger\hat{F}^a - \hat{F}^{a^\dagger}\hat{a}\right)\right\}, \tag{2.30}$$

and

$$\hat{F} = \frac{\Gamma}{2}\hat{F}^a - \frac{iN\Omega}{2}\hat{F}^- + \dot{\hat{F}}^a. \tag{2.31}$$

Here, the annihilation operator $\hat{a}$ is decomposed according to

$$\hat{a} = (a+\hat{r})e^{i\hat{\phi}}. \tag{2.32}$$

Above the threshold, the amplitude fluctuations are minimal, allowing us to neglect $\hat{r}$. Then, the two-time correlation function of the field amplitude is given by:

$$\langle\hat{a}^\dagger(t)\hat{a}(0)\rangle = a^2\langle e^{i[\hat{\phi}(t)-\hat{\phi}(0)]}\rangle \tag{2.33}$$

Substituting Eq. 2.32 into Eq. 2.29 and considering the imaginary part to first order in products of operators, we have:

$$\ddot{\hat{\phi}} = -\frac{1}{2}(\kappa+\Gamma)\dot{\hat{\phi}} + \frac{1}{a}\,\mathrm{Im}[\hat{F}], \tag{2.34}$$

where a factor of $e^{-i\phi}$ has been absorbed into $\hat{F}$. Eq. 2.34 is then integrated, assuming that $(\kappa+\Gamma)$ is large, to arrive at:

$$\hat{\phi}(t) - \hat{\phi}(0) = \frac{2}{a_0(\kappa+\Gamma)}\int_0^t dt'\,\mathrm{Im}\left[\frac{\Gamma}{2}\hat{F}^a - \frac{iN\Omega}{2}\hat{F}^-\right]. \tag{2.35}$$

Since $\hat{F}^a$ and $\hat{F}^-$ are Gaussian, we can express:

$$\langle e^{i[\hat{\phi}(t)-\hat{\phi}(0)]}\rangle = e^{-\frac{1}{2}\langle[\hat{\phi}(t)-\hat{\phi}(0)]^2\rangle}, \tag{2.36}$$

Therefore, we can use Eq. 2.35, along with Eq. 2.11 to find:

$$\langle[\hat{\phi}(t)-\hat{\phi}(0)]^2\rangle = \frac{S_z+1}{2(1-S_z)}\frac{\Gamma}{(w+\gamma)}\frac{\Omega^2\kappa}{(\kappa+\Gamma)^2}t, \tag{2.37}$$

thus, the linewidth $\Delta\nu$, expressed in Hz, is:

$$\Delta\nu = \frac{S_z+1}{2(1-S_z)}\frac{\Gamma}{(w+\gamma)}\frac{\Omega^2\kappa}{(\kappa+\Gamma)^2} \tag{2.38}$$

### 2.1.3 Good cavity and bad cavity regime

Equation 2.38 describes the lasing linewidth of atoms within a cavity, irrespective of whether the cavity linewidth $\kappa$ is broader or narrower than the bandwidth of the gain medium $\gamma$.

Typically lasers operate in the good cavity regime where the cavity linewidth is much narrower than the bandwidth of the gain medium, hence $\kappa \ll \Gamma$. In this scenario, Eq. 2.38 simplifies to:

$$\Delta\nu \approx \frac{S_z+1}{2(1-S_z)}\frac{\Omega^2\kappa}{(w+\gamma)\Gamma} = \frac{S_z+1}{4S_z}\frac{\kappa}{|a|^2} \propto \frac{\kappa}{|a|^2}. \tag{2.39}$$

This expression is the famous Schawlow-Townes equation used to estimate the linewidth of a laser. In a good cavity laser, the linewidth is directly proportional to the linewidth of the cavity, indicating that the macroscopic phase information associated with the coherence of the generated radiation is encoded in the light field.

However, for a superradiant laser operating in the bad cavity regime where $\kappa \gg \Gamma$, Eq. 2.38 transforms into:

$$\Delta\nu \approx \frac{S_z+1}{2(1-S_z)}\frac{\Gamma}{(w+\gamma)}\frac{\Omega^2}{\kappa}, \tag{2.40}$$

In the limit where $d_0 = 1$, $\Gamma \approx w+\gamma$ and $w \gg \gamma, \frac{1}{T_2}$, this can be further simplified to:

$$\Delta\nu \approx \frac{S_z+1}{2(1-S_z)}\frac{\Omega^2}{\kappa} = \frac{1+S^z}{2(1-S^z)}C\gamma. \tag{2.41}$$

The linewidth in the bad cavity regime differs from the Schawlow-Townes linewidth for good cavity lasers. As the cavity linewidth $\kappa$ drops out of the linewidth equation, the coherence property of the bad cavity laser does not depend on the cavity linewidth. In the bad cavity regime, coherence is stored in the atoms, whereas in good cavity lasers, it's stored in the photons. These two types of lasing, normal lasing and superradiant lasing, can be thought of as the two extreme limits of a continuous crossover [68].

The linewidth of steady-state superradiant lasing is shown in Figure 2.4. As the pump rate $w$ increases and reaches the first threshold, $\gamma$, the linewidth starts to decrease. The minimum laser linewidth is $\Delta\nu = C\gamma$. Additionally, the optimal pump rate for achieving the maximum power and the minimum linewidth are compatible with each other, making this condition the target for experimentalists. Moreover, as pump rate $w$ continues to increase beyond $w_{max}$, the collective dipole is destroyed, and the linewidth increases rapidly. Figure 2.4 also presents the effects of different inhomogeneous lifetimes $T_2$. A longer $T_2$ could result in a narrower linewidth, and notably, for $T_2 = 10\,\mathrm{s}$, the narrowest linewidth region can become broader, making the output more stable with less pumping instability.

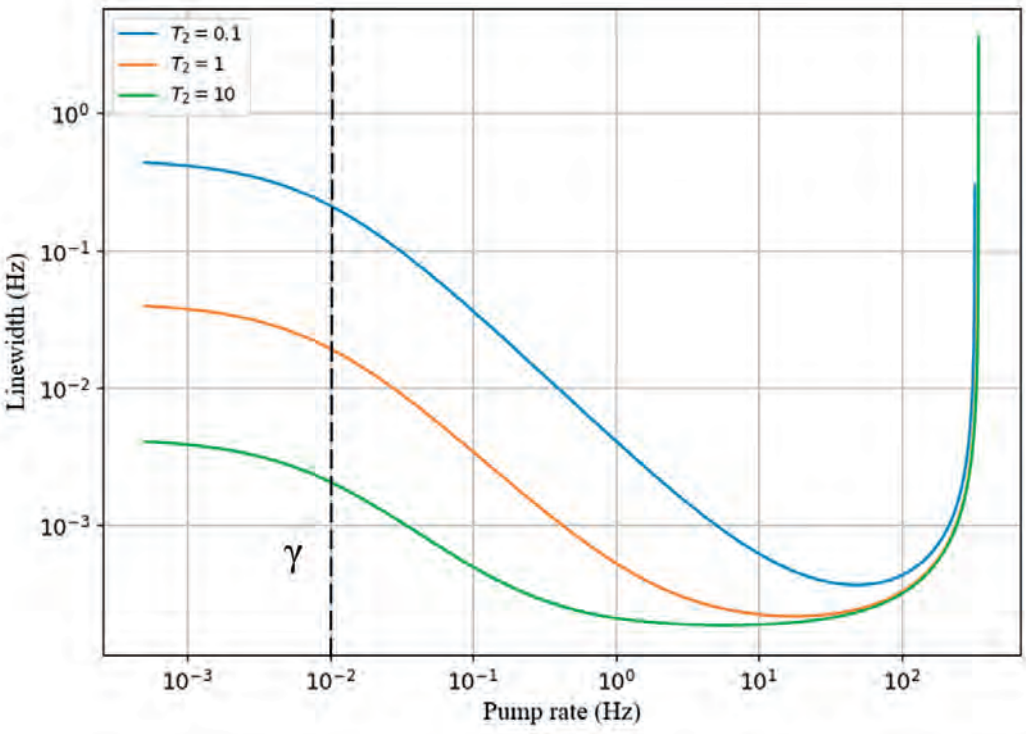


FIGURE 2.4: **Linewidth of steady-state superradiance as a function of pump rate for $10^6$ atoms.** The optimal pump rate, given by Eq. 2.26, achieves the narrowest linewidth $\Delta\nu = C\gamma$. The linewidth varies with inhomogeneous lifetime $T_2$. Longer $T_2$ results in a narrower linewidth within a broader range of pump rates.

In summary, the conditions and performance of steady-state superradiant lasing are listed in Table 2.1.

TABLE 2.1: Requirements for and properties of steady-state superradiant lasing.

| | |
|---|---|
| Required atom number | $2/(C\gamma T_2)$ |
| Optimal pump rate | $N\Omega/(2\kappa)$ |
| Maximum output power | $\hbar\omega_c N^2 C\gamma/8$ |
| Optimal linewidth | $C\gamma$ |

## 2.2 Experimental design

Our goal is to achieve the experimental realization of the first continuous superradiant laser. Based on the conditions outlined for steady-state superradiant lasing, we have devised two approaches to accomplish this goal. The first involves continuous superradiant lasing on the 1.35 mHz-wide $^1S_0$ - $^3P_0$ transition, utilizing ultracold strontium atoms. The second approach entails continuous superradiance on the 7.5 kHz-wide $^1S_0$ - $^3P_1$ transition, employing a hot strontium atomic beam.

Now, let's delve into the design considerations, commencing with the cavity and the process of loading the cavity for the millihertz (mHz) superradiant clock.

### 2.2.1 Linear cavity or ring cavity

As discussed, the cavity mediates the establishment of coherence between the atoms. In the case of the mHz transition ultracold atom superradiant laser, the cavity serves an additional function by supporting a magic wavelength optical lattice. This optical lattice traps the atoms along the cavity axis, ensuring operation within the Lamb-Dicke regime, and thereby suppresses Doppler shifts along this axis. The term "magic wavelength" denotes a specific wavelength at which the polarizabilities of the atomic clock states are the same. Under this condition the differential AC Stark shift induced by the lattice laser on the clock transition vanishes, thereby enhancing the frequency accuracy and precision of the superradiant laser.

The cavity design can follow two main approaches: employing either a linear cavity (Figure 2.1) or a ring cavity (Figure 2.6).

A linear cavity consists of a spacer holding two mirrors that oppose each other. Within this setup, standing waves are established in the cavity by the reflected beams of light between the mirrors. Ordinarily, standing waves can be generated by any two beams of light with the same linear polarization and frequency and propagating in opposite directions, without the need for a cavity. However, the presence of the cavity streamlines this process, requiring only one beam to build up the standing wave and guaranteeing a lattice that is spatially referenced to the cavity mirrors and that has a clean spatial mode. Moreover, the

cavity enhances the power of the lattice within the cavity mode, thereby necessitating less power from the beam.

In terms of cavity parameters, a smaller mode volume enhances the coupling between cavity and atoms. However, decreasing the mode volume increases the density of the atomic gas for a given atom number, resulting in frequency shifts of the clock transition due to collisions. This density-dependent shift can be significant, reaching approximately $8.9 \times 10^{-16}$ for $^{87}$Sr spin-polarized to $\pm 9/2$ [76, 77]. It also increases the inelastic collision losses which we will discuss in more detail later.

If one million atoms are trapped in the cavity mode within a cylindrical volume of 100 µm radius and 1 mm length the gas density is $3 \times 10^{12}\mathrm{cm}^{-3}$. This density causes a fractional frequency shift of about $3 \times 10^{-16}$. To render this shift comparable to other systematic shifts a factor ten reduction is desirable.

A potential solution is to expand the cavity waist by a factor of three. However, this option would diminish the coupling strength between atoms and cavity fields, thereby raising the atom number threshold, making it harder to achieve superradiance.

A second solution is to trap the atoms individually on the sites of a 3D lattice. A volume of $V_{\mathrm{eff}} = \pi(100\,\mu\mathrm{m})^2(1\,\mathrm{mm})$ could yield approximately $1 \times 10^9$ lattice sites. This method holds promise for achieving a large number of atoms while minimizing collisions. Researchers in Torun [78] are actively pursuing this approach.

A third solution is to increase the length of the gas sample along the cavity mode to 10 mm. This option is interesting, but rendered slightly complicated by the small size of the ultracold gas samples prepared by ultracold atom sources. One way to distribute the atoms along the cavity mode is to transport the small ultracold gas samples to different locations along the mode. Sequential loading of atoms into several locations achieves a large cavity-atom interaction volume despite a small atom source volume [79], as depicted in Figure 2.5. This method offers the additional advantage of enabling continuous superradiant lasing even with a pulsed ultracold atom source.

Another approach to distribute the atoms along the cavity is to use a ring cavity. In a ring cavity the magic wavelength lattice is created by the interference of laser beams circulating the cavity in opposite directions. The two beams are independently coupled into the cavity and their frequency can be controlled independently. By adjusting the frequency difference of the counter-propagating laser beams, the speed of the moving lattice can be finely controlled. Atoms can be fed into the cavity mode at a fixed location and are slowly transported along the cavity axis by the moving magic-wavelength lattice. This loading scheme provides flexibility in regulating the number of atoms within the cavity. Leveraging the cavity's large volumes and extended lifetimes, this method simplifies the storage of large quantities of atoms at low densities within the cavity mode.

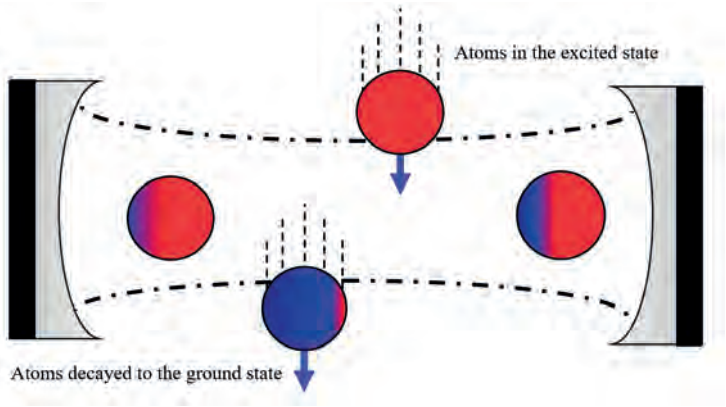


FIGURE 2.5: **Sequential loading of atoms into a linear cavity.** Ensembles of ultracold excited state atoms are prepared outside the cavity and then loaded at various locations into the cavity mode. Once the atoms in an ensemble have mostly decayed to the ground state, they can be removed from the cavity. The atom number in the cavity is kept roughly constant by continually feeding new ensembles into the cavity mode at the locations of the recently removed ensembles. Different colors represent the probability of atoms being in the excited state (red) and in the ground state (blue).

However, employing a ring cavity also comes with its challenges. It necessitates a more intricate cavity design and introduces complexities in atom loading. Furthermore, it is more difficult to avoid inhomogeneities that affect the clock transition frequency over the large volume of the atomic ensemble. Of particular importance is the Zeeman effect. The elongated sample requires us to maintain sufficiently homogeneous magnetic fields over centimeter-length scales, as opposed to sub-millimeter scales in case of the 3D lattice clock, which is a significant technical hurdle.

### 2.2.2 Continuous loading of ultracold atoms into the ring cavity optical lattice

Considering all factors, we ultimately opted for the ring cavity due to its innate ability to seamlessly load atoms from a continuously guided ultracold atomic beam. Given our prior success with guided beams in our atom laser project, we anticipate that the design and debugging of our continuous superradiant laser project will benefit from this choice. Furthermore, the ring cavity enables precise control over the moving lattice, facilitating the controlled loading of multiple atoms — a valuable experimental debugging tool. For the magnetic field uniformity, we simulated the utilization of magnetic shielding to achieve

a spread below 2 mG within 5 cm at a magnetic field magnitude of 2G, which ensures the required magnetic uniformity for $^{87}$Sr in the ring cavity.

The overall concept design of our continuous ultracold atoms "mHz" superradiant laser, as depicted in Figure 2.6, outlines a series of key operational steps. Initially, a continuously guided ultracold atomic beam is produced through a narrow-line red magneto-optical trap (MOT), following methodologies detailed in previous works [51, 53, 55, 56, 80]. This guided atomic beam continuously delivers atoms to a magnetically shielded, dark, and light-shift protected chamber where the superradiant clock operates.

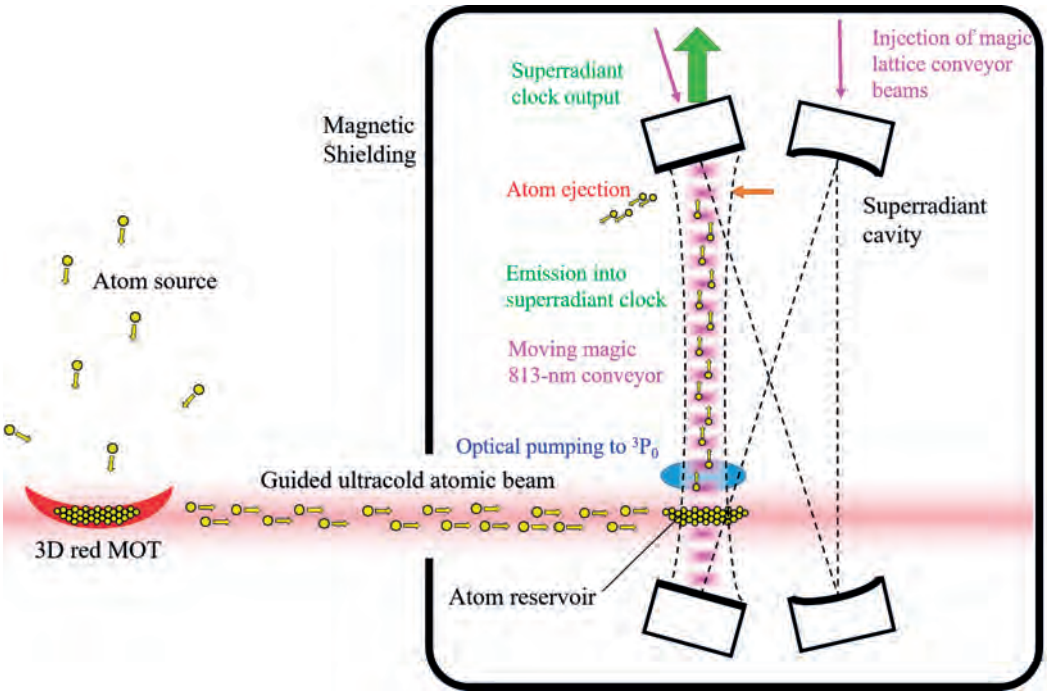


FIGURE 2.6: **The concept design of the continuous ultracold atom "mHz" superradiant laser.** Continuously guided ultracold atoms are slowed by a red molasses and stored in an optical dipole trap reservoir. From there atoms are transferred into the cavity mode by a magic wavelength moving optical lattice. After passing through an optical pumping area, atoms are in the $^3P_0$ excited state and then superradiantly lase into the cavity mode. Lastly, atoms are ejected to prevent them from coating the cavity mirror.

Then the guided atoms are decelerated and cooled by a red molasses into a dipole trap reservoir. Here, the Stark shift ensures that atoms in the optical reservoir are not resonant with and do not interact with the clock line. Subsequently, atoms are loaded into a vertical magic 813 nm conveyor lattice, which transports them through a pumping region where atoms are optically pumped to the $^3P_0$ state. As the atoms ascend through the cavity, they

emit into the superradiant cavity mode. Finally, the atoms are ejected to prevent coating of the high-finesse cavity mirrors.

Typically, only a few atoms are trapped within the vast 1D "pancake" of each lattice site, resulting in extended excited state lifetimes. A notable feature of this setup is the potential to repump atoms back to the $^3P_0$ state at multiple points along the cavity using an array of optical pumping spots, for example achieved by imaging an array of slits. This approach could increase the superradiant laser's output power by over an order of magnitude using the same atom source.

The flexibility of loading atoms longitudinally along the cavity mode also allows the cavity atom number to be continuously tuned by varying the speed of the magic conveyor lattice. By slowing the speed, it is possible to reach the superradiant lasing threshold and detect a signal even with loading fluxes nearly two orders of magnitude smaller than the design values. Similarly, decreasing the lattice speed can compensate for potential construction defects, such as low cavity finesse. Conversely, increasing the conveyor speed or moving the ejection beam to reduce the active cavity length can reduce the cavity atom number and eliminate pulsing. This flexibility is critical to cope with the enormous unknowns in trying to achieve our goal.

To estimate the performance of such a system and the requirements needed to reach the superradiant output threshold, we summarize the system parameters and perform some preliminary calculations in Table 2.2. These estimates primarily use the theory developed in Section 2.1 and assumptions based on existing research [53, 80].

Let's delve into the numerical analysis of continuous superradiant lasing using strontium.

Strontium has four stable, naturally occurring isotopes: $^{84}$Sr (0.56%), $^{86}$Sr (9.86%), $^{87}$Sr (7%) and $^{88}$Sr (82.58%). We'll focus on $^{88}$Sr and $^{87}$Sr. $^{88}$Sr is chosen due to its high natural abundance, enabling a high flux of ultracold atoms. However, its clock transition is strictly forbidden. To overcome this limitation, we can apply a strong magnetic field. With a 200G magnetic field, a linewidth of 12.4 µHz can be achieved. On the other hand, $^{87}$Sr has a natural linewidth of 1.35 mHz, but its flux is ten times lower than $^{88}$Sr. Moreover, its nuclear spin of $I = 9/2$ complicates the cooling and pumping processes.

We opt for a four-mirror ring cavity instead of a three mirror cavity for geometric symmetry. The mirrors include two flat mirrors and two with a radius of curvature of 250 mm, superpolished to minimize scattering. The total loss, including absorption and scattering from one mirror, can achieve 15 parts per million(ppm). The transmission at the clock transition wavelength of 698 nm is designed to be 10ppm, except for one mirror, which acts as an outcoupler for the superradiant laser beam, with a transmission of 40ppm.

TABLE 2.2: Analysis of the requirements for and performance of continuous superradiant lasing.

| | | $^{87}$Sr | $^{88}$Sr | $^{87}$Sr 10x Repumped | $^{88}$Sr 10x Repumped |
|---|---|---|---|---|---|
| **Operating transition** | | $^1S_0$ - $^3P_0$ | | | |
| **Externally applied magnetic field** | B | 1G | 200G | 1G | 200G |
| **Free space spontaneous emission rate/linewidth** | $\gamma/2\pi$ | 1.35 mHz | 12.4 µHz | 1.35 mHz | 12.4 µHz |
| **Cavity length** | L | 204 mm | | | |
| **Free spectral range (ring)** | FSR=c/L | 1.47 GHz | | | |
| **Cavity mode $1/e^2$ waist radius** | $\omega_{waist}$ | 130 µm | | | |
| **Cavity finesse** | F | 41,900 (1600 @ 813 nm) | | | |
| **Cavity linewidth** | $\kappa/2\pi$ | 35 kHz (917 kHz @ 813 nm) | | | |
| **Single atom/cavity cooperativity** | C | $C = \Omega^2/(\kappa\gamma) = 6F\lambda^2/(\pi^3(\omega_{waist})^2) = 0.234$ | | | |
| **Vacuum Rabi frequency** | $\Omega/2\pi$ | 3.3 Hz | 0.32 Hz | 3.3 Hz | 0.32 Hz |
| **Minimum linewidth / Purcell rate** | $C\gamma/2\pi$ | 315 µHz | 2.9 µHz | 315 µHz | 2.9 µHz |
| **Bad cavity regime? ($\gg 1$)** | $\kappa/\gamma$ | $2.6 \times 10^7$ | $2.8 \times 10^9$ | $2.6 \times 10^7$ | $2.8 \times 10^9$ |
| **Active cavity length** | $L_T$ | 25 mm | | | |
| **Optical pumping length** | $L_P$ | 0.5 mm | | | |
| **Cavity loaded atomic flux** | $\Phi$ | $1 \times 10^6$/s | $3 \times 10^7$/s | $1 \times 10^6$/s | $3 \times 10^7$/s |
| **Number of repumping cycles** | $N_R$ | 1 | 1 | 10 | 10 |
| **Maximum emitted power** | $\Phi N_R E_{ph}$ | 0.28 pW | 8.5 pW | 2.8 pW | 85 pW |
| **Collection + detection efficiency** | $\eta_D$ | 16% | | | |
| **Detectable power** | $P_D$ | 46 fW | 1.4 pW | 0.46 pW | 13.7 pW |
| **Detection bandwidth using Thorlabs PDA8A2:** 20dB SNR , NEP = 7.8 pW/$\sqrt{\text{Hz}}$, $P_{Max} = 78$ µW | $\frac{P_{Max}P_D}{(SNR \times NEP)^2}$ | 2.9 Hz | 175 Hz | 29 Hz | 1.76 kHz |
| **Detection bandwidth using [81]:** 20dB SNR, NEP = 12.8 pW/$\sqrt{\text{Hz}}$, $P_{Max} = 1.9$ mW | $\frac{P_{Max}P_D}{(SNR \times NEP)^2}$ | 26 Hz | 1.56 kHz | 260 Hz | 15.6 kHz |
| **Required active atoms $N_A$ in cavity mode for CW operation** | $\sqrt{\frac{8\Phi N_R}{C\gamma}}$ | $6.4 \times 10^4$ | $3.6 \times 10^6$ | $2 \times 10^5$ | $1.2 \times 10^7$ |
| **Cooperativity** | $CN_A$ | $1.5 \times 10^4$ | $8.5 \times 10^5$ | $4.7 \times 10^4$ | $2.7 \times 10^6$ |
| **Total number of atoms $N_T$ in cavity mode for CW operation** | $\frac{N_A(L_T - L_P)}{L_T - N_R L_P}$ | $6.5 \times 10^4$ | $3.7 \times 10^6$ | $2.5 \times 10^5$ | $1.4 \times 10^7$ |
| **Required lattice conveyor speed** | $v = \frac{L_T \Phi}{N_T}$ | 39 cm · s$^{-1}$ | 20 cm · s$^{-1}$ | 9.9 cm · s$^{-1}$ | 5.5 cm · s$^{-1}$ |
| **Required excited state lifetime** | $L_T/(N_R v)$ | $\gg$65 ms | $\gg$ 120 ms | $\gg$ 25 ms | $\gg$ 48 ms |
| **Required atom lifetime** | $L_T/v$ | $\gg$ 65 ms | $\gg$ 123 ms | $\gg$ 251 ms | $\gg$ 478 ms |
| **Required pumping rate** | $N_R v/L_T$ | 15 Hz | 8 Hz | 40 Hz | 21 Hz |
| **Maximum pumping rate** | $C\gamma N_A$ | 126 Hz | 66 Hz | 398 Hz | 209 Hz |
| **Average atoms per 1D lattice site** | $N_T\lambda/2L_T$ | 1.1 | 60 | 4 | 233 |
| **Density in the lattice** | $\rho$ | $1.2 \times 10^{10}$cm$^{-3}$ | $7.0 \times 10^{11}$cm$^{-3}$ | $4.7 \times 10^{10}$cm$^{-3}$ | $2.7 \times 10^{12}$cm$^{-3}$ |
| **Excited state inelastic loss rate** | $\beta$ | $1 \times 10^{-12}$cm$^3$/s | $2 \times 10^{-12}$cm$^3$/s | $2 \times 10^{-12}$cm$^3$/s | $2 \times 10^{-12}$cm$^3$/s |
| **Excited state collisional lifetime** | $\rho/\beta$ | 82 s | 720 ms | 21 s | 190 ms |

The finesse of the cavity is approximately $4 \times 10^4$, corresponding to a cavity linewidth $\kappa$ of $(2\pi)35\,\mathrm{kHz} \approx 220\,\mathrm{kHz}$, placing us in the bad cavity regime.

The finesse for the magic 813 nm moving lattice is about 1600. For a total input laser power of 5 mW, the trap depth for the atoms is about 10 µK. Since our atoms are about 5 µK cold, this ensures effective trapping. The atoms are pulled out of the reservoir by the conveyor belt magic wavelength optical lattice. After leaving the reservoir, they pass through a 0.5 mm long optical pumping region where they are pumped into the $^3P_0$ state. Subsequently, they enter an up to 25 mm-long cavity region where they collectively emit light. After that region the atoms are pushed sideways out of the conveyor lattice using 689 nm resonant light.

Of key importance is the number of atoms $N_A$ needed to interact with the cavity mode to achieve steady-state, continuous wave (CW) emission. We assume that at steady state, the superradiant output power is given by the maximum power output (Eq. 2.27), which also matches the power given by the atomic flux times the number of repumping cycles in the cavity:

$$P_{\max} = \frac{1}{8}\frac{hc}{\lambda}(N_A)^2 C\gamma = \frac{hc}{\lambda}\Phi N_{\mathrm{rp}}, \tag{2.42}$$

$$N_A = \sqrt{\frac{8\Phi N_{\mathrm{rp}}}{C\gamma}}, \tag{2.43}$$

where $C$ is the single atom cooperativity, $N_{\mathrm{rp}}$ is the number of repumping cycles, $\Phi$ is the atom flux loaded into the cavity and $\gamma$ is the transition linewidth.

The atom number $N_A$ also determines the optimal moving lattice conveyor time and the optimal moving lattice speed, as shown in Table 2.2. For a flux of $1 \times 10^6$ $^{87}$Sr atoms per second, the maximum emitted power is about 0.28 pW, while a higher flux of $^{88}$Sr can achieve 8.5 pW. Considering the losses of the cavity and the collection efficiency of the photodetector, 46 fW can be detected using $^{87}$Sr, and 1.4 pW using $^{88}$Sr. Since this power is too low to directly lock a diode laser, a heterodyne beat method can be used to lock a clock laser. For such a system, a low noise and high gain photodetector is needed. We analyze a commercial photodetector (Thorlabs, PDA8A2) and a custom-designed one. With a 20 dB signal-to-noise ratio (SNR), a locking bandwidth of 2.9 Hz can be achieved with the commercial photodetector using $^{87}$Sr, and 88 Hz can be achieved using $^{88}$Sr. With a custom-designed one, the bandwidth can be improved by a factor of 10. A higher locking bandwidth implies faster feedback from the superradiant laser to the clock laser cavity, reducing the requirements on the ultra-stable cavity of the clock laser. Another way to improve the bandwidth is to add more repumping spots to achieve higher superradiant

laser power. Ten times more repumping can result in a locking bandwidth of 15.6 kHz with $^{88}$Sr.

Loading more atoms into the cavity mode requires a slower conveyor lattice and also a longer lifetime of the atoms. Two-body inelastic loss [82–85] limits the lifetime of $^3P_0$ atoms. For $^{87}$Sr, the lifetime is estimated to be tens of seconds and for $^{88}$Sr, the lifetime is about one second. These estimates are calculated for a typical density in a lattice site for $6.4 \times 10^4$ $^{87}$Sr or $3.6 \times 10^6$ $^{88}$Sr atoms distributed over a 25 mm long region. This lifetime is longer than the time atoms stay in the moving lattice.

### 2.2.3 Other candidates

While strontium serves as our primary choice, it's not the sole contender. Our selection is largely dictated by the existing technology and hardware available in our laboratory.

In fact, a range of alkaline earth(-like) atoms (Mg, Ca, Sr, Yb, Hg...) present viable alternatives. Using the transitions for different elements outlined in Figure 2.2 and the continuous superradiance conditions and properties in Table 2.1, we can estimate the requirements for and performance from a continuous superradiant laser based on different elements.

The threshold atom number needed to achieve superradiance is inversely proportional to the transition linewidth $\gamma$. $^{171}$Yb has a natural clock transition linewidth of 10 mHz. This means the minimum atom number required to achieve superradiance would be ten times less than strontium for the same cavity. Alternatively, these additional atoms can increase the gain allowing the atoms to be repumped multiple times as they traverse the cavity increasing output power and locking bandwidths. $^{199}$Hg would even need less atoms or deliver more power with its 100 mHz wide transition.

Let us first assume similar flux cold atom sources and identical cavity parameters for these different elements, we can evaluate their performance and requirements using strontium as a reference, presented in Table 2.3. Then, we can assess the validity of this assumption for different species.

Strontium stands out for continuous superradiant lasing due to the minimum linewidth that can be achieved of about 315 µHz. It is more than two orders of magnitude better than the current best clock laser. An experimental benefit is its 7.5 kHz-wide $^1S_0 - ^3P_1$ transition, which facilitates the creation of a continuous ultracold atom source. However, a drawback of $^{87}$Sr superradiance is its lower output power compared to other species, resulting in a narrower detection bandwidth that demands a more precise clock laser. Moreover, $^{87}$Sr presents challenges with its ten nuclear spin states, making pumping processes more complex.

TABLE 2.3: Analysis of other alkaline earth atoms.

| | $^{87}$Sr | $^{171}$Yb | $^{199}$Hg | $^{24}$Mg |
|---|---|---|---|---|
| **Transition** | $^1S_0$ - $^3P_0$ | $^1S_0$ - $^3P_0$ | $^1S_0$ - $^3P_0$ | $^1S_0$ - $^3P_1$ |
| **Wavelength ($\lambda$)** | 698 nm | 578 nm | 265 nm | 475 nm |
| **Spontaneous decay ($\kappa/2\pi$)** | 1.35 mHz | 10 mHz | 100 mHz | 36 Hz |
| **Atom flux ($\Phi$)** | $1 \times 10^6\,s^{-1}$ | $1 \times 10^6\,s^{-1}$ | $1 \times 10^6\,s^{-1}$ | $1 \times 10^6\,s^{-1}$ |
| **Repump cycles ($N_{rp}$)** | 1 | 5 | 10 | 10 |
| **Required atoms in the cavity ($N_A$)** | $6.4 \times 10^4$ | $5.2 \times 10^4$ | $2.3 \times 10^4$ | $1.2 \times 10^3$ |
| **Required lattice speed ($v$)** | $39\,mm \cdot s^{-1}$ | $43\,mm \cdot s^{-1}$ | $86\,mm \cdot s^{-1}$ | $163\,mm \cdot s^{-1}$ |
| **Required pumping rate** | 15 Hz | 86 Hz | 342 Hz | 6.5 kHz |
| **Maximum pumping rate** | 126 Hz | 766 Hz | 3.4 kHz | 65 kHz |
| **Maximum output power ($\Phi E_{photo}$)** | 0.28 pW | 1.72 pW | 7.5 pW | 4.18 pW |
| **Detection bandwidth using [81]** | 26 Hz | 160 Hz | 696 Hz | 112 Hz |
| **Minimum linewidth** $(C\gamma/2\pi)$ | 315 µHz | 2.34 mHz | 23.4 mHz | 8.4 Hz |

Ytterbium emerges as a promising candidate for achieving continuous superradiance, thanks to its broader clock transition linewidth. This characteristic leads to a higher output power and a broader locking bandwidth, coupled with an impressive minimum linewidth of 2.34 mHz. By employing $^1S_0$ - $^1P_1$ and $^1S_0$ - $^3P_1$ transitions for cooling, a number of high-flux ultracold atom sources have been demonstrated [86]. Furthermore, its $^1S_0$ - $^3P_1$ transition, with a natural linewidth of 180 kHz, facilitates cooling and trapping of ytterbium even directly from the oven without the need for a Zeeman slower [87]. The $^3P_J$ - $^3D_J$ infrared (IR) transitions can also be useful for the optical pumping and cooling of atoms [88]. Additionally, possessing a nuclear spin of $I = 1/2$, $^{171}$Yb streamlines the pumping and cooling processes. Finally, numerous optical lattice clocks and high finesse reference cavities exist at 578 nm making stabilization and performance comparisons highly feasible.

Mercury also presents distinct advantages. Its transitions are situated far from infrared wavelengths, diminishing susceptibility to black-body radiation, which is a drawback faced by strontium and ytterbium. However, while a broader clock transition may facilitate achieving superradiance, it also leads to a wider minimum linewidth, which can be a drawback. Moreover, the clock transition occurs at deep ultraviolet wavelengths, posing challenges in constructing a high-finesse cavity. Additionally, cooling lasers for mercury operate at ultraviolet wavelengths, introducing fabrication challenges and imposing stricter requirements on optics.

Magnesium and calcium also benefit from reduced black-body radiation shifts. However, their excessively narrow clock transition linewidths necessitate the consideration of the $^1S_0$ - $^3P_1$ transitions instead. With natural linewidths in the tens of Hertz range, atoms decay significantly faster compared to other species. To address this challenge, options include loading fresh excited atoms more rapidly or implementing a faster repumping rate.

For these atoms an intriguing approach might be to utilize a hot atomic beam to enable superradiance, opening up new avenues for continuous superradiance.

Another promising candidate is cadmium. It has a very small blackbody radiation shift, can be cooled to 6 µK [89], and has a natural clock transition linewidth of 10 mHz. The clock transition occurs at a wavelength of 332 nm, which may presents challenges for creating a high-finesse superradiant cavity. For reference cavities, a cavity can be created at 662 nm, and the light can be frequency-doubled without introducing significant phase noise [90], a technique commonly used for strontium and ytterbium reference cavities. Additionally, a dispenser can be used to create a cadmium source for the magneto-optical trap (MOT), removing the need for an oven and Zeeman slower [89].

### 2.2.4 Hot atomic beam superradiant clock

Theoretical proposals [2, 91] advocate leveraging the broader $^1S_0$ - $^3P_1$ transitions of calcium or strontium to establish a superradiant laser based on a hot atomic beam. This may be capable of serving as an industrial frequency standard. As highlighted in Table 2.3, broader transitions necessitate faster traversal of atoms through the cavity mode. Thus, utilizing a hot atomic beam for superradiance presents a compelling option.

In the original theoretical proposal [2], a superradiant hot atomic beam laser consists of an oven effusing an atomic beam at a flux of $\Phi$. This atomic beam is pumped into the upper lasing state immediately before it passes through an optical cavity as illustrated in Figure 2.7.

To understand the requirements for hot beam superradiance, we utilize the equation derived in Section 2.2.2, where the atom number $N = \Phi\tau$, with $\tau$ representing the transit time, must exceed the required atom number in Eq. 2.42 with $N_{rp} = 1$ repump cycles. This yields the first requirement:

$$\Phi\tau^2 C\gamma > 8. \tag{2.44}$$

This condition ensures that a sufficient atomic flux traverses the cavity mode to surpass the superradiant lasing threshold.

The second requirement concerns the transverse velocity of the atomic beam. It necessitates that the atoms are sufficiently cold along the cavity axis so that they do not move by more than half the emission wavelength during their lifetime within the cavity:

$$\delta_D\tau < \pi, \tag{2.45}$$

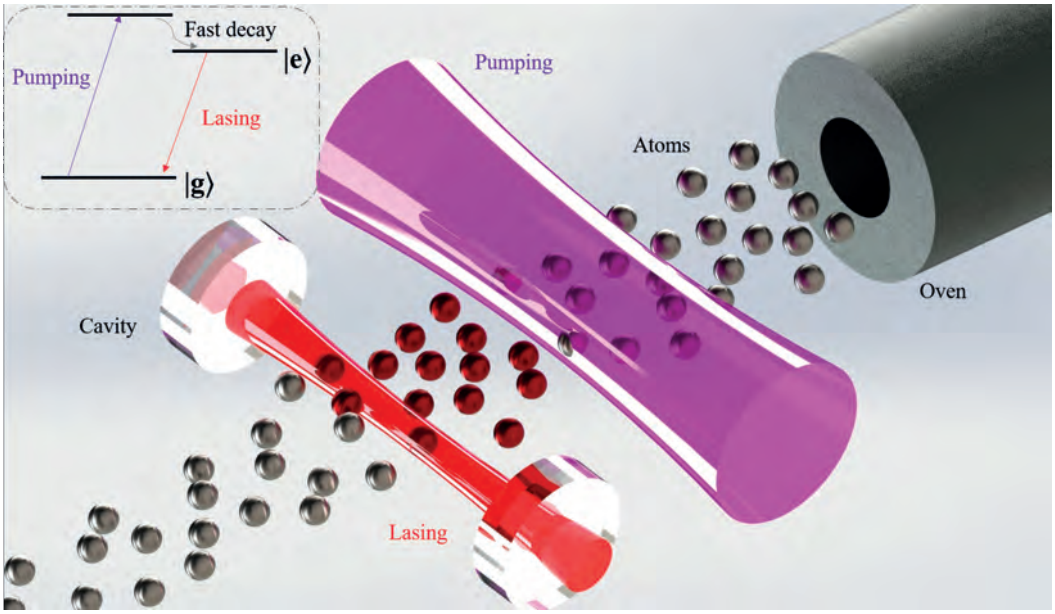


FIGURE 2.7: **The hot beam superradiant active clock architecture proposed by [2].** The hot atomic beam emitted by an oven undergoes optical pumping to reach the excited state before passing through the optical cavity. As the atoms traverse the optical cavity, they function as a continuous gain medium, sustaining the process of continuous superradiant lasing [2].

where $\tau$ represents the transit time of the atoms across the cavity, and $\delta_D$ denotes the Doppler linewidth of the atomic beam.

For a superradiant clock, it is crucial to operate in the bad cavity regime. This requires that the cavity linewidth ($\kappa$) is much greater than the collective coupling ($\sqrt{N}g$), the transit time broadening ($1/\tau$), and the Doppler broadening ($k\Delta v_z$). Additionally, it is assumed that the collective linewidth is much greater than both the Doppler linewidth and the transit time linewidth ($N\Gamma_c \gg k\Delta v_z$, $N\Gamma_c \gg \frac{1}{\tau}$).

The requirements and the corresponding performances for the system we have designed and constructed, as well as from the original proposal [2], are summarized in Table 2.4. In the original proposal, calcium and strontium were compared for the hot atomic beam superradiant laser.

The most significant difference is that the calcium $^1S_0$ - $^3P_1$ transition has a significantly narrower natural linewidth at 400 Hz compared to strontium's 7.5 kHz. Using a cavity designed with a $1/e^2$ waist radius of 310 µm, a length of 20 mm and a finesse of about 20, a calcium superradiant laser could achieve a minimal linewidth of just $(2\pi)7.9$ µHz. This is as good as the performance of state-of-the-art passive clocks. The trade-off when

TABLE 2.4: Theoretical analysis of the hot beam superradiant clock architecture by [2].

| | | Our $^{88}$Sr design parameters | $^{88}$Sr proposed in [2] | $^{40}$Ca proposed in [2] | $^{24}$Mg |
|---|---|---|---|---|---|
| **Operating transition** | | $^1S_0$ - $^3P_1$ | | | |
| **Wavevector** | $k = 2\pi/\lambda$ | $2\pi/689$ nm | | $2\pi/657$ nm | $2\pi/475$ nm |
| **Natural linewidth** | $\gamma/2\pi$ | 7.5 kHz | | 400 Hz | 26 Hz |
| **Atomic transverse velocity** | $v_x$ | $325\,m\cdot s^{-1}$ | $470\,m\cdot s^{-1}$ | $766\,m\cdot s^{-1}$ | $766\,m\cdot s^{-1}$ |
| **Cavity Length** | L | 78 mm | 20.8 mm | 22.8 mm | 22.8 mm |
| **Free Spectral Range (ring)** | FSR=c/(2L) | 5.64 GHz | 2.5 GHz | 4.54 GHz | 4.54 GHz |
| **Cavity mode $1/e^2$ waist radius** | $\omega_{waist}$ | 87 µm | 310 µm | 310 µm | 310 µm |
| **Cavity Finesse** | F | 78 | 20.8 | 22.8 | 22.8 |
| **Cavity linewidth** | $\kappa/2\pi$ | 72 MHz | 120 MHz | 199 MHz | 199 MHz |
| **Transit time** | $\tau = 2\omega_{waist}/v_x$ | 535 ns | 1.32 µs | 810 ns | 810 ns |
| **Transit time broadening** | $1/(2\pi\tau)$ | 297 kHz | 121 kHz | 197 kHz | 197 kHz |
| **Single atom/cavity cooperativity** | $C$ | $9.5\times10^{-4}$ | $2.0\times10^{-5}$ | $2.0\times10^{-5}$ | $2.0\times10^{-5}$ |
| **Vacuum Rabi Frequency** | $\Omega/2\pi$ | 22.7 kHz | 4.2 kHz | 1.3 kHz | 1.3 kHz |
| **Minimum linewidth/Purcell rate** | $\Gamma_c = C\gamma/2\pi$ | 7.1 Hz | 149 µHz | 7.9 µHz | 0.51 µHz |
| **Cavity pulling factor** | $\rho \approx /(\kappa\tau)$ | $1.6\times10^{-2}$ | $4\times10^{-3}$ | $4\times10^{-3}$ | $4\times10^{-3}$ |
| **Threshold flux** | $\Phi = 8/(\Gamma_c\tau^2)$ | $6.3\times10^{11}$ at/s | $4.9\times10^{12}$ at/s | $2.5\times10^{14}$ at/s | $3.8\times10^{15}$ at/s |
| **Threshold atom number** | $N_A = \Phi\tau$ | $3.4\times10^5$ at | $6.5\times10^6$ at | $2.3\times10^8$ at | $3.5\times10^9$ at |
| **Active cavity length** | $L_A$ | 15 mm | 50 mm | 20 mm | 20 mm |
| **Threshold flux irradiance** | $\phi = \Phi/(L_A\omega_{waist})$ | $4.8\times10^{11}$ at/s/mm$^2$ | $7.9\times10^{11}$ at/s/mm$^2$ | $1.6\times10^{13}$ at/s/mm$^2$ | $2.5\times10^{14}$ at/s/mm$^2$ |
| **Optimal flux** | $\Phi_\tau = 2\pi^2/(\Gamma_c\tau^2)$ | $1.5\times10^{12}$ at/s | $1.2\times10^{13}$ at/s | $6.1\times10^{14}$ at/s | $8.7\times10^{15}$ at/s |
| **Optimal atom number** | $N_A = \Phi_\tau\tau$ | $8.3\times10^5$ at | $1.6\times10^7$ at | $4.9\times10^8$ at | $7.5\times10^9$ at |
| **Optimal flux irradiance** | $\phi_\tau = \Phi_\tau/(L_A\omega_{waist})$ | $1.2\times10^{12}$ at/s/mm$^2$ | $2.0\times10^{12}$ at/s/mm$^2$ | $3.9\times10^{13}$ at/s/mm$^2$ | $8.5\times10^{14}$ at/s/mm$^2$ |
| **Maximum emitted power** | $0.7\Phi_\tau E_{ph}$ | 312 nW | 2.44 µW | 128 µW | 312 µW |
| **Maximum axial velocity** | $\pi/(\tau k)$ | $0.64\,m\cdot s^{-1}$ | $0.26\,m\cdot s^{-1}$ | $0.41\,m\cdot s^{-1}$ | $0.41\,m\cdot s^{-1}$ |
| **Target axial velocity** | $0.2\pi/(\tau k)$ | $0.13\,m\cdot s^{-1}$ | $0.05\,m\cdot s^{-1}$ | $0.08\,m\cdot s^{-1}$ | $0.0\,m\cdot s^{-1}$ |
| **Measured axial velocity** | $\Delta v_z$ | $0.5\,m\cdot s^{-1}$ | $0.26\,m\cdot s^{-1}$ | $0.41\,m\cdot s^{-1}$ | $0.41\,m\cdot s^{-1}$ |
| **Doppler broadening** | $k\Delta v_z/(2\pi)$ | 726 kHz | 377 kHz | 624 kHz | 624 kHz |
| **Cavity linewidth $\gg$ Transit linewidths** | $\kappa\tau \gg 1$ | 243 | 996 | 1014 | 1014 |
| **Cavity linewidth $\gg$ Collective coupling** | $\kappa/(\sqrt{N}\Omega) \gg 1$ | 3.5 | 7.1 | 7.2 | 7.2 |
| **Cavity linewidth $\gg$ Doppler linewidths** | $\kappa/(k\Delta v_z) \gg 1$ | 100 | 318 | 319 | 319 |
| **Collective linewidth $\gg$ Doppler linewidths** | $N\Gamma_c/(k\Delta v_z) \gg 1$ | 8.1 | 6.3 | 6.2 | 6.2 |
| **Collective linewidth $\gg$ Transit linewidths** | $N\Gamma_c\tau \gg 1$ | 20 | 20 | 20 | 20 |

using calcium is the higher threshold flux required. Similar calculations indicate that using magnesium could deliver another order of magnitude narrower output linewidth, but requiring another order of magnitude increase in flux.

Achieving higher flux is technically challenging and in practice introduces other unexpected issues. When debugging our hot beam superradiance machine, we realized that higher flux led to significant optical depth unbalancing molasses intensities and disrupting the axial molasses cooling process. Another issue we encountered was that running our hot strontium superradiance machine at a higher oven temperature to obtain more flux caused some parts of the vacuum viewports to become coated with strontium.

Compared with the original proposal [2] our continuous superradiant laser was designed for a lower required flux and more importantly, a lower required axial velocity. The much shorter lifetime of the strontium $^3P_1$ state means that a much smaller cavity waist is required if one wishes to avoid having the atoms decay to the ground state before transiting the mode. To this end, we selected a smaller waist size and a higher finesse cavity design. Specifically, we chose a significantly smaller cavity waist size of 87 µm instead of 310 µm, and a finesse of 78 instead of 20.8. The smaller cavity waist increased the allowable axial velocity by a factor of four but the mode volume and atom number were reduced by 16.

Another way to decrease the effective axial velocity spread of the atomic beam beyond what molasses can do is to incorporate axial cooling and a velocity-selection mechanism before the atoms enter the cavity. For our design, the details are presented in Section 3.1.3. Our key idea is to use the narrow 7.5 kHz transition to select and shelve the atoms with an axial velocity close to zero allowing rapid cooling to a very low effective temperature. In principle, axial molasses cooling can reach the Doppler temperature of the $^1S_0$ - $^1P_1$ 461 nm laser cooling transition of 0.73 mK, corresponding to a mean axial velocity spread of $\pm 0.3\,\mathrm{m/s}$. However, as mentioned earlier, the molasses beams are weakened while traversing the optically dense atomic beam, leading to a power imbalance between the molasses beams that varies across the atomic beam. This power imbalance results in cooling into a spatially varying axially moving frame and practical velocity spread closer to $\pm 2\,\mathrm{m/s}$. Shelving using the 7.5 kHz transition can in principle select and shelve atoms with velocity spreads at the $\pm 0.01\,\mathrm{m/s}$ scale. A new idea was proposed by Florian called the push-pump method where instead of using molasses to try to cool atoms to zero velocity, the atom velocity is instead pushed by imbalanced beams and the atoms are pumped to $^3P_0$ or $^3P_2$ as they pass through zero velocity.

Molasses cooling also functions as a velocity-selective cooling mechanism in the direction of the atomic beam travel. Slower atoms spend a longer time in the cooling beams. Consequently, the effective velocity of the atomic beam after molasses cooling can be lower than what would be expected from the oven temperature.

Another advantage of reducing the waist size is that it increases the single atom-cavity cooperativity due to a smaller cavity mode volume. This lowers the threshold atomic flux required for the superradiant laser. Our use of a higher finesse aimed to further reduce the flux requirements.

During design the flux was considered a less critical constraint due to the in principle rapid increase in vapour pressure and flux achievable from even modest oven temperature increases. An order of magnitude pressure (and thus flux) increase is naively expected for every 70 K temperature rise. In practice this is limited by the flow through the oven's microtube nozzle moving out of the molecular flow regime into the transitional flow regime.

While the parameters were chosen to significantly decrease the risk of not achieving continuous superradiance they also reduce the expected performance. As a result, cavity pulling is increased, the output power is decreased and the expected linewidth is increased. If successful, it was planned that another cavity could be placed into the machine to try a more ambitious parameter set.

To summarize, our hot atomic beam superradiant laser targeted an output power of $\sim$300 nW with a linewidth of 7 Hz, using the 7.5 kHz-wide transition of strontium. The measured experimental parameters are listed in red, and the corresponding calculated flux and velocity requirements are listed in blue in Table 2.4.

## 2.3 Summary

In this chapter, we establish the theoretical framework of superradiance and analyze the requirements and performance of steady-state superradiant lasing. Leveraging our experimental expertise, we identify strontium, ytterbium, and mercury as ideal candidates for realizing continuous superradiant lasing on the $^1S_0$ - $^3P_0$ transition of a cold atomic source. Additionally, superradiant lasing on the $^1S_0$ - $^3P_1$ transition could be effectively achieved using strontium or calcium. The subsequent chapters will delve into the detailed design and operation of a hot beam superradiant laser and a continuous cold atom superradiant laser.

Chapter 3

# Towards a superradiant laser based on a hot atomic beam

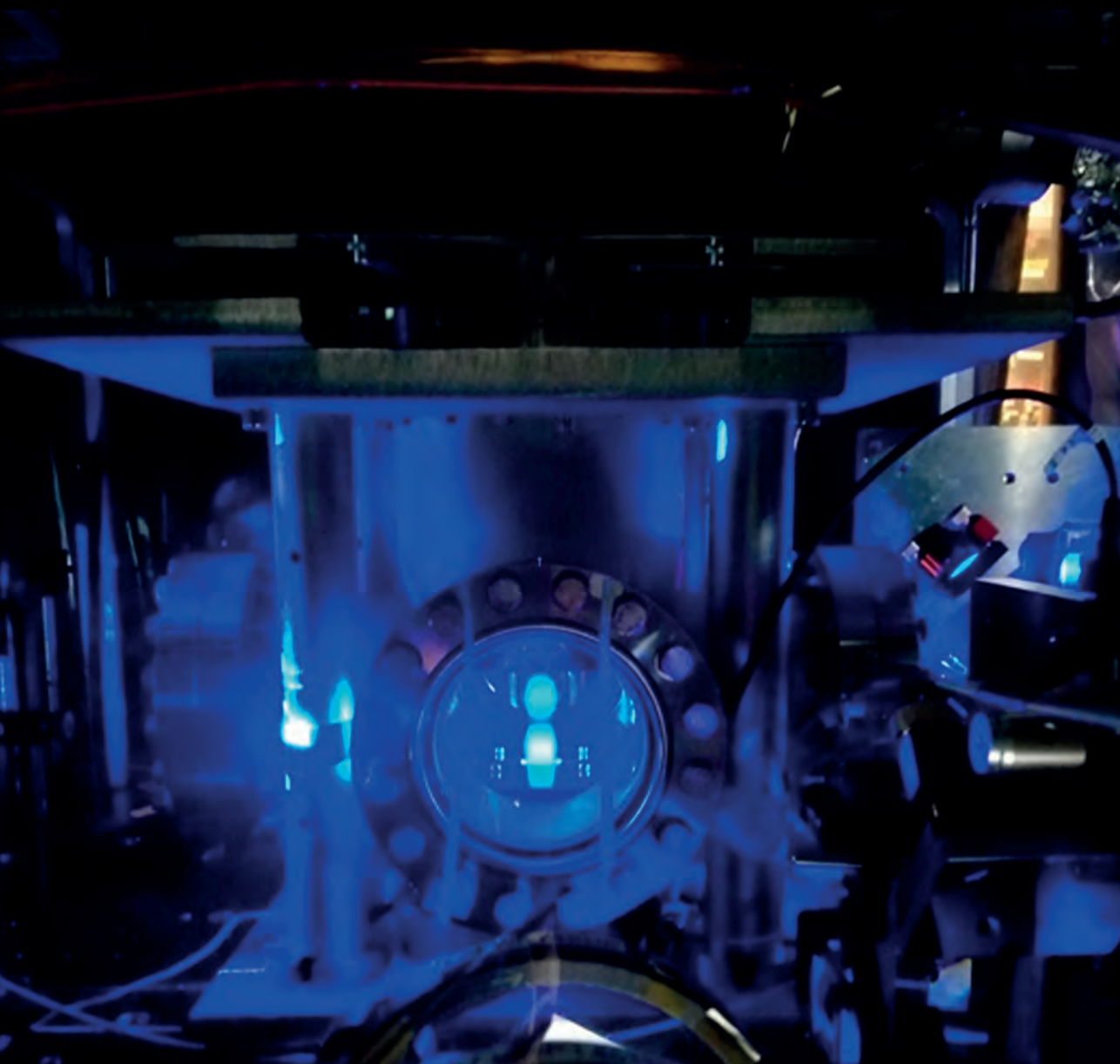

# Chapter 3

# Towards a superradiant laser based on a hot atomic beam

In this chapter, I will present a machine built to rapidly test the concept of using a hot atomic beam to create a superradiant laser. The architecture of the hot atomic beam superradiant clock is extremely simple but the theoretical minimum linewidth [2] is still competitive with excellent clock lasers. Moreover, it naturally works in a continuous modality, which has never been demonstrated for superradiant lasing so far. If this clock could be successfully demonstrated, it would not only be scientifically interesting to study but also industrially useful for implementing a compact, low-cost, rugged frequency reference, particularly for harsh environments without the cost and complexity of ultracold beam active clock approaches [67, 92], which will be presented in Chapter 4.

In Section 3.1, I outline the mechanical design of our vacuum system, featuring a novel atomic beam source and an optical cavity with an isolation stack. Additionally, I will describe the experimental design in detail, covering aspects such as (stage 0) transversal laser cooling, (stage 1) velocity-selected pumping to $^3P_0$,$^3P_2$, (stage 2) Doppler shifting of atoms that remain in $^1S_0$ after the optical pumping stage, and (stage 3) repumping atoms back to the $^3P_1$ state. These design choices are crucial for meeting the experimental requirements for superradiance. I will provide insights into the building processes, offering lessons learned for those interested. Some of the components of the hot atomic beam superradiant clock and the ultracold atom superradiant clock apparatus are very similar (lasers, electronics, an atomic beam oven). Chapter 3 only briefly outlines the design of those components as used for the hot beam apparatus, whereas Chapter 4 describes their details as used for the ultracold atom apparatus.

Lastly, Section 3.2 presents the debugging processes and some preliminary results. At the end of 2021, I moved to focus on developing the ultracold beam active clock that will be presented in Chapter 4 while my fellow PhD student, Francesca Famà continued to work on

the hot beam apparatus. I will not present any of the work done on the hot beam apparatus after this time for which the reader should refer to Francesca Famà's and Camila Beli Silva's PhD theses.

## 3.1 Experimental apparatus design and construction

The experimental aim for the hot beam apparatus was to rapidly test a new concept for producing a continuous active optical clock based on a hot atomic beam [2]. This vacuum system was rapidly designed and manufactured with the entire process from concept to first operation taking less than 8 months. While the hot beam concept has the potential to produce a very simple, compact device if proven viable, this machine is not targeting size, weight, or power considerations. Several design compromises were made to maximize fabrication speed, which could be improved with a second design iteration. Achieving compactness would be objective for a second-generation apparatus once the concept is found viable.

This Section will briefly introduce the design of the apparatus and the construction process. For a more detailed description of the machine design and construction, the reader should refer to our iqClock deliverables 4.3 [93], 4.4 [94] and 4.6 [95].

Our vacuum system for the prototype is shown in Figure 3.1 and a schematic diagram of the atomic processes used in the prototype to produce an active clock is shown in Figure 3.2.

### 3.1.1 Strontium beam source

Figure 3.1(a) illustrates the overall vacuum system and optics support structure and (d) is a photograph of the overall vacuum system. Because vacuum level is not critical to this application as the atoms transit from the oven to the cavity in just $\sim$1 ms, very short lifetimes are sufficient. An Agilent "StarCell" ion pump ($45\,\mathrm{L}\cdot\mathrm{s}^{-1}$) is used to maintain a vacuum in the range of $1\times10^{-7}$ mbar (depending on oven temperature). The ion pump is connected horizontally to a four-way cross, with an angle valve attached to the opposite port. The angle valve enables the initial pumping down of the vacuum chamber using a turbo-molecular pump.

Above the pump cross, a six-way cross provides optical access to both axes of the atomic beam for diagnostics and a potential future experiment, an anti-laser [97–99] with neutral atoms. Along the cavity axis, Brestwer windows are used to lower transmission loss in case an external cavity is needed for the anti-laser experiment. Along the other axis Anti-Reflection (AR) coated windows are used as we had some in stock when we constructed the apparatus.

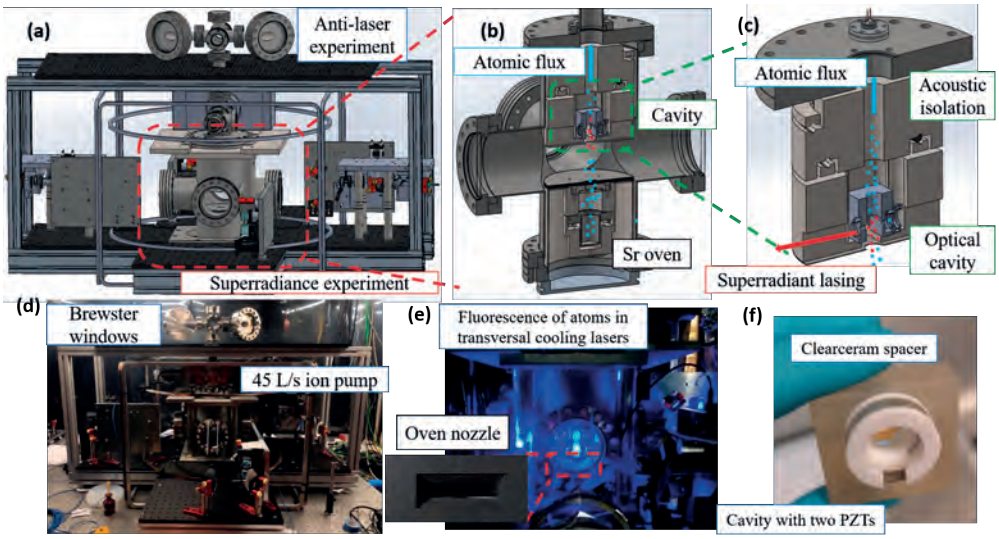


FIGURE 3.1: **CAD design and photos of the vacuum system of the hot atomic beam superradiant clock laser.** (a)-(c) show the CAD design of the vacuum system and zooms into the oven design and the cavity design. (d)-(f) show the physical realizations corresponding to the CAD designs. (a) The CAD design of the vacuum system and surrounding optics. The bottom part of the vacuum system, enclosed in the red dashed box, is the superradiance experiment and the top part was designed for a future experiment, an anti-laser [96, 97] using strontium. (b) The oven source and superradiant cavity assembly are mounted within a cross forming the core of the vacuum system. Atoms are emitted from the strontium oven through microtubes, which collimate the atomic beam. Before atoms enter the cavity mode, they are optically pumped into the $^3P_1$ state, shown with red dots. Newly entering atoms' phase synchronizes with the atoms already in the cavity, leading to collective, superradiant decay to the ground state. (c) The CAD design of the optical cavity is supported by an acoustic isolation stack. (d) The vacuum system is pumped with a 45 $L \cdot s^{-1}$ Aglient "StarCell" ion pump to maintain the vacuum. (e) In operation, one can see the beam of atoms emitted from the oven as it fluoresces blue in the (stage 0) transverse cooling laser light. The oven nozzle has a rectangular shape rather than a standard circular shape to better match the emitted flux to the full length of the cavity mode. (f) The optical cavity spacer is made from a low thermal expansion machinable "clearceram" glass from Ohara and two piezo rings are used to lock the cavity length while compensating for the thermal expansion of the piezos.

Both axes can be illuminated for fluorescence measurements using the 461 nm blue transition, enabling beam profile, flux, and temperature measurements transverse to the cavity axis. Retro-reflected beams on this transition also facilitate measuring transfer efficiencies of optical pumping stages 1 and 3. One example is presented in Section 3.5.

Below the pump cross is the main part of our superradiance experiment. An atomic beam is emitted vertically upwards from an oven, which is capable of operating at temperatures up to about 900 K. A rectangle shaped nozzle, presented in Figure 3.1(b) and (d), collimates the atomic beam. The rectangular nozzle shape is used to somewhat match the atomic beam shape to the cavity mode.

The nozzle consists of an array of 8 mm long stainless steel microtubes. Each has an inner diameter of 305 µm and an outer diameter of 414 µm. To prevent the nozzle from being blocked by strontium, the operating temperature of the nozzle needs to be higher than the oven temperature. Therefore two independent sets of three cartridge heaters (Omega CSH-101100/120V) are used to be able to heat up the oven and the nozzle independently.

One 10 g ampule of strontium (Alpha Aesar 99.95 % distilled dendritic pieces) was placed in the reservoir before baking the vacuum system at around 120 °C for a week primarily to remove water from the system.

### 3.1.2 Optical cavity for superradiant lasing

The centerpiece of the superradiant laser is its cavity. The design for the cavity and its acoustic isolation stack is shown in Figure 3.1 (c) and a photograph of the cavity is shown in Figure 3.1 (f). The cavity is mounted on the isolation stack, which is in turn suspended from a DN160 CF flange within the vacuum system in order to isolate it from environmental acoustic noise.

The optical cavity spacer is made of Clearceram glass-ceramic, which has an ultralow thermal expansion and features good machinability. The spacer was supplied by Laserstates in China. Since the cavity frequency needs to be on resonance with or very close to the atomic frequency, the cavity length must be actively stabilized to maintain resonance with the atomic transition. To achieve this, the mirrors are mounted to piezo-electric rings, shown in Figure 3.1 (f). The mirrors are chosen with an internal 100 mm concave radius of curvature, a nominal reflectivity of 96.5 % and were purchased from stock available at Layertec. The theoretical cavity waist for this geometry at 689 nm is 87 µm and the cavity length is 26.6 mm. These cavity parameters, finesse, mode size, and length are chosen based on a detailed numerical model of the system developed by Mikkel Tang from Copenhagen, which is described in detail in his thesis [100]. Ideally, a magic wavelength (915 nm with appropriate polarizations) would be used to probe the cavity length and lock it to the transition, but this would have required time consuming development of a customized mirror coating. The development of a dual band coating with a high reflectivity (99.98%) at 915 nm and locking using a magic wavelength laser, which is transfer locked to the 1 kHz linewidth stabilized $^1S_0$ - $^3P_1$ laser, could significantly improve the lock precision and thus

the laser's frequency accuracy (since the cavity pulling in this system is about 1%). This is envisaged for another generation of this machine. For the present system, we shift light that is stabilized to the 7.5 kHz-wide $^1S_0$ - $^3P_1$ transition by 2569.56 MHz using an 8-pass AOM and lock a neighbouring TEM02 spatial mode of the cavity to this light with a heavily filtered very slow locking bandwidth (about 1 Hz). In this way, the cavity noise is governed primarily by the performance of the passive acoustic isolation stack, whereas slow length changes are compensated by the piezos.

A two-stage acoustic isolation stack isolates the cavity from vibrations. It consists of 6.1 kg and 6.8 kg 304 stainless steel masses, which are each mounted on a ring of six 8 mm diameter viton balls from qlrubber.com. Since the mass of the first stage is the combined system mass, the resonant frequency for the same restoring force is $\frac{1}{\sqrt{2}}$ that of the second stage. To clean and outgas the viton balls, they are initially washed in isopropanol and then baked under vacuum for a week at about 1 mbar and 200 °C. The stack is supported using M6 304 stainless steel threaded rods with a 0.5 mm wide groove EDM eroded down the side to mitigate any virtual leaks. A 0.5 mm thick stainless steel 304 heat shield offset using stainless wave washers is mounted to the bottom of the isolation stack to reduce radiation from the oven on the cavity. A 17 mm diameter hole in the heat shield provides access for the atomic beam to the superradiant cavity. Initially, 3 mm diameter viton balls were planned to isolate the cavity spacer from the isolation stack to add another layer of acoustic isolation. This was not implemented, in part due to a manufacturing error but more importantly for fear that radiative heating of the viton with little thermal conduction path may overheat the glue, viton or UHV solder used on the cavity. Instead, the cavity location is maintained by squeezing two 6 mm diameter balls between the cavity spacer and each side of the recess in the lower stage of the isolation stack. A 20 mm diameter hole down the central axis provides a path for vacuum pumping and for the atomic beam to pass after transiting the cavity allowing it to be analyzed. Wires for the piezos use twisted pairs of kapton insulated 0.12 mm diameter copper wire (Allectra). The detailed processes of aligning and gluing the cavity mirrors to create the optical cavity were done by Mikkel Tang and is described in his PhD thesis [100].

A magnetic field coil "cage" (see Figure 3.1 (a)) is added to try to cancel earth and ion pump magnet fields, aiming to provide a more uniform bias field along the atomic beam propagation direction. Field non-uniformity, particularly along the ion pump axis, has been observed but hasn't significantly impacted transfer efficiencies due to the strong powers applied at 679 nm, 688 nm, and 707 nm. However, to address this non-uniformity, potential future improvements could include introducing smaller, localized coils to cancel the ion pump axis and adding additional shielding around the pump.

### 3.1.3 Laser cooling and optical state preparation

The processes used to cool and prepare the atomic beam for emission in the superradiant cavity are described in Figure 3.2. These processes all take place within the 85 mm clear aperture of a CF100 viewport in a customized six-way cross shown in Figure 3.1(b). The fluorescence from the laser cooling is clearly visible in Figure 3.3(a)(e).

Due to the need for operation at both 461 nm and 679-707 nm, off-the-shelf anti-reflection (AR) coated windows were not available. Delivery times for vacuum windows with customized AR coatings were 12 weeks, a timeline considered too long for this project. For this reason, uncoated windows were used with the chamber rotated with a 1° tilt to minimize the impact of stray reflections. While this choice may have been expedient for the rapid assembly of the vacuum system it created many problems downstream, particularly for the (stage 0) transverse cooling. (Stage 0) transverse cooling requires high illumination powers that are finely balanced over the entire beam. Diffraction edges or beam non-uniformities can have a serious adverse effect on the temperatures achieved. Each axis is illuminated by half the fiber coupled output power from an injection locked 0.5 W single mode diode laser (Nichia NDB4916).

To further increase the effective power a multipass beam configuration is used orthogonal to the cavity axis whereby a configuration of polarizers and waveplates allows each beam to pass the chamber up to 3 times increasing the spatial extent of the (stage 0) transverse cooling beams (see Figure 3.3(f)). Overall, a length up to 50 mm long could be illuminated with the first pass being at the output nearest the cavity and the second pass immediately above the oven nozzle. This complex arrangement was implemented to try to mitigate the impact of the reflection losses from the chamber windows but proved difficult to work with and keep optimized. With hindsight it would have been better to delay the vacuum system construction to be able to use fully AR coated windows. Later, as part of the vacuum system orders for the "ultracold superradiant laser" AR coated windows were purchased and exchanged.

Numerous laser systems are needed to operate this machine. The transitions they address are illustrated in Figure 3.2, while the arrangement of lasers around the vacuum chamber is shown in Figure 3.3. These lasers were initially built for the ultracold superradiant laser and as such the details of the laser systems will be presented in the next Chapter 4. Here, I will only briefly describe the parameters of these lasers as relevant for the hot beam machine. The 461 nm and 689 nm master lasers were locked to spectroscopy cells giving the 689 laser an absolute stability of around 1 kHz. The 679, 688, and 707 nm master lasers consisted of home-made external cavity diode lasers (ECDLs) that we constructed using an angle tuned narrow bandpass filter with "cat-eye" design [101]. We transfer locked these

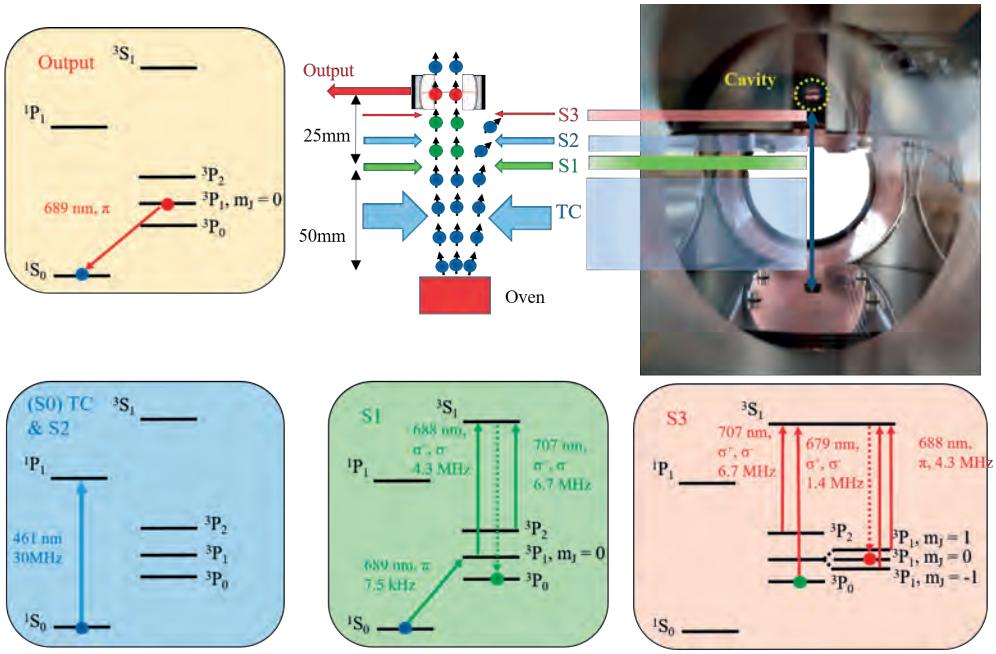


FIGURE 3.2: **Schematic of the hot beam superradiant clock apparatus.** (top) Schematic of the process used to produce an active clock. An atomic beam is emitted from an oven at around 900 K. The beam is transversally cooled (TC) over a length of about 50 mm. Stage 1 (S1): The atoms are then pumped to $^3P_0$ using a 5 mm diameter beam containing 689 nm ($\pi$ polarized), 688 nm ($\sigma^+$ and $\sigma^-$), and 707 nm ($\sigma^+$ and $\sigma^-$) light. The narrow 689 nm laser Doppler selects only atoms with a low velocity in the direction of the cavity axis, which is needed to meet the requirements of Table 2.4. Stage 2 (S2): Atoms remaining in the ground state are then heated using a blue detuned 461 nm laser beam in order to Doppler shift them out of resonance with the lasing transition. Stage 3 (S3): Immediately before entering the cavity mode, atoms are pumped from $^3P_0$ to $^3P_1, m_J = 0$. This is achieved using a $1 \times 15$ mm beam covering the cavity length to begin this process at a well-defined location. This beam contains 707 nm ($\sigma^+$ and $\sigma^-$), 688 nm ($\pi$ polarized) and a narrower $0.5\times$ 15 mm 679 nm ($\sigma^+$ and $\sigma^-$) beam. Output: Finally atoms in $^3P_1, m_J = 0$ pass through the cavity allowing them to phase lock and superradiantly emit, producing the optical clock output. The entire process takes place over a distance of less than 100 mm suggesting the size scale this device could be engineered to. The magnetic field is controlled to be aligned to the atomic beam propagation direction. (bottom) Level diagrams showing the transitions and states involved in each of these processes.

master lasers to our 1 kHz spectroscopically locked 689 nm laser using an approximately 10,000 finesse cavity with a free spectral range of 1.5 GHz. An array of injection locked diode lasers was used to amplify the laser power at each of the wavelengths used.

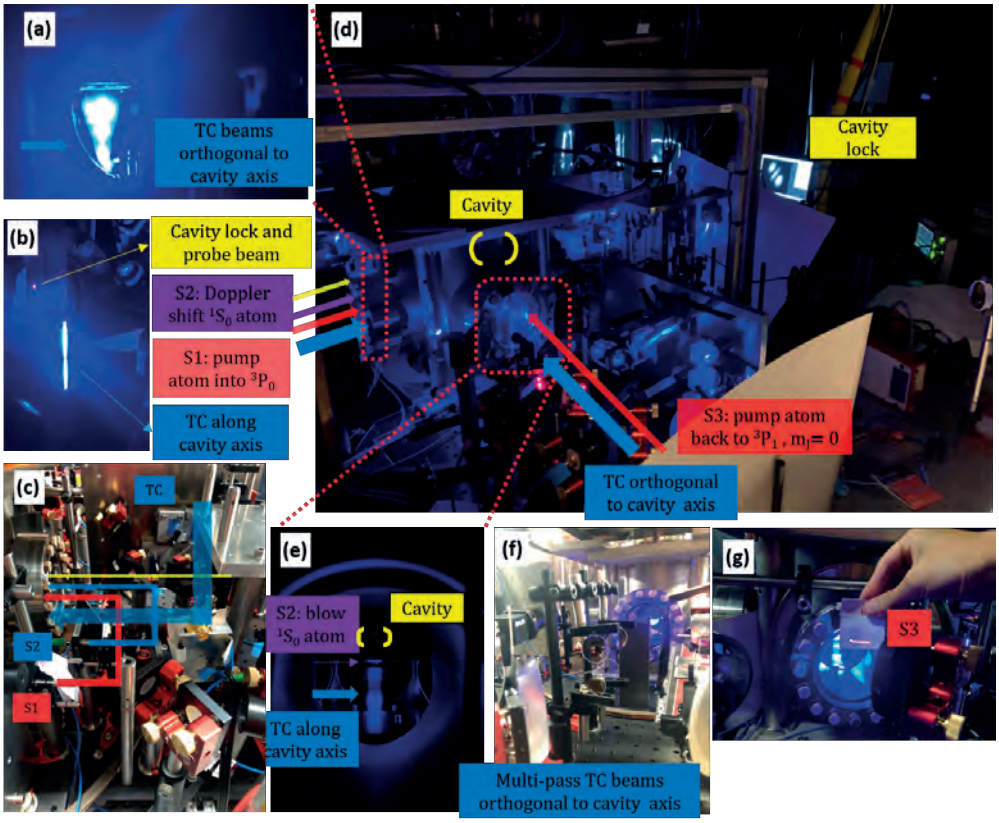


FIGURE 3.3: **Optics surrounding the hot atomic beam machine** (a) A side view shows the fluorescence from the hot atomic beam and the (stage 0) transverse cooling beams orthogonal to the cavity axis. (b)-(c) (stage 0) transverse cooling beams along the cavity, the stage 1 (S1) velocity-selected pump beam, stage 2 (S2) Doppler shift beam, and cavity lock and probe beam. (d) The alignment of all lasers presented in Figure 3.2. (e) Another side view displays fluorescence emanating from the atomic cloud and the S2 beam. (f)-(g) (stage 0) transverse cooling beams orthogonal to the cavity axis and stage 3 (S3) pump atoms back to the $^3P_1$ state.

The "cage" of magnetic field coils is employed to establish a vertical and uniform bias field of 1.5G, defining the field quantization axis. However, significant field non-uniformity was found particularly in the axis of the ion pump but also vertically due to insufficient separation and shielding between the ion pump and the active clock cavity. This problem was exacerbated by the use of large preexisting cage coils, which actually loop over the ion pump rather than designing and building an optimized coil set. So far the magnetic non-uniformity has not shown a noticeable effect on the stage 1 and stage 3 transfer efficiencies due to the strong powers applied at 679 nm, 688 nm and 707 nm, which are able

to accommodate the higher Zeeman splitting and the additional polarization components. However, the polarization of the 688 nm beam used for stage 3 is quite sensitive, so a much stronger vertical bias field may be used to overwhelm the non-uniformity and enforce the field orientation. A second mitigation, which has been prepared but not implemented, is the introduction of smaller more localized coils for the ion pump axis together with additional soft iron or mu-metal shielding around the ion pump magnet.

## 3.2 Debugging and preliminary results

The overall experimental setup is shown in Figure 3.4. It includes electronics, the laser and distribution system, the physics package, ECDL lasers, the transfer lock cavity as well as a reference clock laser needed to characterize the anticipated superradiant output. This reference clock laser consists of a Toptica ECDL locked to a commercial spherical cavity [102] from Stable Laser Systems using a FALC [103]. This provides the local oscillator that we need for the heterodyne measurements on the laser.

After I left the team, a modified oven was installed that has improved heating of the nozzle to reduce clogging. The cavity was also exchanged with one that has 10 times higher finesse. The higher finesse should dramatically reduce the atom flux requirements needed to achieve continuous superradiant lasing, although perhaps at the cost of being in the crossover regime between a laser and a superradiant laser rather than clearly a superradiant laser (meeting the conditions discussed in Chapter 2 and in [2]). These changes will be described in Francesca or Camila's theses. Here, I will present the debugging of the first generation hot beam superradiant laser setup and the preliminary results achieved while I was part of the team.

The most important parameters we wanted to measure were the atom number in the cavity mode and the average velocity of atoms along the cavity axis. With these two parameters, it is possible to estimate how close the experiment is to meeting the requirements for superradiant lasing as presented in Section 3.1.

### 3.2.1 Indirect measurements of atom number in the cavity mode and velocities along the cavity axis

Several methods were used to measure the atom number in the cavity mode. One indirect way is to use a fluorescence image to measure the atom number in the top chamber, shown in Figure 3.5. With a measurement of the atomic density, the atom number in the cavity mode can be calculated geometrically. To achieve this measurement, two 461 nm probe beams that propagate orthogonal to the atomic flux, one parallel to the cavity axis and

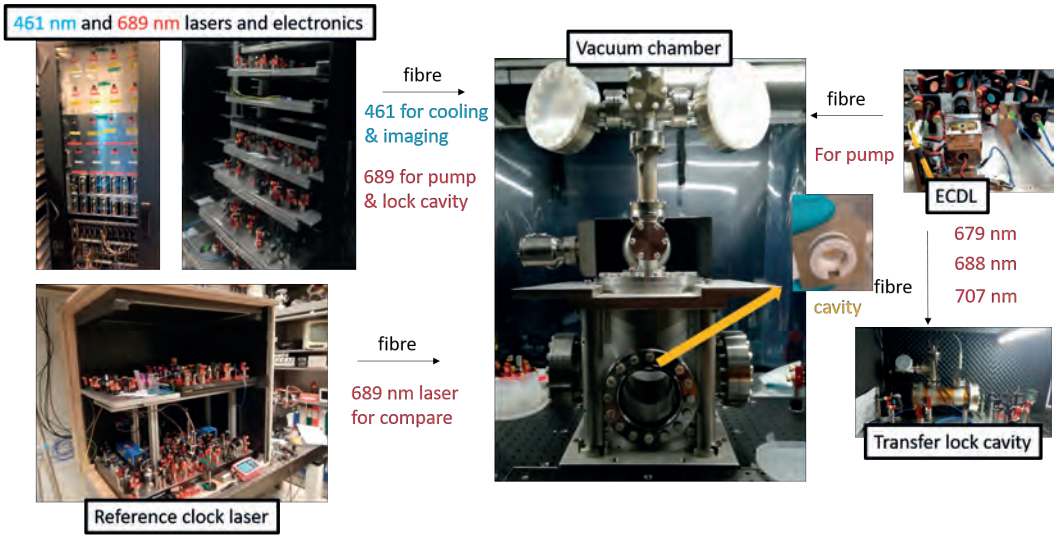


FIGURE 3.4: **The hot atomic beam superradiant clock.** This clock includes 461 nm and 689 nm injection locked laser sources, laser beam control and distribution systems, and electronics needed for cooling, probing, and pumping the atoms. The laser beams are delivered through fibers to the vacuum chamber. Inside the vacuum chamber, there is a Sr oven and an optical cavity. 679 nm, 688 nm, and 707 nm repump lasers are transfer locked to a cavity. The cavity length is stabilized by locking it to a kHz-linewidth 689-nm laser, which is itself locked onto another cavity for short-term stability and a spectroscopy cell for long-term accuracy. A reference "clock laser" consisting of an ECDL locked to a Stable Laser Systems cavity was built to provide the local oscillator needed for heterodyne characterization of the superradiant output and to help with debugging.

one orthogonal, were used at the top of the vacuum chamber. These probes were used to monitor how the atom number changed when applying one or more of the preparation stages, which are (stage 0) transverse cooling, (stage 1) pumping of atoms to $^3P_0$, (stage 2) blowing away remaining $^1S_0$ atoms with 461 nm light, and (stage 3) pumping of atoms from the $^3P_0$ state to the $^3P_1$ state. The advantages of this method are: 1) it can estimate atom numbers and density profiles quickly to see if every stage is working, as shown for example in Figure 3.5, and 2) it provides a two-axis measurement of the atoms' velocity along the cavity axis and orthogonal to the cavity axis. The disadvantages are: 1) the measurement is rough, and 2) it is not a direct measurement as the beams are about 0.5 m above the cavity.

Two more absorption imaging setups were built around the cavity. One uses a blue probe beam along the cavity axis. The other uses a blue probe beam orthogonal to the cavity. They monitor flux close to or in the cavity mode rather than estimates from measurements in the top chamber. This makes them more precise and accurate for measuring the atomic

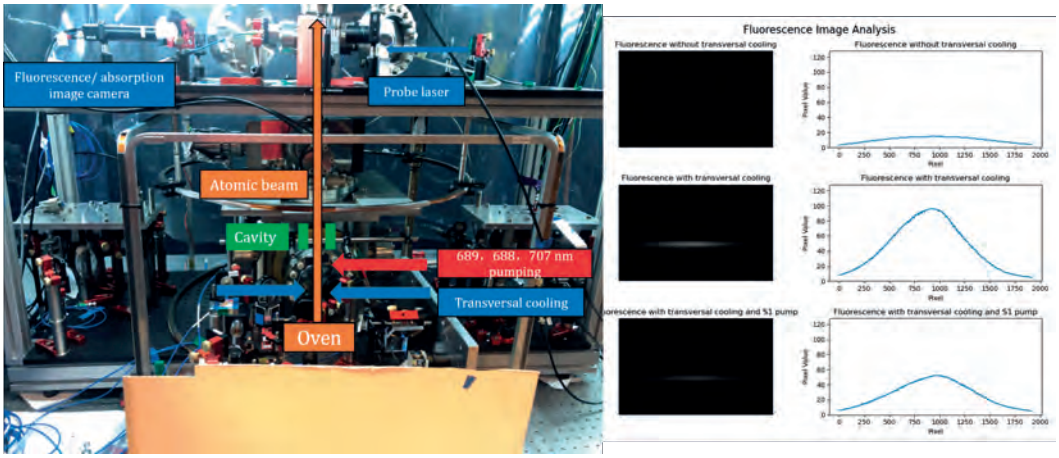


FIGURE 3.5: **Blue fluorescence imaging of atoms in the top chamber.** The probe beams are located in the top chamber. They are very useful for aligning the laser beams used for the different stages and for monitoring if every stage is working. The example images show how the fluorescence changes with and without (stage 0) transverse cooling.

flux in the cavity mode.

A third approach to measure the atom number density is measuring the probe absorption by the atomic beam rather than fluorescence. Absorption is more quantitative than fluorescence especially in optically dense beams.

I set up these measurements and performed the initial data collection at low oven temperatures. The indirect measurements estimated typical intra-cavity atom numbers of around 5000 atoms at an oven temperature of 350 °C. The design temperature for the oven source was 600 - 650 °C and the simulated threshold for superradiance was an intracavity excited state atom number of just over $6 \times 10^5$ atoms [100]. Given that the vapor pressure for strontium increases by around one order of magnitude for every 70 °C this gave an exciting prospect with initial flux measurements consistent with numerical estimations. Measurements at higher oven temperatures were undertaken in the following weeks and are documented in Figure 3.6 of iqClock deliverable 4.6 [95]. These will be included in Francesca Famà's or Camila Beli's thesis.

Transverse laser cooling was able to reduce the mean velocity along the cavity axis to below 1 m/s and along the orthogonal axis to below 0.5 m/s.

Stage 1 of the optical state preparation achieved 90% transfer efficiency from the $^1S_0$ to the $^3P_0$ and $^3P_2$ metastable states.

### 3.2.2 Direct measurements of atom numbers in the cavity mode and velocities along the cavity axis

To more precisely estimate atom numbers and velocities, two frequency-modulated (FM) spectroscopy systems were constructed, each probing with light near the 689 nm $^1S_0$ - $^3P_1$ transition. The first system used a probe beam located just below the cavity. That beam has a large waist (0.5 mm) to reduce the transit time broadening compared to the one experienced by atoms traversing the cavity mode itself. The second system used a beam coupled to the fundamental mode of the cavity with the cavity locked on resonance with the transition. Phase modulation was applied to the beams below and through the cavity at 20.44 MHz and 12.7 MHz respectively, forming sidebands on the FM spectroscopy probe. For the system probing the cavity mode, this spectroscopy is similar to the NICE-OHMS technique [104]. To separate the signal components that are due to atoms with relevant axial velocities, the number of atoms in $^1S_0$ with relevant velocities is modulated by turning the 689 nm stage 1 component off and on (typically at 2.5 kHz). The narrow 7.5 kHz transition used by stage 1 allows the selection of the velocity classes pumped to $^3P_0$ and $^3P_2$. The $^1S_0$ atom number modulation passing through the probes causes sidebands to appear on the detected signal at the modulation frequency. The sidebands caused by the presence of the modulated atomic beam are shown in Figure 3.6(a). This allows atom numbers in the cavity mode as well as their axial velocity distributions to be calculated.

The atoms from the atomic beam passing through the cavity mode can be imaged by fluorescence along the cavity axis as shown in Figure 3.6 (b). Here atoms passing through the cavity are illuminated by a retro-reflected $^1S_0$ - $^1P_1$ beam propagating orthogonal to the cavity axis, giving a fluorescence signal. Atoms traveling through the cavity mode itself can be pumped to $^3P_1$ by a resonant beam. Atoms in the $^3P_1$ state no longer fluoresce, casting a "shadow" of the cavity mode into the atomic beam that has passed through the cavity mode. By strobing the fluorescence illumination light and the cavity probe beam, the atomic beam velocity can also be estimated from the spacing of the region containing $^3P_1$ atoms giving an estimated mean velocity of $325 \pm 25$ m/s.

Next we measure the efficiency of the transfer of atoms to the excited $^3P_1$ state. First the stage 2 Doppler shifting beam is used to Doppler shift any atoms remaining in the $^1S_0$ state out of resonance. Then the stage 3 pumping beam is used to transfer the atoms stored in $^3P_0$ back to $^3P_1 m_J = 0$, the upper lasing state. In total, the optical state preparation achieved 50% transfer efficiency from the $^1S_0$ to the $^3P_1 m_j = 0$. We observed a beat between a very weak (<100 nW) probe beam on the $^1S_0$-$^3P_1$ transition passing through the cavity and the 689 nm reference laser. When we modulate the stage 3 pumping beam we were able to observe sidebands at the modulation frequency on the beat signal. The existence of

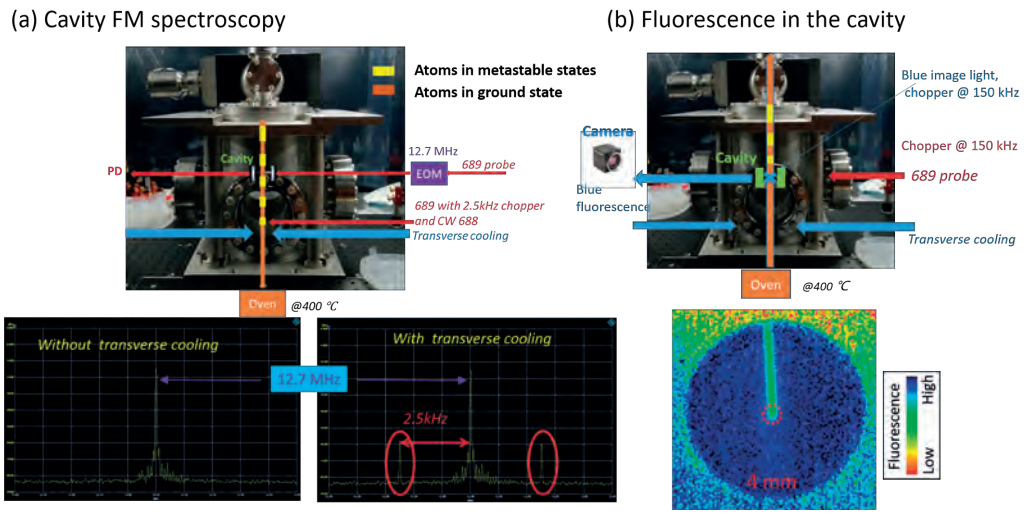


FIGURE 3.6: **Preliminary results showing atoms coupling to the cavity mode on the $^1S_0$ - $^3P_1$ transition.** (a) 2.5 kHz sidebands introduced by modulating S1 at that frequency on an FM spectroscopy signal at 12.7 MHz, which probes atoms passing through the cavity mode on the $^1S_0$ - $^3P_1$ transition. (b) Normalized $^1S_0$ - $^1P_1$ fluorescence image of atoms passing through the cavity mode imaged along the cavity axis through the 4 mm aperture of the cavity spacer. The atomic beam travels vertically with a mean velocity of 325±25 m/s. At the center of the image, a resonant 689 nm $^1S_0$ - $^3P_1$ beam pumps atoms passing through the cavity mode into the $^3P_1$ state where they no longer fluoresce reducing the fluorescence from the cavity mode upwards along the flight path of the atoms.

these sidebands, this beat, showed that there was a modulation in the number of atoms in the cavity mode in either the $^3P_1$ or the $^1S_0$ states which modulate the transmitted 689 nm probe laser power.

If the distance between the stage 3 pumping beam and the cavity mode is large, most atoms pumped from $^3P_0$ and $^3P_2$ to $^3P_1$ by stage 3 will have decayed to $^1S_0$ before crossing the cavity mode. In that case, the atomic population in the cavity alternates between not influencing the probe beam and absorbing the beam, creating the sidebands. If the distance is small, the population alternates between $^3P_0$, $^3P_2$ and $^3P_1$, leaving the probe beam uninfluenced or amplifying it. In our preliminary study reported here we didn't distinguish these two scenarios. Nevertheless this initial detection of sidebands showed that we successfully transferred atoms to $^3P_1$, indicating potential gain even at very low oven temperatures of just 500 °C. This result is shown in Figure 3.10 of the final iqClock deliverable 4.6 [95]. After that, the machine was characterized as a function of oven temperature indicating that the atom number measured in the cavity in the excited $^3P_1$ state

was almost reaching the threshold for superradiant lasing calculated by Mikkel [100]. This result is shown in the final iqClock deliverable 4.6 [95].

While preliminary, these initial results showed great promise and it was expected that this machine would rapidly progress to the first successful demonstration of continuous superradiance and an active optical clock.

Chapter 4

# Towards a continuous ultracold superradiant laser on the mHz transition

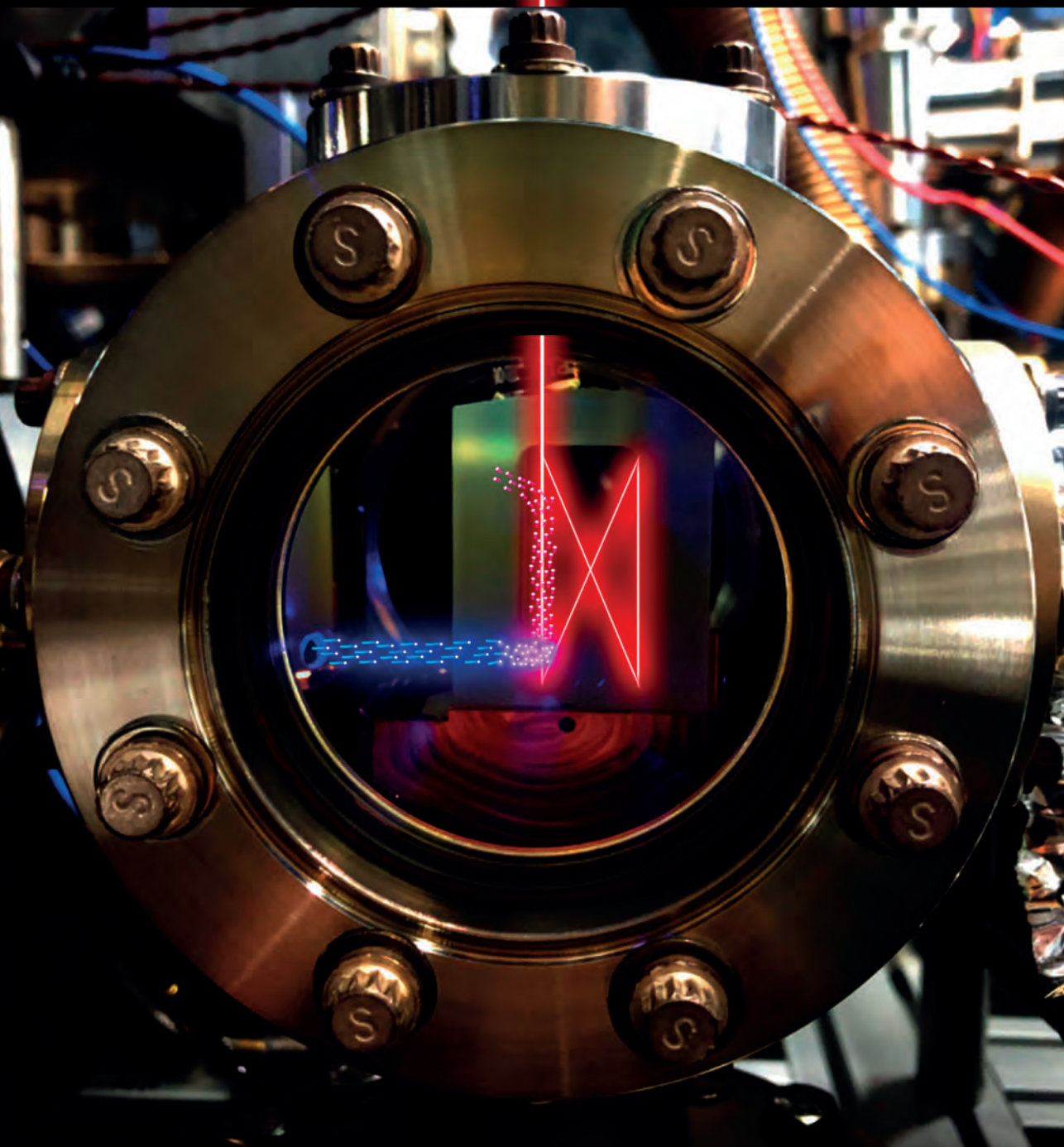

# Chapter 4

# Towards a continuous ultracold superradiant laser on the mHz transition

In this chapter, I will detail the design and construction of our continuous superradiant laser that operates on the $^1S_0$ - $^3P_0$ (698 nm) "clock" transition of ultracold strontium atoms. This transition has a natural linewidth of just 1.35 mHz for fermionic $^{87}Sr$ and is typically much narrower using bosonic isotopes like $^{88}Sr$. The core concept of the laser revolves around the creation of a continuous ultracold atom source, followed by loading these atoms into an optical cavity. A passive optical clock operating at 698 nm that is currently in the construction phase will be utilized to characterize the frequency stability and accuracy of the superradiant laser. The subsequent sections will offer a comprehensive overview of the design and construction processes involved in creating a continuous source of ultracold strontium atoms, in designing the superradiant laser cavity, and in loading ultracold atoms into this cavity.

## 4.1 Continuous ultracold strontium source

The complete conceptual and CAD designs for the ultracold atom $^1S_0$ - $^3P_0$ superradiant clock are depicted in Figure 4.1. The system involves a continuous cold beam of strontium atoms being created, loaded, and trapped within a magic moving lattice that propagates along the superradiant cavity mode. This approach allows for the controllable loading of many atoms into the cavity mode while maintaining low atomic densities and long lifetimes.

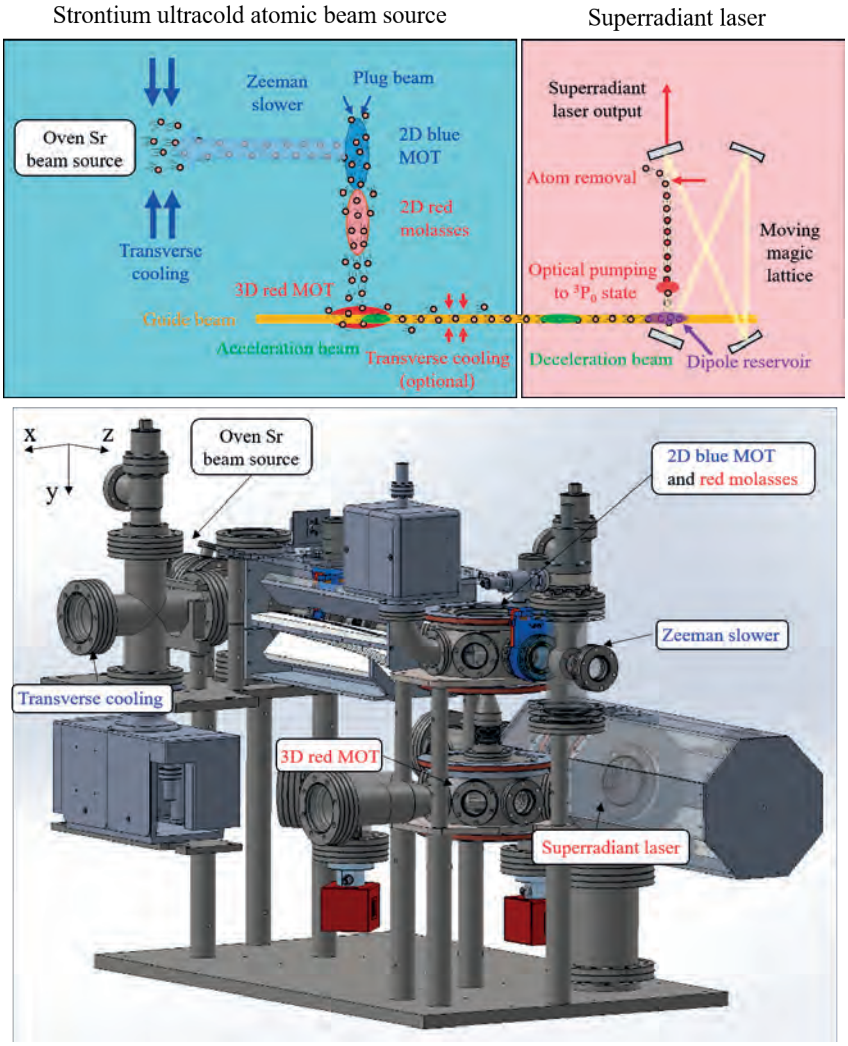


FIGURE 4.1: **The concept design and CAD representation of the continuous superradiant clock.** The continuous ultracold atom source consists of an oven, transverse cooling, a Zeeman slower, a 2D blue MOT, 2D red molasses and a 3D red MOT. The atoms are then transferred to an optical cavity to achieve superradiance. Atoms are accelerated to escape the red MOT, then decelerated and stored in a dipole trap overlapped with the cavity mode. Finally, the atoms are loaded into the cavity by a moving lattice and pumped to the excited state. Harnessing the capabilities of the cavity, the atoms collectively emit radiation, serving as a clock signal.

The process begins with strontium gas produced by the sublimation of metallic strontium in a heated oven. Subsequently, the strontium gas effuses through a collimating

nozzle and is further collimated by transverse cooling lasers. The atoms are then slowed along their emitting axis using a Zeeman slower and subsequently captured by a 2D blue Magneto-Optical Trap (MOT). Atoms trapped in the 2D blue MOT escape vertically and are transversally cooled by 2D broadband red molasses before being decelerated and captured by a 3D red MOT in a separate, lower chamber. The steady-state red MOT is established in a separate chamber to prevent heating from scattered blue light and to avoid magnetic field interference from the blue MOT.

This section will systematically outline each component of the design and construction process, while also discussing the lessons we learned and proposing potential improvements for future iterations of the active clock machine.

### 4.1.1 Oven source

Our requirements for the oven design included three main objectives. Firstly, the oven must be able to heat up to $\sim$550 °C to create a high flux of strontium. Secondly, there must be a temperature difference of $\sim$30 K between the nozzle and the reservoir to avoid strontium blocking the nozzle. Finally, we aimed to try a new approach of using a vacuum between the heater and the outside of the vacuum chamber to isolate the hot oven in order to reduce the oven size and the heating and cooling power requirements. The CAD design of our oven based on these considerations is shown in Figure 4.2. I will now briefly describe the various components.

**Strontium reservoir** Two 5 g samples of metallic strontium (purity of 99.95% sourced from Alfa Aesar) are loaded within a stainless-steel nipple featuring a DN16CF flange. The strontium reservoir is sealed using an annealed nickel gasket, connecting it to a specially designed tube. The opposite end of this tube is joined with the nozzle (refer to Figure 4.3(b)).

**Collimation nozzle** The nozzle comprises an array of microtubes shown in Figure 4.3(a), which is apertured by a 5 mm diameter cover plate to select the microtubes close to the desired beam axis in order to efficiently use the emitted flux. The microtubes were purchased precut and deburred from microgroup.com. They were type 304H27X, 8 mm in length, with a nominal inner diameter of 305 µm and an outer diameter of 414 µm, all fabricated from stainless steel 304. The array consisted of 650 tubes, with approximately half within the 5 mm diameter aperture and being actively utilized. Silver plated socket head vented screws from Vacom were used throughout the installation in the vacuum to try to avoid seizing of the screws.

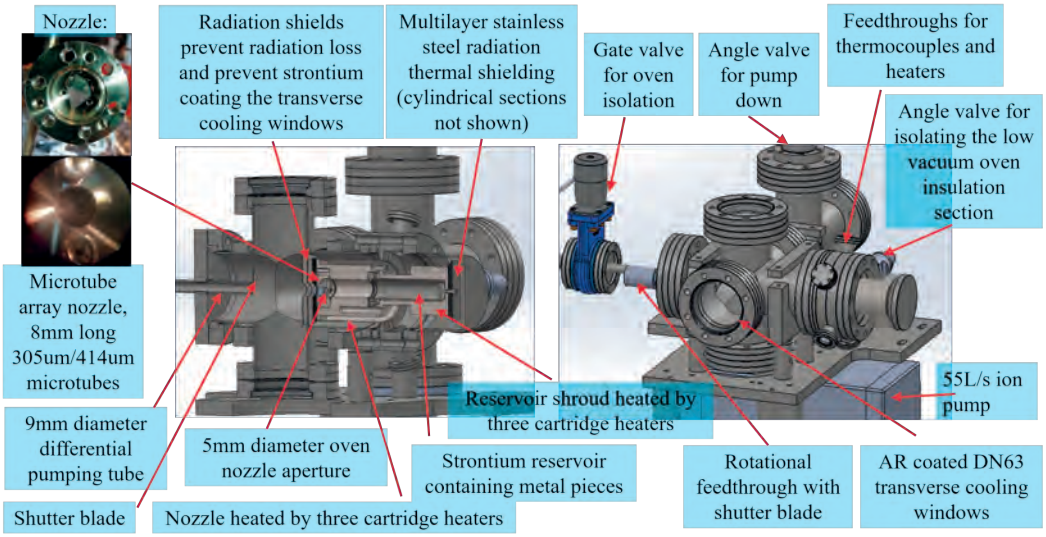


FIGURE 4.2: **The oven and transverse cooling section of the atom source.** CAD design for the strontium reservoir, the nozzle, heaters, heat shields, and the transfer cooling.

**Heating and temperature sensing** Heating is achieved through two sets of three cartridge heaters from Omega Engineering. Model CSH-101120/120V, 6.35 mm diameter, 38 mm length, 120 W were used for heating the reservoir and model CSH-101100/120V, 6.35 mm diameter, 25 mm length, 100 W were used for heating the nozzle. The set of three cartridge heaters for the nozzle was inserted into three holes within the designed tube. The heat transfer to the nozzle occurs via the nickel gasket and radiation. Similarly, the second set of three cartridge heaters for the reservoir is positioned within a stainless steel block covering the DN16 half-nipple reservoir. The original oven design aimed to use the high power, lower power density longer heaters for the nozzle as well but manufacturing errors meant these plans needed to be adjusted in order to avoid further delays. Stainless steel 316 is used throughout the oven construction due to its high temperature resistance and since it is known to not react with strontium even at very high temperatures. Unfortunately the thermal conductivity of stainless steel is poor compared with other materials like copper, which limits the heat transfer from the cartridge heaters and the power that can be applied. Each set of heaters is monitored by two K-type thermocouples, type TJ36-CASS-116U-6-CC from Omega Engineering. Two sensors were used in case one fails and care was needed to avoid overheating the cables. The thermocouple and cartridge heaters were electrically connected through a series of DN16CF UHV feedthroughs 4.3(h)-(k). Notably,

the thermocouples were connected with a specialized thermocouple feedthrough (TFT2KP00002, Lesker).

**Heat insulation** The key divergence between this oven design and our prior strontium machines lies in the insulation approach. This design incorporates a CF-sealed low vacuum chamber, albeit unpumped, surrounding the oven, complemented by up to five layers of radiation shielding 4.3(e)-(g) comprising stainless steel 304 disks, rings, and foil ranging from 200 µm - 500 µm in thickness. In contrast, the previous oven relied on a ∼200 mm thick layer of Superwool 607 insulation. The primary aim was to enhance insulation within a significantly smaller volume, facilitating the insertion of the oven into a CF75 cross, as opposed to the CF150 cross utilized in the hot beam superradiance setup 3.1(c) while also keeping the propagation path to the transverse cooling short and thus the atomic beam divergence small. The thermal conduction path through the steel chamber walls occupies less than half the area compared to the hot beam superradiance design, thus mitigating heat losses through this pathway. The cartrige heaters used in the oven nozzle were specified to withstand temperatures of up to 760 °C. Consistent with typical oven designs, the nozzle is maintained at a temperature of 30 K-50 K hotter than the reservoir to prevent clogging of the microtubes. Supplementary heat shields were installed at the oven's exit, accompanied by the addition of a double-faced flange spacer to draw the oven deeper into the cross to avoid line of sight to the transverse cooling windows of any surface that might emit Sr, i.e. the oven nozzle and the potentially hot edges of the heat shields that may be Sr coated by the atomic beam. While this adjustment may marginally reduce capture efficiency, it was imperative to forestall the coating of the transverse cooling windows, an issue observed in the hot beam superradiance machine.

In building and operating the oven we encountered several issues.

1. **Oven nozzle heater overheated.** The custom-designed tube for heating the nozzle (see Figure 4.3(c)) was constructed by our workshop. It encountered several mechanical issues. Multiple reworks taking more than a year were needed to overcome large leaks in the UHV welds. To reduce delays, many of the pieces of flawed oven versions were reused and modified to build improved oven versions, instead of being fabricated a second time from scratch. Trying to make the welding process easier and easier, multiple changes were made to the original design. Machining errors made during the reworks required further adaptations to the design. As a result of this process the originally planned 1.5-inch-long cartridge heaters did not fit in the holes and the heater holes ended up underneath the reservoir flange meaning the heaters could

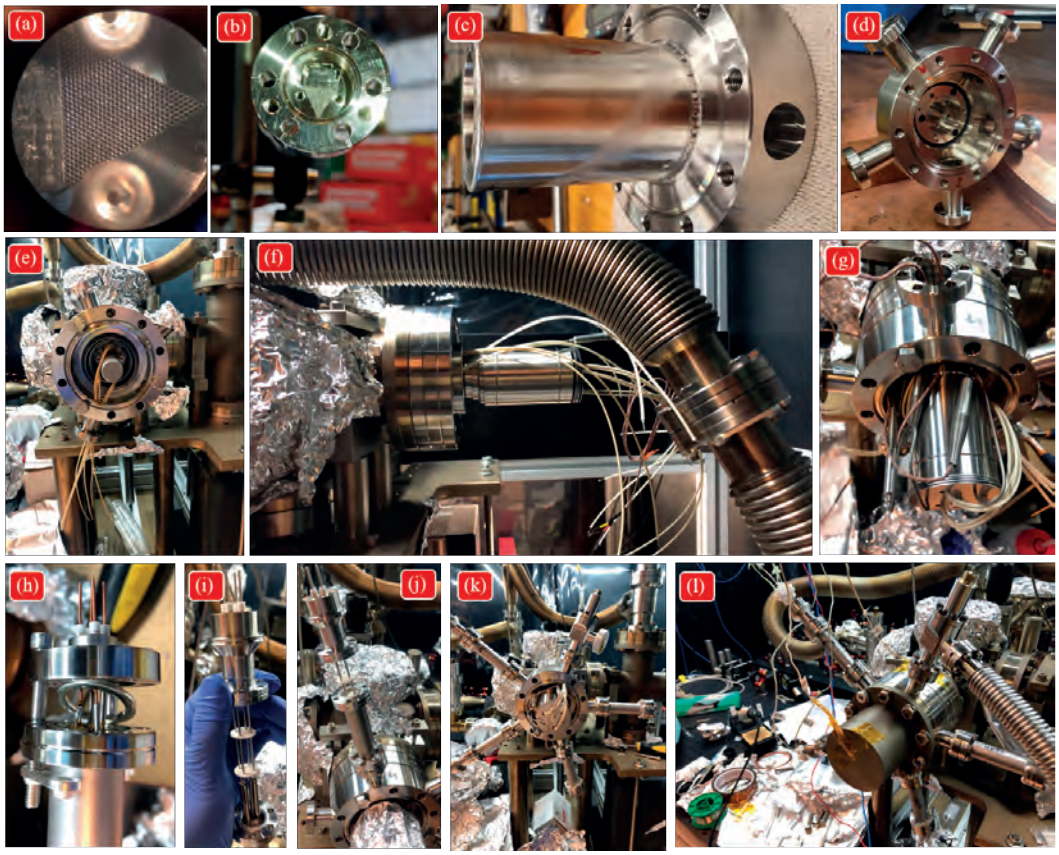


FIGURE 4.3: **The oven construction.** (a)-(b) Microtubes in the DN16CF nozzle. (c) The heater for the nozzle with thermocouple. (d) DN16CF nipple facilitates electronic connections. (e)-(g) The oven is assembled with cartridge heaters, thermocouple, and heat shields. (h)-(i) connections for thermocouples and heaters. (j)-(l) The oven is fully assembled.

no longer be exchanged if there was a failure without also breaking vacuum and removing the strontium reservoir. Consequently, we had to resort to using higher power density 100 W 1-inch-long heaters and we have no way to change them in event of a failure. The holes for the cartridge heaters were also oversized resulting in poor thermal transfer. Finally, the holes for the thermocouple sensors around the nozzle were forgotten to be machined and impossible to add after welding. This means it was not possible to monitor the nozzle temperature accurately. As a result, the thermocouples for the nozzle had to be placed between the tube and the heat shields, resulting in underestimated heater temperatures. Together this likely led to one of the heaters overheating and failing when we tested (gently) what temperature the

oven could reach. Due to the new position of the heaters, which are now obstructed by the strontium reservoir as shown in 4.3(e), once the reservoir was loaded with strontium, replacing the heaters would require breaking vacuum and likely replacing the strontium. Our temporary solution is to operate with only two of the three nozzle heaters at reduced power and to increase thermal conduction between the heater and the nozzle by operating in air rather than vacuum. With hindsight we should have allocated one or two weeks to conduct oven testing without the presence of strontium. This would have allowed us to evaluate the significance of these mechanical errors. However, since the machine is currently operational, we plan to modify and fabricate a replacement oven in parallel, a process that has been ongoing in our workshop over the last year.

2. **Welding the star-shaped DN16CF nipples** Welding the star-shaped DN16CF nipple (see Figure 4.3(d)) resulted in numerous leaks and reworks reportedly due to limited space for welding. Although this part was very similar to a low cost standard part CF35/38DX3/16 from Hositrad, we needed it with 5 ports instead of 3 and for a larger DN75 main flange size instead of the off the shelf DN35, so a custom version was manufactured by our workshop. During manufacture, the pre-welded half nipples purchased proved difficult to weld to the main flange due to their use of welded rather than seamless tubing. Consequently, replacement half nipples using seamless tubing were purchased and welded by our skilled workshop mechanical engineer Hans Ellermeijer, which finally solved the long-running problem.
3. Several design aspects can be improved. Firstly the screws used to seal the strontium reservoir, as depicted in Figure 4.3(c). Tightening these screws proved very challenging due to interference from the flange, hindering the process. Additionally, the space between the heat shields and the vacuum chamber is excessively tight, particularly for components like the thermocouple, as illustrated in Figure 4.3(c), which has a large spring structure built into it. These constraints made installation and adjustment cumbersome and potentially compromised the overall functionality of the heat shields. It would be much easier using a larger feedthrough like DN35. Furthermore the use of M4 socket head screws in screwing on the nozzle (Figure 4.3(b,c)) and the reservoir (Figure 4.3(e)) risked stripping or breaking the head off the screws to achieve the required torque needed to close the flanges for the very hard annealed nickel gaskets. With air now oxidizing these screws this problem may be acute if it comes time to open the reservoir. Similarly if the reservoir sticks due to high temperature operation it may be very hard to remove without damage.
4. Ideas for enhancing the oven: Given that the nozzle is connected to the heating tube via a gasket, augmenting the contact surface area from the side can enhance heat

transfer efficiency. However, a significant amount of heat is still absorbed by the heating tube, which compromises the overall efficiency of the design. One possible improvement could involve increasing the length of the heated tube to facilitate easier access to the reservoir screws. However, this would result in a larger volume of heating storage within the tube. Alternatively, other approaches [105, 106] integrate the reservoir and nozzle into a single structure. By incorporating additional heaters for the nozzle to create temperature differentials, these designs effectively utilize vacuum as a heat insulator and offer a more elegant solution. The challenge is perhaps the use of heating wire and ceramic electrical insulators which makes the heating more complex than just using a cartridge heater. Additionally, increasing the space for wires and avoiding the use of the star DN16CF structure for electronic connections would also be beneficial enhancements to consider. Another approach is to increase the thermal conductivity to the nozzle from the cartridge heaters by making large parts of the nozzle structure out of oxygen free high conductivity copper rather than stainless steel. In this case a stainless steel liner can be used for the reservoir and nozzle avoiding any potential reactivity with strontium. This approach was implemented by Sumit Sakar in the zero-dead-time clock now under construction and will likely be described in a future thesis by András Gácsbaranyi.

Loading strontium was smooth, taking only about 5 min for one person to break the glass cell in which the strontium was delivered with a hammer (see Figure 4.4(a)-(b)) and to pour out the strontium into the nipple reservoir, while another person used tweezers to collect the strontium dropped on the ground. The entire process was conducted within a nitrogen flow (see Figure 4.4(a)-(c)) to reduce the strontium oxidation. After baking, the machine was relocated to the lab and mounted to a Boikon framework, specially designed for accommodating the optics around the machine, presented in Figure 4.4(d)-(f). This framework facilitates easy recovery of the system with minimal effort for optical realignment, should the machine need to be moved out for any reason. The mounting of the entire machine and optics on the framework also makes it easy to acoustically isolate the machine by placing the frame on a series of Sorbothane feet (AV6 from Thorlabs).

### 4.1.2 Transverse cooling, Zeeman slowing and 2D blue MOT

Figure 4.5 shows the machine structure through the transverse cooling, Zeeman slower, 2D blue MOT, and heated Zeeman slower window sections. I will now go over this list and describe each part.

The ejected atomic beam from the oven was designed to next be transversally cooled using a 3-pass retro-reflected beam passing through CF63 AR coated window (from Torr


FIGURE 4.4: **Loading strontium and moving the machine back after the bake.** (a)-(c) Loading strontium from the glass cell into the oven reservoir. (d)-(f) Moving the machine to the lab and building up the Boikon framework it sits on.

Scientific) on a cross similar to the continuous atom laser machine [56]. In that machine this stage was observed to enhance flux by a factor of ten using around 25 mW of cooling power on each axis and a similar performance was observed in the first strontium BEC machine [107]. Only a single pass of transverse cooling was eventually implemented on our superradiance machine (using an elongated elliptical beam) but the three times higher available power of 80 mW per axis allowed a similar factor of ten flux improvement.

A rotational feedthrough shown in Figure 4.1, capable of rotating a stainless steel 304 blade, serves as a shutter regulating the atomic flux entering the remainder of the apparatus. This worked nicely compared to the "wobble stick" design implemented on the previous RbSr, atom laser, and microscope machines in our group. A $55\,\mathrm{L}\cdot\mathrm{s}^{-1}$ ion pump pumps the oven section, alongside the strontium coating of the chamber walls, which also serves as a getter pump. An angle valve, in conjunction with a gate valve, enables independent venting of the oven section from the rest of the apparatus, should reloading the oven with additional strontium be necessary.

Figure 4.5 shows the next vacuum chamber section, which consists of a set of 170 mm long, 9 mm inner diameter and 300 mm long, 11 mm inner diameter differential pumping tubes. These double as a Zeeman slower. The purpose of the differential pumping tubes is to shield the later ultra-high vacuum (UHV) and extremely high vacuum (XHV) sections from the lower vacuum quality present around the oven. To design the pumps and differential

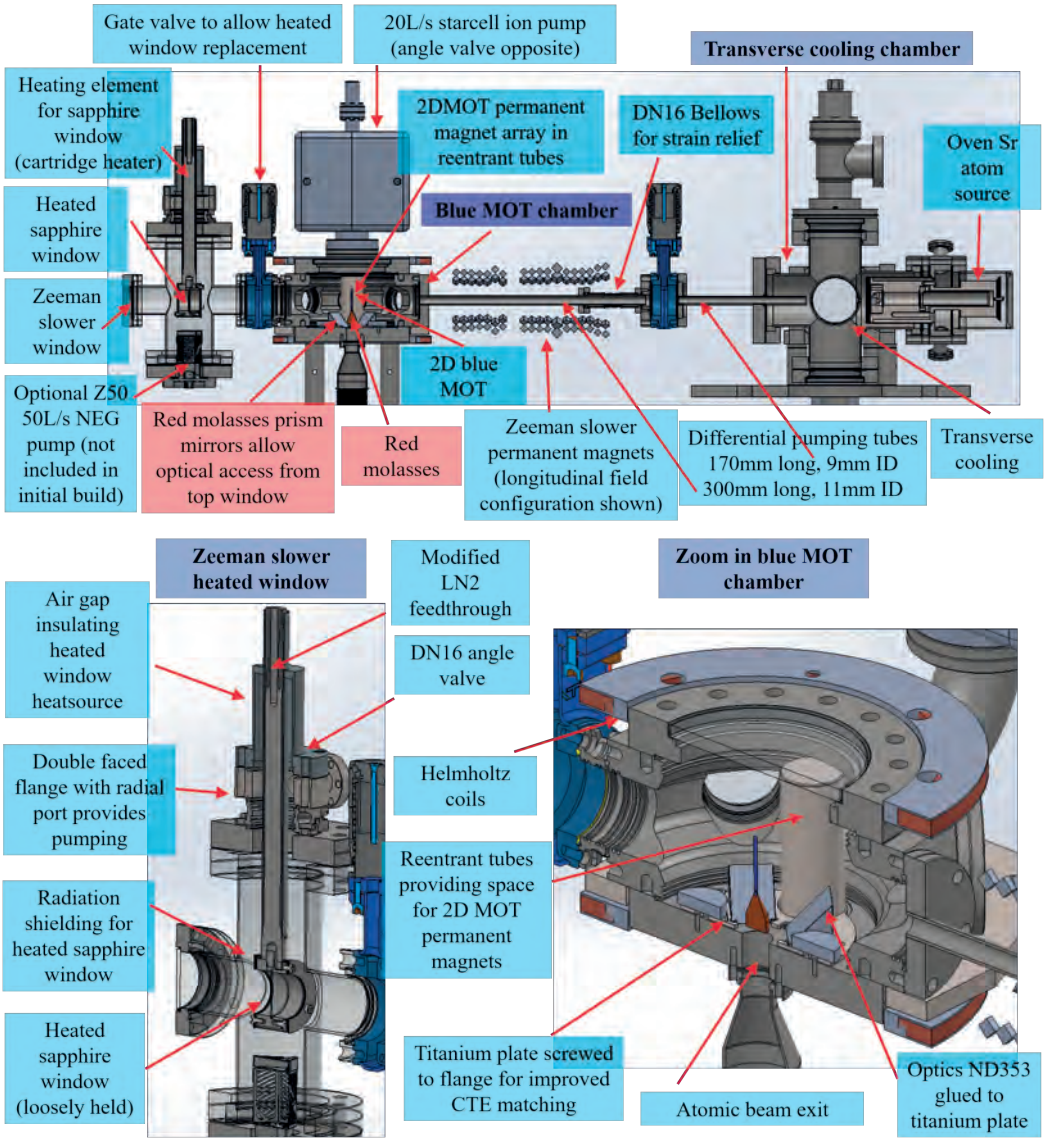


FIGURE 4.5: **The permanent magnet Zeeman slower, the 2D blue MOT and red molasses chamber and the heated Zeeman slower window.**

pumping tubes the pressures and gas flows throughout the machine were calculated assuming hydrogen surface outgassing loads of $10^{-13}$ mbar L/s/cm$^2$. These gas loads are consistent with loads after a 300 °C hydrogen bake and using the oven source loads estimated from our previous atom laser machine [56]. The results from these calculations are depicted in Figure 4.6. To provide strain relief a CF16 bellows was positioned along one

of the differential pumping tubes.

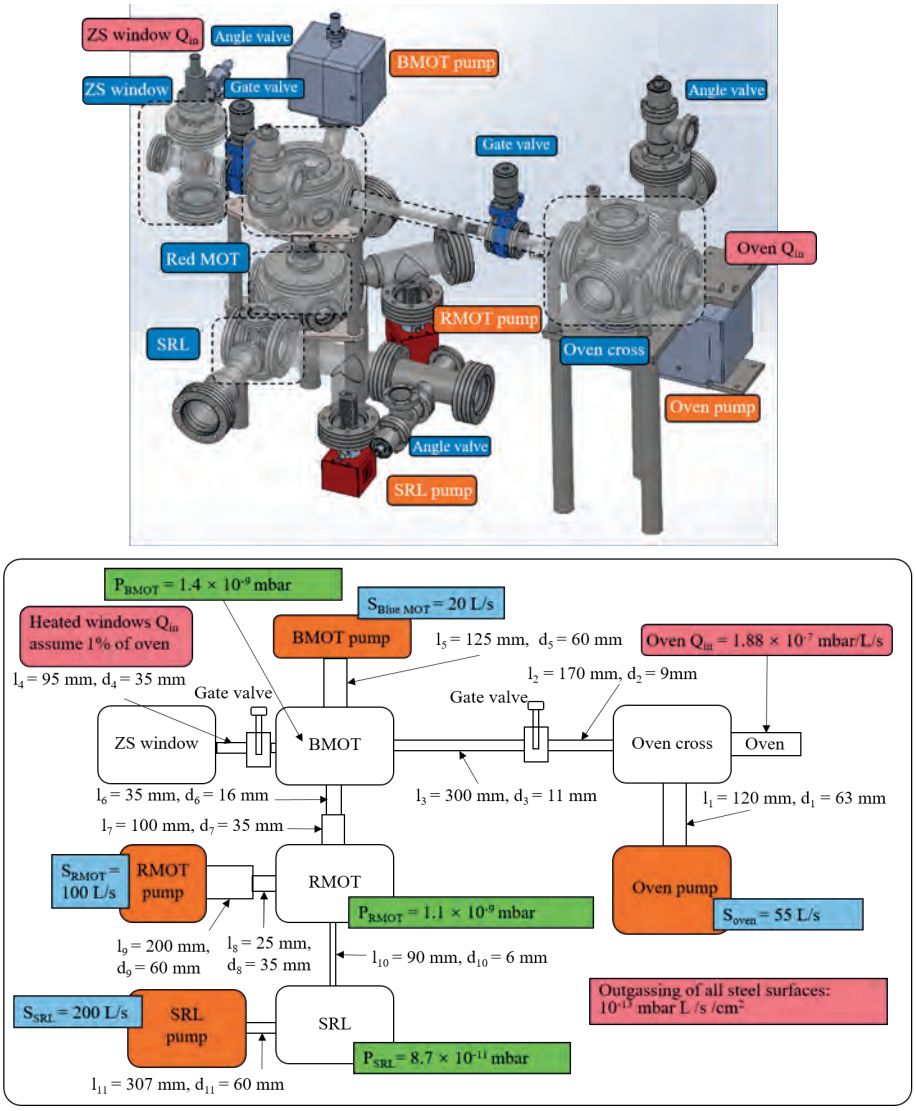


FIGURE 4.6: **The tube diameters, lengths and gas loads and the resulting calculated pressures throughout the continuous superradiant clock apparatus.** These results were used to inform the pump and tube size choices. Oven gas loads are assumed to match the gas load observed in a previous machine at maximum oven temperature (560 °C) of $1.9 \times 10^{-6}$mbar L/s and surfaces are assumed to outgas at $10^{-13}$mbar L/s/cm$^2$.

A permanent magnet Zeeman slower operating on the blue $^1S_0$ - $^1P_1$ transition is employed to decelerate the atomic beam. Utilizing permanent magnets embedded within

low-cost and rapidly prototypable 3D-printed or laser cut plastic support structures offers significant flexibility. The magnetic field of the Zeeman slower can be easily adjusted, and two magnet designs were developed: one featuring an axial or longitudinal magnetic field (refer to Figure 4.8) and the other featuring a transverse magnetic field (refer to Figure 4.7) configuration. The techniques for calculating the magnetic fields produced by the magnets to facilitate rapid iteration of designs are elaborated in [56]. Both transverse and longitudinal field setups, along with simulated velocity trajectories and capture velocity ranges, were computed, as well as the fields generated by the 2D MOT permanent magnets. For the transverse field configuration, the trajectories assume a uniform Zeeman slower beam with ideal linear polarization, an intensity of $1, I_{\mathrm{sat}}$, and a frequency detuned by 300 MHz from resonance. Only half of the laser power is effective, as the other half has the incorrect circular polarization. For the longitudinal field configuration, it assumes a uniform Zeeman slower beam with ideal circular polarization, an intensity of $1, I_{\mathrm{sat}}$, and a frequency detuned by 540 MHz from resonance.

It becomes immediately evident from Figure 4.7 when compared to Figure 4.8 that the velocity capture range of the longitudinal Zeeman slower magnet configuration is notably inferior to that of the transverse field configuration. Furthermore, the longitudinal configuration halts atoms well before they reach the 2D MOT, causing the beam to expand and further decreasing capture efficiency. One might question the utility of the longitudinal version in light of these observations. However, the fact that the magnetic field direction is parallel to the Zeeman slower beam direction enables a longitudinal field Zeeman slower beam with pure circular polarization, whereas the transverse field configuration leads to an equal mix of both circular polarizations, rendering only half of the Zeeman slower light useful. In cases where the Zeeman slower power is low (for instance, if strontium coats the Zeeman slower window or before the availability of high power blue diode lasers), the longitudinal slower may offer significant advantages. Nonetheless, the introduction of 500 mW 461 nm diode lasers from Nichia has dramatically improved the availability of power in the blue. Previous machines [55, 56, 107] relied on every milliwatt of power from the 100 mW diodes to operate their Zeeman slowers, making it problematic to discard half of the light. However, with the current higher power technology, the transverse magnetic field configuration significantly outperforms the longitudinal configuration. Consequently, we decided to use the transverse field configuration.

The process of constructing permanent magnet arrays for the Zeeman slower, presented in Figure 4.9, was as follows:

1. **Characterize each magnet.** Prior to assembly, the magnetic field strength of each magnet was individually measured at a fixed distance using a Gauss meter. Any magntes significantly deviating from the average performance were discarded from

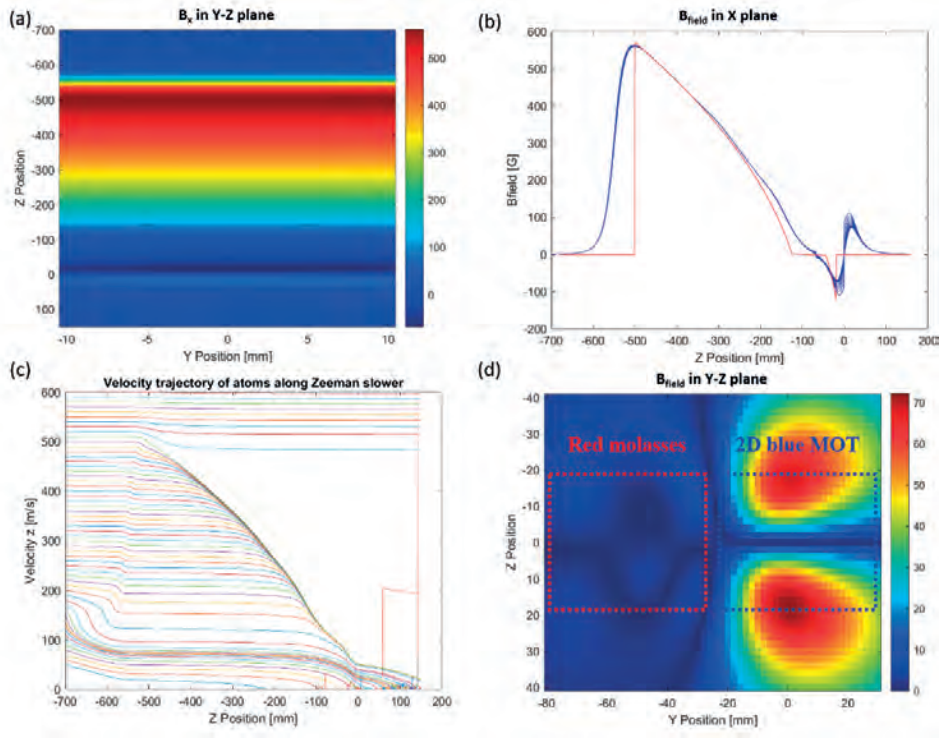


FIGURE 4.7: **Transverse field permanent magnet Zeeman slower design.** (a) Magnetic field in the transverse direction plotted against position along the Zeeman slower, with the Z axis (originating at the blue MOT location) and the radius from this axis indicated. (b) The blue plots represent the transverse field strength for radii up to 10 mm off axis, with the more extreme values observed furthest from the axis. The red line denotes the required magnetic field for an idealized Zeeman slower with parameters $\eta = 0.33$ [56], length of 0.4 m, a frequency offset of 300 MHz, and a spin flip length of 8 cm. (c) Simulated velocity trajectories for various input velocity atoms illustrate the velocity capture range. (d) The absolute magnetic field strength in the plane of the 2D blue MOT is depicted, showing the 2D blue MOT region (on the right) and the weak red molasses section (on the left). The Y axis is oriented vertically upwards with the origin in the plane of the Zeeman slower. Notably, the 2D MOT field exhibits strong components in the transverse direction, seamlessly contributing to the Zeeman slower, as demonstrated in (a) and (b). This eliminates the effects of the gap between the MOT and Zeeman slower, which causes loss in a longitudinal Zeeman slower (shown in Figure 4.8(e)).

use. Figure 4.9(c) presents the results, revealing only approximately 3% variation in magnetic field strength among the 200 magnets measured. The magnets used for the Zeeman slower were model W-10-N from supermagnete.nl and they had a 860-995

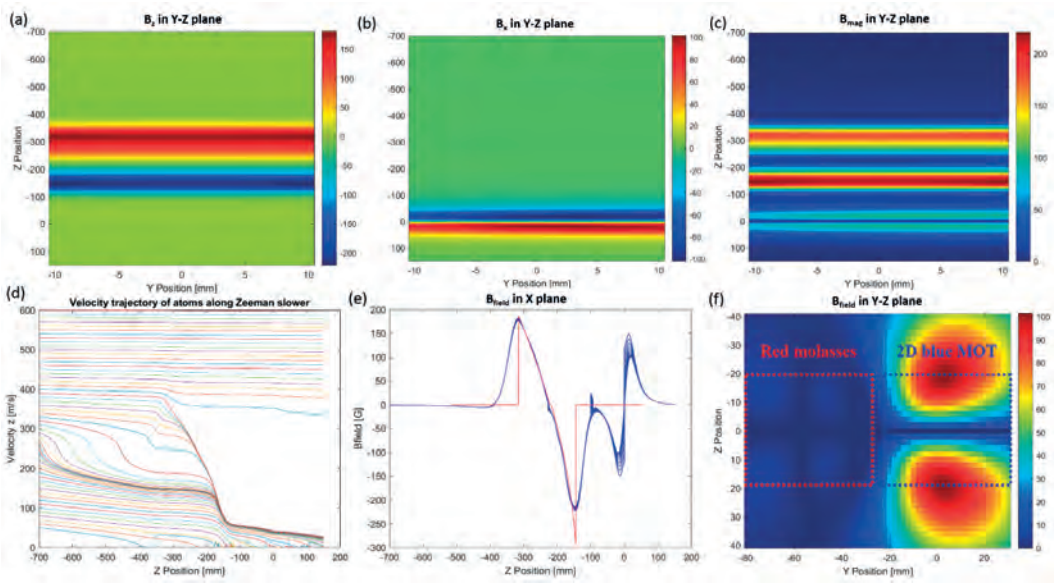


FIGURE 4.8: **Longitudinal field permanent magnet Zeeman slower design.** (a) Magnetic field in the axial direction plotted against position along the Zeeman slower axis (Z axis) and radius from this axis. (b) Magnetic field in the transverse direction plotted against position along the Zeeman slower axis and radius from the axis, generated by the 2D MOT permanent magnets. (c) Absolute magnitude of the magnetic field plotted against position along the Zeeman slower axis and radius from the axis. (d) Blue plots show the absolute magnitude of the field strength for radii up to 10 mm off axis, with more extreme values observed furthest from the axis. The red line represents the required magnetic field for an idealized Zeeman slower with parameters $\eta = 0.42$ [56], length of 0.165 m, a frequency offset of 540 MHz, and a spin flip length of 0.5 cm. (e) Simulated velocity trajectories for various input velocity atoms illustrating the velocity capture range. (f) Absolute magnetic field strength in the plane of the 2D blue MOT, showing the 2D blue MOT region on the right and the weak red molasses section on the left. The Y axis is vertically upwards with the origin in the plane of the Zeeman slower. Note that the significant gap between the end of the Zeeman slower and the 2D MOT can cause substantial loss in longitudinal Zeeman slowers due to rapid divergence of the now slow-moving atomic beam.

kA/m specified field strength (a $\pm 8\%$ uncertainty).

2. **Assemble magnets.** The selected magnets were then glued into 3D-printed or laser-cut holders and subsequently mounted onto an aluminum frame. Magnetic field strength measurements along the center indicate a smaller field strength of around 10% from the calculated values. This deviation could largely be attributed to the wide specification for the magnetic field strength but it could also be related to the inherent

5% inaccuracy of the magnetic sensor (SS495A, Honeywell). Following cavity and strontium baking to achieve the required vacuum, the assembled permanent magnets for the Zeeman slower were installed on the machine. However, it's noted that there are some machining and design errors in the aluminum case, resulting in the need to misplace or skip some screws which reduced the rigidity.

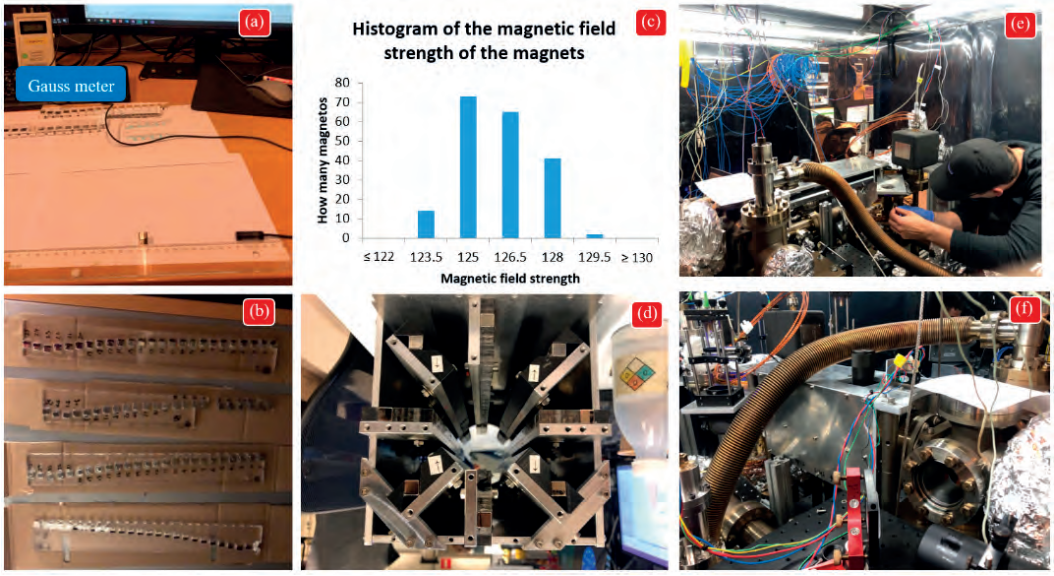


FIGURE 4.9: **Construction of two hundred magnets for the Zeeman slower.** (a)-(c) The magnetic field strength of each magnet was measured using a Gauss meter before the magnets were assembled into 3D-printed or laser-cut holders. (d)-(f) The magnet arrays were then assembled into an aluminum frame. After baking the vacuum chamber, the permanent magnets are installed on the machine.

The very long lever arms of the Zeeman slower tubes together with a gate valve, which regularly has forces applied to it, was a cause for concern. In order to provide additional mechanical support, the framework depicted in Figure 4.1 incorporated an extra pole to help support the gate valve although this did not make it to the final design due to its interference with the Zeeman slower magnet assembly. Assembly of the differential tube for the Zeeman slower required meticulous attention to detail. Figure 4.10(b) shows a side view of the differential tube, revealing significant insights. Figure 4.10(a), captures a view from the oven side, the differential tube looks aligned in the center and also well aligned with the mechanical atomic beam shutter. However, Figure 4.10 (c) from the blue MOT side exposes an initial misalignment issue — the differential tube was noticeably off-center. To correct this problem, before recording Figure 4.10 (d), strategic adjustments

were made. Spacers were added, and the chambers were very carefully rotated resulting in the successful alignment of the differential tubes. An improved structure was designed by Sumit Sarkar for the zero-dead-time clock machine, which should be detailed in a future thesis from András Gácsbaranyi.

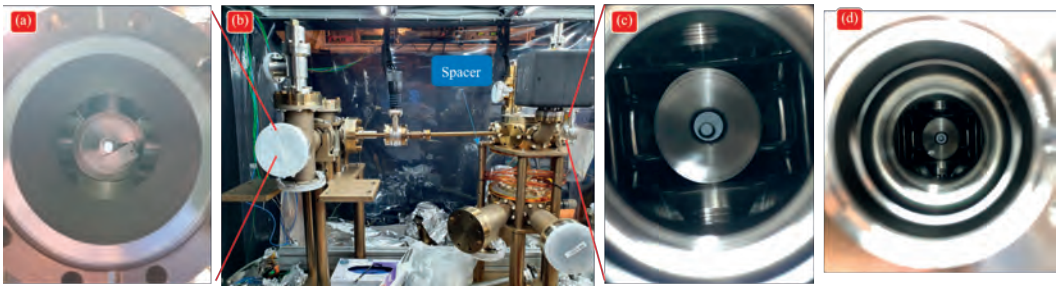


FIGURE 4.10: **Alignment of the differential pumping tubes.** A side view of the tubes provides valuable insights. In photograph (a), taken from the oven side, the presence of the mechanical atomic beam shutter is visible and the differential tubes look aligned. However, in photograph (c), taken from the blue MOT side, a misalignment is evident — the differential tubes are not centered. To address this issue, spacers were added between vacuum chambers and their holders, resulting in the improved alignment of the differential tubes shown in photograph (d). This process ensured precision in the functioning of the Zeeman slower and optimal flux.

After the Zeeman slowed atoms enter the blue MOT chamber, a 2D permanent magnet blue MOT slows and concentrates the atoms before releasing them into a cold downwards propagating beam. The designs for the magnet configurations, shown in Figure 4.11(a), are described in detail elsewhere [56]. The array of permanent magnets that define the 2D MOT magnetic field were originally designed to provide a strong 20 G/cm gradient in the 2D blue MOT region while providing a weak 2 G/cm gradient immediately below optimized for a 2D red MOT. The magnet structure aimed to create a sharp transition between the blue and red regions while keeping the magnets themselves a significant distance from the 2D MOT axis 5 cm to allow good optical access. The time constant of a red MOT is very long due to its weak restoring force, so a red molasses was instead used in the atom laser machine [56]. This molasses operates on the magnetically insensitive $\pi$ transition between $^1S_0$ and $^3P_1$ $m_J = 0$. In order to avoid producing a MOT, the $^3P_1$ $m_J = \pm 1$ states are shifted away from the $^3P_1$ $m_J = 0$ state by adding a vertical component of a 2G to the 2D quadrupole magnetic field, i.e. a component along the axis of the 2D quadrupole field. This field configuration allows addressing of the $\pi$ transition with vertically polarized red molasses beams. The field is weak enough to not significantly modify the behaviour of the 2D blue MOT, but dominates over the quadrupole field in the red molasses region. The

high 2D quadrupole gradient region covers the blue MOT extending upwards by around 5 cm from the chamber centre as shown in Figure 4.7(b). Meanwhile the array produces only a small residual magnetic field in the region designated for the red molasses, shown in Figure 4.7(d), which can easily be dominated by the field from a simple set of bias field coils.

To accommodate the permanent magnets creating the 2D MOT field, the vacuum chamber contains pockets, created by 25 mm diameter steel tubes that are open to air. 3D printed magnet holders are inserted into these tubes (see Figure 4.11(b)-(d)). The 30 mm diameter 2D blue MOT beams are directed through four of the AR coated CF35 chamber windows from four separate fibers with cage telescopes as shown in Figure 5.2.

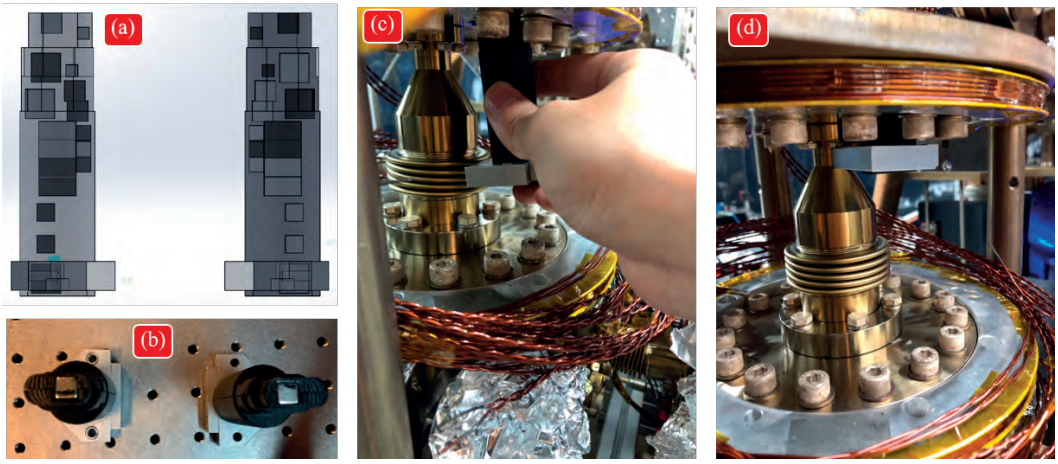


FIGURE 4.11: **Permanent magnets for blue MOT.** (a) The design of these magnet arrays was optimized with Matlab simulations [56]. (b) The magnets were positioned by gluing them into 3D-printed holders, ensuring precise alignment and stability. (c)-(d) The assembly process involved simply inserting the magnet assemblies into pockets in the blue MOT chamber and fixing them to the chamber.

Helmholtz coils add a vertical component to the magnetic field in the red molasses region, allowing the 689 nm vertically polarized red molasses beams to address the atomic beam using the magnetically insensitive $\pi$ polarization. Unlike previous work [56], more intense red beams will be used here ($10\text{mW}/\text{cm}^2$) to make use of the sawtooth wave adiabatic passage (SWAP) cooling technique [49, 108]. This technique is needed to efficiently work with the many sublevels of $^{87}$Sr [53]. Since the chamber's DN35 windows were fully utilized for the blue MOT beams and without wanting to reduce the size of the blue MOT beams, red molasses beams were inserted from above. This was achieved using four protected silver-coated BK7 right angled prisms glued using ND353 from Epotek to a

titanium holder plate (for coefficient of thermal expansion mismatch reduction) as shown in Figure 4.12(a). This in turn is screwed to the chamber vacuum flange with vented silver plated screws from Vacom. In the design, low power (50 µW) blue push beams could be injected on a ∼45° angle as in [56] to plug the top of the blue 2D MOT. With this additional push in the downwards direction the 2D blue MOT could in principle double the flux with typically a 50% flux improvement observed in the atom laser machine [56]. Currently around 0.5 mW is used to plug the top of the 2D blue MOT with a relatively shallow angle and a 30% flux improvement was recorded. In addition, a red MOT beam (which forms a sixth beam of the 3D red MOT in the lower chamber), can be directed downwards, towards the bottom red MOT chamber. This beam was design to allow optical pumping and SWAP cooling of the $^{87}$Sr atoms and it also provides an additional nudge in the downwards direction at the 2D blue MOT. The optics for this beam were constructed but this system is currently disabled by the addition of a different camera system configuration around the blue MOT. All our cameras are connected to our open-source Vision software [1] via Ethernet. Repump lasers at 679 nm and 707 nm or 448 nm are designed to be overlapped with the blue MOT to pump atoms that leaked into the $^3P_2$ state [56] back to $^1S_0$ state. Again the optics were built but are not currently being used, which offers another opportunity to easily double the machine flux above the initial values I present in this thesis.

To monitor, optimize, and characterize the 2D MOT system, an imaging system is needed. Without any optical access through the side chamber ports, we needed to observe the MOT through the top window. Fluorescence of the blue MOT down its axis should be sufficient for monitoring and diagnosis and has been used as a secondary approach on our previous machine for optimization [56]. We also set up an absorption imaging system (on the blue transition) illuminated from below for quantitative analysis of loading rates and fluxes but although the optics were constructed this is currently disabled by the positioning of the blue fluorescence camera for the 2D blue MOT.

To cross check the MATLAB magnetic field models of [56] and our designs for the Zeeman slower and MOT magnet arrays, the fields from the permanent magnets and coils were simulated using COMSOL. The results were in good agreement and certainly within the experimental uncertainties given by the uncertainty in the magnetic field strength. Examples of the simulated results from COMSOL and MATLAB are shown in Figure 4.13.

To maintain vacuum the blue MOT chamber is pumped using a 20 L/s "StarCell" ion pump from Agilent and includes an angle valve for initial pump down and bakeout as shown in Figure 4.5.

[1] See our website: https://www.strontiumbec.com/

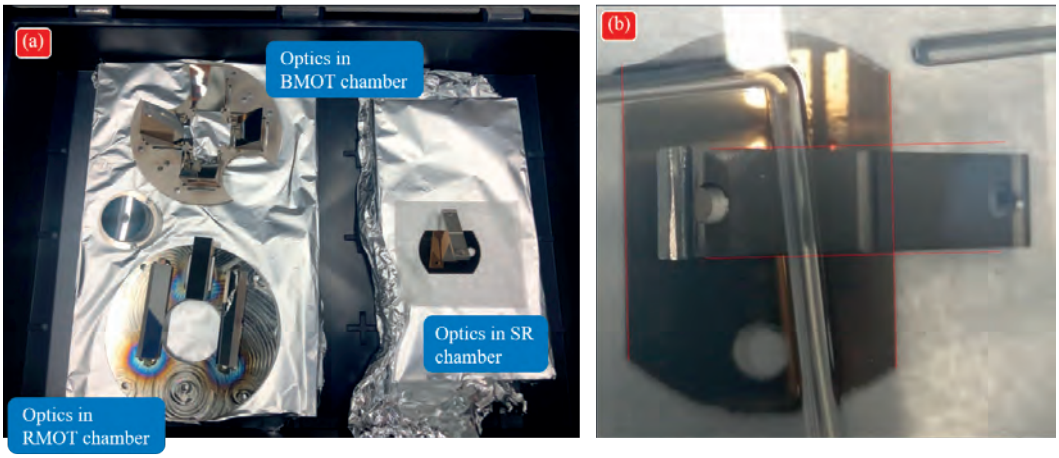


FIGURE 4.12: **Optical assemblies before insertion into the vacuum chamber.** The in-vacuum optics were fixed onto titanium baseplates using 353ND adhesive. Within the blue MOT chamber, these optics serve the red molasses cooling, while those within the red MOT chamber provide optical access to implement a moving lattice and transverse cooling on the guided atomic beam. Similarly, optics within the superradiant chamber are utilized for red molasses cooling. While most optical assemblies relied on the structure of the titanium holder to align the optics, in the superradiant chamber, photos and guides were used to position the in-vacuum mirror to match the CAD design. An illustrative example of misalignment is depicted in photo (b).

### 4.1.3 Heated Zeeman slower window

Most of the atomic flux from the oven is not captured by the 2D blue MOT and can quickly coat the window through which the Zeeman slower laser beam enters the vacuum chamber, breaking the Zeeman slower. Traditionally, this problem has been addressed by shining the laser through an uncoated sapphire viewport, which is kept heated to around 200 °C[2]. This has been found to greatly reduce the rate at which strontium coats the window [56, 107]. The drawback of this approach is that viewports exposed to thermal shock, such as that it happens if the window heater power fails, can crack, catastrophically venting the machine. We have in the past placed thermal mass around the window and insulated it to reduce the risks of such a failure, but leading to significant bulk and complexity [56]. For this machine, we decided to explore two alternative approaches to reduce both risks. One approach is a strontium coated in-vacuum mirror and the other is a heated in-vacuum sapphire plate window.

[2]In recent discussions with James K. Thompson from JILA he mentioned that they had used 350 °C heated AR coated sapphire viewports and found they worked, indicating that there is no need for sapphire and that optical losses from uncoated surfaces can be avoided.

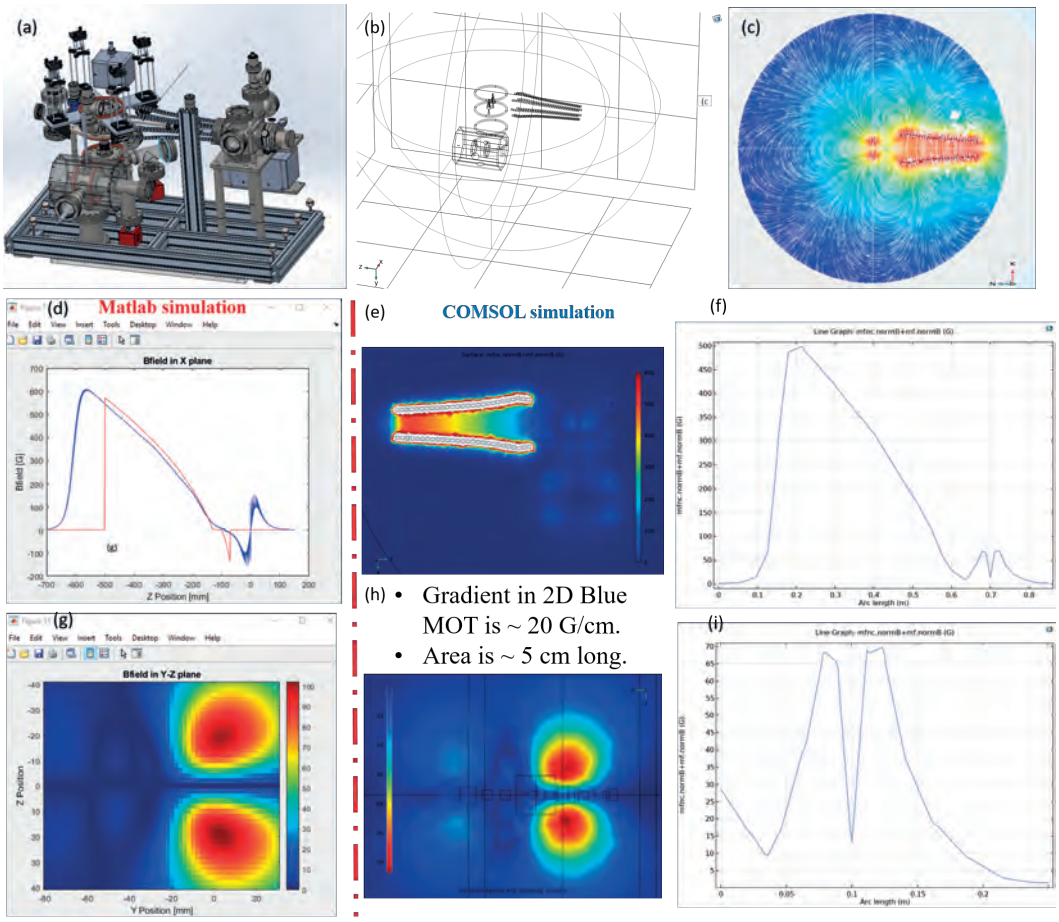


FIGURE 4.13: **Cross-checking the magnetic field designs using COMSOL.** (top) The magnetic components were imported into COMSOL from 3D CAD files. (top, right) A cross-section of the generated magnetic fields in a horizontal plane centered on the Zeeman slower and 2D MOT. (middle) MATLAB simulation of the magnetic field strength for the transverse field Zeeman slower, the field modeled using COMSOL, and a line plot showing the absolute value of the field strength down the axis of the Zeeman slower for comparison. (bottom) 2D MOT magnetic fields simulated using the MATLAB design code, then modeled using COMSOL, showing the 2D blue MOT field on the right, the low field red molasses in the middle, and then residual fields. Finally, a plot of the field strength entering the 2D MOT along the Zeeman slower axis.

In a strontium-lithium mixture machine recently built by Meng Khoon Tey's group at Tsinghua University [109], a 45° gold-coated copper mirror was placed in the vacuum system to redirect the Zeeman slower laser from a side window down the Zeeman slower

axis. This mirror can be quickly coated with strontium but if the reflectivity remains high this is an elegant and simple solution. A previously published exploration of strontium coated surfaces was inconclusive but suggested that low and degrading reflectivity from the strontium-coated surfaces can be a problem [110]. To explore this option we put together a risk reduction experiment, shown in Figure 4.14, to measure the reflectivity of the strontium coated mirrors on a variety of substrates over a 6-week period.

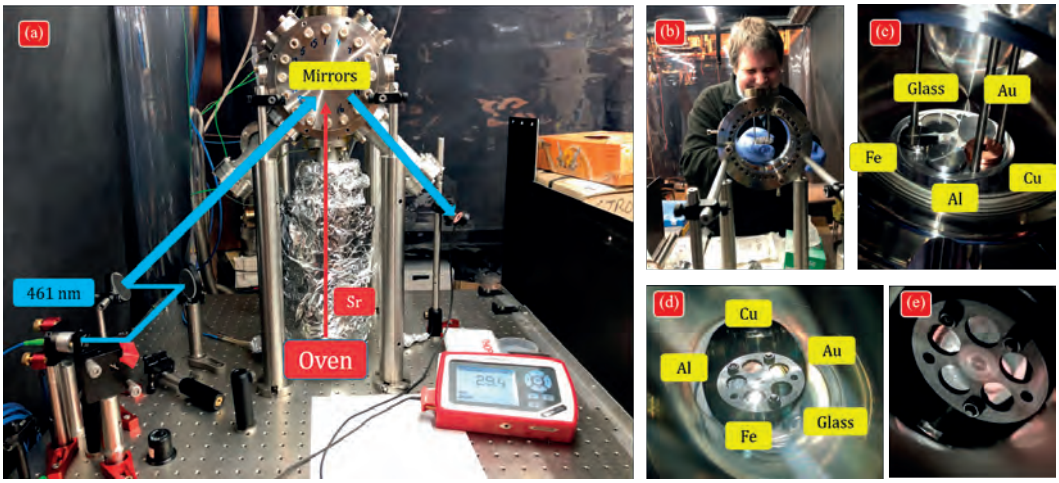


FIGURE 4.14: **Strontium coated mirror test for Zeeman slower.** (a) Setup of the strontium-coated mirror test. A 461 nm laser was employed to measure the reflectivity of various types of mirrors while being coated with strontium. (b)-(d) The selection of mirrors included an unprotected gold mirror, a copper mirror, a glass mirror, an iron mirror, and an aluminum mirror. A comparison of photos (d) and (e) shows that all the mirrors depicted in (e) were coated with strontium.

Our experiment aimed to assess the degradation of mirror reflectivity caused by a strontium coating. We employed a vertically mounted simplified oven containing strontium metal pieces heated to a temperature range of 450 to 500 °C. Heating was achieved using three cartridge heaters (Omega model CSH-101120/120V), while temperature monitoring was conducted via two thermocouples (omega model ME61-K-1.0-500).

The oven did not include a nozzle, but simply an aperture, as we wanted a highly divergent atomic beam to evenly coat the test pieces. The oven was insulated by 50 mm thick Superwool 607, wrapped in aluminium foil for dust control and tied together with wire.

The oven was affixed to a 100 mm long CF38 nipple, which in turn was attached to a 6-inch Kimball Physics octagon, serving as the primary vacuum chamber. Suspended

from the top flange were five half-inch mirrors, positioned with their coated sides facing downward towards the oven.

The mirrors that we tested included a polished copper mirror, a polished aluminium mirror, a polished stainless steel mirror, a gold coated BK7 mirror and an uncoated BK7 glass mirror. A DN35 nipple and tee were used to connect a turbo pump and a pressure gauge (via a bellow). This nipple and tee also distanced the windows from the central chamber, thereby protecting them from being coated with strontium. A 461 nm probe beam was used to periodically measure the reflectivity of each mirror for each linear polarization with a 45° angle of incidence as the mirrors were coated by strontium over the course of 6 weeks.

The results are plotted in Figure 4.15. The lack of a nozzle on the oven was new for us so it was expected that the flux from this oven could be much higher than in our usual experience. Therefore we began ramping up the oven temperature slowly. However, even after operating at 500 °C for days we still observed no effect on the mirror reflectivity. Fearing the strontium may have oxidized we decided to keep raising the temperature until we saw something change in the reflectivity. We raised the temperature to 600 °C and saw a small effect and continued on to 650 °C at which point we saw a dramatic collapse in the reflectivities over just a few tens of minutes. We then rapidly lowered the temperature back to around 530 °C. The reflectivity continued to fall over the following half day after which there is a interruption in the data because of a long weekend. One possible explanation for the sudden and rapid reflectivity change is that the strontium surface was indeed oxidized and a very high temperature was needed to break through the oxide and start the evaporation of strontium. We also observed that at high oven temperatures freshly coated strontium surfaces appear to act as "getter" pump, rapidly improving vacuum quality. This is in good agreement with "conventional wisdom". At a lower oven temperature of 530 °C the vacuum pressure improved and mirror reflectivity gradually improved again to 15-25% for P polarization and 20-40% for S polarization. The variation in the reflectivity is likely due to the roughness of the substrate rather than a property of the substrate material itself. At this point the substrates polished by the mechanical workshop had significantly higher scatter and lower measured "reflectivity" when compared to the optical mirror substrates. After around a week at 530 °C we again increased the temperature to around 580 °C. This time we found the reflectivity increased rather than decreased stabilizing at 15-35% for P and 20-50% for S depending on the substrate. We continued to increase the oven temperature to 630 °C over the coming days but the reflectivity stayed in the 15-35% range for P and the 20-45% range for S, while the pressure rose, indicating a high vapour pressure. Our conclusion was that either we had depleted the strontium source and were just observing outgassing or that we must have gone to *much* higher oven temperatures in

the initial burst without realizing it. Seeing no further evolution in the mirror reflectivity we turned off the oven and observed the pressure and reflectivity evolution over the following 6 weeks with no strontium coating. We observed the reflectivity gradually decay to 5-15% for P and 15-30% for S polarization. The vacuum pressure also continued to decline perhaps in part due to getter pumping by the strontium coating.

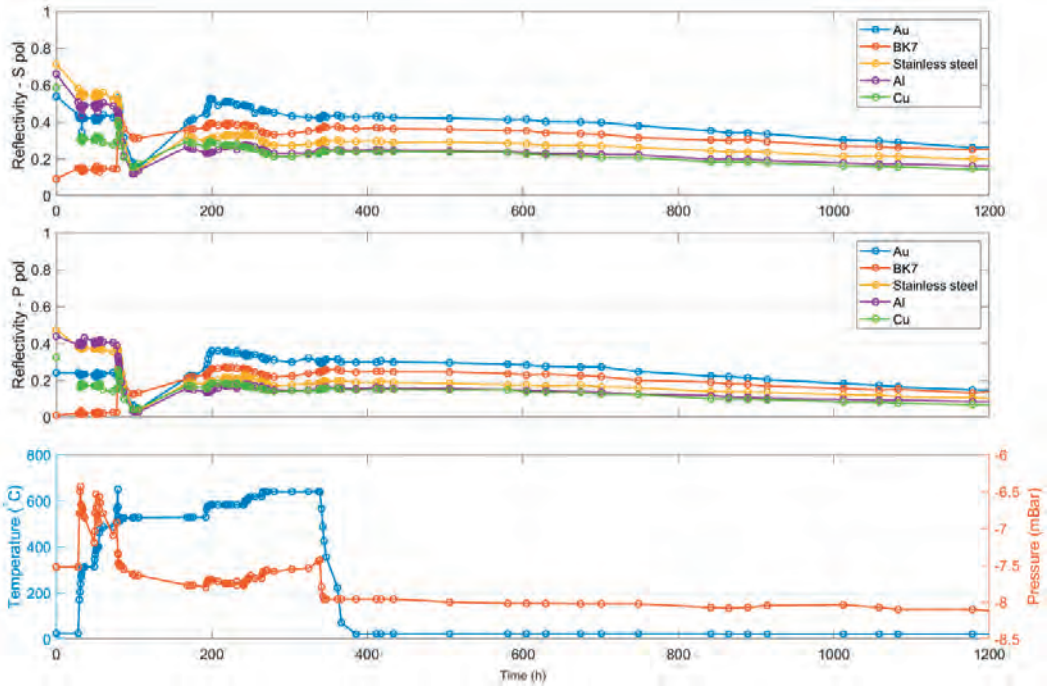


FIGURE 4.15: **Results from strontium coated mirrors test for Zeeman slower.**

The reflectivity difference between S and P polarization will make it more difficult to obtain a good circular polarization for a longitudinal Zeeman slower. For the transverse Zeeman slower the additional 50% loss will make it more difficult to send sufficient laser power onto the atoms. However, a Zeeman slower laser power of 2-3 times greater than required is still practical with the 0.5 watt diode lasers now available at 461 nm. Therefore an in-vacuum strontium coated mirror at 45° angle does appear to show promise as a solution to the window coating challenge [109]. The reflectivity decay to values of just 15% for P polarization without continuous and sufficient strontium coating is a concern. The formation of a rough strontium oxide layer on the mirror surface could be quite problematic, creating a rough surface that scatters, a surface that can not be repaired by simply using the oven to recoat the surface. For these reasons we considered it too risky to take the

in-vacuum mirror approach for our Zeeman slower.

A second approach to solve the window coating challenge involves the placement of a heated uncoated sapphire window within the vacuum to shield the AR-coated vacuum chamber viewport from strontium, while allowing the Zeeman slower beam to pass through. This method effectively mitigates the risk of catastrophic vacuum failure from a power outage switching the window heaters suddenly off, as the worst-case scenario would entail the sapphire plate becoming coated with strontium and rendered opaque. In this case, the sapphire plate can be readily replaced without necessitating the venting of the main chamber or oven, if one implements a gate valve that isolates the Zeeman slower window subsystem. The mechanical design for this configuration is illustrated in Figure 4.5, featuring a CF16 angle valve for independent pump down and bakeout of the ZS window chamber, along with an option to add a vacuum pump in order to address potential vacuum issues arising from additional gas load resulting from the heated window.

We decided to implement the heated in-vacuum window approach due to its perceived lower risk and higher performance, despite the increased complexity involved. However, we also acknowledge the merits of the in-vacuum mirror approache for potential utilization in future machines. As this was our first time using the heated in-vacuum window design, a temperature test was conducted to ensure its functionality. Figure 4.16 illustrates the testing procedure, where the heated sapphire window was assembled with a thermocouple affixed to it (see Figure 4.16(c)). Heat was transferred from a cartridge heater (OMEGA model CSH-101120/120V) to a stainless steel rod welded to the bottom of a liquid nitrogen feedthrough, which then screwed to the copper holder for the sapphire window. A series of heat shields around the copper holder provided some radiation shielding. An additional thermocouple (OMEGA model ME61-K-1.0-500) near the cartridge heater monitored its temperature. Testing was conducted within a vacuum environment. Initial results were inadequate due to poor heat conduction along the long stainless steel 304 rod holding the cartridge heater. One might ask why we used stainless steel rather than copper or aluminium? This was because the cartridge heater was on the air side and we were afraid that copper would oxidize, sealing the cartridge heater in place, which might be a problem if it broke. Secondly, the use of a liquid nitrogen feedthrough would not work as there would be no way to weld it to copper. To improve heat conductivity, we remade the stainless steel heating rod as short as possible to increase its conduction to the copper. Additionally, we incorporated a threaded stud at the end to increase surface contact and enhance heat transfer to the copper window holder. The system was retested and the results are plotted in Figure 4.16(e). The results indicated that with a heating power of 17 W the sapphire window reached a temperature of 220 °C, which is sufficient to protect it from strontium coating. There are many opportunities to improve this design such as making the entire

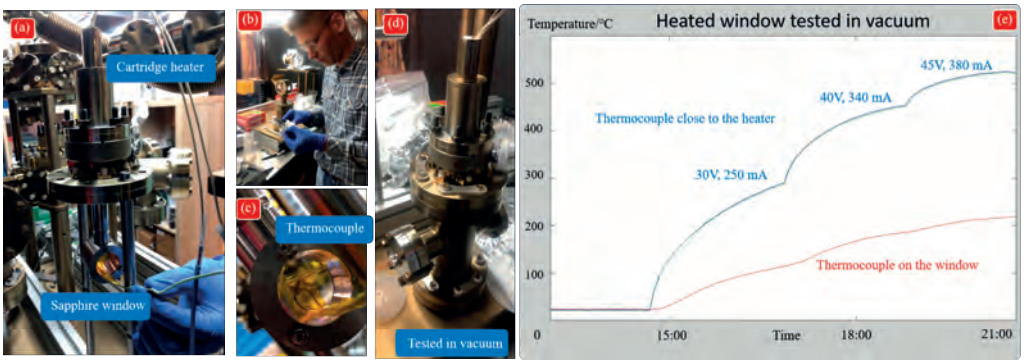


FIGURE 4.16: **Test of the heated window.** (a)-(d) The heated window undergoes assembly with a thermocouple in direct contact. An additional thermocouple is positioned proximate to the cartridge heater. Testing is conducted within a vacuum environment. With a heating power of 17 W, as depicted in (e), the sapphire window attains a temperature of 220 °C. This temperature adequately safeguards against strontium coating the window.

window heater out of copper with the cartridge heater directly heating it. Instead of a feedthrough the copper heater can be directly sealed against the CF knife edge. The design used by Sumit Sarkar in the zero-dead-time clock uses an evolved design based on this approach, which will likely be described in the thesis of András Gácsbaranyi.

### 4.1.4 A steady-state 3D red MOT

The cold atomic beam, falling at a slow speed of approximately 2 to 3 m/s, exits the 2D blue MOT chamber and descends 20 cm under the influence of gravity into a second chamber containing the red MOT, see CAD design in Figure 4.17. In this chamber, the atoms are loaded into a steady-state 3D red MOT, operating solely on the narrow 7.5 kHz $^1S_0$ - $^3P_1$ red transition. Effective operation on this extremely weak transition necessitates isolation from the blue light used by the 2D blue MOT and Zeeman slower.

Our previous research found that optimal MOT performance for such a weak transition required extremely weak magnetic field gradients, typically ranging from 0.25 to 0.5 G/cm [51, 53, 80]. Therefore, it is essential to ensure significant separation from the high magnetic field gradients produced by the permanent magnets of the Zeeman slower and 2D blue MOT. While this part of the machine closely resembles our previous machine design [51], we have made several important adjustments to reduce risks and to optimize its design for our superradiant clock application.

Firstly, the baffle system designed to shield the lower chamber from scattered blue light is unnecessary as the small scattered power will not noticeably heat our 10 µK 3D red MOT

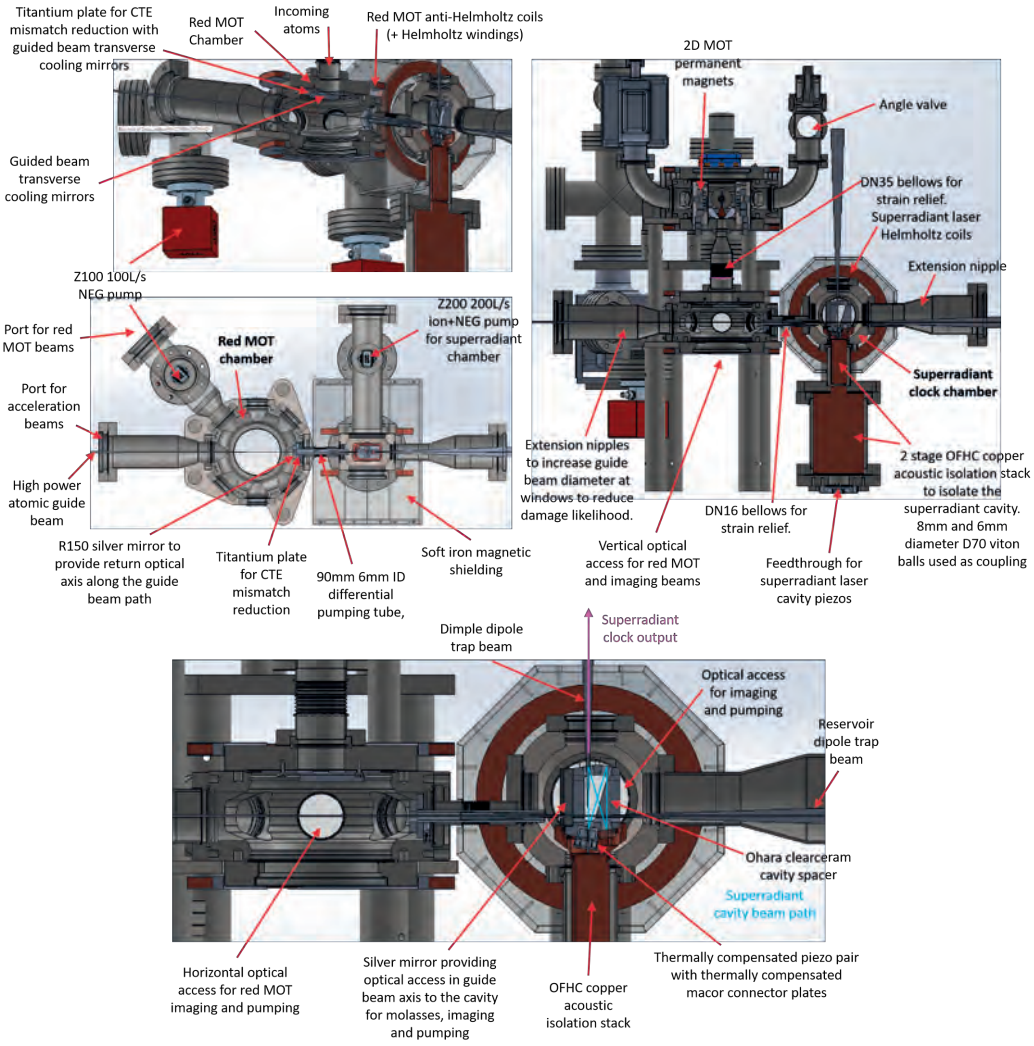


FIGURE 4.17: **The steady-state 3D red MOT.** Freely falling atoms from the 2D blue MOT chamber are slowed and captured by the 3D red MOT.

(unlike the situation with a Bose-Einstein condensate in our previous work). Consequently, we can enlarge the aperture between the upper and lower chambers from 8 to 16 mm in diameter, thereby enhancing the cold atom flux.

Secondly, a red MOT beam is designed to run through the top chamber forming a sixth beam of the 3D red MOT in the lower chamber. Using a 6-beam red MOT instead of a 5-beam red MOT reduces bouncing of atoms thus improving the robustness and capture efficiency of the MOT.

The red MOT magnetic field will be formed by a set of quadrupole coils (with additional Helmholtz coils for biasing) with a gradient on the order of 0.25 to 0.5 G/cm [51, 53, 80]. Additional (undrawn) biasing coils will be used to transfer the MOT by small distances in the horizontal plane, although this was found to be of little importance in previous work. Two imaging axes will be available for absorption imaging on the blue transition, the vertical axis, and the side axis as noted in Figure 4.17.

The red MOT chamber is pumped using a Z100 NEG pump from SAES. We opted for a simple NEG pump over an ion+NEG pump, given the presence of a $20\,\mathrm{L}\cdot\mathrm{s}^{-1}$ ion pump in the blue MOT chamber and the considerable conductance between these chambers, which can efficiently handle noble gas loads. This was primarily motivated by cost savings.

To provide strain relief, a bellow is incorporated between the blue and red MOT chambers, enhancing the structural integrity of the setup.

## 4.2 Continuous loading of atoms into the cavity

The 3D red MOT should capture and cool atoms to temperatures of approximately 10 µK, achieving storage densities of about $10^{10}\mathrm{atoms/cm}^3$. Our subsequent goal is to transfer these ultracold atoms into the superradiant lasing cavity, as illustrated in Figure 4.18. This cavity is situated within a separate chamber and shielded from magnetic fields. Placing the cavity in a separate chamber serves two purposes. First, it prevents scattered light, which could otherwise lead to the loss of atoms by radiative heating and by projecting them out of the superradiant supposition state. Second, it allows the creation of a stable, uniform magnetic field. Uniformity is necessary to ensure indistinguishability of the atoms, thereby facilitating superradiance.

To transfer atoms from the MOT into the cavity an elongated optical dipole guide is used. The MOT atoms are loaded into that guide and accelerated to flow along it. The guide keeps the atomic beam collimated and counteracts gravity during the transfer process. The guide is formed by a 1070 nm, 200 µm waist radius, Gaussian laser beam. By overlapping the MOT cloud with the 50 µK deep dipole guide, similar to the approach described in [80], high transfer rates from MOT to guide can be obtained.

### 4.2.1 Transferring atoms into an optical dipole guide

The next challenge lies in effectively transferring the ultracold atoms in the guide to the superradiant clock cavity. In our previous studies [51, 80], one horizontal pair of red MOT beams was co-linear with the guide. A small dark spot was generated within the beams at the location of the guide. This dark spot substantially suppresses scattering of

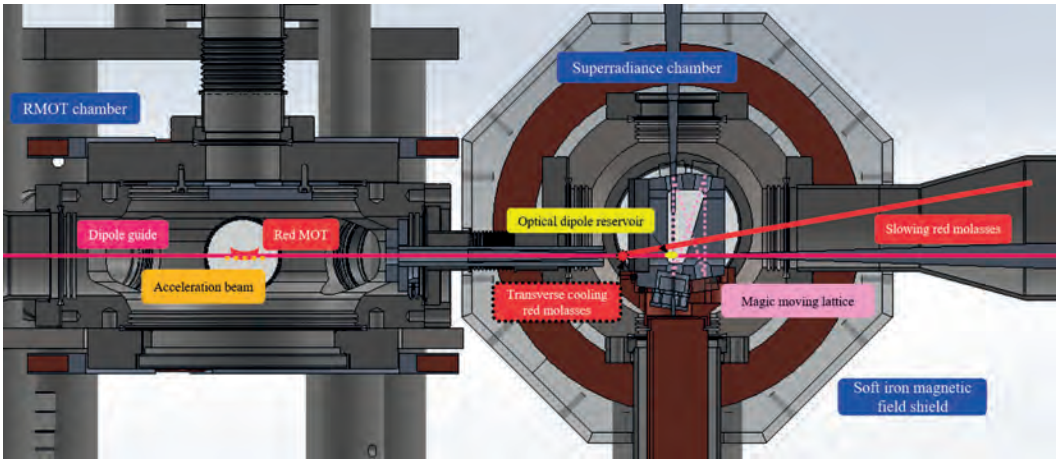


FIGURE 4.18: **Continuous atom transfer from the 3D red MOT to the superradiant lasing cavity.** Atoms initially confined within the red MOT are first loaded into an overlapping optical dipole trap. Subsequently, they are accelerated to depart from the red MOT and directed towards the cavity. Upon reaching the superradiance chamber, they undergo deceleration via red molasses and are then loaded into an optical dipole reservoir, which coincides with the bow-tie cavity mode.

photons from these MOT beams for atoms in the guide, which would otherwise push the atoms back into the MOT. However, this method is unsuitable for our mHz clock transition superradiance apparatus, as it would require passing a MOT beam pair through the superradiant laser cavity, projecting atoms out of superposition states and removing them from the superradiant ensemble.

Efficient and timely transfer of atoms along the guide to the superradiant chamber necessitates acceleration to velocities on the order of 0.2 m/s, resulting in a transfer time of 1 s. This ensures minimal losses caused by the limited vacuum lifetime. We avoid using an even slower atomic beam due to concerns about scattered light in the chamber heating up the atoms. Utilizing a relatively fast atomic beam ensures that atoms spend little time exposed to this scattered light.

In the red MOT, ultracold atoms, when accelerated, tend to be pushed back toward the center of the MOT. Therefore, the primary objective of accelerating atoms is to facilitate their escape from the MOT confinement. One approach involves directly pushing ultracold atoms until a Doppler shift is achieved, causing atoms to move out of the MOT's capture velocity range and rendering the MOT effectively invisible. Alternatively, temporarily reducing the red MOT laser frequency bandwidth or even shutting down the MOT presents yet another viable approach. Another method for pushing atoms out of the MOT is akin to

the previously employed dark spot scheme, where the MOT comprises some dark spots or otherwise spatially distinct regions.

**Acceleration and transfer of atoms in the $^1S_0$ ground state**

Our initial plan is to accelerate atoms in the $^1S_0$ ground state out of the MOT using either a 689 nm detuned laser to create an accelerating moving lattice (also called Bloch accelerator [111]) or using a resonant push beam. A resonant push beam can accelerate atoms at the most of 15g. It also leads to transversal heating. An accelerating optical lattice can reach higher accelerations and does only heat from off-resonant scattering. These beams can accelerate atoms within the red MOT, ideally to sufficient Doppler shift to escape the influence of the MOT beams. A beam velocity of 0.2 m/s corresponds to a Doppler shift of approximately 290 kHz, while the light shift from the dipole guide beam is estimated to be around 100 kHz. These values are relatively small compared to the typical frequency modulation bandwidth of our broadband red MOT, which ranges from 0.1 MHz to 2 MHz in our current machine and from 0.7 MHz to 3 MHz in our previous machine [51, 56]. Restricting the frequency bandwidth of the red MOT to around 250 kHz could seriously affect capture efficiency. However, if the reduced bandwidth beams are spatially small within the larger MOT beams, particularly along the Z-axis (see Figure 4.1) as observed in our atom laser machine [56], their impact on overall capture efficiency and temperature might be negligible. While this engineered solution introduces complexity, it presents an appealing approach. One concern is the potential interaction with the vertical MOT beam, which could lead to heating of the guided atoms, necessitating aperturing of the vertical capture beam along certain sections of the guide as the atoms exit. Alternatively, with all six red MOT beams this vertical beam could effectively transversally cool the atomic beam.

To avoid engineering the MOT beams to have different frequencies spatially, the entire horizontal MOT beams could be momentarily deactivated or have their frequency bandwidth reduced. This would allow the accelerator laser beam to operate freely, unaffected by MOT forces during the atom acceleration process. The entire acceleration procedure can be completed in 2 ms or less, facilitating the potential recapture of nearly all atoms, as the original MOT cloud will have undergone minimal expansion in the horizontal plane. Nevertheless at 0.2 m/s it takes around 50 ms for the accelerated atoms to exit the MOT region during which the horizontal MOT beam bandwidth will need to remain restricted. One trick we can apply is to make the accelerator laser beam larger than the red MOT beam. We accelerate the atoms in the guide at the MOT center to a speed that Doppler shifts them out of resonance from the red MOT beams (e.g. 2 m/s). Then, we conservatively slow them down again to a speed that can be easily recaptured when they arrive at the supperradiant chamber (e.g. 0.2 m/s). This approach would not require any adjustment of the red MOT frequency or power, and relies instead on an optimized moving lattice acceleration and

deceleration sequence. Although the sequence of ultracold atom loading into the guide and acceleration is pulsed, this acceleration sequence could be repeated every few 10 ms. This would result in atomic clouds drifting down the guide and coalescing into a continuous beam before reaching the superradiant laser chamber.

The optical configuration utilizing a 689 nm Bloch accelerator is presented in Figure 4.19 (Top view). From the side viewport of the red MOT chamber, two beams of different frequencies can be introduced. One beam is slightly tilted to overlap with the red MOT beam, while the other is reflected on an in-vacuum mirror to generate the counter-propagating beam for the former beam to build a moving lattice toward the cavity chamber. The advantage of the Bloch accelerator lies in the fact that only the overlap region between the Bloch accelerator beams can generate the moving lattice to accelerate atoms; elsewhere, the beams simply give a background light shift with little scattering of the atoms since it is not resonant.

The in-vacuum mirror is a 150 mm radius of curvature silver mirror mounted to the differential superradiant chamber pumping tube and aligned axially with the guide, as illustrated in Figure 4.17. This mirror was fixed using ND 353 adhesive to a titanium disk screwed to the bellows flange, which also features a thread for securing a 6 mm diameter, 70 mm long aluminum differential pumping tube.

Another optical alignment option to create the Bloch accelerator involves sending the laser beams onto the MOT through the bottom viewport, as shown in Figure 4.19 (Side view). However, it is important to note that atoms in the overlap between the Bloch accelerator and the red MOT would all be accelerated and decelerated. However, only the atoms also in the dipole guide beam can be transferred to the cavity chamber; others will fall down and become waste. Therefore, from the bottom view, it is preferable to at least reshape the Bloch accelerator beams into an elliptic shape to better match with the dipole guide beam.

Although the on-resonant push beams can only push the atoms and not slow them within their fixed optical alignment and frequency, there is a potential way to also accelerate ultracold atoms to 'escape' from the MOT. For this, we need to engineer the horizontal red MOT beam similar to the beams with dark spots in our atom laser machine. The concept is to create a dark tunnel where atoms are not trapped in the red MOT. This approach involves casting slit-like shadows into the MOT beams and compensating for the absence of MOT light in these critical regions by introducing additional tilted MOT beams.

The push beam will be aligned with the horizontal shadow, as presented in Figure 4.19 (Top view). Here, the two push beams are angled to overlap with the red MOT and the dipole trap beam. The push beams need to be symmetric to provide a balanced directional force along the guide towards the cavity chamber. The pushing beam can exert force on the atoms in the dipole guide, toward the cavity chamber, without being pushed back due to

the absence of the red MOT beams pushing back. Assuming the acceleration from the push beam is approximately $100\,\mathrm{m}\cdot\mathrm{s}^2$, it would take only 2 ms to accelerate atoms by 0.2 m/s. The accelerating tunnel is approximately 0.2 mm long, which is very small. Since the push beam method requires careful engineering of the red MOT and push beams [55, 56], we will first try to use the Bloch accelerator to achieve the transfer of atoms.

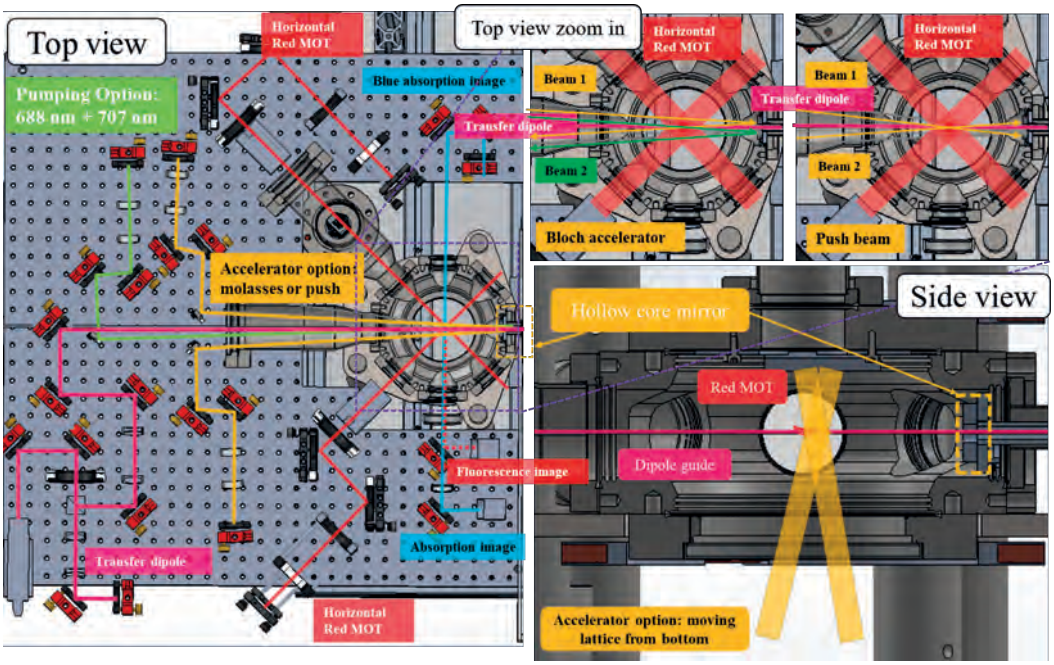


FIGURE 4.19: **Atom acceleration options.** Viewing the red MOT chamber from the top, two tilted beams (illustrated by orange lines in the diagram) can be utilized to accelerate atoms within the red MOT through methods such as pushing, moving molasses or moving lattice. The dashed box indicates a hollow-core mirror, offering additional optical access for these beams. The green line denotes the optical pathway for optionally pumping atoms into the $^3P_0$ metastable state. From a side perspective, two tilted beams (also depicted by orange lines) can be employed to construct an elongated moving lattice for accelerating the atoms.

**Accelerate in $^1S_0$ and transfer in metastable $^3P_0$ or $^3P_2$ states**

If our previously mentioned methods do not have high transfer efficiency due to the atoms being recaptured by the red MOT or turning off the red MOT causing other issues, we have a backup plan. The challenge with ground state atoms is their difficulty in escaping from the red MOT due to being pushed back by the red MOT beams. One solution to this problem is to optically pump the atoms to the $^3P_0$ or $^3P_2$ metastable states, where they would no longer interact with the red MOT beams. This could be done before or after

having accelerated the atoms in $^1S_0$. By pumping the atoms to $^3P_0$ using 689 nm, 688 nm, 679 nm and 707 nm beams, the 689 nm beam could be used to Doppler select the already accelerated atoms. This could make the transfer efficient and relatively easy.

**Acceleration and transfer in metastable $^3P_0$ or $^3P_2$ state**

Atoms can be transferred to the metastable state and then accelerated. The metastable state atoms offer two optical transitions suitable for accelerating them. One transition involves the $^3P_0$ to $^3S_1$ transition, which has a visible wavelength of 679 nm and a linewidth of 1.5 MHz. The other transition is the $^3P_2$ to $^3D_3$ transition, which is an infrared transition (2923 nm) with a narrower linewidth, as depicted in Figure 2.2. We have considered various acceleration techniques for atoms in metastable states [78], and I will now provide a brief overview of these options.

A resonant 679 nm beam can push the atoms utilizing their $^3P_0$-$^3S_1$ transition, in a similar way as the 689 nm beam can push ground state atoms. The advantage, compared with the 689 nm push beam, is that the 679 nm beam works also without a dark spot in the red MOT beam. A disadvantage is that the 679 nm beam needs to co-propagate with the 688 nm and 707 nm repumper laser beams to repump atoms decaying from $^3S_1$ to the $^3P_1$ or $^3P_2$ states. Another disadvantage is that the 1.5 MHz linewidth of the $^3P_0$-$^3S_1$ transition (instead of the 7.5 kHz linewidth of the $^1S_0$-$^3P_1$ transition) is likely to result in far less control over the final velocity and increases the atomic beam temperature. Unlike in [52], where atoms simply Doppler shift out of resonance upon reaching their selected target velocity, using a broader linewidth transition may lead to a loss of precision in controlling the final velocity.

Strobed 679 nm Bloch acceleration can also be utilized here, offering several advantages. Firstly, a very shallow lattice depth of 20 µK is sufficient for extreme acceleration, while still allowing for significantly higher accelerations and a well-defined final speed compared to a push beam. Additionally, the required beam intensities can be kept quite small, resulting in minimal photon scattering, thereby eliminating the need for repumping. Furthermore, this approach does not rely on any specific spatial state transfer location, greatly enhancing robustness and efficiency. At high Bloch strobe frequencies, atoms from neighboring pulses will intermingle while traversing the guide and ultimately be collected into a single reservoir at the superradiant chamber, ensuring essentially continuous loading of the superradiant clock cavity.

Another option involves accelerating atoms from $^3P_2$ using the $^3P_2$ to $^3D_3$ transition at 2923 nm [112–114]. This approach offers the advantages of a narrow transition and a closed cycling transition. The magnetic tunability of this transition provides spatial selectivity, which may be advantageous or disadvantageous depending on the specific application. Implementing a moving molasses for $^3P_2$ on the 2923 nm cycling transition

can also accelerate atoms in the dipole guide beam. However, this scheme may encounter obstacles for $^{87}$Sr due to its numerous sublevels.

**Challenges in accelerating metastable $^3P_J$ state atoms.** The first challenge arises from imperfect optical alignment of repumper lasers with the dipole guide beam. Once the atoms are transferred to the $^3P_0$ metastable state, the MOT beams are effectively invisible to the atoms, which is desired for atoms captured by the guide. However atoms that are not captured will be lost. If this loss is not tolerable, repumping beams at wavelengths of 679 nm ($^3P_0$ - $^3S_1$) and 707 nm ($^3P_2$ - $^3S_1$) have to illuminate the red MOT, but not the guide, and transfer atoms not captured by the guide back to $^1S_0$, so that they can be recaptured by the red MOT.

To minimize the creation of non-guide-loaded $^3P_0$ atoms, the 688 nm ($^3P_1$ - $^3S_1$) pumping laser beam should have a slightly smaller radius than the guide beam. Additionally, it should intersect the guide at the MOT location at the smallest possible angle (a few degrees) that avoids sending it into the superradiance chamber (where it could have undesired effects), while keeping the volume small that is irradiated by the pumping beam but lays outside of the guide.

Another challenge lies in the fact that transitions from $^3P_0$ to $^3S_1$ (or $^3D_1$) are not closed. As a result, an atom can be pumped out of $^3P_0$ by a single scattered 679 nm photon.

Using the $^3P_2$ to $^3D_3$ transition presents laser construction challenges. Despite the uncoated fused silica end window's reasonable transmission at 2923 nm, challenges remain due to the difficult laser wavelength and numerous sublevels in the case of $^{87}$Sr.

**Summary**

While thorough consideration has been given to all these approaches in the optical design surrounding the vacuum chamber, our initial focus will be on implementing pulsed Bloch acceleration of $^1S_0$ atoms using 5 MHz detuned 689 nm light. This approach is particularly appealing due to its simplicity, as it does not require the construction of exotic lasers or complex spatial pumping and repumping configurations. Initially we will briefly reduce the red MOT bandwidth to facilitate the exit of atoms after each acceleration sequence. This can later be improved by accelerating atoms to approximately 2 m/s, which Doppler shifts them out of the full bandwidth of the red MOT beams, even considering the Zeeman shifts from the quadrupole field of the MOT. Rendering the accelerated atoms invisible to MOT light in that way facilitates their escape. Once the atoms have escaped the influence of the MOT they can be slowed down again in order to be easily captured in the superradiance chamber.

### 4.2.2 Optical dipole guide

One final crucial consideration is the configuration of the guide beam. This guide keeps the atomic beam collimated and provides support against gravity during the transfer of atoms from the 3D red MOT to the superradiant cavity over a distance of approximately 25 cm in length.

By employing a 1070 nm, linearly polarized, single spatial mode fiber laser (IPG, YLR-400-LP-WC-Y14), we can generate a 250-W Gaussian beam along with an optional 190-W retro-reflected beam. Each of these beams is focused to a waist radius of 180 µm, with their focus locations offset by 160 mm along the propagation path. Interference between the beams is avoided because the laser source has a large linewidth of 3 nm. Employing techniques detailed in [52, 80], we can achieve a deep guide over a significant propagation distance.

As illustrated in Figure 4.20, this configuration enables the maintenance of a guide depth of approximately 120 µK for atoms in the $^3P_0$ state and 200 µK for atoms in the $^1S_0$ state throughout the entire propagation path. The depths stated here take gravity into account.

This depth appears more than sufficient to retain atoms from a 10 µK MOT accelerated to 0.2 m/s, especially considering our previous success using a 20-30 µK deep guide to transfer atoms at 0.1 m/s [51, 52, 80].

The high intensity of the laser spot on the vacuum windows prohibits the use of anti-reflection coatings like those used on the other windows used on our apparatus. To further reduce the risk of surface damage from dust on the windows, extension nipples were incorporated into the vacuum system, as depicted in Figure 4.17. These extensions provide additional distance between beam focus and window, allowing diffraction to increase the beam size and reduce the intensity at the window surfaces.

While the power levels required for a Gaussian guide beam are manageable, the risk of optical damage to the viewports remains concerning. As a potential alternative we also considered the feasibility of using a Bessel beam for the guide [115]. Bessel beams are famed for their non diffracting central structure, which can in principle provide longer distance beam propagation. Plots showing the potential for a suitable Bessel guide beam are presented in Figure 4.21. These plots show that a 150 µK deep guide can be sustained for $^1S_0$ atoms over a 25 cm propagation path with approximately 240 W of 1070 nm laser power.

A Bessel beam offers significantly reduced beam sizes (inner diffraction spot) compared to a Gaussian beam, capable of achieving high radial trapping frequencies, which can be sustained over long propagation distances. Another advantage of employing a Bessel beams is the substantial reduction in intensity at the location of the viewports, while still

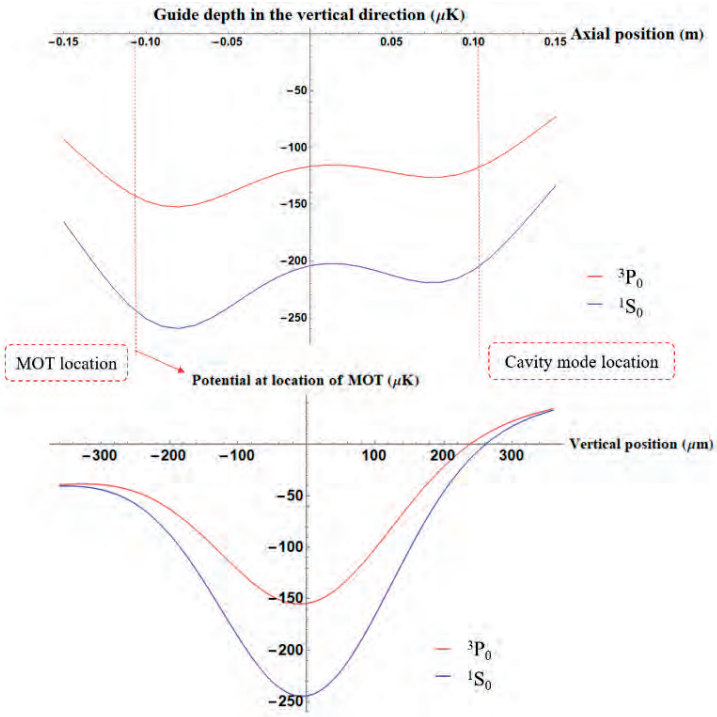


FIGURE 4.20: **Trap depth for Gaussian beam dipole guide.** The trap depth along the vertical direction, accounting for gravity, is depicted for atoms in the $^3P_0$ and $^1S_0$ states over a 25 cm propagation distance. A 1070 nm dipole guide laser beam with 250 W power is propagating forward. By retro-reflecting the laser beam a 190-W beam is sent into the opposite direction. Interference between the beams is avoided by using a 3-nm linewidth laser source. Both the forward and reverse propagating beams are focused to a waist radius of 180 µm, with the focal planes offset by 160 mm.

preserving a deep guide capable of propagating over a considerable distance. With a 0.5 deg axicon, the intensity reduction at the window surface can be approximately two orders of magnitude, mitigating the risk of optical damage and enabling the use of AR coated windows, which would be essential for a Bessel beam to prevent secondary interferences.

Nevertheless, there are several drawbacks to consider. For applications such as creating a continuous atom laser [54], the high trapping frequencies and small trap volume are highly desirable - provided atoms can be loaded. However, for our application of long-distance transport, a small trap volume is disadvantageous, due to two-boday losses in case we guide atoms in $^3P_0$ [83]. Despite similar power requirements, the trap volumes are significantly reduced, leading to decreased loading efficiency from the MOT and increased density losses. Additionally, atoms may also be trapped in the outer rings of the Bessel beam, potentially

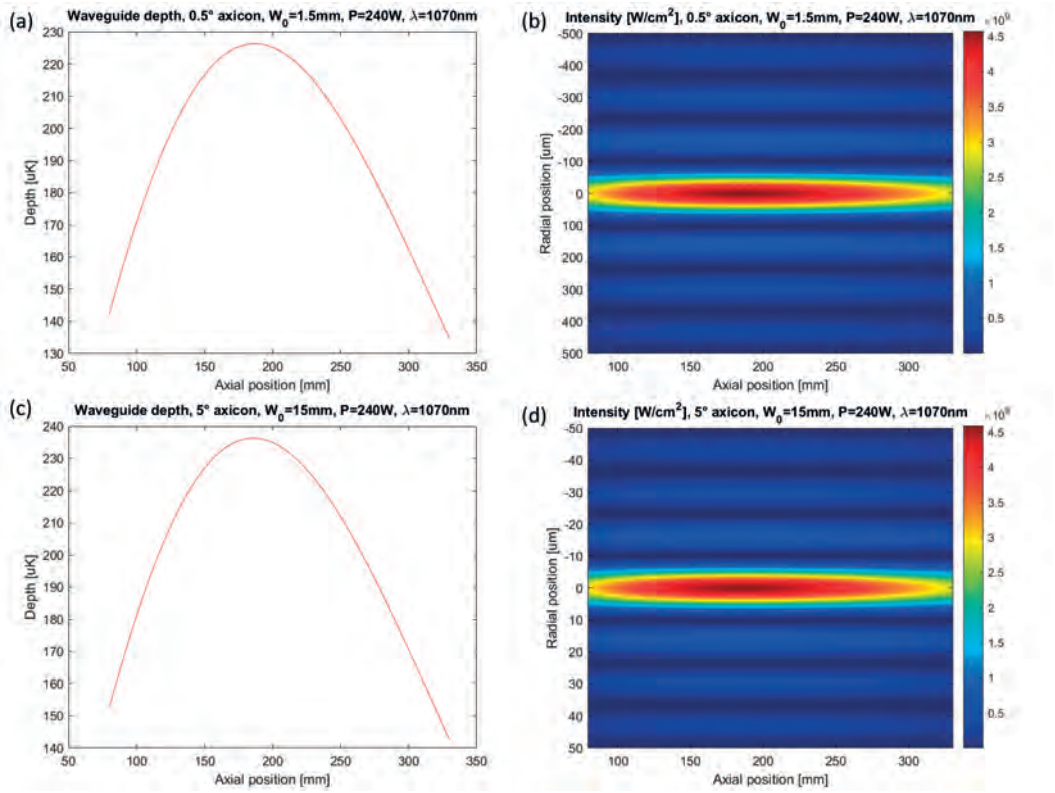


FIGURE 4.21: **Potential of a Bessel beam guide.** A Bessel beam can provide a smaller beam size while offering a 150 µK deep guide for atoms in the $^1S_0$ state. This depth can be sustained over a 25 cm propagation length, similar to the Gaussian guide beam. This requires a similar power to the Gaussian beam (240 W), but without the need for retro-reflection. Depending on the axicon angle and beam size, very tight beams can be propagated over long distances, enabling high trapping frequencies and efficient evaporation (although evaporation is not desirable in the application considered here). In the scenario shown in panels (a) and (b), an ideal Bessel beam, generated by sending a 1.5 mm waist radius Gaussian beam through a 0.5° axicon, generates a beam with a $1/e^2$ radius of around 50 µm (compared to the 200 µm needed for a Gaussian beam). In the scenario shown in panels (c) and (d), an ideal Bessel beam, generated by sending a 15 mm waist radius Gaussian beam through a 5° axicon, creates a beam with a $1/e^2$ radius of around 5 µm (compared to the 200 µm needed for a Gaussian beam).

impacting loading efficiency from the 3D red MOT to the guide. Outer diffraction rings could induce Stark shifts, potentially several mm away from the guide at the location of the superradiant cavity, resulting in substantial inhomogeneities. Furthermore, real axicons exhibit curvature at their tips, leading to a washboard effect along the guide unless

meticulously spatially filtered [115]. Lastly, the large effective beam size due to the outer diffraction rings may cause clipping on both the differential pumping tube between the 3D red MOT chamber and the superradiant laser chamber, as well as on the superradiant cavity spacer and mirror structure. This could induce heating of the aperture and scatter the Bessel beam, generating additional diffraction edges and Stark shifts in the region of the superradiant laser.

For these reasons, for our application a Gaussian guide beam is a better choice than a Bessel beam.

### 4.2.3 Transversally cooling the guided dense atomic beam

In our prior investigations [52, 56, 80], we observed that transverse cooling of the guided atomic beam using a molasses on the 689 nm transition played a crucial role in achieving efficient atom transfer. However, in the case of $^{87}$Sr, the presence of magnetic field inhomogeneity, coupled with the intricate level structure of $^{87}$Sr, hindered effective transverse cooling of the guided atomic beam. Consequently, although a steady-state $^{87}$Sr red MOT has been successfully demonstrated [53], creating a guided beam of $^{87}$Sr remains a formidable challenge.

To not be restricted to bosonic Sr isotopes, we have implemented several strategies to address the $^{87}$Sr beam challenges found in [53]. Firstly, we are substantially deepening the guide, which will mitigate atom loss even for similar temperatures as those previously employed. In our previous work the limited laser power available for the guide, just 12 W at 1070 nm, necessitated the use of smaller beam and Rayleigh ranges, resulting in suboptimal guide depths on the order of 20-30 µK depending on location. Secondly, we have incorporated mirrors into the vacuum system to provide optical access, facilitating the option of transverse cooling using the 689 nm transition once atoms have cleared the red MOT beams. In the case of transfer in $^3P_0$ this would also require pumping atoms back to $^1S_0$ prior to transverse cooling. Finally, we have the option of transferring atoms to the metastable $^3P_0$ state, which can eliminate the scattering and heating in the first place.

The in-chamber mirrors added for transversally cooling the guided atomic beam are shown in Figure 4.17 and Figure 4.12. Like the in-vacuum optics discussed previously, these mirrors are fixed to a titanium plate using ND353 glue instead of being directly glued to the steel vacuum chamber. This reduces the thermal expansion coefficient mismatch between the glass mirrors and their support. The plate is subsequently screwed to the vacuum flange. An additional mirror provides vertical access, facilitating access to pure polarization states for more efficient state pumping.

### 4.2.4 Deceleration of the atomic beam

Upon reaching the superradiant clock cavity, atoms require deceleration and loading into an optical dipole trap. This dipole trap acts as a reservoir for storing atoms before they are loaded into the magic moving lattice propagating in the superradiant cavity.

Since our primary plan involves accelerating atoms in the $^1S_0$ ground state, the strategy to slow them down entails using a 0.3 MHz broadband molasses operating on the $^1S_0$ - $^3P_1$ transition. While this method is straightforward, it also generates a relatively warm reservoir. This concern prompted considerations of improved approaches that extract much of the energy from the incoming atoms, especially for high transfer speeds. Collaboration with our research partners, Swadheen Dubey and Georgy Kazakov of TU Wien Vienna, has yielded simulations showing that a slowing stage that starts a few mm before the reservoir, combined with a low power broadband red molasses, can efficiently cool atoms from 20 cm/s to 1 cm/s and load them into the reservoir. A paper is in preparation on this simulation work [116].

Alternatively if we choose to transfer atoms in the metastable $^3P_0$ state, we can employ a 679 nm laser beam for deceleration. One option is strobed Bloch deceleration using a 679 nm + 100 GHz lattice that can reduce atom velocity by a factor of 10, mirroring the acceleration method outlined in Section 4.2.1. Once slowed, atoms can be pumped back to $^1S_0$ upon reaching the reservoir center, where a red 689 nm molasses can cool them. In principle, this could also be achieved using a lattice at 689 nm, detuned 5 MHz from the $^1S_0$ - $^3P_1$ transition. However, the deceleration beams would interact with and likely heat the reservoir atoms. Another deceleration approach would be use the Sisyphus optical lattice decelerator (SOLD) technique [52], once atoms have been pumped back to the $^1S_0$ state.

Optical access for slowing is facilitated by an in-chamber silver mirror mounted behind the cavity spacer, as shown in Figure 4.18.

## 4.3 Superradiant cavity

The design of the superradiant clock cavity is shown in Figure 4.22. The cavity features a symmetric bow-tie structure with a long axis of 50 mm and a short axis of 13 mm. A ring resonator accommodates a magic wavelength conveyor to move atoms along the cavity axis. The cavity, comprising two flat high reflectivity (HR) mirrors and two curved HR mirrors with a curvature radius of 500 mm (or 250 mm), supports a mode with a waist radius of about 175 µm (or 130 µm) at the atom's location. The mirrors are aligned and glued to an ultra-low expansion clearceram cavity spacer.

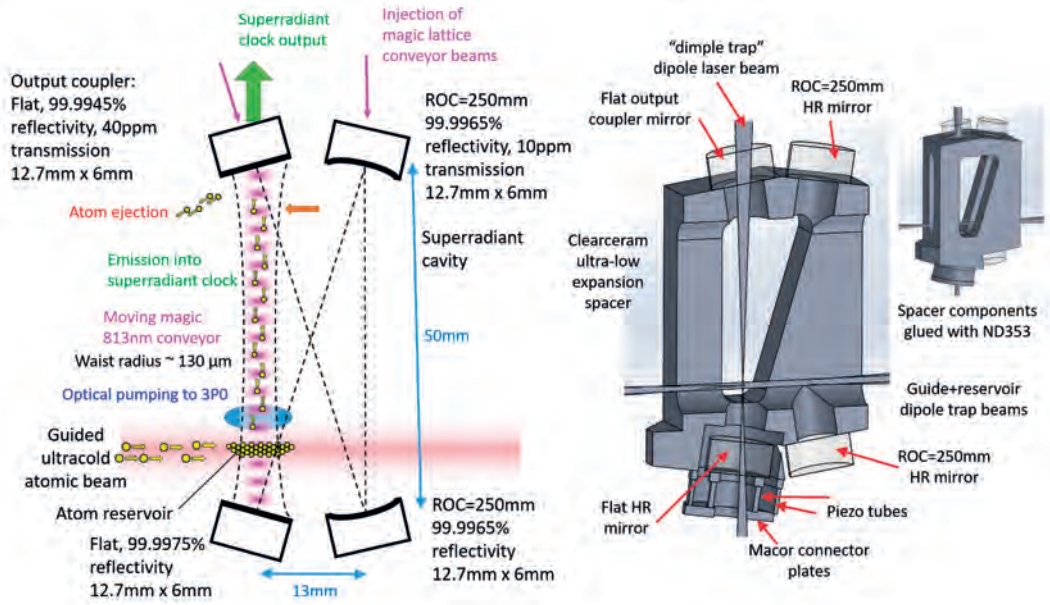


FIGURE 4.22: **The concept design and CAD design of the continuous superradiant clock cavity.**

Two substrate classes were available: "premium polish" (surface roughness <0.2 nm rms) and "superpolished" (surface roughness <0.1 nm rms)[3]. The expected losses for different substrate types are detailed in Table 4.1, which also presents data for scenarios where the losses are doubled, as stated by the company, suggesting that scatter losses could potentially be twice as high as initially anticipated.

The reflectivity of the HR mirrors at 698 nm was chosen to be as high as possible from the manufacturer (LASEROPTIK), 10ppm transmission, while a transmission of 40ppm (>20ppm spec) was targeted for the output coupler at 698 nm. The transmission on the output coupler is enhanced in order to capture at least 27% of the power emitted by the atoms within the cavity, ensuring a detectable output beam. Large uncertainties in both the scatter and transmission specifications result in a finesse range of 27,000 to 42,000, as presented in Table 4.1. A finesse of 30,000 was set as the minimum requirement to achieve the necessary high cooperativity within the cavity, as discussed in the calculations outlined in Table 2.2 in Chapter 2. The ideally expected coating values are calculated to yield a finesse of 41,900 at 698 nm.

[3]For superpolished, only 500 mm radius of curvature and flat substrates were available. Although we made cavities with both the superpolished 500 mm radius of curvature mirrors and the premium polished 250 mm radius of curvature mirrors, the cavity with the superpolished mirrors was eventually used in the vacuum system so I will focus on that.

| | Expected losses @ 698 nm | 2 x more losses @ 698 nm | Ideal losses @ 689 nm | 5 x more losses @ 689 nm |
|---|---|---|---|---|
| Losses + scatter of superpolished mirror (ppm) | 15 | 30 | 15 | 75 |
| Losses + scatter of premium mirror (ppm) | 25 | 50 | 25 | 125 |
| Transmission of output coupler (flat mirror) | 40 | 40 | 45 | 40 |
| Transmission of the flat mirror on the piezo | 10 | 10 | 10 | 10 |
| Transmission of the curved mirror | 10 | 10 | 10 | 10 |
| Total reflectivity | 0.99985 | 0.99977 | 0.99982 | 0.9995 |
| Finesse | 42000 | 27000 | 40000 | 13000 |
| Coupling efficiency (calculated with Finesse2 [117]) | 0.5 | 0.35 | 0.45 | 0.25 |
| Percentage of output power | 0.27 | 0.17 | 0.3 | 0.096 |

TABLE 4.1: Cavity performance comparison of different mirror setups

The superradiant cavity must be maintained in resonance with the clock transition, which we achieve by tuning the cavity length using a piezo. A thermally compensated piezo actuator arrangement is used, similar to the design for the hot beam machine [56, 107]. The piezo will be servoed using a Pound-Drever-Hall (PDH) lock, employing a probe beam detuned by (at least) one free spectral range (1.47 GHz) from the clock transition frequency. This frequency will be derived from the clock reference laser using a fiber EOM. The clock laser in turn is transfer locked to the spectroscopically locked 689 nm red master laser.

The frequency of the 813 nm magic-wavelength lattice laser is adjusted to resonate with the cavity resonance closest to the magic wavelength for the $^1S_0$ - $^3P_0$ transition. This will not be much better than half an FSR detuned from magic so there will be some light shift. This shift might be mitigated by introducing an additional frequency component resonating with the cavity on the opposite side of the magic wavelength, as implemented in the UMK machine [59].

Given the necessity for a magic moving lattice (propagating upwards), distinct frequencies are required for forward and backward propagating cavity modes, resulting in neither lattice beam precisely being resonant with the cavity. The lattice speeds typically range from 0.02-0.2 m/s, corresponding to a frequency difference of 25-250 kHz. Consequently, the magic moving lattice light may be detuned by up to 125 kHz from resonance. Hence, a relatively low finesse cavity of 1600 at 813 nm was targeted, corresponding to a mirror

reflectivity of 99.8%. Since this is not the main design wavelength there is a large uncertainty on the finesse at this wavelength due to manufacturing tolerances. The target magic moving lattice depth is approximately 50 recoil energies (8.2 µK), necessitating injection powers of around 1.1 mW from each magic moving lattice beam (disregarding cavity and coupling losses).

### 4.3.1 Cavity construction

The building process involved the efforts of multiple team members. Francesca and Shayne designed and ordered the cavity spacer, mirrors, piezos and glues. Upon receiving the materials, Camila and Francesca endeavored to devise construction processes, measured the transmission and reflectivity of each mirror, also built a linear cavity to measure the reflectivity of each mirror, and checked the parallelism of the ring cavity spacer surfaces. Later, Benedikt, along with Camila, constructed some piezo stacks. I began to focus on the cavity construction after Camila moved to Copenhagen for a 6-month secondment, after which she focused primarily on the hot beam machine.

Ultimately, our cavity did not achieve the expected finesse. The best finesse we obtained for the ring cavity was four times lower than anticipated based on mirror parameters provided by LASEROPTIK, the coating company. Shayne and I suspected higher-than-expected scattering losses, prompting considerations for repeating the linear cavity measurements to validate our observations. However, with the vacuum system waiting and due to time constraints, I decided to proceed without further investigation and constructed several cavities with Benedikt and Ananya. Due to the large number of people who owned the cavity construction project over a period of years I will only provide a minimalistic description of the building processes in my thesis. Nevertheless, the insights gained from the ring cavity construction are valuable for those interested in such endeavors. Hence, in this presentation, I will concentrate on detailing key aspects of the work completed during the construction of the ring cavity.

I began by investigating losses and transmission of the mirrors to try to understand inconsistencies between the manufacturer's specifications and earlier measurements made with a linear cavity. To accomplish this, I set up the experiment as illustrated in Figure 4.23. A 9-mW 689 nm laser served as the light source. Our out-coupler mirrors boasted a transmission of 40ppm, presented in Figure 4.24, resulting in approximately 400 nW of transmitted power, while the other mirrors had a transmission of 10ppm, yielding 90 nW. To ensure accurate measurements, I opted for a calibrated commercial power meter (S130C, Thorlabs), chosen for its capability to measure a minimum power of 500 pW. I positioned the power meter far from any mirror to minimize scattered light, and inserted an additional black

tube in front of the sensor to reduce background light as much as possible. The ambient background light resulted in a measurement offset of around 4 nW when the room light was off.

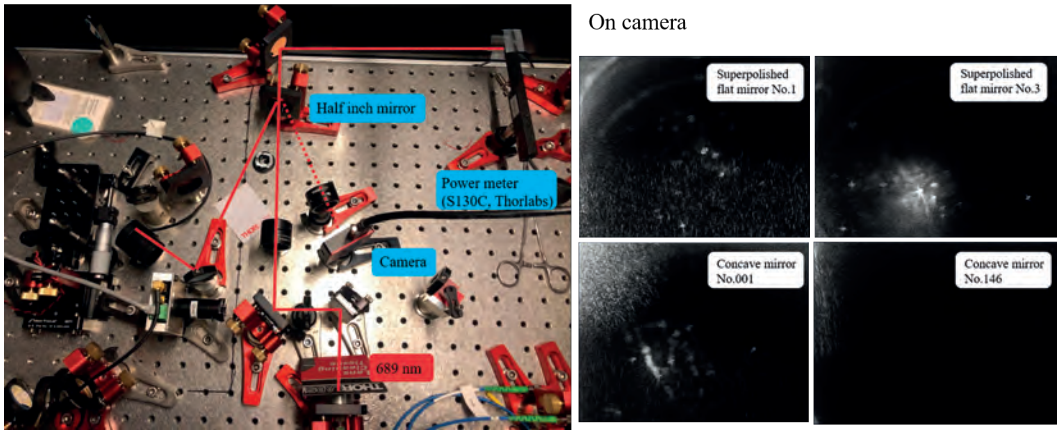


FIGURE 4.23: **Transimission measurement setup for cavity mirrors.** The transmission measurement setup for cavity mirrors starts with a 689 nm laser beam with a power of about 9 mW. On average, the transmission of the out-coupler mirrors was 50ppm, while that of the other mirrors averaged 10ppm, which both were consistent with the parameters provided by the coating company. Despite this alignment with expectations of the transimission, the image captured by the camera revealed a significantly higher level of scattered light than anticipated.

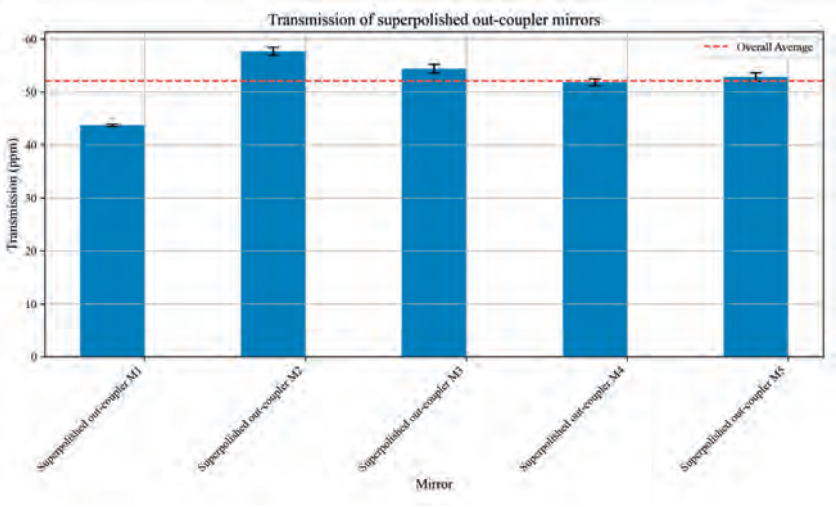


FIGURE 4.24: **Transmission measurement of the out-coupler mirrors.**

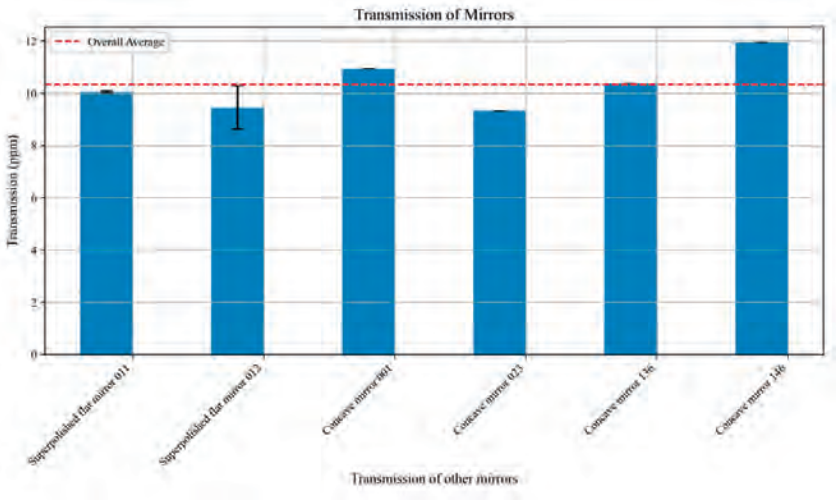


FIGURE 4.25: **Transmission measurement of other highly reflected mirrors.**

The average transmission of our out-coupler mirrors was approximately 52ppm, presented in Figure 4.24, very close to the parameter claimed by the company. Similarly, the average transmission of the other highly reflective mirrors was 10ppm, shown in Figure 4.25, exactly as claimed by the company. When I measured the transmission, I also rotated the mirrors to check if there were defect on the mirror. Notably, a camera was positioned and focused on the mirrors to monitor any scattering. Numerous points where scattered light flashed up were observed, presented in Figure 4.23, indicating dirt accumulation on most cavity mirrors. All the mirrors were not fresh out of their original packaging but had been opened before and stored in their original plastic box. Randomly, we found that one particular mirror (concave mirror No.146) had very little particulate scattering indicating that the camera imaging system was clean and that the scattering observed was not an artifact from the imaging system. This observation was further corroborated when attempts were made to clean the mirrors, as confirmed by microscopic examination, as shown in Figure 4.29. My conclusion was that the mirror coating transmission was likely within spec and that excess losses were due either to surface contamination or excess scattering.

The next phase involved constructing the cavity, which entails the placement and adhesive bonding of the four mirrors onto the cavity spacer. Two of these four mirrors are flat, which makes it easier to align them compared to curved mirrors, as the radial degree of freedom is uncritical. Therefore we started affixing the flat mirrors. We employed EPO-TEK 353ND glue (curing in an oven at 130 °C). We initially glued the parts of the thermally compensated piezo stack assembly together and to a flat mirror. Next, we

glued this assembly and the flat output coupler mirror to the spacer. The adhesive was carefully weighed using precision scales (available in the chemistry laboratory) to ensure correct component ratios and subsequently degassed for 20 min with a primary pump. The procedure unfolded smoothly, as depicted in Figure 4.26. The 0.1 mm diameter kapton insulated copper wires (Allectra 311-KAP-010-10M) needed to control the piezo tubes were soldered to the piezos using UHV compatible solder (Allectra 315-LF-SOLDER-1M). These wires proved very fragile and difficult to work with as they needed to be coiled and kept UHV vacuum clean, while simultaneously used to control the piezo during cavity alignment. Occasionally, the wires became detached, and reattachment required a dedicated soldering iron specifically reserved for UHV soldering.


FIGURE 4.26: **Processes of gluing flat mirrors.** One flat mirror was glued on the piezo stack with a structure to protect the mirror from moving when the glue was curing in the oven. Then the piezo stack and another flat mirror were glued on the cavity spacer. The wires to the piezo stack were shorted and covered with aluminum foil.

For the remaining two curved mirrors, our initial plan involved orienting the spacer vertically, allowing one curved mirror to rest gently on the spacer while being moved horizontally with minimal vertical effect. There were some drawbacks to this approach, including difficulties in mounting and limited optical access. Consequently, we opted for a horizontal orientation, as illustrated in Figure 4.27, which showcases the CAD design for the cavity holder and optical alignment of the cavity.

Optical alignment, shown in Figure 4.27, was facilitated using lasers at 689 nm and 780 nm. Given that the cavity finesse at 780 nm is only in the range of a few hundred, alignment at this wavelength proved more manageable compared to 689 nm. These lasers were further frequency modulated using a homemade electro-optic modulator (EOM) for

sideband measurements and sent through a double-pass acousto-optic modulators (AOM) to achieve rapid switch-off times in the hundreds of nanoseconds range, which was essential for ringdown measurements. Prior to entering the cavity, a mode match for the 689 nm laser was achieved with the adjustment of two lenses.

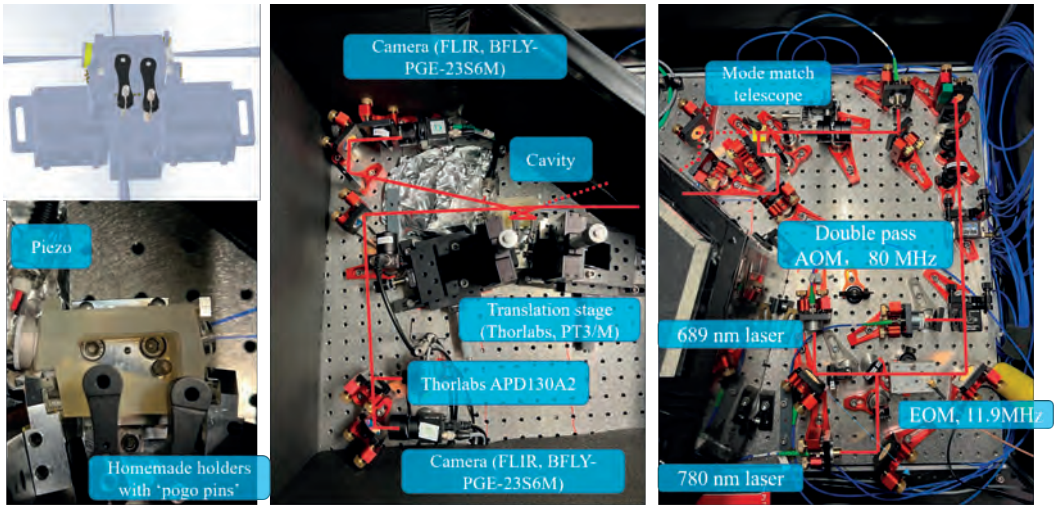


FIGURE 4.27: **Cavity alignment.** The two curved mirrors were spring pressed to the cavity spacer using an array of 'pogo pins', with the spacer mounted on an optical breadboard. The setup for aligning the curved mirrors of the cavity and measuring the cavity finesse features an EOM to create sidebands on the light injected into the cavity, a double-pass AOM for fast switching in prder to perform cavity ringdown measurements, and a mode matching telescope optimized at the wavelength of 689 nm.

The first signal, as depicted in Figure 4.28, while not flawless, was nonetheless cheerful. At this early stage, our experience with the ring cavity alignment was limited. Among the most valuable techniques we employed was the use of an IR viewer to visualize the propagation of the 780 nm laser beam. To enhance visibility, we incrementally increased the laser power from 1 mW to 10 mW. By delicately holding a piece of optical cleaning tissue with tweezers, we observed the scattered light on the tissue, which provided insight into the laser's propagation within the cavity. As we progressively closed the loop of propagation, the cavity mode emerged, marking a significant milestone in our alignment process. This method was used also for measuring the beam location within the cavity spacer to compare it with the CAD design.

Following the initial signal acquisition, the optimization phase commenced, focusing on aligning the cavity by offsetting the two curved mirrors while maintaining their contact with the spacer. Utilizing a three axis translation stage (Thorlabs PT3/M), we iteratively

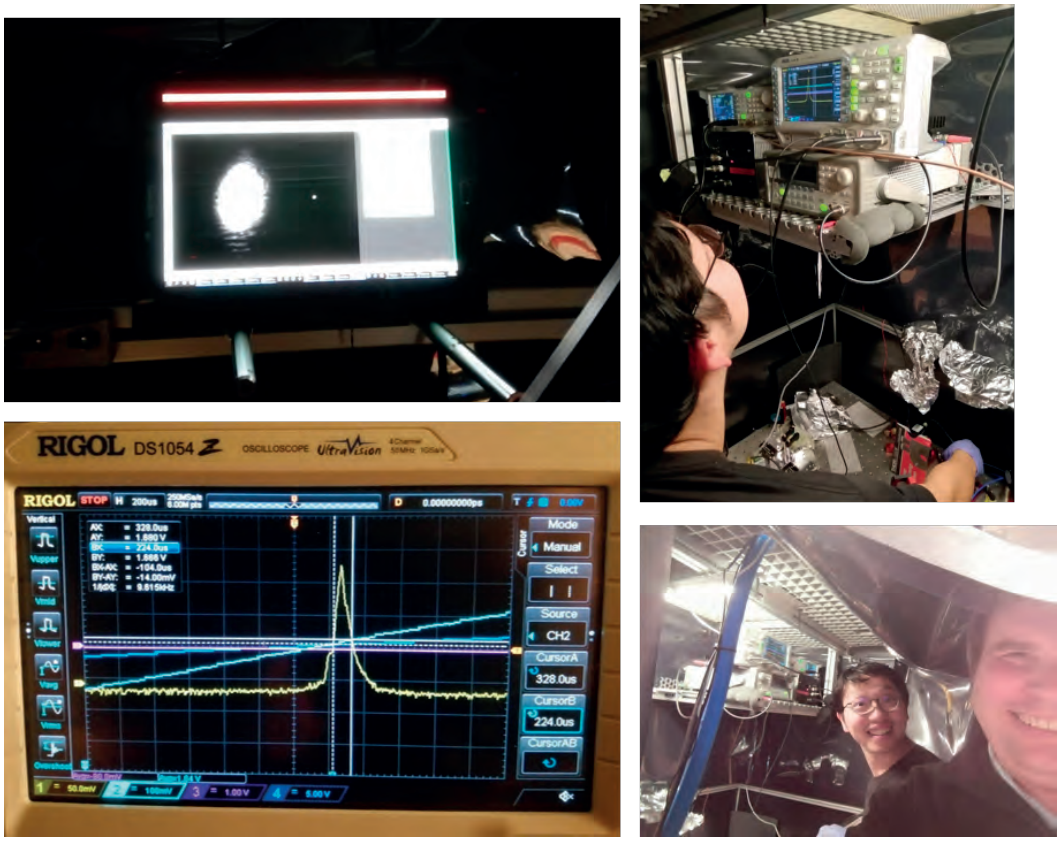


FIGURE 4.28: **The first cavity mode signal from the ring cavity.** The cavity mode observed was the TEM00 Gaussian mode, albeit not perfect. Despite the broad appearance of the linewidth, the expressions on the faces of the two individuals present reflect a sense of satisfaction and happiness.

adjusted the positions of these mirrors to maximize finesse. We found that, with a periodic horizontal movement, we can repeatedly build up the TEM00 Gaussian mode. Despite our efforts, the best finesse achieved was approximately 14,000, falling significantly short of our target and theoretical finesse of 40,000.

Suspecting dust accumulation on the mirrors as the potential culprit, we procured "first contact" optics cleaner and meticulously cleaned the curved mirrors and all remaining unglued mirrors. While this action reduced the scattering effect and improved mirror clarity, presented in Figure 4.29, the finesse remained at around 10,000.

Next, we glued the curved cavity mirrors. For the cavity used on the hot beam machine, we used Epotek 353ND and constructed an "oven" around the spacer to aid the process. During the curing of the hot beam machine cavity and with previous transfer lock cavities,

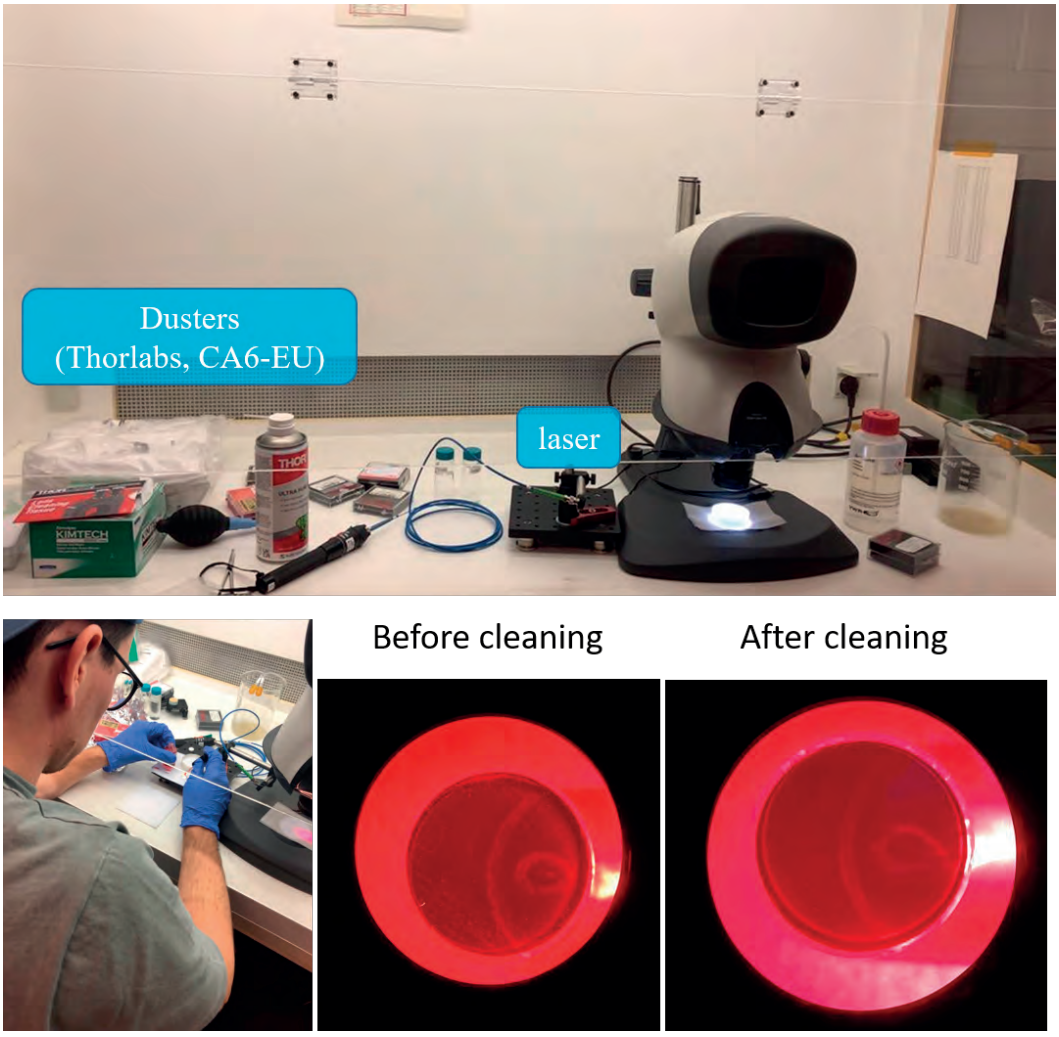


FIGURE 4.29: **Cavity mirror cleaning.** We used "first contact" cleaner to clean the cavity mirror. The reduction of scattered light showed that the dust was removed after cleaning.

we observed significant changes in the finesse during the glue curing process. This is likely due to heating and differing coefficients of thermal expansion. To address this, we opted for a new room-temperature curing glue for our superradiant cavities, which has a long 24-hour curing time (Masterbond EP21TCHT-1). This slow curing time was advantageous as it allows for potential corrections in alignment during the curing process.

In our first attempt to glue the curved mirrors, we applied the glue to the most accessible interface between the spacer and mirrors, which was the top. The glue had the consistency

of chewing gum, making it difficult to work with. We glued one mirror at a time. After a few hours of gluing the first mirror, the finesse dropped by around 10%, but we decided not to intervene, hoping it might recover. It didn't, and the finesse settled at 8,300. After gluing the first mirror, we reoptimized the cavity alignment for the second mirror and aimed to apply the glue more symmetrically. However, after gluing the second mirror, the finesse dropped to around 7,200.

Additionally, during in-vacuum measurements, we found that the TEM01 mode of the cavity coupled much better than the TEM00 mode, indicating misalignment during the gluing process. We also considered the possibility that the spacer holder might have bent the cavity spacer, which could have been released when mounting the cavity in its target holder, under vacuum. Numerical calculations suggested that applying a worst-case force of 200 N to the spacer could halve the cavity finesse, but we concluded that this was unlikely to be the cause of our issues.

Next, we glued a second cavity. From our three cavity spacers and limited quantity of mirrors, we chose the worst spacer and lower performance "premium polished" mirrors. Our goal was to demonstrate that we could glue a cavity without significant performance loss during the process.

To improve the gluing technique, we redesigned the curved mirror holder to allow better access for symmetrical glue application, using three 1 mm diameter glue drops. Apart from this change, we followed the same process as before. This time, the initial finesse of 4,100 remained around 3,950 after gluing.

In light of these findings, we carefully selected our best and final spacer along with the best remaining mirrors to construct a final cavity. The gluing process was successful once again; however, we only achieved a finesse of 8,000 before gluing, which dropped to 7,000 after gluing. Examples of our results are presented in Figure 4.30.

We concluded that increased and possibly out-of-specification scattering on the mirrors likely contributed to the diminished cavity finesse. As shown in Table 4.1, doubling the losses would decrease the finesse by a factor of two, while five times more losses would decrease the finesse by a factor of four, aligning with the finesse achieved in our best cavity. Furthermore, our cavity achieved a coupling efficiency of 25%, consistent with the calculated coupling efficiency when losses are increased fivefold.

Additionally, we discovered that one of the piezo wires had detached. While we resoldered it, the piezo suffered thermal damage, resulting in one of the two piezos (used for bias and locking) not functioning properly and exhibiting strong hysteresis.

We then purchased additional cavity spacers and built a fourth cavity with the remaining premium polished mirrors, but the performance did not improve. We considered purchasing additional mirrors from Five Nine Optics, but due to potential delays, we

decided to proceed with integrating our third cavity, which had a finesse of 7,000, into our vacuum chamber. To build the third and fourth cavities, an imaging system was added to observe the cavity mirror surface. This system was very useful for constructing the ring cavity, eliminating the need for the 780 nm laser since the camera can detect the 689 nm laser even with minimal light.

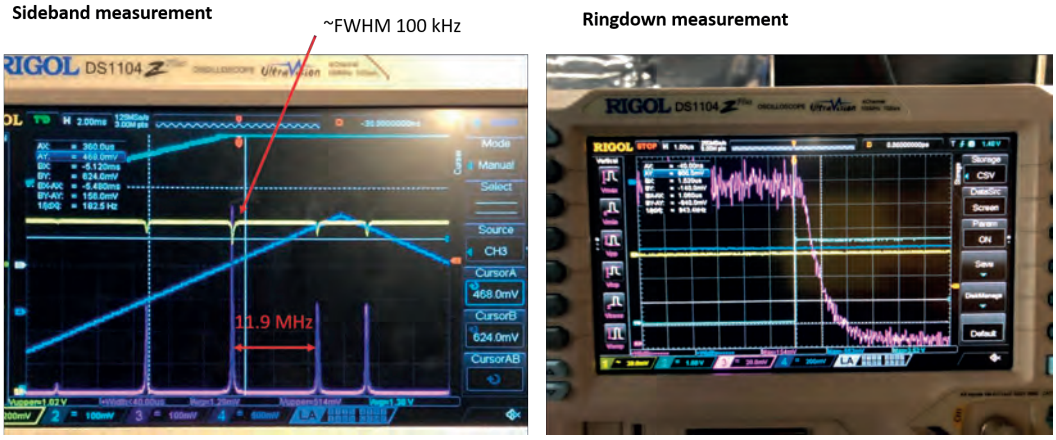


FIGURE 4.30: **Example cavity finesse measurements.** The sideband measurement of the linewidth of the transition peak using the well-known modulation frequency as the reference. Another method was ringdown measurement. The cavity was locked and once the input laser was turned off, the decay time from the output shows how many rounds photons bounce in the cavity, giving the finesse of the cavity.

### 4.3.2 Superradiant cavity chamber

The superradiant cavity is placed in a dedicated vacuum chamber, connected to the rest of the vacuum system through a differential pumping tube, as depicted in Figure 4.17(a). This chamber is pumped by a SAES 200 $L \cdot s^{-1}$ Z200 ion + NEG pump and is surrounded by a 5 mm thick ARMCO Telar 57 soft iron magnetic shield (with rather large holes to pass the vacuum system tubes) from AK Steel International. All components within the shield are constructed from stainless steel 316L and the windows are nonmagnetic to avoid the use of magnetic Kovar. A set of Helmholtz coils can provide homogeneous fields up to 200G for opening the $^{88}$Sr clock line although the design is primarily focussed on the weak 1G needed to provide a quantization axis definition and line separation for $^{87}$Sr. The coil system is constructed with multiple circuits, offering independent control for field curvature adjustment across the cavity.

The effectiveness of the magnetic shield was assessed using COMSOL simulations utilizing CAD step files, which include permanent magnets, shields, and coils. As depicted in Figure 4.31, the simulations showcase the shield's significant efficacy. This is achieved despite the presence of relatively large perforations, primarily intended for accommodating the vacuum pumping port. The residual field nonuniformity along the superradiant cavity mode is primarily attributed to higher moments from the Helmholtz coils, which could be further mitigated by employing additional weak coils for refinement.

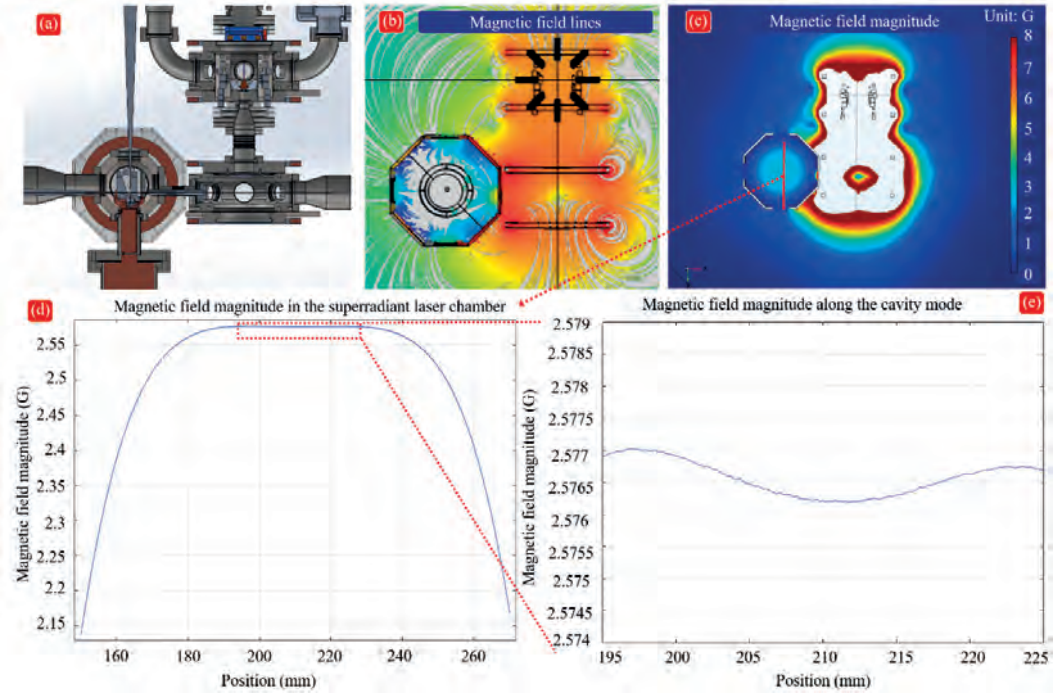


FIGURE 4.31: **Simulated magnetic field in the superradiance chamber.** (a) The CAD design of the superradiance chamber shows an optical cavity on top of the vibration isolation stack. The magnetic field is generated by a pair of water cooled coils surrounded by a magnetic shield. (b)-(e) depict the simulated magnetic field strength obtained through COMSOL analysis. In (c), the red line denotes the cavity axis utilized for atom loading. Notably, the magnetic field exhibits variability, ranging from 1 mG to a strength of 2.5G, as observed in panels (d) and (e).

The connection between the superradiant chamber and the red MOT chamber is facilitated by a bespoke CF16 bellow, engineered to alleviate strain. Housed within this bellow is an aluminum 6061 differential pumping tube, with a 6 mm inner diameter and 90 mm length, serving to reduce stray light and enhance vacuum isolation from the red MOT

chamber, although predominant load factors are likely attributable to outgassing across the numerous chamber components.

To mitigate acoustic disturbances, the design includes multiple vibration isolation stages, each characterized by distinct resonant frequencies. The spacer for the superradiant cavity is fashioned from a block of clearceram ultra-low expansion glass, affixed with mirrors and piezos using ND353 adhesive. This assembly is supported by an oxygen-free high conductivity (OFHC) copper holder, with 3.18 mm diameter Viton balls (ShoreA 70 hardness) utilized for gentle tensioning and securing the cavity in position. This structure is fixed to the upper stage of the OFHC copper isolation stack shown in Figure 4.17 by a flexure mechanism milled into the top of the stack. The lower stage comprises an approximately 10 kg block of OFHC copper, selected in preference to stainless steel for its density, lack of magnetism and absence of hydrogen outgassing.

Six Viton balls, each measuring 8 mm in diameter, act as springs, supporting the isolation stack from the vacuum chamber. The vibration isolation stack was designed with two stages, using another six 6 mm diameter Viton balls as springs between the upper and lower stages. However, machining errors and concerns about the arrangement tipping over during transport between the oven and the lab led us to ultimately decide to bolt the lower and upper stages together.

A laser-cut 0.5 mm thick stainless steel 304 guide ensures the Viton balls are evenly spaced around the groove, and the spring constant can be adjusted by varying the number of balls in the system. The superradiant vacuum chamber assembly is firmly attached to a 20 mm thick stainless steel 304 baseplate, forming a rigid 300 kg structure. This assembly is mounted on an 80 x 80 mm aluminum profile frame and further supported by 25 mm thick Sorbothane vibration isolators (Thorlabs AV6/M), providing an additional layer of vibration mitigation from the underlying floating optical table.

### 4.3.3 The choice of isotope

As previously discussed, both $^{88}$Sr and $^{87}$Sr can be used for superradiant lasing within this apparatus. Unlike the hot atomic beam system, which relies on the high abundance of $^{88}$Sr to achieve elevated flux levels, the continuous ultracold superradiant laser offers two viable options: utilizing either $^{88}$Sr or $^{87}$Sr. Each is associated with distinct advantages and disadvantages, making neither inherently superior to the other. The $^1S_0$ - $^3P_0$ transition of $^{88}$Sr is strictly forbidden but may be slightly opened and allowed by the presence of a strong external magnetic field. The effective transition linewidth

$$\Gamma = \alpha B^2 \tag{4.1}$$

is proportional to the square of the magnetic field strength B, with the proportionality constant $\alpha = 1.95 \times 10^{-9} s^{-1} G^{-2}$ for $^{88}$Sr, as shown in Figure 4.32.

It is estimated that field strengths of around 200G are needed to open the transition for $^{88}$Sr sufficiently to render superradiance possible with a practical atom number in the cavity. However, the quadratic Zeeman shift then makes magnetic field stability and homogeneity extremely challenging.

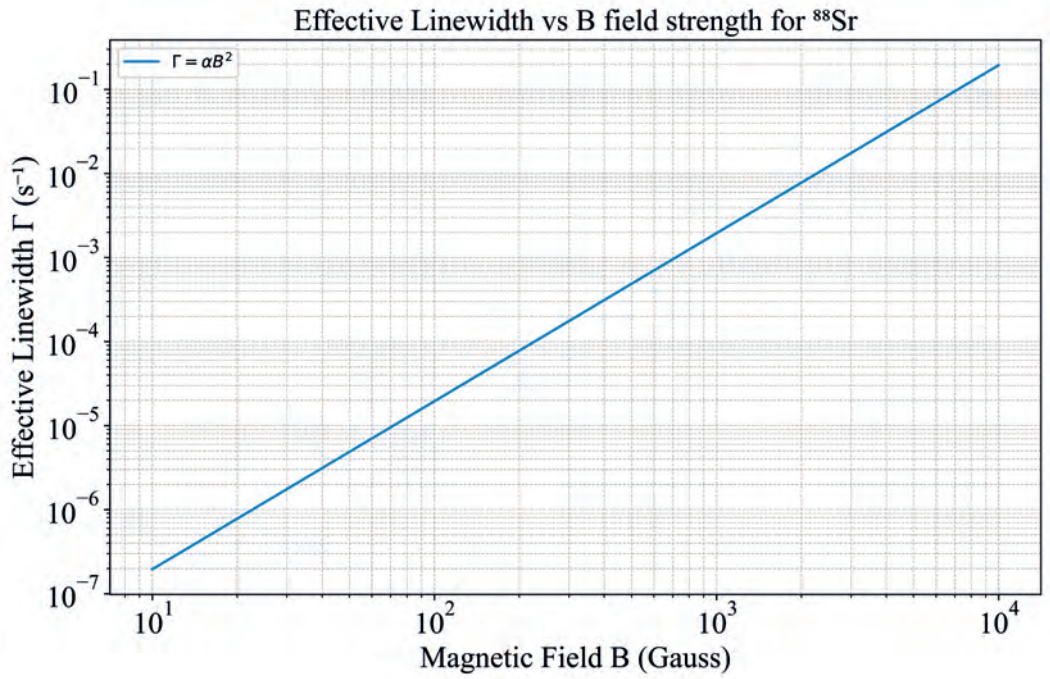


FIGURE 4.32: The mHz-transtion can be open in bosonic strontium atoms by strong magnetic fields.

By contrast, $^{87}$Sr has a nuclear magnetic spin, which provides a very strong internal magnetic field corresponding to an effective field strength around 2 kG, which opens the line of the clock transition to $\Gamma/(2\pi) = 1.35$ mHz. Despite this greatly advantageous feature, $^{87}$Sr is not necessarily the best isotope to work with as it has also disadvantages. It has much lower abundance compared to $^{88}$Sr (7% for $^{87}$Sr compared to 82.7% for $^{88}$Sr [107]). Furthermore, the internal structure of $^{87}$Sr greatly complicates laser cooling reducing the atomic source efficiency and flux [53]. Finally, the existence of ten magnetic sub-states within the ground $^1S_0$ state necessitates pumping and a substantially higher atom count to support the concurrent operation of two magnetically sensitive superradiant lasers targeting two stretched states.

### 4.3.4 Atomic density and inelastic collisions

Reaching the superradiant phase transition requires high atom numbers, but higher atom density does not help. High density can result in collisions, which can cause loss and shifts to the clock transition frequency. Inelastic loss rates are summarized in Table 2.2 with $^3P_0$ - $^3P_0$ collisions having an inelastic scattering loss rate of $2 \times 10^{-11} \mathrm{cm}^3/s$ for $^{88}$Sr and $1 \times 10^{-11} \mathrm{cm}^3/s$ for $^{87}$Sr [56]. Losses for $^1S_0$ - $^3P_0$ are an order of magnitude smaller. Two approaches can be taken to avoid this problem, firstly a higher dimensional (2D or 3D) magic lattice can be used in which the site occupancy is reduced to significantly less than one. Alternatively, very low densities can be achieved by spreading atoms over a large volume.

### 4.3.5 Reservoir dipole trap

A dipole trap, optimized geometrically for BEC production [56, 107], is incorporated at the junction of the guide and the magic moving lattice. Termed the 'reservoir' trap, this dipole trap utilizes a 1070 nm beam with a power output of a few Watts, focused to a waist radius of 200 µm and a height of 15 µm. The axial extent of the trap is constrained to approximately 1 mm due to the Rayleigh range along the vertical axis. This configuration offers a spacious volume with high trapping frequencies, facilitating efficient collection of atoms from the guide. It mainly serves to confine our atom reservoir at the intersection of the cavity mode and the guide, facilitating the loading of atoms into the magic moving lattice. Furthermore, it enables efficient evaporative cooling of large atom ensembles in pulsed operation of the machine, with the guide deactivated.

A smaller 'dimple trap' with a power of 0.3 W, focused to a waist radius of 20 µm, is positioned horizontally at the reservoir's base. This forms a minute collection and condensation focal point, allowing for the creation of a $^{84}$Sr BEC within the dimple.

The ability to create and load BECs into our moving cavity lattice offers an enormous range of possible research directions beyond superradiant clocks for our apparatus. On a more practical level, the ability to load BECs within our cavity gives the opportunity to use high resolution imaging and spectroscopy techniques on the 689 nm red transition of the BECs. This can be used to map and optimize the magnetic field uniformity and light shifts across the superradiant cavity system, allowing these effects and inhomogeneities to be compensated. BECs are also precisely located test clouds that make dipole trap alignment and characterization easier.

Another important feature is that the reservoir, in conjunction with the guide, serves to light shift the trapped atoms' resonance away from the $^1S_0$ - $^3P_0$ clock transition, rendering

them impervious to interaction with the superradiant laser field. This is crucial to prevent the superradiant clock light from interacting with the reservoir atoms.

### 4.3.6 Atom state preparation and superradiant emission

Atoms are loaded from the reservoir into the magic moving lattice 'pancakes' via the red molasses cooling beams. They are then carried vertically upwards by the lattice, first passing through a state preparation stage where they are pumped into the $^3P_0$ state and subsequently into the superradiant emission region of the cavity.

Replacing the single state preparation (pumping) region with an array of such regions, each separated by an unperturbed region could enable atoms to be pumped and emit multiple times as they traverse the cavity. This arrangement would allow for the generation of multiple photons per atom, thereby increasing the effective flux. One approach to implement this involves creating an array of pump spots or regions by imaging pumping light onto the plane of the atoms moving through the cavity mode using an aperture array. One potential issue is that the atoms might heat up during the repumping process, preventing them from being trapped by the magic moving lattice and causing a loss.

Although Doppler broadening in atomic spectroscopy is mitigated by trapping atoms in the 1D optical lattice, the moving lattice introduces two Doppler-shifted lasing modes corresponding to the forward and backward propagating cavity modes. The speed of the moving lattice, ranging from 0.02 to 0.2 m/s, induces a Doppler shift of 28 to 280 kHz. Despite our cavity linewidth being 150 kHz in reality (but 50 kHz in theory), atoms autonomously compete to determine which mode emits more. The collective superradiant lasing is a positive feedback loop, which prompts more excited atoms to contribute to the dominant mode. Ultimately, only one Doppler-shifted mode emerges, forming the collective superradiant laser. This allows the output to be efficiently captured in a single output beam, mixed with a local oscillator on a beamsplitter and detected with a balanced heterodyne detection scheme.

For $^{87}$Sr, with its numerous magnetic sublevels for both $^1S_0$ and $^3P_0$, atoms could be pumped into any $m_F$ state. The first-order Zeeman shift for each transition is given by [118]

$$\Delta\nu_g = -m_F g_I \mu_0 B, \tag{4.2}$$

$$\Delta\nu_e = -m_F (g_I + \delta_g) \mu_0 B, \tag{4.3}$$

where the subscripts g and e refer the ground state $^1S_0$ and the excited state $^3P_0$. B represents the magnitude of the magnetic bias field in Gauss. The differential Zeeman shift, $\Delta\nu_g$ or the $\Delta\nu_e$, is approximately 100 Hz/G [56, 118, 119].

Both $^1S_0$ and $^3P_0$ states exhibit Zeeman shifts for their 10 $m_F$ states. And most $^3P_0$ $m_F$ states can emit $\sigma^-$, $\pi$ and $\sigma^+$ light. Given the 1G magnetic field for $^{87}$Sr is perpendicular to cavity mode, the frequency difference between $\pi$ emission and $\sigma^-$ of the excited atoms in $^3P_0, m_F = 9/2$ would be only about 100 Hz. One method is to initially seed the system with $\pi$-polarized laser light, which ensures that the $\pi$ emission is dominant, as desired.

In the passive clock, the clock laser is usually interrogated by alternating measurements between the $m_F = \pm 9/2$ transitions to determine and correct for the first-order Zeeman shift. For our active clock, can we also utilize these two $m_F = \pm 9/2$ emissions? The maximum different frequency between the $m_F = \pm 9/2$ emissions is approximately $10 \times$ B $\times$ 100 Hz/G [56, 118, 119]. The separation between these frequencies remains small (1 kHz at 1G) compared to the Doppler shift between forward and backward propagating cavity modes. This allows the selection of only forward propagating modes by choosing the cavity resonance. We can resolve the different $m_F$ emissions from their beats with the local oscillator at the superradiant laser output.

Minimizing inhomogeneity across the extensive atomic cloud within the cavity mode is critical. Inhomogeneity primarily arises from magnetic field irregularities and light shifts from laser beams or scattered light. To mitigate light shifts, resonant light exposure in this chamber is minimized through meticulous control of reflections and beam termination. As depicted in Figure 4.31, making a magnetic field of 1G with 1 mG uniformity suitable for operation on $^{87}$Sr appears achievable. Simulations[120] suggest that field inhomogeneities as high as 100 mG may be tolerable. For $^{88}$Sr, fields of 200G are necessary. At these higher fields our coil design is expected to produce inhomogeneities approaching 100 mG due to higher order moments from the simple Helmholtz design. Additional coil pairs of different radii could be used to cancel out these higher moments, further enhancing uniformity.

Two mitigation strategies are available should inhomogeneities pose issues. Firstly, by slowing the conveyor speed, more atoms can be loaded into the cavity to compensate for the higher superradiant phase transition threshold. Secondly, these inhomogeneities can be spectroscopically measured by placing atoms (ideally a Bose-Einstein condensate - see Section 4.3.5) at various points along the cavity and spectroscopically measuring the local light shift and magnetic field. This data could facilitate adjustments using a painted light shift potential to dress the atoms or by adding additional external magnetic field trimming coils.

A final consideration involves protecting the high finesse mirrors of the cavity from strontium coating, which would increase losses. While the quantity of strontium atoms

is likely minimal, this risk can be averted by incorporating a small, low power 689 nm + 679 nm + 707 nm beam. This beam can eject atoms from the moving lattice a few millimeters before they reach the cavity mirror.

### 4.3.7 Characterization and seeding

The estimated powers from the superradiant clock were analyzed and presented in Table 2.2. These were limited by the flux of the atom source and by the number of photons obtainable from each atom. For $^{87}$Sr operation with an atomic flux of $10^6$ atoms per second and without repumping, the output powers were found to be approximately 280 fW. However, considering losses and collection efficiencies, the actual emitted and detectable power amounted to just 46 fW. These powers are too small for direct detection but by beating the laser output with a pre-stabilized reference laser in a balanced heterodyne configuration the difference could be fed back to stabilize the reference laser output. The question then is not whether an output signal can be detected but instead, what locking bandwidth can be maintained with a sufficient signal to noise ratio. The calculated locking bandwidths for a generous 100x signal to noise ratio were calculated for various system configurations and for two different detector types. These are tabulated in Table 2.2. Notably, the performance of the detector plays a crucial role, exhibiting orders of magnitude variation depending on the detector type. For instance, a specialized low-noise detector [81] can significantly enhance the detection bandwidth compared to a general-purpose amplified detector from Thorlabs (PDA8A2). Moreover, additional superradiant power can be utilized to expand the locking bandwidth, thereby reducing the dependence on the quality of the reference laser, or to augment the signal-to-noise ratio.

Initially, cavity atom numbers may be insufficient to autonomously phase lock and initiate the superradiant laser output. Consequently, the system was designed to allow seeding using an initial pulse of 698 nm light injected from the reference laser into the superradiant cavity mode. This approach comes highly recommended by Matt Norcia from the Thompson group at JILA [119], particularly for system debugging and optimization purposes. It's worth noting that, once seeding has initiated the superradiant laser output, the seed can be removed. After initiation, the reference laser can be frequency stabilized to the ongoing output from the superradiant laser.

The reference laser currently consists of a 698 nm ECDL that is PDH-locked to a ULE ball cavity manufactured by Stable Laser Systems, utilizing a FALC PID from Toptica. This cavity is mounted on a vibration isolation platform (Minus K Technologies Model BM-4) [103] and housed within a temperature-stabilized multilayer-insulated soundproof

enclosure. Light is then transmitted to the ultracold superradiant laser via an optical fiber, employing fiber noise cancellation techniques.

To keep the cavity approximately in resonance with the clock transition, spectroscopy could in principle be conducted on the clock transition using any of the ultracold strontium machines within our group. In the medium term however, the zero-dead-time clock together with a more advanced reference cavity is being developed by Sumit Sarkar, Scott Wolzak and András Gácsbaranyi. This will provide a dedicated strontium 1D passive optical lattice clock. Additionally, the introduction of a second, improved ultrastable reference cavity will further facilitate cavity linewidth comparison and optimization.

Several additional tools were planned to thoroughly characterize the operation, loading, and homogeneity of atoms within the cavity mode and to facilitate the debugging and optimization of the machine. These tools include cavity frequency modulation (FM) spectroscopy operating on either the 689 nm or 698 nm lines. This will use probe light injected into the ring cavity and heterodyne detection making use of these ultrastable cavity locked reference lasers. FM spectroscopy has proven invaluable for providing initial signals for debugging the hot beam superradiant clock machine. Another tool is fluorescence using 461 nm light injected into the cavity mode, a method highly recommended by the Thompson group [57]. Other tools are absorption spectroscopy of the $^1S_0$ state using 461 nm or 689 nm light and of the $^3P_0$ state using 679 nm light (+repumpers), either through the cavity or transversally to it. When imaging through the cavity, spatial resolution along the cavity axis can be achieved by loading only a small cloud of atoms into the cavity (for example a BEC) and moving it to the location of interest.

### 4.3.8 Framework

The vacuum assembly and all the optics utilized to implement the multiple beams described above will all be affixed to a single framework. This framework, depicted in Figure 4.1, is designed for vibration isolation from the optical table through Sorbothane isolators.

The vacuum system is mounted to a 304 stainless steel frame, which in turn is mounted to the main baseplate — a robust 2 cm thick stainless steel plate. This arrangement provides a stable platform, enabling the entire vacuum assembly to be transported to and baked in our homemade baking oven, which has an inside volume of $1.0 \times 1.25 \times 1.25$m. Stainless steel was selected to endure a lengthy (6-week) hydrogen bake at 350 °C, aimed at removing hydrogen from the vacuum chamber steel and enhancing outgassing rates and vacuum quality. Aluminium, due to its softening at such high temperatures, was unsuitable for this purpose. Additionally, the baseplate is reinforced by an aluminium profile framework, serving as lifting points for maneuvering the structure and as mounting points for breadboards

supporting the optics surrounding the vacuum chamber. This aluminium framework can be detached during high-temperature bakes.

## 4.4 Laser systems, electronics and control systems

The laser systems, electronics, and control systems used to run this machine are extensive and in fact, represent the majority of the work needed to construct the apparatus. Particularly noteworthy are the cooling laser systems, which are fully modular, a series of drawers racked in a mobile rolling cabinet. These drawers can be opened and closed to allow tweaking and optimization without impacting laser performance.

### 4.4.1 Cooling and probe lasers in the cabinet

The cooling lasers, including 461 nm blue lasers and 689 nm red lasers, have been designed to electronically tune to address any of the four natural isotopes of strontium. The precise frequency differences among strontium isotopes have been accurately determined by our group members [56, 107].

The frequency-shifting mechanism of the 461 nm blue cooling lasers, which address the strontium $^1S_0$ - $^1P_1$ transition, is illustrated and explained in Figure 4.33. The seeding light comes from an ECDL that is spectroscopically locked to $^{88}Sr$. This ECDL was already in use before our project began and serves multiple experimental setups within our group. We obtain light from it through a fiber. Two AOMs are utilized to electronically tune the frequency to any strontium isotope. Additionally, three AOMs are employed for scanning a wide detuning range of up to 100 MHz to optimize the Zeeman slower. Other AOMs allow fast switching of frequency and intensity of beams for example for imaging. These are configured either to realign the laser to resonance for imaging or pushing atoms, or to adjust the frequency to around one linewidth (30 MHz) red detuned of the strontium $^1S_0$ - $^1P_1$ transition for transverse cooling (referred to as oven TC seed in the diagram) or 2D blue MOT.

One 100 mW diode laser (Nichia, NDB426) is configured as an injection-locked laser from our spectroscopy-locked blue laser for generating all seeding laser beams. Three 500 mW diode lasers (Nichia, NDB4916-E) are constructed as injection-locked lasers to amplify the seeding light power for the Zeeman slower, transverse cooling, and 2D blue MOT. Additionally, AOMs are driven by our in-house amplifiers, typically delivering less than 30 dBm (1 W). Radiofrequency signals are generated by direct digital synthesizers (DDS) controlled by a National Instruments (NI) card.

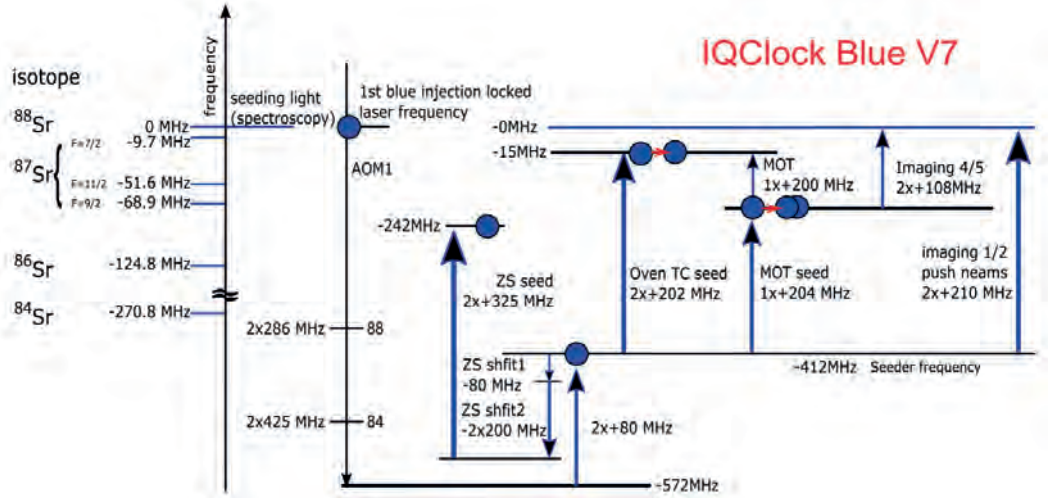


FIGURE 4.33: **The architecture of the** 461 nm **lasers.** The blue cooling lasers begin with two isotope shift AOMs, which seed an injection-locked laser with -420 MHz detuning from resonance for any isotope. From here various AOMs shift light to seed additional injection-locked lasers at various frequencies.

The 689 nm red laser system uses a similar frequency-shifting architecture to the blue system and is depicted in Figure 4.34. It enables isotope shifts and frequency shifts for laser cooling and probing. However, there are two primary differences compared to the blue laser system.

Firstly, due to the narrow natural linewidth of the red atomic transition, which is approximately 7.5 kHz, lasers are sometimes modulated using AOMs to produce a frequency comb of light spanning up to 10 MHz. This broader spectrum facilitates more efficient atom capture during initial cooling stages, albeit at the expense of higher temperatures. The laser can be switched to a single frequency to achieve further cooling when colder atoms are required.

Secondly, a significant difference arises concerning the $^{87}$Sr isotope. Given the presence of hyperfine structure in $^{87}$Sr and the absence of a closed laser cooling cycle, an additional stirring beam is necessary to repump atoms back to the laser cooling ground state, as outlined in previous studies [121]. To accomplish this, two laser beams are combined using a beam splitter to generate beams with two frequency components, denoted seed A $^{87}\mathrm{Sr}(9/2)$ for stirring and seed B $^{87}\mathrm{Sr}(11/2)$ for cooling in Figure 4.34.

After completing the concept design, schematic designs were created, see Figure 4.35 for blue, 461 nm lasers and Figure 4.36 for red, 689 nm lasers. The schematics describe modules

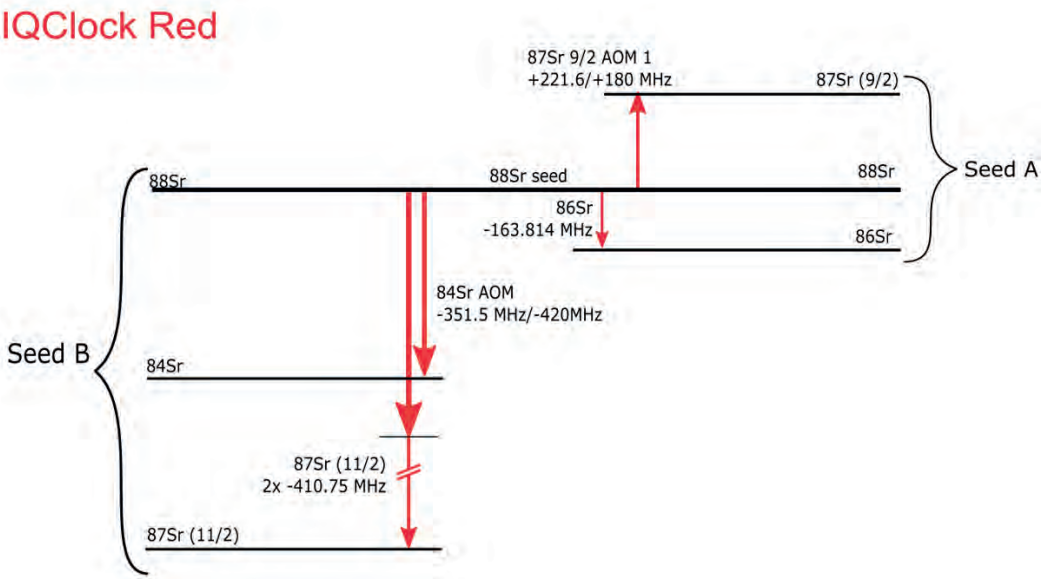


FIGURE 4.34: **The architecture of the** 689 nm **lasers.** Our red laser starts with an injection-locked laser 80 MHz blue detuned of the $^{88}$Sr $^1S_0$ - $^3P_1$ transition. Two sets of frequency shifting AOMs are used to seed two injection-locked lasers(seed A and seed B). Seed A can address $^{88}$Sr, $^{86}$Sr or $^{87}$Sr$(9/2)$ while seed B can address $^{88}$Sr, $^{84}$Sr or $^{87}$Sr$(11/2)$. Operation of both, seed A and seed B, is needed to produce light for both the cooling and stirring beams. These seeds can be used to seed multiple injection-locked lasers at 689 nm depending on the amount of power required. Output from these seeded lasers is 80 MHz blue detuned of the atomic resonance so it needs to be shifted using an 80 MHz AOM providing the opportunity to rapidly and easily control the frequency, frequency spectrum and power of each beam.

that are designed to amplify, distribute, and control the power of each laser in the experiment. Two types of modules are employed: one is an injection-locked laser module, used to amplify a seed laser, while the other module employs AOMs to electronically adjust laser frequencies and intensities. Both module types facilitate laser beam distribution. Apertures remove the unwanted orders from the AOMs. Each module is built on a homemade 20 mm thick aluminium breadboard of standardized size mounted and isolated by a set of 12.7 mm thick Sorbathane isolators. These modules seamlessly integrate into an array of drawers within a relatively compact, transportable cabinet.

Figure 4.37 offers detailed insights into the construction of the laser modules.[4] The first row delineates the processes involved in creating the injection-locked lasers. The process

[4]The blue laser system was constructed by my colleague Francesca.

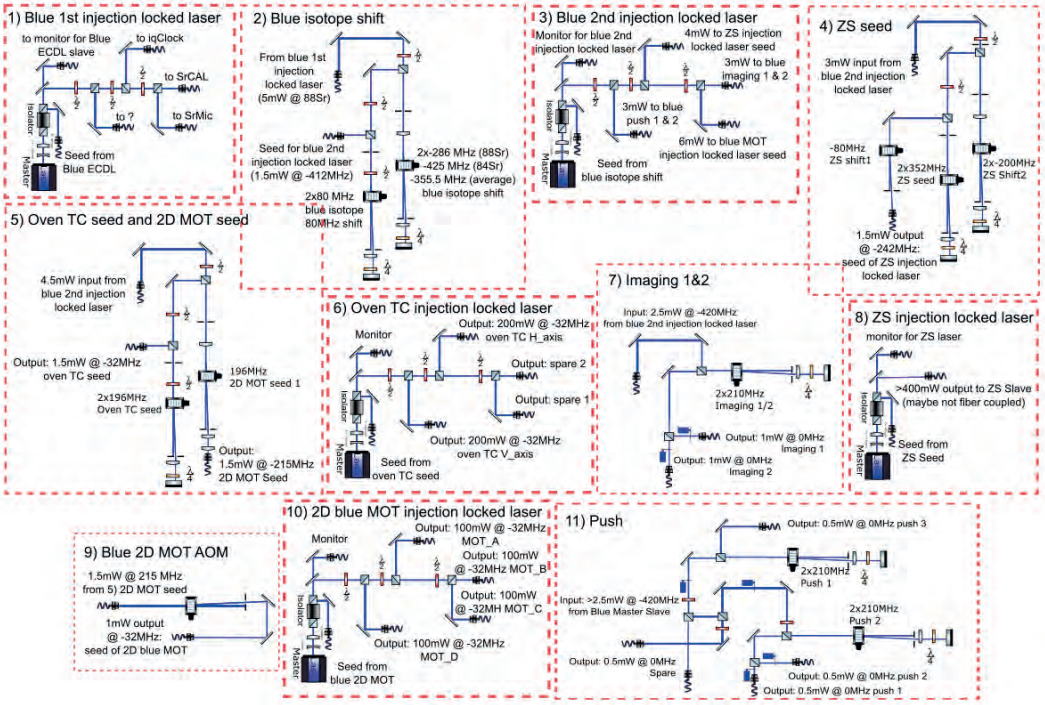


FIGURE 4.35: **The design of the** 461 nm **blue laser system.** There are two types of laser breadboard modules. One type utilizes an injection-locked laser to amplify and distribute power. The other type employs AOMs to shift the frequency and adjust the intensity of laser beams and can also block the beams with shutters.

begins with the mounting of a diode laser (Thorlabs HL6750MG) into a commercial laser diode collimation and focusing tube (Thorlabs LT230P) with a 3.1 mm focal length collimator. The diode is then secured in a homemade copper holder equipped with a thermoelectric cooler (TEC) for temperature stabilization. Copper was chosen for its superior thermal conductivity. To refine the laser beam's shape for optimal fiber coupling, a pair of cylindrical lenses ($f_1 = 40\,\text{mm}$, $f_2 = -15\,\text{mm}$) are employed, as depicted in Figure 4.37(a). Figure(b) shows an example of the beam shape with a fiber coupling efficiency of 80%. Following this, the laser assembly is encased within a plastic box to protect against airflow and dust. Optical isolators are then installed to prevent optical feedback and to inject the seed laser through the isolator's side port. Finally, half-wave plates and cubes are utilized to distribute power, with additional half-wave plates for polarization maintenance preceding the fiber collimators.

The second row depicts the process of constructing AOM modules, used to tune the

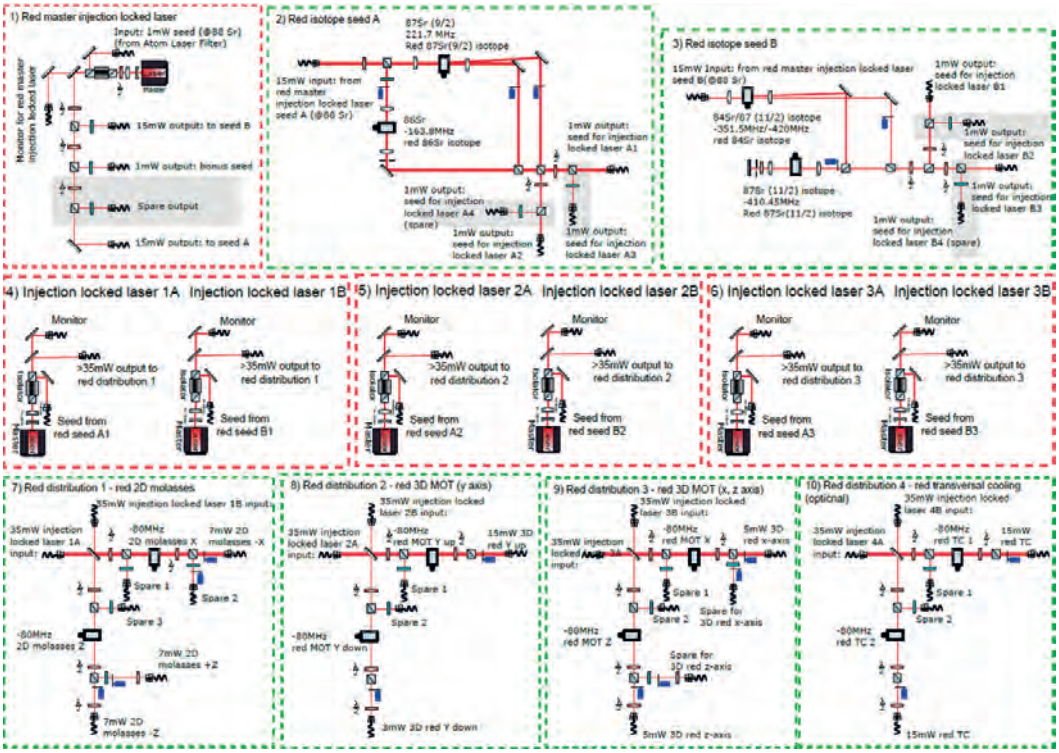


FIGURE 4.36: **The design of the** 689 nm **red laser system.** There are two basic laser breadboard modules. The injection-locked laser modules amplify 689 nm laser beams. The AOM modules shift the frequency of the laser beams, e.g. in order to address different isotopes, modulate the frequency for broadband cooling, or adjust the beam intensity. For $^{87}$Sr, the cooling laser and the stirring laser are mixed in modules (7)-(10).

laser frequency. With pre-designed optical alignment apertures and fixed mounting holes for optical components, assembling the AOM modules resembles playing with Lego bricks. However, sometimes we discovered mistakes in the placement of the mounting holes after having started placing components. While drilling the correct holes we protected the already installed components with plastic covers (refer to Figure 4.37(k)). In Figure 4.37(i), three workspaces for building the module are depicted, each supported by long posts to bring the modules to a convenient height during assembly and to allow easy insertion of screws placed from below. Since our laser system is modular, several people can easily work on it in parallel, speeding up construction. As the modules are similar to each other, it is very easy to build and debug a second one after having gained experience by building


FIGURE 4.37: **The construction of laser modules.** The first row presents the construction processes for the injection-locked laser module. The second row details the AOM frequency shift and power distribution module construction. The last row shows some debugging tricks used while building the lasers.

the first one.[5]

All the optical breadboards are mounted in the drawers of a cabinet on wheels, as depicted in Figure 4.38. The breadboards are positioned atop Sorbothane isolators to minimize vibration and stress on the boards. The fibers (from OZ Optics) and cables from each layer are routed through bendable plastic "cable chain" tracks, with optical fibers entering from the left side and electronic cables entering from the right side, as shown in Figure 4.38(a)-(c). When we first placed an injection-locked laser, we used it for testing. We repeatedly opened and closed the drawer to check if the fibers or electronic cables were affected, and we observed no issues. Some cross talk between the high power 80 MHz AOM cables was noted later. The laser system was placed next to the room's windows so temperature was not particularly well controlled. After running the setup for three years, we have not encountered any significant problems. The setup only requires optical alignment maintenance roughly once per month. The lasers needed for the experiment are coupled with fibers that are directed to the optical table via PVC tubes, ensuring protection against damage, as illustrated in Figure 4.38(d)-(e).

[5]However, upon completing the first one, assembling subsequent breadboards feels like a robotic task. :) Still, making the second boad faster and better than the first is always a new challenge.

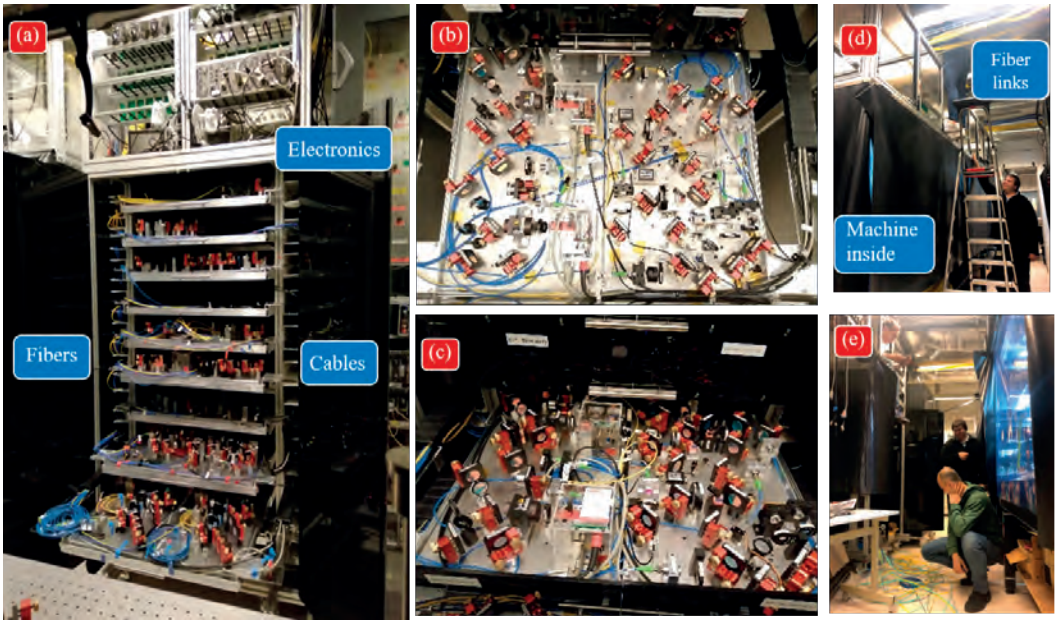


FIGURE 4.38: **The semi-transportable optical cabinet.** All the laser modules are placed in a wheeled cabinet. Optical breadboards that are optically directly connected, but couldn't be placed into the same drawer, were separated by at least two drawers, allowing both drawers to be opened simultaneously for maintenance of the fiber coupling and polarization, or for debugging purposes. Fibers are used to connect the laser modules and to route the output to the optics around the experiment.

The electronics for stabilizing the temperature of the laser diodes, along with the laser diodes' current drivers, were mounted in racks above the optical cabinet, as shown in Figure 4.39(a). Shutter drivers were used to control the servo-motor shutters that block the laser beams, along with a function generator and an oscilloscope used for monitoring the homemade Fabry-Perot cavities used to monitor whether the injection-locked lasers remain injection-locked and single mode. A web camera allows us to observe the signals remotely. Linear power supplies for the homemade electronic boards were housed in a separate, enclosed, 19" rack cabinet. This electronics cabinet also included the DDS and RF amplifiers used to drive the AOMs in the optical cabinet. The electronics cabinet, presented in Figure 4.39(b), is equipped with water cooling and fans to efficiently remove a lot of the heat generated by the electronics.

Both the DDSes and shutters as beam blockers are controlled by a Data Acquisition (DAQ) System using our open-source software program, as shown in Figure 4.39(c) and accessible at `https://www.strontiumbec.com/`. The control system also communicates

with cameras that are dedicated to absorption or fluorescence imaging. The Helmholtz coils or anti-Helmholtz coils are driven by our homemade current drivers, which can provide maximum 5 A. The drivers also can be controlled by our digital to analog converters, which are programmed by the control system. The control system can be programmed for any desired sequences with a clock cycle time of 0.5 µs. Versions of all this hardware and software are open-source and available on our website.

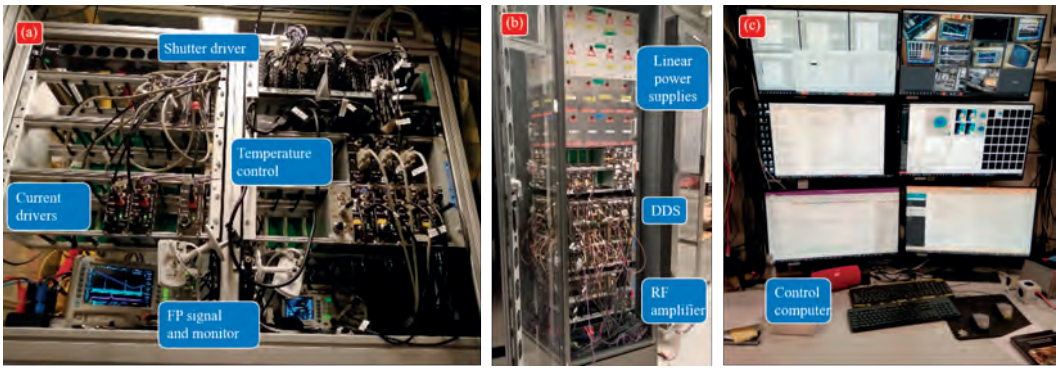


FIGURE 4.39: The electronics used to drive the cooling and probe lasers and our control system.

### 4.4.2 Repumpers

For pumping atoms to the desired states, we have constructed state manipulation lasers to produce light at 679 nm for the $^3P_0$ - $^3S_1$ transition, 688 nm for the $^3P_1$ - $^3S_1$ transition and 707 nm for the $^3P_2$ - $^3S_1$ transition. These lasers include master lasers using an ECDL based on a cat-eye design [101, 122, 123], and injection-locked lasers for power amplification. These ECDLs were designed by Shayne but assembled by my colleagues Francesca and Camila so I will not present them here. Here, I will focus on the transfer lock system, which was briefly mentioned in Chapter 3.

We need to lock the ECDLs because even very low drift ECDLs still experience a slow frequency drift of about 2 MHz per hour [124]. The repumping transitions have a linewidth of several megahertz. Targeting a steady-state superradiant clock requires operation for long periods so the repumper laser frequencies need to remain stable. To achieve this we developed a two-stage lock to stabilize the ECDL lasers with respect to a well-defined atomic transition.

In the first stage, we used our 1-kHz linewidth, spectroscopically locked 689 nm laser to stabilize the length of a moderate finesse in-vacuum Fabry-Perot optical cavity. We use a PDH lock with feedback provided to a piezo glued to one of the cavity mirrors. Our

cavity [107], which we inherited from a former group member (Dr. Simon Stellmer), had a minor misalignment issue, causing the best mode coupling to be TEM01 instead of TEM00. Despite this, the cavity has a finesse of approximately 10,000 with a free spectral range of 1.5 GHz.

In the second stage, we lock the three repumper frequencies to this stabilized cavity using PDH locks. We also considered using a scan lock method [125] to lock the 689 nm and the repumper lasers to each other. This method involves scanning the cavity length with the piezo and measuring the voltages corresponding to the resonances of the 689 nm laser and each repumper laser. Locks may then be used to maintaining a constant voltage separation between the laser peaks. While this method is simpler as it doesn't require frequency modulation for any lasers, we still opted for the PDH lock method. We chose this approach as a learning opportunity for the PDH lock of the superradiant cavity and because the resulting transfer lock will be able to maintain excellent coherence between all of our lasers. This could be useful by potentially allowing coherent state transfer or pumping schemes.

The entire setup is constructed on a 0.75 m by 1.8 m optical table, shown in Figure 4.40. The lower layer consists of the transfer lock cavity (with space allocated for an additional, future cavity). The ECDL lasers are placed in an acoustically isolated set of "shelves" along the side. In the top layer, we combine the repumper lasers and the spectroscopically locked 689 nm laser light. The mixed light is then fiber-coupled to transport it to the lower cavity layer for the PDH lock. This setup has the advantage of coupling all the lasers into a single cavity and then monitoring the transmission of all the lasers simultaneously. A grating and a camera are used to split and monitor the light transmitted through the cavity to verify that all the lasers remain locked.

A particular challenge arises because the laser frequencies are very close to each other. This makes it difficult to separate them with optical filters before photodetector. To address this, we employ different modulation frequencies on each EOM to distinguish the PDH signals from each laser. The locking signals for each laser can then be separated electronically after detection. Four homemade EOMs are used to modulate the beams from each individual laser, as illustrated in Figure 4.40. To prevent overlap between modulation frequencies (including harmonic frequencies), we tuned the resonances of our EOMs and selected specific values: 8.14 MHz for modulating the 689 nm laser beam, 12.896 MHz for the 688 nm laser beam, 18.815 MHz for the 707 nm laser beam, and 24.78 MHz for the 679 nm laser beam. The maximum frequency is limited because we want to use low cost Rigol DG1022 function generators. These can directly drive our homemade EOMs without the need for RF amplifiers and they also provide two synchronized phase adjustable outputs for easy demodulation of the error signal. The maximum frequency from the DG1022 is

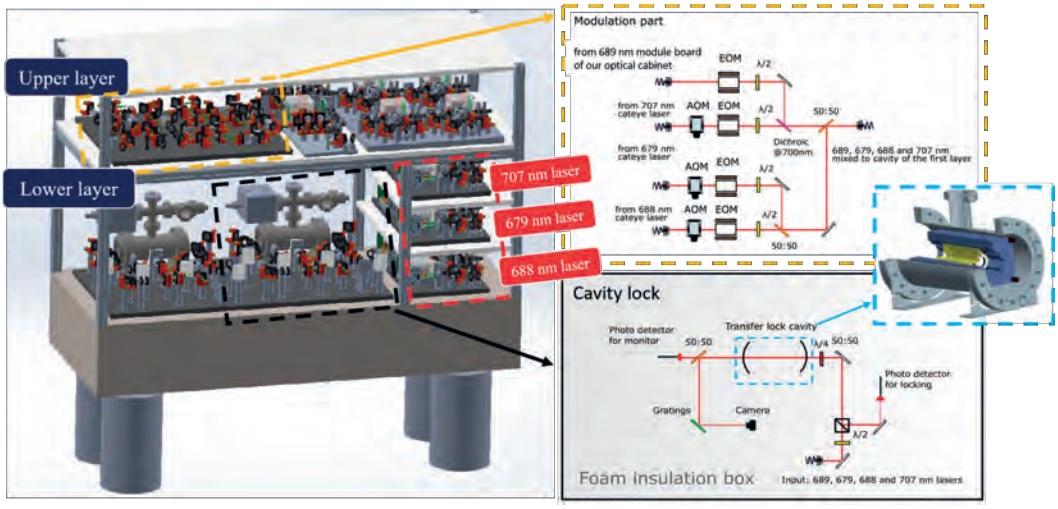


FIGURE 4.40: **The transfer lock for the** 679 nm**,** 707 nm **and** 688 nm **lasers.** A transfer lock cavity [107] is placed under vacuum and locked to the 689 nm master laser, which is itself locked to a moderate finesse cavity and the $^1S_0$ - $^3P_1$ transition of strontium. Then the repumper lasers (679 nm, 707 nm, and 688 nm) are locked to the transfer lock cavity. All the lasers are frequency-modulated with home made EOMs for PDH locking, which is implemented in the upper layer. The combined light is then sent to the cavity by fiber in the lower layer, where a photodetector is used to detect PDH lock signals from the cavity reflected light. A camera is used to monitor the transmission to double check the lasers and the transfer lock cavity are locked. A grating is used to disperse the different frequencies in the transmitted light.

25 MHz, which is enough for our purpose. We can use a grating to separate the laser beams of different frequencies, which are then used for transmission to a web camera.

The cavity resonance is locked to our 689 nm laser. While we would like to also lock our repump lasers to this cavity the repumper ECDL frequencies will not be resonant with the cavity at the same time. Therefore, AOMs are used to shift the repump lasers to match the cavity resonance. The AOM offset frequency for each laser was then optimized first using a High Finesse wavemeter (High Finesse model, WS/8-30) and then spectroscopically on atoms using the hot beam machine.

Since the cavity was built by a former group member, our primary task was to place it in a vacuum chamber, bake it, and pump it down to our desired vacuum pressure of $1 \times 10^{-7}$ mbar. This was my first experience achieving such a low pressure, making it a valuable learning opportunity for vacuum techniques as well.

After baking, the cavity was mounted to a 0.6 m $\times$ 1.2 m 60 mm thick honeycomb breadboard (Thorlabs B60120A) on 12.7 mm thick Sorbathane isolators placed on the optical

table. Around this breadboard, an acoustic isolation box was contructed from high pressure laminate (HPL) and acoustic isolation foam as shown in Figure 4.41(b). The frequency modulation, beam combination and distribution system were built on a higher layer of the table, on a 0.6 m $\times$ 1.2 m 12.7 mm thick aluminium breadboard (Thorlabs MB60120/M). The system is shown in Figure 4.41(a). The repumper ECDL lasers were also built and placed within the acoustic isolation enclosure, as presented in Figure 4.41(c)-(d).


FIGURE 4.41: **Building the repumper lasers and the transfer lock system.** (a) Frequency modulation with EOMs, frequency shifting with AOMs and beam distribution and combination. On the right hand side a homemade scanning Fabry Perot cavity monitors three lasers to ensure they remain single mode. (b) The transfer lock cavity. (c)-(d) The ECDL repump lasers. (e)-(h) The cavity and lasers construction processes.

The repumper laser frequencies were found [107] firstly by measuring them with our wavemeter and then by cross-checking their effect on atoms using the beam preparation stages of our hot strontium beam machine. This was described in Section 3.1.3. Specifically, the frequency for the 679 nm transition was found to be 441.332 75 THz, the 688 nm transition was 435.731 69 THz, and the 707 nm transition was 423.913 38 THz. These measurements facilitated the determination of the appropriate AOM models and frequencies needed to lock each ECDL to the cavity spectroscopy. Double pass, 350-MHz AOMs (Part number 3350-199 from G&H) were all used to frequency shift the 679 nm, 688 nm and 707 nm lasers. One unlikely coincidence was that our 707 nm atomic transition was just 200 MHz from a cavity TEM01 resonance at 423.913 18 THz. None of the AOMs we had in the lab operated at 100 MHz as would be needed for our double pass optical system and in any case we also preferred to maintain a larger tunability than using a 100 MHz AOM would provide. With the double pass 350 MHz AOM already placed, we locked the 707 nm laser to the weaker TEM00 of the cavity, which proved a quick and easy solution as

presented in Figure 4.42.

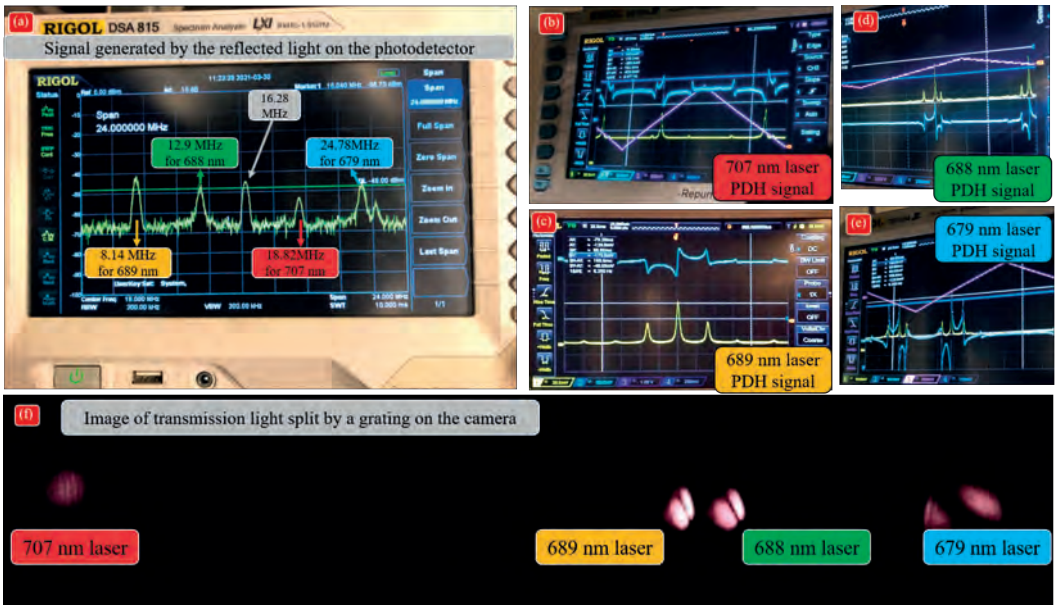


FIGURE 4.42: **The transfer lock of repump lasers.** (a) The reflected signal from the cavity displays all the frequency modulations on the photodiode from the EOMs used to lock each laser. (b)-(e) present the PDH signals from the 689 nm, 707 nm, 688 nm and 679 nm lasers used for locking. Also shown in yellow is the corresponding transmission of the cavity. (f) The transmission from the cavity on camera, separated by a grating, when all the cavity and lasers are locked.

Figure 4.42(a) shows the four different modulation frequencies detected in the beam reflected from the cavity. There is a second harmonic at 16.28 MHz from 8.14 MHz, which does not overlap with other modulation frequencies, as designed. This photodiode signal was amplified and split into four RF mixers, each with its laser's demodulation frequency, to generate the PDH lock error signal for each laser. The PDH signals as the cavity is scanned are shown in Figure 4.42(b)-(e). These error signals are used to provide feedback to the cavity piezo to lock the cavity with the signal from the 689 nm laser, and to feedback to the ECDL's current driver and piezo to lock the 679 nm, 688 nm, and 707 nm lasers.

One problem that we spent a lot of time on was to identify why the locking of the 707 nm laser was unstable. The PDH signal was not symmetric when the ECDL's PZT was scanned, and the error signal oscillated when the ECDL was locking. Ultimately, we discovered that the issue was due to optical feedback from the 707 nm injection-locked laser and we solved it by adding an additional optical isolator.

The locking system can keep the cavity and the repump lasers locked for up to a week. Our repump laser system has been used at various stages (see in Section 3.1.3) in the hot beam superradiance machine and it is designed to be used in the ultracold superradiant laser machine for multiple purposes. It will be used in the 2D blue MOT to repump atoms that decay to $^3P_2$ via the $^1P_1 - ^1D_2$ transition (see in Figure 2.2). It will be used to prepare excited state $^3P_0$ atoms as the gain medium for the superradiant laser. Optionally it could also be used to pump atoms to the $^3P_0$ state to escape from the 3D red MOT (see Section 4.2.1).

### 4.4.3 Dipole trap, magic wavelength moving lattice, and reference laser

A 400-W single spatial mode, linearly polarized fiber laser was purchased from IPG (YLR-400-LP-WC-Y14) for the dipole trap. This laser has a broad spectral bandwidth of around 3 nm. As no special filtering or temperature stabilization of the water for the laser heatsink is needed, cooling can be provided by the building process water already plumbed to the optical table. The optics around the chamber are designed to create the dipole trap, as shown in Figure 4.18. A safety box made from 6 mm thick aluminium sheet, sufficiently thick that a focused 400-W laser can not burn through it, along with interlock electronics on the lid was designed to prevent any unsafe situations. Additionally, continuous filtered air is introduced into the safety box to prevent dust accumulation, which could cause damage if it gets onto optics or the vacuum windows in the beam path. A second purged window was designed to fit over the vacuum windows to offer the option to further protect the viewports from any dust, but has not been implemented. The retro-reflected high power laser beam is directed into a water-cooled beam dump. Some of the laser power is also fiber-coupled, split and passed through intensity control AOMs to create the optical dipole reservoir and dimple trap, mentioned in Section 4.3.5.

The magic-wavelength (813 nm) lattice laser transfer lock was designed and built by our visitor Stefano Condio from the Istituto Nazionale di Ricerca Metrologica (INRiM) with help from Sumit Sarkar. As shown in Figure 4.43, an 813 nm ECDL from Toptica (DL pro) is transfer-locked to a 689 nm master laser using a similar method to the one described in Section 4.4.2. This laser can then be amplified by an injection-locked laser and distributed to our experiment as well as to our passive optical clock. Due to the resonant cavity enhancement in our superradiant ring cavity only a few milliwatts are needed to reach a lattice depth around 10 µK.

A reference 698 nm clock laser is essential for characterizing the performance of the ultracold superradiant laser. This was discussed in section 4.3.7. Currently, a commercially available Stable Laser Systems cavity is used to provide short term stability for our

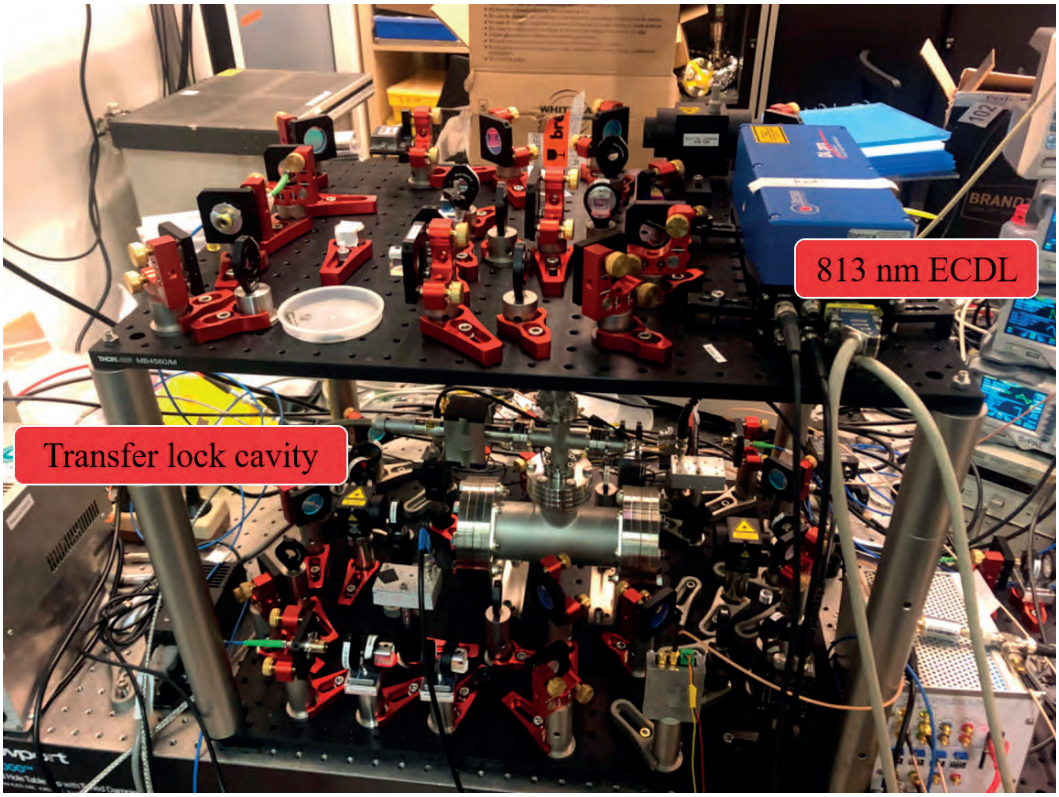


FIGURE 4.43: **The 813 nm magic-wavelength laser.** An 813 nm laser is locked to our 1 kHz linewidth 689 nm laser using a transfer lock cavity. The 689 nm laser is stabilized by locking it to a medium finesse (15,000) cavity for short-term stability and to the atomic transition for long-term stability.

698 nm ECDL (Toptica, DL pro). A higher performance ultrastable reference cavity is being developed by Sumit Sarkar, András Gácsbaranyi and Scott Wolzak.

## 4.5 Summary

We have designed and built a platform for continuous ultracold superradiant lasing as shown in Figure 4.44. With this machine we aim to achieve the first continuous superradiance on the $^1S_0$ - $^3P_0$ mHz-wide clock transition. Active superradiant optical clocks promise stability derived directly from the ultra-narrow atomic transition at short time scales. They should dramatically reduce the required averaging times and allow significantly greater bandwidths for optical clocks and related sensors. If realized, this would lay the groundwork for a new generation of active optical clocks capable of achieving the pinnacle of clock

performance, an advancement that has been pursued for the past twenty years.

This continuous ultracold atomic source is also an improved version compared with our previous continuous BEC project in many respects. We developed a more compact vacuum chamber with fields generated largely by permanent magnets, a transportable laser system and a transportable electronics system. The continuous ultracold atomic source can be used not only for our clock setup but also for other cold atom physics, such as continuous atom lasers and cold atom interferometry. A second edition of our machine is now being constructed and adapted for the zero-dead-time optical lattice clock being developed under the Quantum Delta NL project. By making it more compact and transportable, we have taken important steps to transfer the core technology of continuous cold atom quantum devices from the lab to broader societal applications.

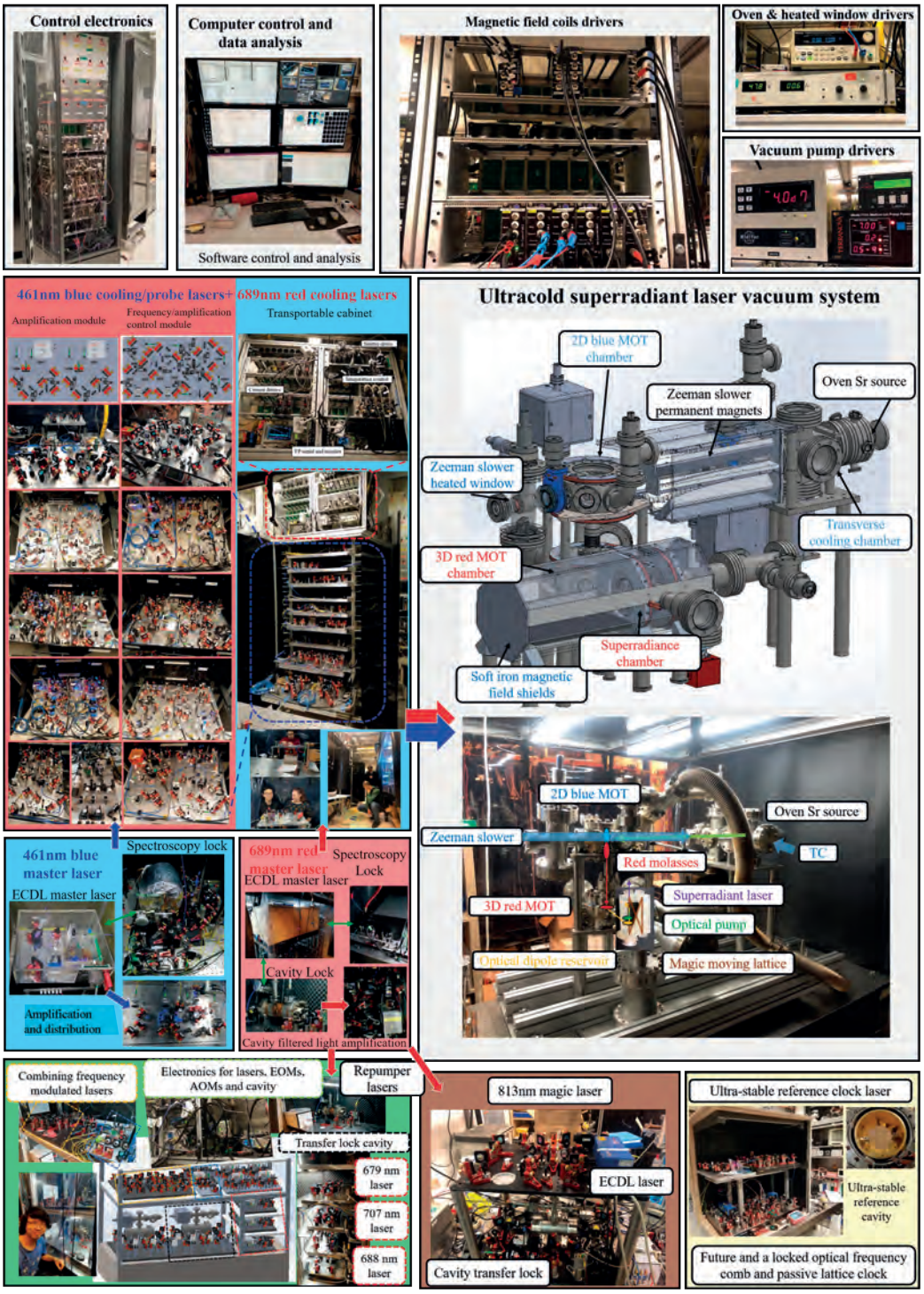


FIGURE 4.44: **Ultracold superradiant laser.**

Chapter 5

# An improved Sr red MOT for a continuous mHz superradiant clock

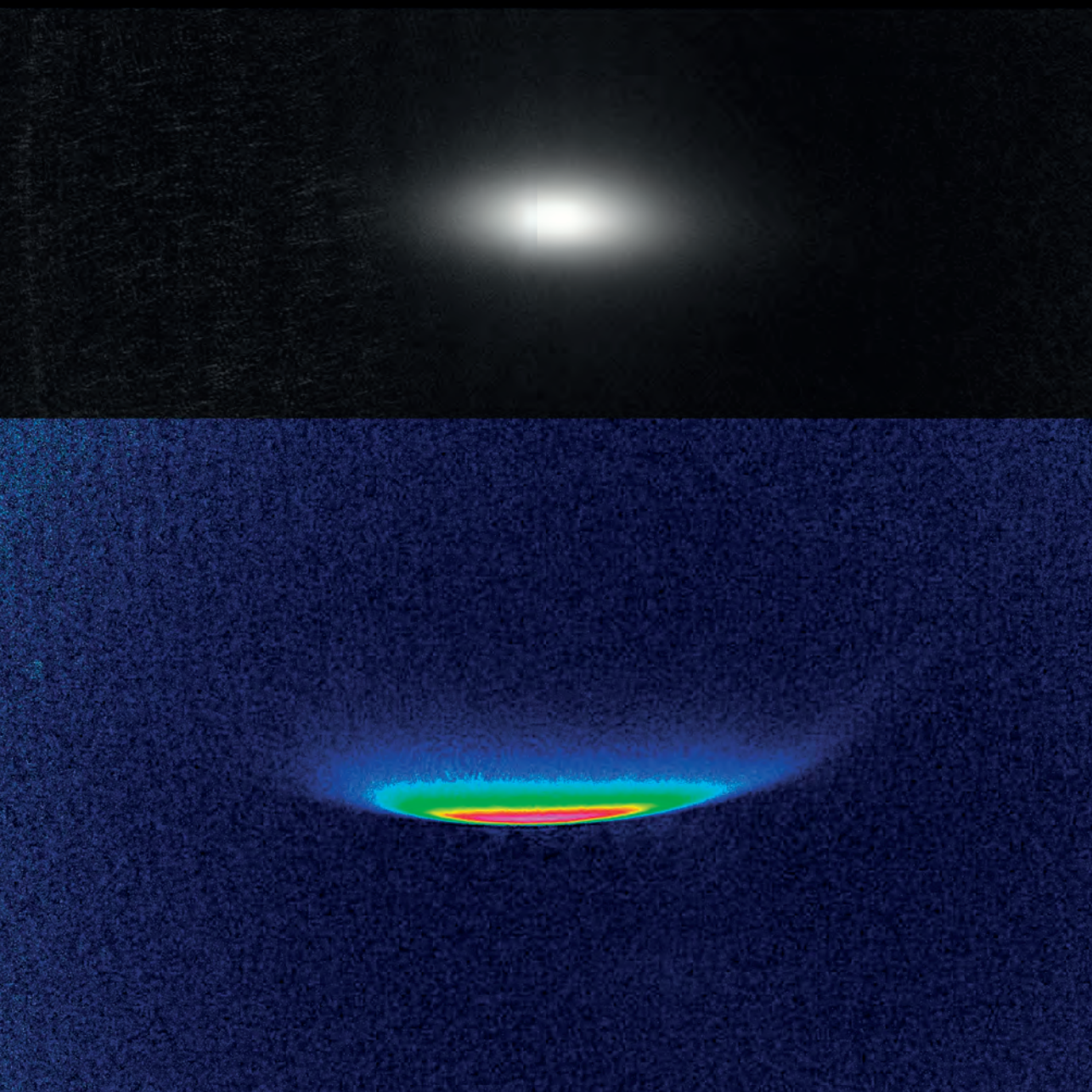

# Chapter 5

# An improved Sr red MOT for a continuous mHz superradiant clock

Cold-atom quantum technology has evolved rapidly, transitioning from laboratory research setups to practical devices capable of operating in real-world environments. Quantum devices offer remarkable improvements in performance compared to classical techniques and have found application in diverse fields such as timekeeping [126–128], gravimetry [129], inertial sensing [130], and fundamental physics research.

A crucial component for cold-atom quantum technology is the cold-atom source that lies at the heart of these devices. Typically, cold-atom sensors operate in a time-sequential manner and have distinct phases for cold-atom preparation and measurement. This pulsed operation limits the performance. For example, the Dick effect [21] mentioned in Chapter 1, arises due to aliasing of noise around the measurement frequency into measurement results. This is caused by the dead time during cold-atom preparation between sample interrogations. This inherently constrains the performance of typical optical lattice clocks.

Continuous cold atom sources play a crucial role in enabling precise measurements by providing a steady stream of laser-cooled atoms. They offer the potential to boost the data sample rate in atomic inertial sensors and mitigate the Dick effect in optical lattice clocks. Of particular interest to us is their capability to enable continuous superradiant lasing. This not just eliminates the frequency uncertainty from the Fourier limits of a pulsed signal but it enables superradiance to provide a continuous clock signal output.

Here, we demonstrate a compact steady-state $^{88}$Sr MOT on the 7.5 kHz-wide $^1S_0$ - $^3P_1$ transition within the continuous ultracold superradiant laser apparatus described in Chapter 4. The creation of this steady-state MOT is achieved using modulated, broadband 689 nm red lasers to cool and trap $3 \times 10^7$ atoms at a loading rate of $1 \times 10^7$ atoms/s. The

average temperature of ultracold atoms is about 10 µK. Further cooling can be accomplished by tuning the 689 nm broadband lasers to a single frequency. This results in nearly recoil-limited ultracold atoms with temperatures as low as 800 nK measured. This chapter will provide a detailed exploration of the debugging process undertaken to achieve these significant milestones. Additionally, it will address opportunities for enhancing machine performance and discuss potential avenues for advancing continuous superradiance.

## 5.1 Seeing is believing

Our exploration of the steady-state 689 nm red MOT (ROMT) begins with the observation of strontium atoms within the vacuum chamber. While my previous experience with strontium in the hot atomic beam machine provided some familiarity, witnessing the fluorescence from strontium in our current setup continues to evoke excitement. However, this excitement was tinged with uncertainty due to a mishap involving the heater for the oven nozzle, which created doubts about whether atoms would emit from the oven.

Previously, we encountered an issue with one of the heaters for the oven nozzle (as discussed in Section 4.1.1) while attempting to raise the nozzle temperature to the desired 500 °C. Due to a machining error, our temperature sensor could not properly be attached to the desired location, resulting in an underestimation of the temperature. Consequently, we continued to increase the heater power until it overheated at a "measured" nozzle temperature of only 270 °C. This broken heater caused an electrical short in the output from the current driver since it was connected in parallel with the other two heaters. Disconnecting the faulty heater from the current driver resolved the issue, allowing us to continue operating the remaining heaters at a current per heater below the setting that caused that broken oven heater. As a result, the nozzle now operates at a nominal 210 °C. This raised concerns about the possibility of the nozzle being blocked by solidified strontium, potentially hindering strontium emission. In such a scenario, the oven nozzle would need to be replaced.[1]

Keeping the nozzle temperature unchanged, we then activated the heaters for the strontium reservoir. Fortunately, at a nominal strontium reservoir temperature of 300 °C, we were able to observe the fluorescence of strontium atoms (see Figure 5.1), illuminated by a blue 461 nm on-resonant laser. This moment was met with a sense of relief, dispelling concerns about the oven emitting strontium. However, our attention turned to the potential for strontium to block the nozzle. To monitor this, we utilized a web camera to observe any decrease in fluorescence and conducted daily visual inspections for changes.

[1] A backup, simplified oven was manufactured by our workshop and was ready within two weeks.

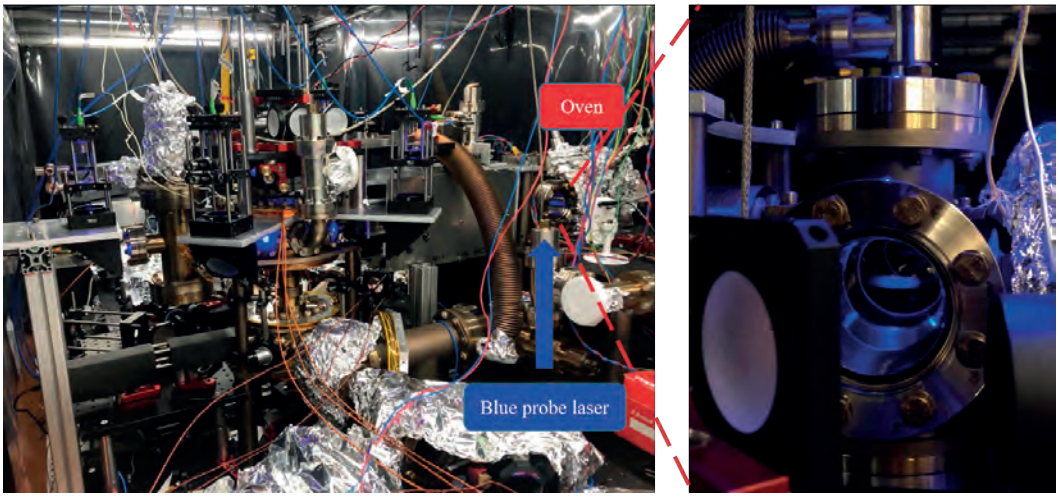


FIGURE 5.1: **Fluorescence of strontium atoms emitted from an oven.** A 3-mW, 50-mm diameter on-resonant blue beam is sent vertically through the vacuum chamber. In the center of the chamber, fluorescent light can be seen by eye, showing atoms being emitted with high flux by the oven.

After operating the machine for three months, we observed no significant changes in fluorescence, and the signal strength of our blue MOT remained strong and consistent. Subsequently, we removed the camera to make space for the construction of a transverse cooling stage to collimate the atomic beam emitted from the oven. However, it appears that both the nozzle temperature and the strontium oven reservoir temperature may be dramatically underestimated because strontium was observed by eye at an oven reservoir temperature of nominally 300 °C, which for our other strontium machines happens only above about 400 °C.

## 5.2 Zeeman slower and 2D blue MOT

The optical alignment for the Zeeman slower and the 2D blue MOT beams was done using a cage structure, as depicted in Figure 5.2(a). Consequently, each cooling laser beam was initially aligned roughly by this structure. Subsequent fine-tuning of the optical alignment was achieved through two methods: utilizing a small, central hole in a plastic cap covering the viewports to center the laser beams (see Figure 5.2(d)) to the viewport, or employing a beam blocker to center the beam to the cage (see Figure 5.2(e)).

Once each blue MOT laser beam was power-balanced with the correct polarization, blue fluorescence from atoms became visible on the camera (Basler, a2A1920-51gmPRO).

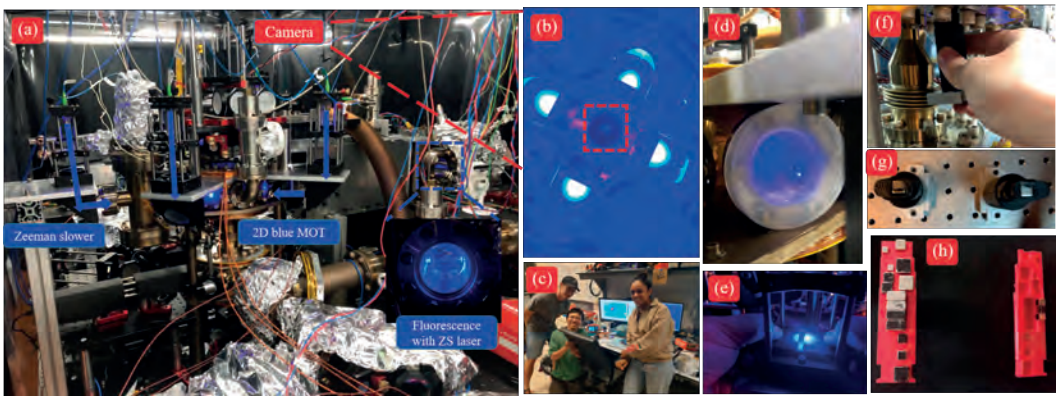


FIGURE 5.2: **Debugging the Zeeman slower and 2D blue MOT.** (a) When the Zeeman slower is activated, fluorescence emission is observed from the transverse cooling chamber. The Zeeman slower beam and the blue MOT beam are mounted on the cage and optimized using the methods shown in (d-e) to center the beams. (f)-(g) We discovered that the permanent magnets were assembled in the reverse direction. After correcting this and using the correctly polarized laser beams, the blue MOT became visible from the top viewport (b) and through a camera, as shown on our computer screen (c).

However, the top-view shape of the fluorescence signal was weak, not round and was not centered with the differential tube to the red MOT chamber. The parameters easily available for optimization included the lasers (such as alignment, power, frequency, and polarization) and the magnetic bias fields. We found that it was not possible to make a bright dense 2D blue MOT simply by adjusting these available parameters.

Interestingly, when the blue MOT permanent magnets were rotated by 180° and the MOT beam circular polarizations were flipped, a bright blue MOT unexpectedly emerged, as illustrated in Figure 5.2(c). Realignment of the blue MOT laser beam resulted in a more rounded blue MOT structure from the top view, as depicted in the dashed line box of Figure 5.2(c). It turned out that the Zeeman slower field was initially aligned with the residual field of the 2D MOT magnet array instead of being in the opposite direction as intended.

We therefore 3D printed additional MOT magnet holders and assembled magnet arrays with the magnets in reverse orientation (see Figure 5.2(f)-(h)). This time the 2D MOT worked as intended.

## 5.3 Steady-state red MOT

### 5.3.1 Atoms in the red MOT chamber

Following the 2D blue MOT, two red molasses setups, oriented orthogonally to each other, are employed to cool atoms horizontally, facilitating their transfer down to the red MOT chamber. The $^1S_0$ to $^3P_1, m_J = 0$ transition is utilized for red molasses cooling as this transition is not sensitive to the magnetic field strength. A 2G, vertical magnetic field is provided by a Helmholtz coil. This field clearly defines the quantum axis for atoms, overwhelming the residual quadrupole field of the 2D MOT magnets in this region, and simultaneously shifting the magnetically sensitive transitions several megahertz away. Vertically, atoms are not trapped and start to descend approximately 20 cm to the center of the red MOT chamber.

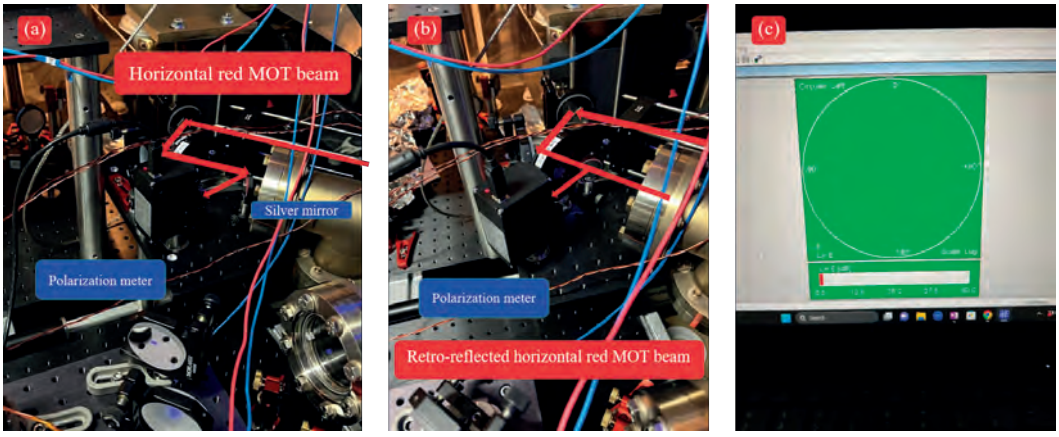


FIGURE 5.3: **Measurement and optimization of the polarization of the RMOT beams.** (a) A silver mirror was used to collect a part of the horizontal RMOT beam to measure the polarization of the beam. (b) The measurement was also done with the retro-reflected RMOT beam. (c) One measurement of the required circular polarization is presented here.

Once atoms enter the red MOT chamber, a red MOT is designed to capture and cool the atoms. The red MOT in our design is configured as a six-beam MOT to enhance its robustness, currently however, only five laser beams are in place, missing the beam from the top to the bottom. This temporary change was based on the proven functionality of the red MOT with five beams, as demonstrated in the atom laser machine. Additionally, the space originally designated for the top red MOT beam is currently being used for a blue MOT camera (without the dichroic beam combiner originally constructed).

We found that adjusting the magnetic field and the vertical beam that slows the atoms from the top chamber were the two most important factors in creating the steady-state red MOT. Two retro-reflected horizontal laser beams complete the 5-beam red MOT, as shown in Figure 5.4. Unlike the 2D blue MOT, even when we carefully placed these beams with proper power balance and correct polarizations (see Figure 5.3), we did not observe atom fluorescence. Instead, significant scattered light was observed in the camera, even with the use of an optical bandpass filter.

With no immediate red MOT, the experiment finally at last became much more fun in terms of physics. First things first, we wanted to observe the presence of atoms in the red MOT chamber. Since atoms can scatter many more photons excited by a blue laser, a 2-mW blue, on-resonant probe laser was utilized to illuminate atoms free falling into the red MOT chamber. The signal was detectable with a 100 ms shutter time on the camera, shown in Figure 5.4(c). This probe beam fluorescence later turned out to be a valuable tool for debugging the steady-state red MOT, allowing us to conduct various simple experiments for gathering information.

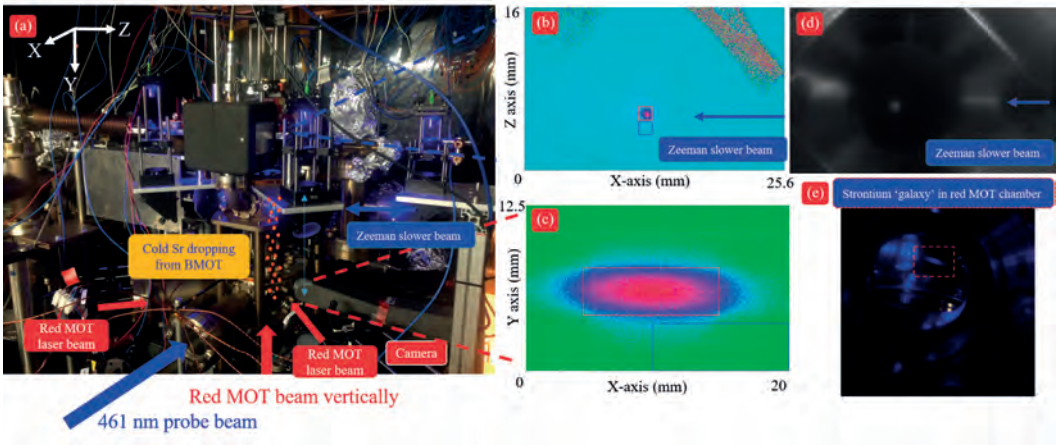


FIGURE 5.4: **Atoms arrive at the red MOT chamber.** (a) An on-resonant blue laser is utilized to probe strontium atoms arriving in the red MOT chamber. Five red lasers are positioned to create the red MOT, with one beam propagating from bottom to top. This beam has a diameter of two inches at the lower viewport and is focused to 5 mm at the bottom of the blue MOT chamber to easily pass through the 16 mm diameter differential tube. The remaining beams are used for horizontal cooling and trapping, with a diameter of approximately 30 mm and retro-reflected. (b) The blue fluorescence monitors the status of the blue MOT. (c) The strontium atoms, upon arrival in the bottom chamber, fluoresce on the blue transition when probed with the laser.

Activating the red molasses beam in the blue MOT chamber significantly increased the

fluorescence at the probe beam, by a factor of five. The red molasses beams play a crucial role in collimating the atomic beam falling to the bottom chamber. Without them, atoms would diverge to the sides of the chamber and only few of them would reach the red MOT section.

Another intriguing observation pertained to the bottom (i.e. upwards propagating) red MOT beam, which can also act as a Zeeman slower beam for the atoms falling from the blue MOT chamber. When activated, the probe fluorescence strength decreased, indicating fewer atoms reaching the blue probe laser. This observation led us to consider a tradeoff regarding the timing of atom deceleration. Decelerating the atoms too early might cause them to spread horizontally beyond the probe beam (or later beyond the red MOT capture volume), preventing them from reaching the probe position. Conversely, decelerating them too late might result in insufficient slowing for capture by the red MOT. Achieving this delicate balance necessitated precise calculation and optimization of the red Zeeman slower beam parameters. This involved determining the magnetic field and Doppler shift to ensure proper matching of the frequency and power of this beam.

### 5.3.2 Velocities of the free-falling atoms

Several methods are available for measuring the vertical velocity of free-falling atoms. One approach involves detecting the blue probe fluorescence of atoms while adjusting the detuning of the bottom red laser beam. This method measures the Doppler effect across different detunings by leveraging the 7.5 kHz-wide transition.

Alternatively, the vertical velocity can be determined by disabling the blue Zeeman slower or the blue MOT to halt the loading of atoms into the blue MOT, consequently halting the entry of new atoms into the red MOT chamber. The decay in the strength of the blue probe fluorescence at the red MOT location can then be utilized to calculate the atoms' velocity, given the known distance involved and gravity.

Figure 5.5 and Figure 5.6 respectively present results obtained from these two methods, demonstrating close agreement in atomic velocity measurements. The detuning measurement reveals that the majority of atoms interact with the bottom laser beam at a red detuning of 1.5 to 2 MHz. The bottom red MOT beam, with a power of 5.3 mW and a roughly 2-inch diameter, is focused on a position below the red molasses. Figure 5.7 illustrates the appearance of the bottom red MOT beam in front of the bottom viewport in the red MOT chamber and after the top viewport in the blue MOT chamber. Due to its focused nature, the intensity of the bottom red MOT beam varies with position. At the center of the red MOT chamber, it reaches about 300 $\mu W/cm^2$, which is 60 times higher than the saturated intensity of the

$^1S_0$ - $^3P_1$ transition. This results in a power broadening of 450 kHz. Considering the detuning of the bottom red MOT beam, the velocity of the atoms is estimated to be in the range of 1.4 to 1.7 m/s. However, the exact interaction point of the atoms with the laser beam is unknown, leading to uncertainty in the power broadening effect. The laser is coupled into a fiber after the single-pass AOM, resulting in a change in power when the frequency detuning is adjusted.

The alternative method involves measuring the decay time of probe fluorescence in the red MOT chamber when either the blue Zeeman slower or the blue MOT is deactivated. Given the known distance of 20 cm between the 2D blue MOT and the probe beam, vertical velocities can be determined when the last group of atoms is probed by the blue probe beam in the bottom chamber, as depicted in Figure 5.6(a-b). The measurement results are presented in Figure 5.6(c), indicating velocities ranging from approximately 1.8 $m \cdot s^{-1}$ to 2.5 $m \cdot s^{-1}$. Additionally, considering the size of the atomic cloud, the calculated horizontal velocity is approximately 5 $cm \cdot s^{-1}$, corresponding to a temperature of about 14 µK.

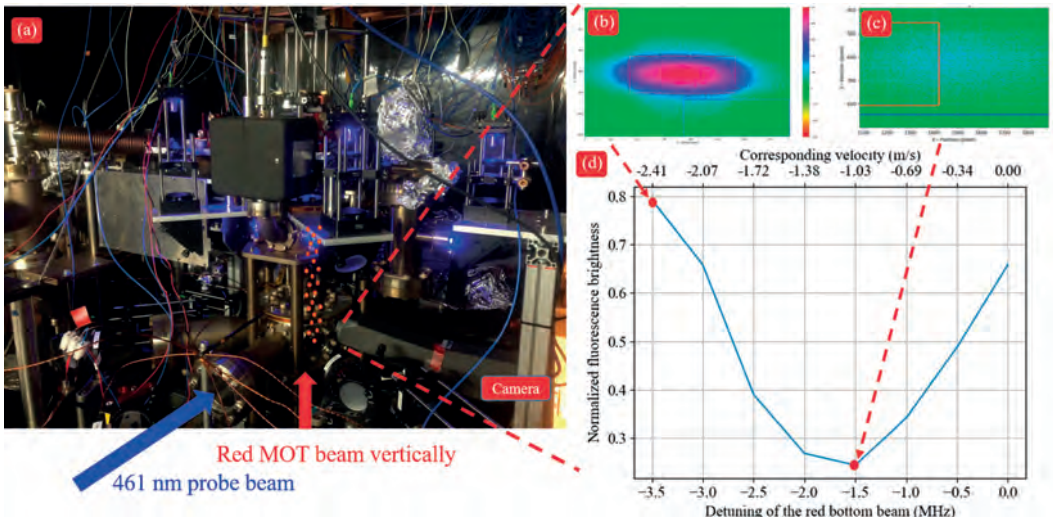


FIGURE 5.5: **Doppler spectrum with the bottom red MOT beam.** A 461 nm blue probe laser is used to illuminate atoms falling from the 2D blue MOT chamber. By scanning the detuned frequency of the bottom red MOT beam, the probe fluorescence brightness can change, as atoms are pushed and cannot reach the region of the blue probe laser beam.

### 5.3.3 Slowing atoms with the bottom beam

After determining the Doppler shift of the atoms, our next step was to adjust the magnetic field and beam frequency parameters to enable the bottom beam to slow and capture the

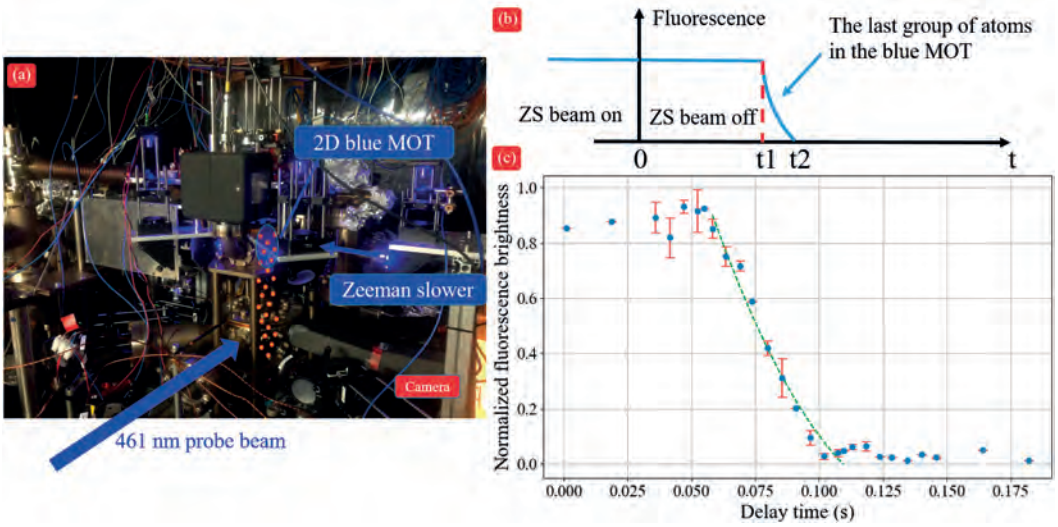


FIGURE 5.6: **The decay of the probe fluorescence caused by blocking the Zeeman slower beam.** Once the Zeeman slower beam is blocked, atoms quickly stop being loaded into the 2D blue MOT. This results in a gradual decrease of the atom flux arriving in the red MOT chamber, which is measured by recording the fluorescence of a blue probe beam horizontally crossing the red MOT chamber.

atoms. Three slowing mechanisms are supported by this bottom beam; a "white light slower" due to its broad frequency distribution acting on the non-magnetic transition, the "MOT beam" which provides a restoring force towards the quadrupole center and a "Zeeman slower" which uses the magnetic field of the MOT in combination with the other magnetic transitions [51]. Insights gleaned from the continuous BEC machine indicated that a magnetic field gradient of approximately $0.5\,\mathrm{G}\cdot\mathrm{cm}^{-1}$ is necessary for achieving a steady-state red MOT. Atoms descend to the red MOT chamber experiencing a maximum magnetic field of around 2.5G about 5 cm above the quadrupole center with a corresponding Zeeman splitting of approximately 5 MHz.

We set the frequency of the red MOT bottom beam to a band from 1 MHz red detuned of the atomic transition to 2 MHz red detuning with a modulation frequency of 15 kHz. This should be able to capture atoms at the speed of around $2\,\mathrm{m}\cdot\mathrm{s}^{-1}$. By scanning the vertical bias field from the Helmholtz coil set in the blue MOT chamber as well as the Helmholtz coil set in the red MOT chamber, we identified some coil operating parameters for which this beam successfully slowed the atoms. Notably, an increase in probe fluorescence was observed upon activation of the bottom beam.

The magnetic field environment around the chamber is complex. It includes fields from

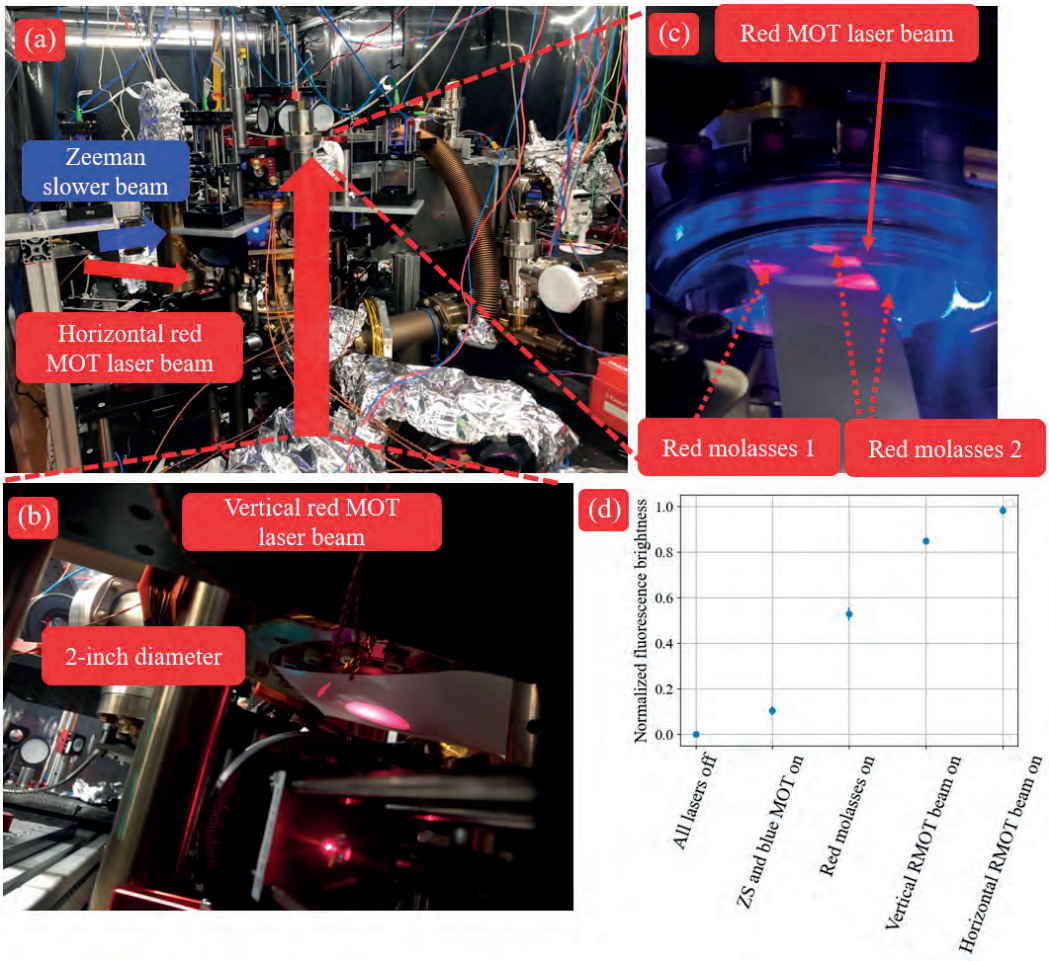


FIGURE 5.7: **The vertical red MOT laser beam alignment.** The vertical red MOT laser is focused and passes through the 2D blue MOT section. The beam diameter is roughly 2 inches in front of the red MOT chamber viewport. We also plotted the probe fluorescence under different conditions. When the Zeeman slower and 2D blue MOT are active, atom fluorescence appears. With the red molasses on, the fluorescence increases fivefold. When the bottom vertical red MOT beam is added, the fluorescence increases by an additional 80%. Finally, with the horizontal red MOT beam, there is an additional 15% increase in fluorescence.

the permanent magnets of the Zeeman slower and the blue MOT, as well as fields from ion pumps, despite their magnetic field shielding, and coils for red molasses in the blue MOT chamber. In the end, we optimized the vertical bias field for the bottom chamber by maximizing the effect of slowing the atoms.

In the atom laser machine the bottom MOT beam was focused and tilted to the side so that it doesn't travel up and overlap with the 2D blue MOT in the top chamber. I explored options with and without this tilt in my Monte Carlo simulation, which suggested that a vertical beam without the tilt should also work. Trusting the simulation, we maintained the original focused beam design but without the tilt on the bottom beam.

### 5.3.4 Steady-state red MOT

By activating and fine-tuning the horizontal beams of the red MOT, the blue probe fluorescence can be enhanced by up to 15%. At this point, the blue probe beam becomes unnecessary and it acts as a pushing beam, potentially disrupting the red MOT. Another camera (Basler, a2A1920-51gmPRO) equipped with a bandpass filter centered at a wavelength of 690 nm (bandwidth 10 nm) was added and used to detect any red fluorescence from atoms.

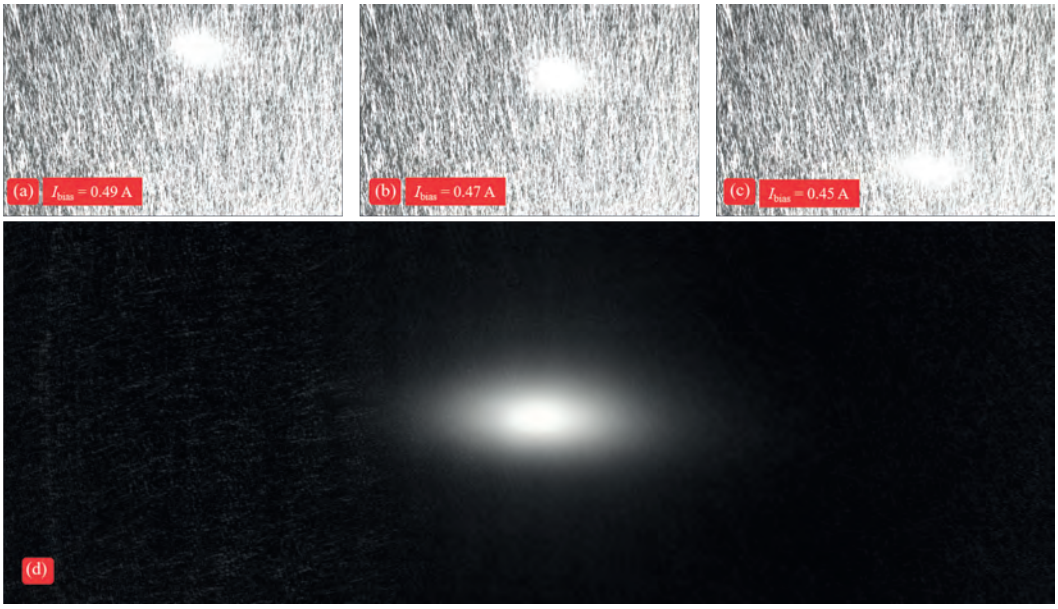


FIGURE 5.8: **The first red fluorescence of our steady-state red MOT.** (a-c) Atoms are trapped in the broadband red lasers and moved vertically by adjusting the magnetic field. (d) After optimizing the position of the bottom red MOT beam, scattering is significantly reduced, resulting in a bright steady-state red MOT.

Fortunately, after meticulously adjusting the vertical magnetic field, a small, fluorescing atom cloud was detected by our camera! It is important to clarify that this observation was not just the red fluorescence of freely falling or diffusing atoms, but of a trapped red

MOT. This was verified by moving the red MOT with the offset magnetic field, shown in Figure 5.8(a)-(c). This first steady-state red MOT in our new machine marked a significant milestone in our research. Starting from this small MOT, it was easy to optimize and vastly increase the red MOT atom number and flux over the next months. The very good performance of the optimized machine proved our concept of a compact ultracold atom source for strontium, which can now with confidence be used also by my colleagues from the QDNL zero-dead-time clock team and others. Later, when I began tightening all the screws, I discovered a 'sweet position' for the bottom 3-inch mirror that is the last mirror for the vertical red MOT beam. In that position, the red MOT remained visible on the camera with significantly less scattering, shown in Figure 5.8(d). The alignment of the red MOT bottom beam didn't change much, so I inferred that the scattering was likely due to the larger beam size being cut at the bottom of the differential tube.

### 5.3.5 Characterization of the steady-state red MOT

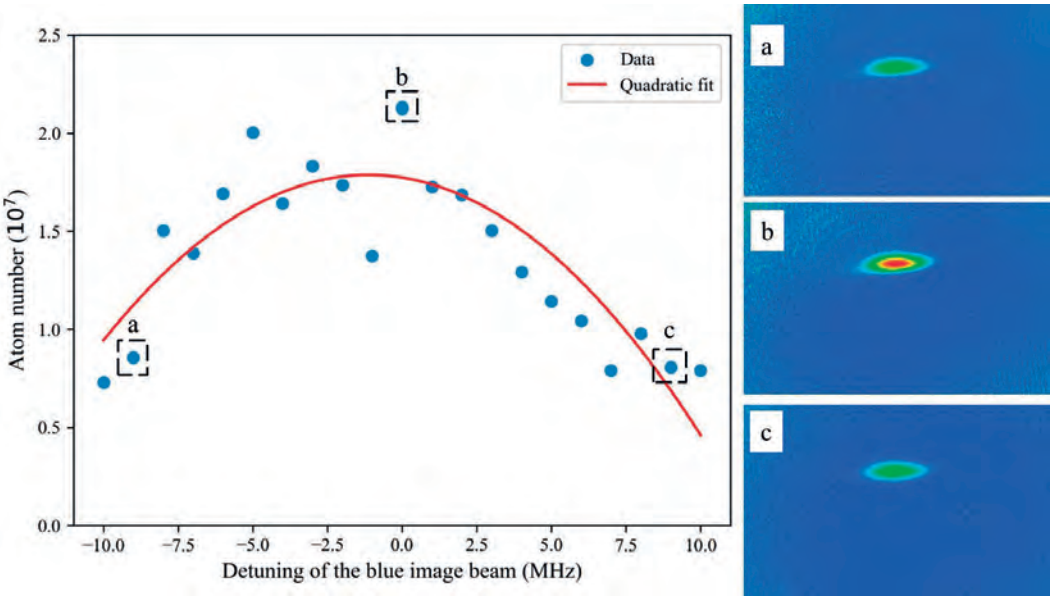


FIGURE 5.9: **Optimizing the blue probe beam frequency.** Atoms number measured by absorption imaging as function of the blue probe laser frequency. The optimized frequency of the blue probe laser corresponds to the resonance of the blue transition of the atoms.

After establishing the steady-state red MOT, we began utilizing absorption imaging to obtain a more precise measurement of the atom number and to optimize the steady-state red MOT.

Our first step was to conduct a frequency scan of the blue probe beam used for the absorption imaging to confirm the resonance frequency. The results of this scan are depicted in Figure 5.9. Satisfyingly, when the probe laser was tuned to the resonance of the $^1S_0$ to $^1P_1$ atomic transition, the measured atom number was maximized, aligning perfectly with expectations.

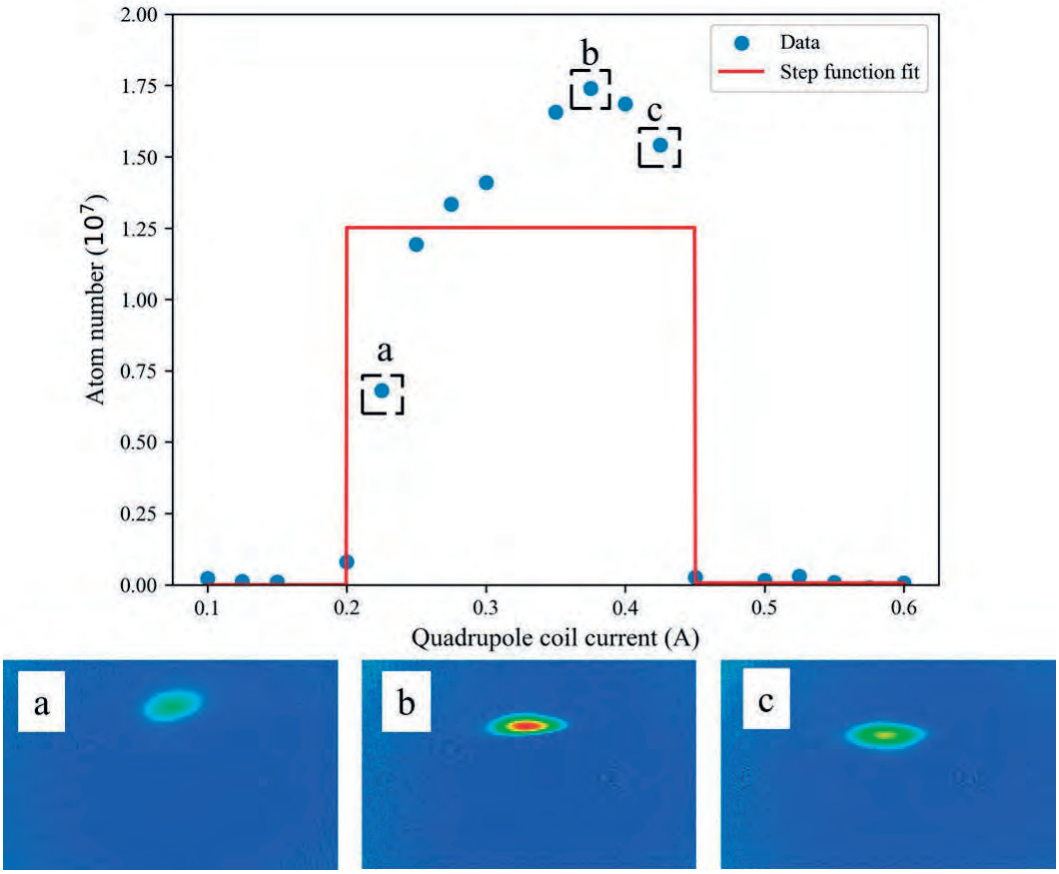


FIGURE 5.10: **Optimization of the red MOT with the quadrupole coil current.** The graph depicts the relationship between the current applied to the quadrupole coil and the efficacy of atom trapping in the red MOT. Within the range of 0.2 to 0.43 A, we observe the gradual establishment of a steady-state red MOT. Notably, as presented in (a)-(c), the position of the red MOT shifts in dependence of this current.

Afterwards, we proceeded to scan the quadrupole coil current to determine the optimal magnetic field gradient. The findings from this scan are illustrated in Figure 5.10. As the current running through the quadrupole coil increased, we observed a gradual increase of

the MOT atom number. The optimal current for the coil was found to be approximately in the range of 0.35 to 0.4 A. However, when the gradient of the magnetic field increased beyond a certain threshold, we noticed that no further atoms could be effectively cooled and trapped within the red MOT.

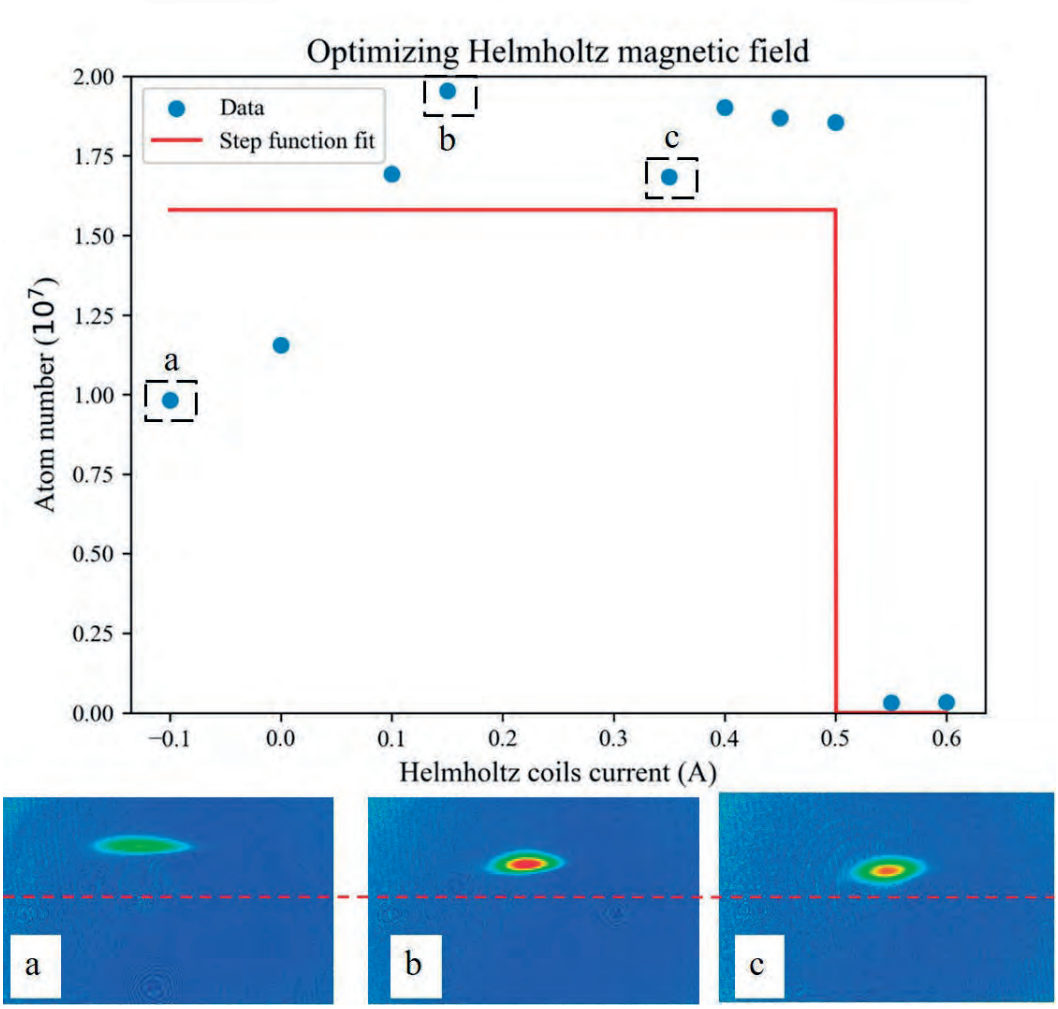


FIGURE 5.11: **Optimization of the red MOT with the horizontal bias field using the Helmholtz coil.** The atom number remains relatively constant over a broad range until the current exceeds 0.5 A, where the red MOT vanishes. As the current through the Helmholtz coil varies, the vertical position of the red MOT also changes, shown in (a)-(c).

Next, we proceeded to optimize the horizontal bias magnetic field. The relationship between the atom number and the horizontal bias field is shown in Figure 5.11. Interestingly,

we noted that the atom number remained relatively constant over a large range until the current reached approximately 0.5 A. As expected, increasing the vertical bias field moved the position of the red MOT downwards.

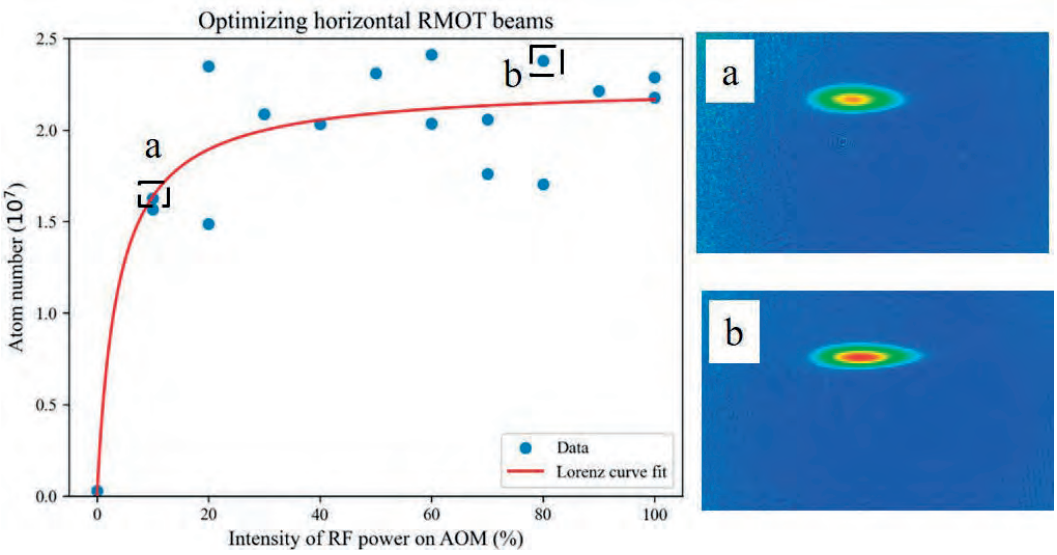


FIGURE 5.12: **Optimization of horizontal red MOT beam laser power.** The atom number increases with the power of the horizontal red MOT laser beams. The red MOT atom number reached saturation when the RF power on the horizontal MOT beam AOM was just 20%.

Measurements were conducted to assess the atom number as a function of the intensity of the red MOT beams to determine whether the power of the beams was adequate. For the horizontal MOT beams, the atom number remained constant after reaching around 20% of the RF power on the AOM, see Figure 5.12. This suggests that the available power for the horizontal beam significantly exceeds the requirement, allowing for potential future reallocation of spare red power to other applications. Conversely, the atom number continued to rise as the vertical red MOT beam power was increased. The apparent saturation shown in Figure 5.13 is from the saturation of the AOM diffraction efficiency. Increasing the power available for the vertical RMOT beam has the potential to significantly increase the MOT atom number.

After the initial round of optimization, we proceeded with measurements to evaluate the maximum atom number, loading rate, lifetime, and temperature of the red MOT. The loading rate was around $10^7$ strontium atoms per second with a saturated atom number around 25 million atoms, as depicted in Figure 5.14. While I was writing this thesis, my colleagues Benedikt Heizenreder and Ananya Sitaram implemented the transverse cooling

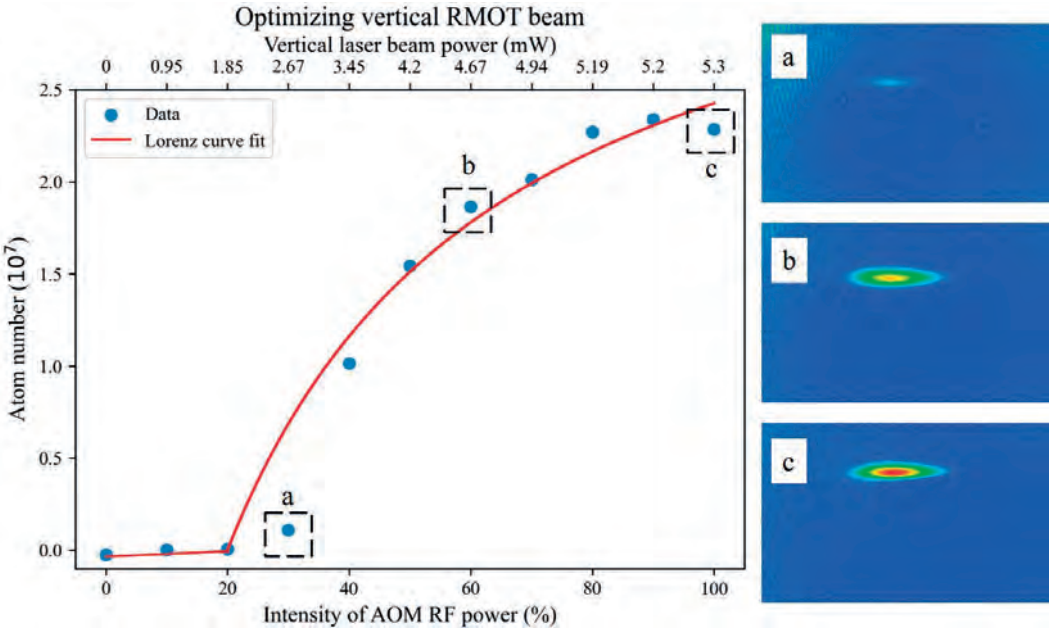


FIGURE 5.13: **Optimization of vertical red MOT beam laser power.** The red MOT atom number increases with the power of the vertical red MOT laser beam. The "saturation" at the highest few points is due to saturation of the AOM efficiency, the output power is constant in this region. These results indicate further improvements in atom number may be obtainable with additional laser power. The peak power was equivalent to 5 mW with a beam diameter of about 25 mm.

of the atomic beam from the oven, which increased the total atom count by a factor of 12 to give a loading rate around $10^8$ $^{88}$Sr per second and a MOT of around $3 \times 10^8$ $^{88}$Sr atoms. The operational flux of this apparatus closely resembles the performance of our atom laser machine, which makes me happy.

Subsequently, we determined that the lifetime of the red MOT was approximately 2 s, as depicted in Figure 5.15. This short lifetime raised suspicions that the blue probe beam, whose intensity was controlled by an AOM, might not be fully blocked, causing atom heating. Later, with the addition of a mechanical shutter to block the blue probe beam, the lifetime of the red MOT increased to 3-4 s.

In an effort to demonstrate a higher phase-space-density (PSD) ultracold atom source, adjustments were made to both the magnetic field and laser parameters. After loading the red MOT for 5 s, we swiftly ramped the laser frequencies from broadband to a much narrower range to further cool the atoms and adjusted the magnetic field gradient to match the laser frequencies. Specifically, the modulation frequency of the vertical red MOT laser

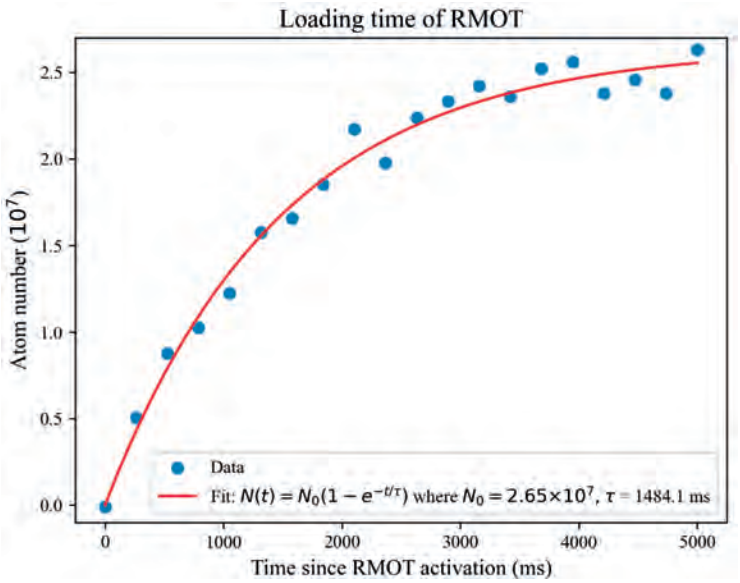


FIGURE 5.14: **Loading time of the red MOT.** The loading rate of the steady-state red MOT was around $10^7$ $^{88}$Sr per second with saturation at around 25 million strontium atoms loaded within 3 s.

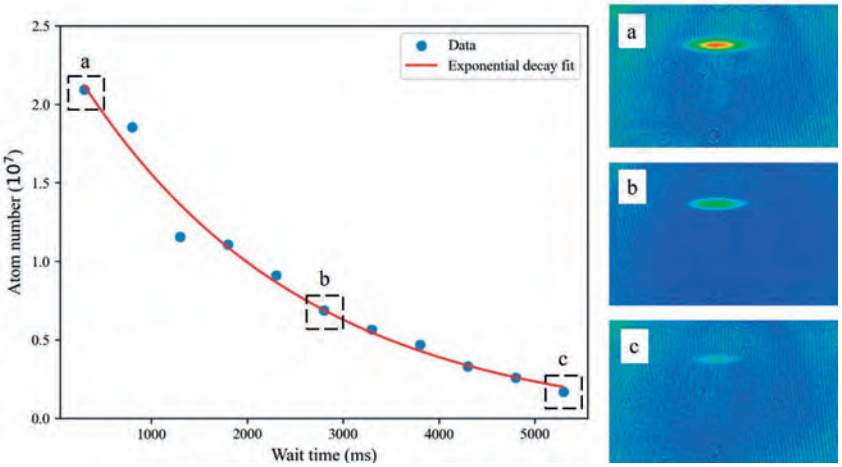


FIGURE 5.15: **Lifetime of the red MOT.** Beginning from 20 million atoms, the atom number decrease to 1/e within 2 s. Lifetime was limited by scattering of the blue absorption imaging probe beam. The later addition of a mechanical shutter to the blue probe increased the lifetime to 3-4 s.

was changed from a range of -0.1 to -2 MHz to a range of -0.3 to -0.4 MHz. The power of this laser beam was adjusted from 5.3 mW to 0.95 mW. Similarly, the modulation frequency of

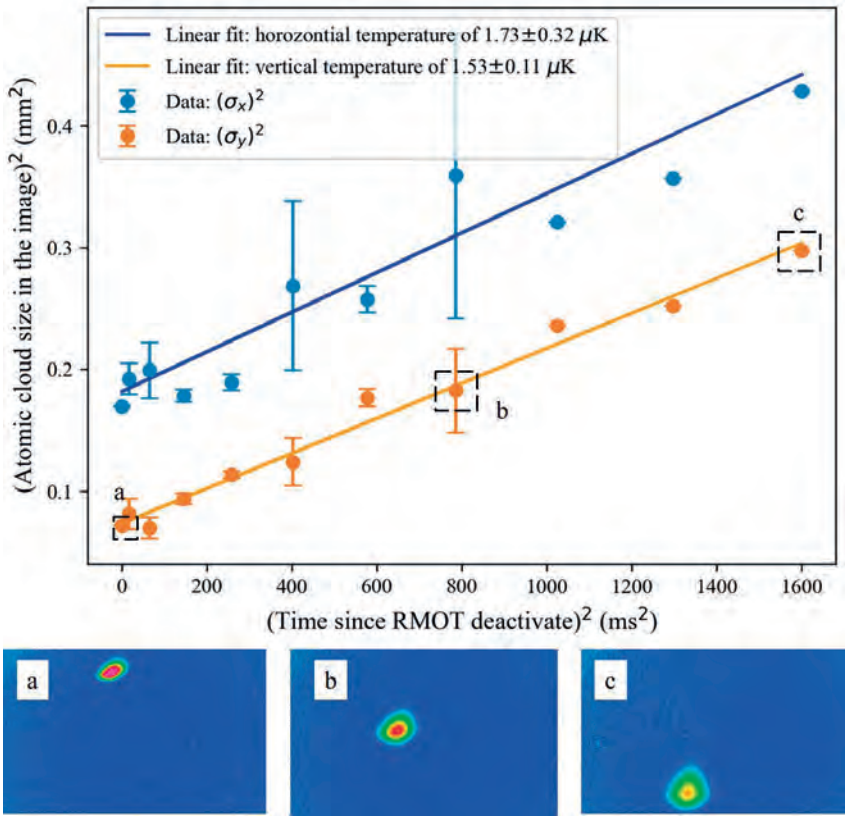


FIGURE 5.16: **Temperature measurement of a higher PSD ultracold red MOT.** Atoms are trapped and further cooled by adjusting the magnetic field and laser parameters. They are then moved to the top side of the image by the vertical magnetic field, allowing more time for free fall before exiting the image. The time sequence of laser parameters and magnetic field changes is described in the text. The temperature of the cold atom cloud is approximately 1.5 μK.

the horizontal red MOT laser was adjusted from a range of -0.1 to -2 MHz to a range of -0.1 to -0.2 MHz with a power of the beam decreased from 2.5 mW to 0.08 mW. Concurrently, the magnetic field gradient was changed from 0.3 G/cm to 0.2 G/cm over a ramp time of 200 ms. After that, we elevated the atomic cloud by moving the quadrupole centre up with an vertical offet magnetic field within 200 ms to perform a time-of-flight measurement. Figure 5.16 presents a time-of-flight (ToF) measurement of a higher PSD ultracold red MOT. A Gaussian fit was applied to ascertain the cloud's dimensions in both the horizontal and vertical axes. The size of the cold atom cloud expands during free fall and is monitored over time. Since the temperature of the atomic cloud is determined by,

$$\frac{1}{2}k_B T = \frac{1}{2}mv^2, \tag{5.1}$$

I plot the cloud size squared as a function of time squared. The slope of a linear fit gives the velocity squared, which corresponds to a cloud temperature of 1.73 µK along the horizontal direction and 1.53 µK along the vertical direction. This yields a phase space density of $3.1 \times 10^{-6}$ [131], calculated with the following equation.

$$\rho = n(\frac{h^2}{2\pi m k_B T_i})^{3/2}. \tag{5.2}$$

Here, n represents the number density. With 25 million atoms confined within a volume of $0.125\text{cm}^3$, the number density (n) is calculated as $2 \times 10^8$ $\text{cm}^{-3}$.

## 5.4 Smiling MOT

The PSD of our steady-state MOT is not very high because the frequency of the MOT lasers is modulated. Addressing the red MOT transition with a single frequency can cool the atoms much more strongly. A single-frequency red MOT has a low capture velocity and can't load the atoms falling from the blue MOT chamber. In order to still profit from the improved PSD of a single-frequency red MOT, we can swiftly ramp from broadband to single-frequency operation just before using the atoms, e.g. sending them off into the transfer guide, reverting back to broadband operation immediately thereafter.

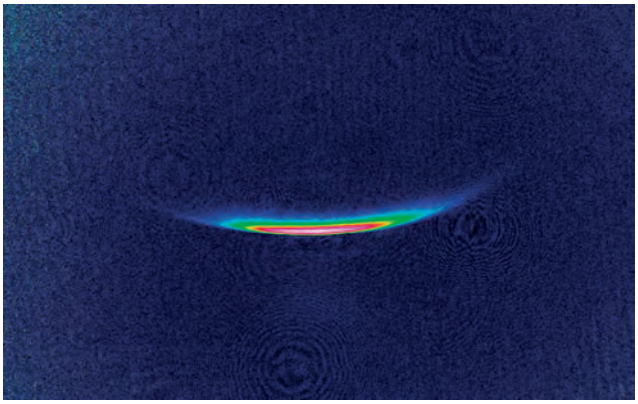

FIGURE 5.17: **Single frequency red MOT.** The single-frequency red MOT is smiling and has a temperature of about 800 nK.

Here we demonstrate the time-sequential production of a high PSD single-frequency MOT. The modulation of the red lasers is ramped off in a time-sequential manner after

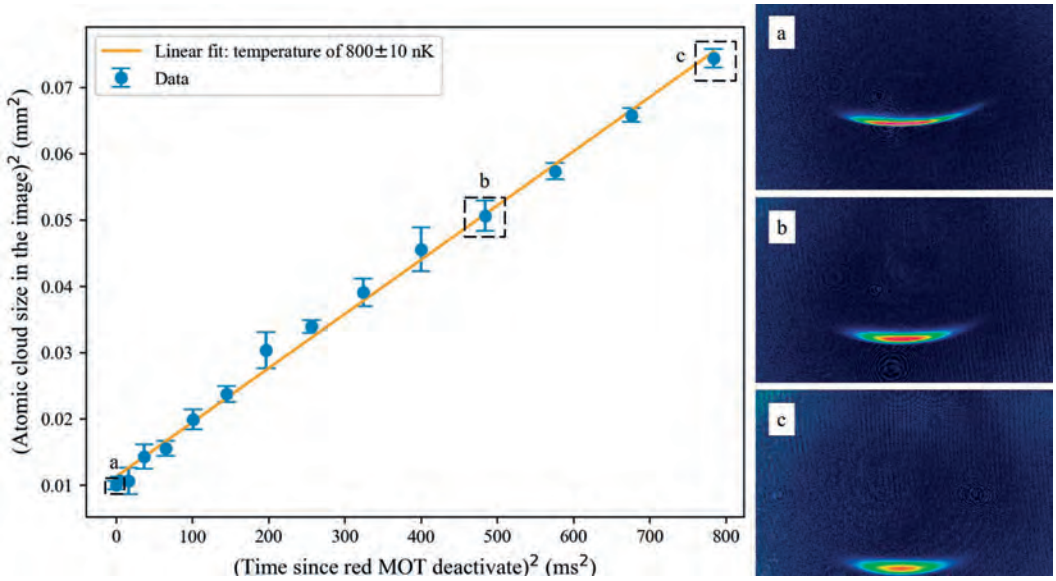


FIGURE 5.18: **Temperature of the smiling MOT.** Fit to time-of-flight data delivers the temperature T=800 nK, close to a recoil-limited temperature.

5000 ms of broadband red MOT loading with two steps. In the first step, the modulation frequency of the vertical red MOT laser is shifted from a range of -0.1 to -2 MHz to a single frequency detuning of 0.5 MHz. Simultaneously, the power of this laser beam is reduced from 5.3 mW to 0.95 mW. For the horizontal red MOT laser, the modulation frequency is adjusted from a range of -0.8 to -2 MHz to a single frequency detuning of -0.5 MHz with a power of the beam decreased from 2.5 mW to 0.08 mW. Concurrently, the magnetic field gradient is changed from 0.3 G/cm to 0.19 G/cm over a ramp time of 200 ms. In the second step, the single-frequency detuning of the red MOT beams is further adjusted to -0.3 MHz and the magnetic field gradient is increased to 0.5 G/cm over a ramp time of 50 ms. The atom number decreased by about 20% after transitioning to the single-frequency MOT. With our postdoc Shayne's experience, this optimization was done within one hour. The result is presented in Figure 5.18 and Figure 5.20. The temperature was measured with the time-of-flight method to be about 800 nK, which is very close to the recoil limit of 480 nK [56, 132].

This nearly recoil-limited red MOT can also be used to measure the magnetic field gradient, as the position of the MOT is dependent on the magnetic field and the detuning of the bottom red MOT beam. This beam is resonant with the Zeeman detuned atomic transition on a thin ellipsoid around the quadrupole center. The atoms fall by gravity till they reach the lower part of this shell and get accelerated upwards. The atoms "stay" at the

position where the gravitational force equals the force from the vertical red MOT beam, as shown in Figure 5.19.

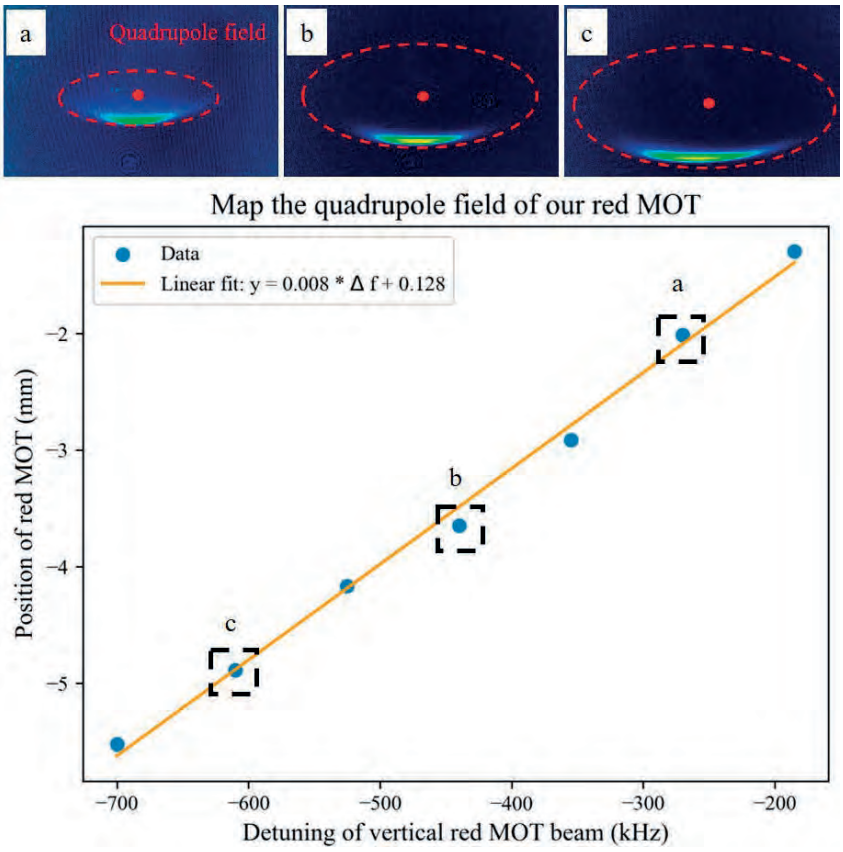


FIGURE 5.19: **Smiling MOT position as function of the detuning of the vertical red MOT beam.** We used ultracold atoms, nearly at recoil-limited temperatures, to measure the magnetic gradient of the red MOT. By scanning the detuning of the single-frequency red MOT, the atoms balance at different location, where the light-induced force equals with gravity. The location depends on resonance with the vertical red MOT beam. Based on this method, we found that the magnetic field gradient is approximately 0.57 G/cm, which matches our design.

Keeping the coil currents constant we can fit the position of the cold atoms for different detunings of the vertical red MOT beam. This is plotted in Figure 5.19 which shows the magnetic field gradient equals 0.57 G/cm. We can also calculate the quadrupole gradient from the current and coil geometry which gives 0.5 G/cm, an excellent agreement.

In summary, we have demonstrated a steady-state strontium red MOT and a pulsed single-frequency red MOT with a temperature close to the recoil limit of 480 nK.

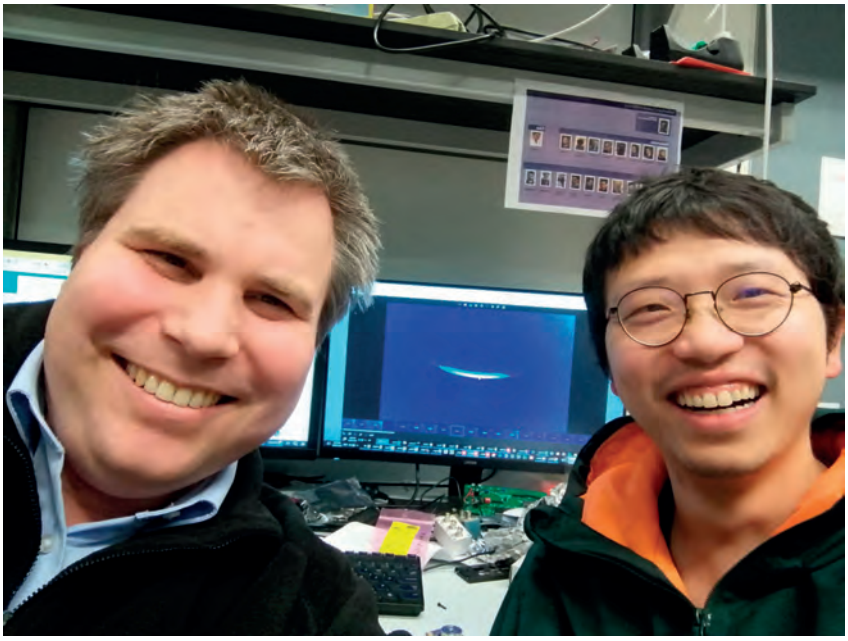

FIGURE 5.20: **The first time our machine created a "smiling" single frequency red MOT.** This project from the very beginning was a partnership with Shayne. From applying for the project to design, simulation, building, and debugging, it was a joint effort by many people. Here, the three of us all smile together.

## 5.5 Outlook and improvements

Our machine is working and has achieved the performance targets we originally hoped for. We now have a second, improved, steady-state source of ultracold stontium with a performance matching the atom laser machine. With most of the hard work done, the exciting, fun part remains, transferring atoms to the cavity and achieving continuous superradiance.

Our next steps involve:

1. Aligning the optical dipole trap with the red MOT to guide atoms to the superradiance cavity.

2. Constructing a 689 nm Bloch accelerator to facilitate atom escape from the red MOT. To avoid re-trapping by the steady-state red MOT after acceleration, the red MOT beams can be temporarily switched off allowing easy transfer. Later additional efforts can be made to introduce dark spots or other measures we have discussed to improve the flux and continuity of the atoms transferred.

3. Aligning optics for the superradiance chamber to decelerate atoms with a red molasses, store them in a dipole trap reservoir, and load them into the ring superradiance cavity.

4. Optically pump the atoms to $^3P_0$, potentially multiple times.

5. Install the heterodyne detection system and characterize the pulsed and later continuous superradiant emission.

6. Optimize the machine for continuous superradiant laser output.

With these next steps hopefully excited atoms in the cavity will soon be emitting collectively, and the signal frequency may soon be utilized as an optical frequency standard.

In addition to these next key steps a number of other improvements remain to enhance the steady-state red MOT performance.

1. Including repumper lasers (707 nm, 679 nm) in the blue MOT can repump excited atoms in $^3P_2$ that leak from $^1P_1$ through $^1D_2$ in the 2D blue MOT. This way they can be pumped back to the $^1S_0$ ground state, preventing them from being lost from the blue MOT.

2. Verifying the performance and optimizing the machine for operation of the fermionic isotope, $^{87}$Sr remains an important milestone to be achieved.

Apart from achieving a continuous ultracold superradiant laser, there are many other experiments and research lines that we can explore with this machine.

### 5.5.1 Continuous strontium clock transition spectroscopy

Once atoms are continuously loaded into the cavity, continuous cavity-enhanced clock spectroscopy of $^1S_0$ atoms can be an interesting clock operation mode. We can implement continuous Rabi or Ramsey operation modes [35] by sending the desired pulsed clock laser to the atoms and using feedback to lock the clock laser. This continuous atomic spectroscopy is not only interesting for building a frequency reference, but it has also been used to search for dark matter [133]. Dark matter searches taking this approach could also be explored exploiting the new capabilities our machine offers.

Another interesting direction is suggested by recent theoretical research [134] that shows spectrally pure light can be generated by coherently driving the collective atomic dipoles inside an optical cavity. In our setup, we can use our clock laser to continuously drive the atoms in our cavity, with the light exciting the cavity offering a clock reference. In this system the light exiting the cavity carries information not only about the detuning between the driving light and the atomic transition but it is also affected by noise from all

the decoherence processes acting on the combined atom-cavity system. The theory proposes that based on the limits of state-of-the-art cavity experiments, the achievable linewidths can be comparable to those of a superradiant laser.

### 5.5.2 Superradiant cooling

With the mHz machine, we can create nearly recoil-limited cold atoms, and possibly go beyond that. If atoms collectively absorb and emit one photon, the momentum of this cold atom group changes by one photon momentum divided by the number of atoms. In principle, the atoms can be cooled far beyond the recoil-limited temperature.

Furthermore, laser cooling requires spontaneous decay to cool the atoms. In the superradiant regime, atoms can decay much faster from the excited state, increasing cooling power. This can allow the mHz transition to also be used for cooling.

To demonstrate this, we don't need to operate in continuous mode. We can load atoms and attempt to cool the atoms using a laser red-detuned from the ring cavity resonance. The atoms would then collectively emit photons into the resonant cavity mode, reducing their momentum. There are also proposals [135–137] suggesting that in the bad cavity limit atoms can create a sufficiently strong field inside the resonator, allowing them to be trapped and cooled via superradiant lasing action. Thus, cooling atoms and achieving superradiant lasing can occur simultaneously.

### 5.5.3 Single photon emitter

Considering the enhanced decay rate in the superradiant regime, we can also create a very fast and long coherence time single photon source [138]. When only one atom is excited in the atom-cavity system, the photon will be emitted by the system much faster than the spontaneous decay rate. The advantage of using the mHz transition is that the coherence time of the photon will be extremely long, potentially lasting several minutes. This makes it suitable for quantum communication within our solar system, provided the losses are low.

### 5.5.4 Entanglement of cavity QED

Imagine three atoms in the excited state ($|111>$) in the superradiant regime, and then we detect one photon emitted from the system. Since we don't know which atom emitted the photon, the atoms would be in a superposition state $1/\sqrt{3}(|011> + |101> + |110>)$. Now, if we detect the third atom and it is in the excited state, the other two atoms are in the entangled state ($|01>+|10>$). There are many theoretical proposals for entangling atoms using superradiance [139].

### 5.5.5 Squeezed superradiant clock

A recent theory [140] proposes a method to create and store scalable and long-lived entangled spin-squeezed states within the manifold of many-body cavity dark states using collective emission of light from multilevel atoms inside an optical cavity. This can be achieved with our setup, as we can use $^{87}$Sr with its ten sublevels in the collective strong coupling regime. Theory shows that this system can be tuned to generate squeezing in a dark state, making it immune to superradiance. More generally, squeezing can be generated using a combination of superradiance and coherent driving in a bright state, and subsequently transferred via single-particle rotations to a dark state where the squeezing can be stored.

Another proposal [141] shows that squeezing arises even when atoms are in the ground state. Identifying any interesting observable physics parameters that are squeezed in the superradiant regime would be highly interesting and valuable for further research.

### 5.5.6 Transition between superradiance and subradiance

While we know how to achieve superradiance, creating subradiance remains an unknown and intriguing experiment.

Beyond these ideas, achieving the first continuous superradiant laser with the mHz transition would be a significant milestone. It could also greatly benefit the quantum sensor community.

# Chapter 6

# Conclusion

In my thesis, I present two continuous superradiant laser machines that we built. The first is a hot strontium atomic beam machine based on the $^1S_0$ - $^3P_1$ 7.5 kHz-wide transition. This machine aimed at achieving a rugged, compact superradiant laser with a linewidth performance at the 10 Hz level. The second machine is an ultracold strontium superradiant laser based on the $^1S_0$ - $^3P_0$ 1.35 mHz-wide transition. This machine aims to demonstrate not just the first continuous active optical clock but also one with state-of-the-art short-term frequency stability suitable for use as a frequency reference.

From the hot atomic beam machine, we have already observed the potential gain of a 689 nm probe laser with the excited atoms in the cavity. With this machine we are very close to realizing the first continuous superradiant laser. This setup allows for many interesting physics experiments, such as measuring the collective emission of an atomic beam into an off-resonant cavity mode [142] and exploring the multicomponent superradiant phase [143]. Additionally, this setup could be implemented in a very compact package, similar to a cesium beam atomic clock, but using strontium or calcium's optical transition. This could prove particularly well suited for field applications, which could help bring the optical clocks from the lab to the world.

From the ultracold superradiant laser using the mHz transition, we have achieved an improved steady-state red MOT with similar performance compared with our atom laser machine. Our new machine is more compact and incorporates several new design features, such as an in-vacuum oven and heated window, as well as a permanent magnet Zeeman slower. This platform holds great promise for achieving a continuous superradiant laser on the mHz transition. Our unique design also offers numerous opportunities to explore interesting cavity physics and technology.

# Bibliography


[1] J. M. Robinson, E. Oelker, W. R. Milner, W. Zhang, T. Legero, D. G. Matei, F. Riehle, U. Sterr, and J. Ye, *"Crystalline optical cavity at 4K with thermal-noise-limited instability and ultralow drift"*, Optica **6**, 240–243, 2019, DOI: 10.1364/OPTICA.6.000240.

[2] H. Liu, S. B. Jäger, X. Yu, S. Touzard, A. Shankar, M. J. Holland, and T. L. Nicholson, *"Rugged mHz-Linewidth Superradiant Laser Driven by a Hot Atomic Beam"*, Phys. Rev. Lett. **125**, 253602, 2020, DOI: 10.1103/PhysRevLett.125.253602.

[3] E. Bruton, *"The History of Clocks and Watches"*, Collectors Reference Series, Crescent Books, 1989, ISBN: 9780517689097.

[4] F. Riehle, *"Frequency Standards"*, John Wiley and Sons, Ltd, 2003, ISBN: 9783527605996, DOI: https://doi.org/10.1002/3527605991.

[5] D. Judy, *"100 Years of Vintage Watches"*, 100 Years of Vintage Watches, Krause Publications, 2002, ISBN: 9780873494533.

[6] C. Orzel, *"A Brief History of Timekeeping: The Science of Marking Time, from Stonehenge to Atomic Clocks"*, Oneworld Publications, 2022, ISBN: 9780861542154.

[7] D. Rooney, *"About Time: A History of Civilization in Twelve Clocks"*, Penguin Books Limited, 2021, ISBN: 9780241985403.

[8] C. Vincent, J. Leopold, and E. Sullivan, *"European Clocks and Watches in The Metropolitan Museum of Art"*, Fashion Studies, Metropolitan Museum Of Art, 2015, ISBN: 9781588395795.

[9] the International earth rotation and reference systems service, *Earth orientation data*, tech. rep., IERS, 2024, URL: https://www.iers.org/IERS/EN/DataProducts/EarthOrientationData/eop.html.

[10] J. W. Wells, *"Coral Growth and Geochronometry"*, Nature **197**, 948, 1963, DOI: 10.1038/197948a0.

[11] K. E. Wojciechowski, M. S. Baker, P. J. Clews, and R. H. Olsson, *"A Fully Integrated Oven Controlled Microelectromechanical Oscillator—Part I: Design and Fabrication"*, Journal of Microelectromechanical Systems **24**, 1782–1794, 2015, DOI: 10.1109/JMEMS.2015.2441037.

[12] L. S. Cutler, *"Fifty years of commercial caesium clocks"*, Metrologia **42**, S90, 2005, DOI: 10.1088/0026-1394/42/3/S10.

[13] T. P. Heavner, S. R. Jefferts, E. A. Donley, J. H. Shirley, and T. E. Parker, *"NIST-F1: recent improvements and accuracy evaluations"*, Metrologia **42**, 411, 2005, DOI: 10.1088/0026-1394/42/5/012.

[14] T. P. Heavner, E. A. Donley, F. Levi, G. Costanzo, T. E. Parker, J. H. Shirley, N. Ashby, S. Barlow, and S. R. Jefferts, *"First accuracy evaluation of NIST-F2"*, Metrologia **51**, 174, 2014, DOI: 10.1088/0026-1394/51/3/174.

[15] G. W. Hoth, J. A. Sherman, A. G. Radnaev, P. Mitchell, and V. Gerginov, "NIST-F3, a cesium fountain frequency reference", *2023 Joint Meeting of International Frequency and Time Forum and IEEE International Frequency Control Symposium (IEEE/IFCS)*, 2023, DOI: https://tf.nist.gov/general/pdf/3232.pdf.

[16] T. Nicholson, S. Campbell, R. Hutson, G. Marti, B. Bloom, R. McNally, W. Zhang, M. Barrett, M. Safronova, G. Strouse, W. Tew, and J. Ye, *"Systematic evaluation of an atomic clock at* $2 \times 10^{-18}$ *total uncertainty"*, Nat. Commun. **6**, 6896, 2015, DOI: 10.1038/ncomms7896.

[17] M. Takamoto, F.-L. Hong, R. Higashi, and H. Katori, *"An optical lattice clock"*, Nature **435**, 321, 2005, DOI: 10.1038/nature03541.

[18] A. K. A. Al-Masoudi, *"A strontium lattice clock with reduced blackbody radiation shift"*, PhD thesis, University of Hannover, 2016.

[19] T. Bothwell, C. J. Kennedy, A. Aeppli, D. Kedar, J. M. Robinson, E. Oelker, A. Staron, and J. Ye, *"Resolving the gravitational redshift across a millimetre-scale atomic sample"*, Nature **602**, Article, 420–424, 2022, DOI: 10.1038/s41586-021-04349-7.

[20] N. F. Ramsey, *"A Molecular Beam Resonance Method with Separated Oscillating Fields"*, Phys. Rev. **78**, 695–699, 1950, DOI: 10.1103/PhysRev.78.695.

[21] L. Maleki, *"Introduction To The Special Issue On The Dick Effect"*, IEEE Transactions on Ultrasonics, Ferroelectrics, and Frequency Control **45**, 876–876, 1998, DOI: 10.1109/TUFFC.1998.710542.

[22] S. Häfner, S. Falke, C. Grebing, S. Vogt, T. Legero, M. Merimaa, C. Lisdat, and U. Sterr, *"*$8 \times 10^{-17}$ *fractional laser frequency instability with a long room-temperature cavity"*, Opt. Lett. **40**, 2112–2115, 2015, DOI: 10.1364/OL.40.002112.

[23] S. A. Diddams, K. Vahala, and T. Udem, *"Optical frequency combs: Coherently uniting the electromagnetic spectrum"*, Science **369**, eaay3676, 2020, DOI: 10.1126/science.aay3676.

[24] W. Zhang, J. M. Robinson, L. Sonderhouse, E. Oelker, C. Benko, J. L. Hall, T. Legero, D. G. Matei, F. Riehle, U. Sterr, and J. Ye, *"Ultrastable Silicon Cavity in a Continuously Operating Closed-Cycle Cryostat at 4 K"*, Phys. Rev. Lett. **119**, 243601, 2017, DOI: 10.1103/PhysRevLett.119.243601.

[25] D. G. Matei, T. Legero, S. Häfner, C. Grebing, R. Weyrich, W. Zhang, L. Sonderhouse, J. M. Robinson, J. Ye, F. Riehle, and U. Sterr, *"1.5 μm Lasers with Sub-10 mHz Linewidth"*, Phys. Rev. Lett. **118**, 263202, 2017, DOI: 10.1103/PhysRevLett.118.263202.

[26] G. D. Cole, W. Zhang, J. Martin Michael J.and Ye, and M. Aspelmeyer, *"Tenfold reduction of Brownian noise in high-reflectivity optical coatings"*, Nature Photonics **7**, 644, 2013, DOI: 10.1038/nphoton.2013.174.

[27] J. Yu, S. Häfner, T. Legero, S. Herbers, D. Nicolodi, C. Y. Ma, F. Riehle, U. Sterr, D. Kedar, J. M. Robinson, E. Oelker, and J. Ye, *"Excess Noise and Photoinduced Effects in Highly Reflective Crystalline Mirror Coatings"*, Phys. Rev. X **13**, 041002, 2023, DOI: 10.1103/PhysRevX.13.041002.

[28] N. O. Zhadnov, K. S. Kudeyarov, D. S. Kryuchkov, G. A. Vishnyakova, K. Y. Khabarova, and N. N. Kolachevsky, *"48-cm-long room-temperature cavities in vertical and horizontal orientations for Sr optical clock"*, Appl. Opt. **60**, 9151–9159, 2021, DOI: 10.1364/AO.437473.

[29] T. Grogan, C.-C. Chen, D. Nicolodi, X. Zhang, Y. Hassan, J. Siegel, W. McGrew, and A. Ludlow, "A High Finesse Cryogenic Sapphire Cavity for Ytterbium Optical Atomic Clocks", APS Division of Atomic and Molecular Physics Meeting 2022, 2022.

[30] QuantXLabs, *CryoClock*, tech. rep., QuantXLabs, 2023, URL: https://quantxlabs.com/capabilities/products/cryoclock/.

[31] B. J. Bloom, T. L. Nicholson, J. R. Williams, S. L. Campbell, M. Bishof, X. Zhang, W. Zhang, S. L. Bromley, and J. Ye, *"An optical lattice clock with accuracy and stability at the $10^{-18}$ level"*, Nature **506**, 71–75, 2014, DOI: 10.1038/nature12941.

[32] S. Zhou, *"Digital servo system based on FPGA"*, MA thesis, Institute of quantum electronics, Peking University, China, 2016.

[33] J. Lodewyck, P. G. Westergaard, and P. Lemonde, *"Nondestructive measurement of the transition probability in a Sr optical lattice clock"*, Phys. Rev. A **79**, 061401, 2009, DOI: 10.1103/PhysRevA.79.061401.

[34] G. W. Biedermann, K. Takase, X. Wu, L. Deslauriers, S. Roy, and M. A. Kasevich, *"Zero-Dead-Time Operation of Interleaved Atomic Clocks"*, Phys. Rev. Lett. **111**, 170802, 2013, DOI: 10.1103/PhysRevLett.111.170802.

[35] H. Katori, *"Longitudinal Ramsey spectroscopy of atoms for continuous operation of optical clocks"*, Applied Physics Express **14**, 072006, 2021, DOI: 10.35848/1882-0786/ac0e16.

[36] S. Cook, T. Rosenband, and D. R. Leibrandt, *"Laser-Frequency Stabilization Based on Steady-State Spectral-Hole Burning in* $Eu^{3+} : Y_2SiO_5$*"*, Phys. Rev. Lett. **114**, 253902, 2015, DOI: 10.1103/PhysRevLett.114.253902.

[37] P. V., T. Y., and D. N., "Frequency Stability Improvement of an Active Hydrogen Maser with a Single-State Selection System", *2021 Joint Conference of the European Frequency and Time Forum and IEEE International Frequency Control Symposium (EFTF/IFCS)*, 2021, pp. 1–4, DOI: 10.1109/EFTF/IFCS52194.2021.9604270.

[38] J. Chen, *"Active optical clock"*, Chin. Sci. Bull. **54**, 348–352, 2009, ISSN: 1861-9541, DOI: 10.1007/s11434-009-0073-y.

[39] D. Meiser and M. J. Holland, *"Steady-state superradiance with alkaline-earth-metal atoms"*, Phys. Rev. A **81**, 033847, 2010, DOI: 10.1103/PhysRevA.81.033847.

[40] R. H. Dicke, *"Coherence in Spontaneous Radiation Processes"*, Phys. Rev. **93**, 99–110, 1954, DOI: 10.1103/PhysRev.93.99.

[41] J. G. Bohnet, Z. Chen, J. M. Weiner, D. Meiser, M. J. Holland, and J. K. Thompson, *"A steady-state superradiant laser with less than one intracavity photon"*, Nature **484**, 78–81, 2012, DOI: 10.1038/nature10920.

[42] M. A. Norcia, M. N. Winchester, J. R. K. Cline, and J. K. Thompson, *"Superradiance on the millihertz linewidth strontium clock transition"*, Sci. Adv. **2**, e1601231, 2016, DOI: 10.1126/sciadv.1601231.

[43] J. Kim, D. Yang, S.-h. Oh, and K. An, *"Coherent single-atom superradiance"*, Science **359**, 662, 2018, DOI: 10.1126/science.aar2179.

[44] T. Laske, H. Winter, and A. Hemmerich, *"Pulse Delay Time Statistics in a Superradiant Laser with Calcium Atoms"*, Phys. Rev. Lett. **123**, 103601, 2019, DOI: 10.1103/PhysRevLett.123.103601.

[45] S. L. Kristensen, E. Bohr, J. Robinson-Tait, T. Zelevinsky, J. W. Thomsen, and J. H. Müller, *"Subnatural Linewidth Superradiant Lasing with Cold* $^{88}$Sr *Atoms"*, Phys. Rev. Lett. **130**, 223402, 2023, DOI: 10.1103/PhysRevLett.130.223402.

[46] A. Goban, C.-L. Hung, J. D. Hood, S.-P. Yu, J. A. Muniz, O. Painter, and H. J. Kimble, *"Superradiance for Atoms Trapped along a Photonic Crystal Waveguide"*, Phys. Rev. Lett. **115**, 063601, 2015, DOI: 10.1103/PhysRevLett.115.063601.

[47] S. Okaba, D. Yu, L. Vincetti, F. Benabid, and H. Katori, *"Superradiance from lattice-confined atoms inside hollow core fibre"*, Communications Physics **2**, 136, 2019, DOI: 10.1038/s42005-019-0237-2.

[48] H. Keßler, J. Klinder, M. Wolke, and A. Hemmerich, *"Steering Matter Wave Superradiance with an Ultranarrow-Band Optical Cavity"*, Phys. Rev. Lett. **113**, 070404, 2014, DOI: 10.1103/PhysRevLett.113.070404.

[49] M. A. Norcia, R. J. Lewis-Swan, J. R. K. Cline, B. Zhu, A. M. Rey, and J. K. Thompson, *"Cavity-mediated collective spin-exchange interactions in a strontium superradiant laser"*, Science **361**, 259, 2018, DOI: 10.1126/science.aar3102.

[50] M. A. Norcia, J. R. K. Cline, J. A. Muniz, J. M. Robinson, R. B. Hutson, A. Goban, G. E. Marti, J. Ye, and J. K. Thompson, *"Frequency Measurements of Superradiance from the Strontium Clock Transition"*, Phys. Rev. X **8**, 021036, 2018, DOI: 10.1103/PhysRevX.8.021036.

[51] S. Bennetts, C.-C. Chen, B. Pasquiou, and F. Schreck, *"Steady-State Magneto-Optical Trap with 100-Fold Improved Phase-Space Density"*, Phys. Rev. Lett. **119**, 223202, 2017, DOI: 10.1103/PhysRevLett.119.223202.

[52] C.-C. Chen, S. Bennetts, R. González Escudero, F. Schreck, and B. Pasquiou, *"Sisyphus optical lattice decelerator"*, Phys. Rev. A **100**, 023401, 2019, DOI: 10.1103/PhysRevA.100.023401.

[53] R. G. Escudero, C.-C. Chen, S. Bennetts, B. Pasquiou, and F. Schreck, *"Steady-state magneto-optical trap of fermionic strontium on a narrow-line transition"*, Phys. Rev. Res. **3**, 033159, 2021, DOI: 10.1103/PhysRevResearch.3.033159.

[54] C.-C. Chen, R. G. Escudero, J. Minář, B. Pasquiou, S. Bennetts, and F. Schreck, *"Continuous Bose Einstein condensation"*, Nature **606**, 683–687, 2022, DOI: 10.1038/s41586-022-04731-z.

[55] C.-C. Chen, *"An atomic marble run to unity phase-space density"*, PhD thesis, Institute of Physics, University of Amsterdam, The Netherlands, 2019.

[56] S. Bennetts, *"1000 times closer to a continuous atom laser: Steady-state strontium with unity phase-space density"*, PhD thesis, Institute of Physics, University of Amsterdam, The Netherlands, 2019.

[57] J. R. K. Cline, *"Continuous Collective Strong Coupling Between Atoms and a High Finesse Cavity on a Forbidden Optical Transition"*, PhD thesis, University of Colorado, 2021.

[58] M. Hauden, M. Matsuko, F. Ponciano-Ojeda, J. E. Badawi, C. Rivera-Aguilar, and D. M., "Fabry Perot cavity for ytterbium based superradiant laser", *2022 Les Houches School - From Basics to Applications of Optical Fiber Links and Frequency Combs*, 2022, URL: https://www.houches-school-physics.com/program/program-2022/from-basics-to-applications-of-optical-fiber-links-and-frequency-combs-938385.kjsp.

[59] M. Bober, S. Bilicki, G. Kazakov, A. Gogyan, D. Kovacic, A. Ledzinski, P. Morzynski, M. Naroznik, M. Witkowski, O. Vartehparvar, M. Zarei, and M. Zawada, "Superradiant Active Atomic Clock at UMK", *2022 Joint Conference of the European Frequency and Time Forum and IEEE International Frequency Control Symposium (EFTF/IFCS)*, 2022, pp. 1–2, DOI: 10.1109/EFTF/IFCS54560.2022.9850669.

[60] B. Laburthe-Tolra, Z. Amodjee, B. Pasquiou, and M. Robert-de-Saint-Vincent, *"Correlations and linewidth of the atomic beam continuous superradiant laser"*, SciPost Phys. Core **6**, 015, 2023, DOI: 10.21468/SciPostPhysCore.6.1.015.

[61] T. Shi, J. Miao, J. Zhang, and J. Chen, *"Active optical clock lasing on the Cs 7S1/2-6P3/2 transition under a weak magnetic field"*, Frontiers in Physics **10** 2022, ISSN: 2296-424X, DOI: 10.3389/fphy.2022.967255.

[62] D. Pan, B. Arora, Y.-m. Yu, B. K. Sahoo, and J. Chen, *"Optical-lattice-based Cs active clock with a continual superradiant lasing signal"*, Phys. Rev. A **102**, 041101, 2020, DOI: 10.1103/PhysRevA.102.041101.

[63] R. Takeuchi, H. Chiba, S. Okaba, M. Takamoto, S. Tsuji, and H. Katori, *"Continuous outcoupling of ultracold strontium atoms combining three different traps"*, Applied Physics Express **16**, 042003, 2023, DOI: 10.35848/1882-0786/accb3c.

[64] X. Zheng, J. Dolde, M. C. Cambria, H. M. Lim, and S. Kolkowitz, *"A lab-based test of the gravitational redshift with a miniature clock network"*, Nature Communications **14**, Article, 4886, 2023, DOI: 10.1038/s41467-023-40629-8.

[65] R. J. Glauber and F. Haake, *"Superradiant pulses and directed angular momentum states"*, Phys. Rev. A **13**, 357–366, 1976, DOI: 10.1103/PhysRevA.13.357.

[66] M. Gross and S. Haroche, *"Superradiance: An essay on the theory of collective spontaneous emission"*, Phys. Rep. **93**, 301–396, 1982, ISSN: 0370-1573, DOI: 10.1016/0370-1573(82)90102-8.

[67] D. Meiser, J. Ye, D. R. Carlson, and M. J. Holland, *"Prospects for a Millihertz-Linewidth Laser"*, Phys. Rev. Lett. **102**, 163601, 2009, DOI: 10.1103/PhysRevLett.102.163601.

[68] D. A. Tieri, M. Xu, and M. D. C. J. H. M. J., *"Theory of the crossover from lasing to steady state superradiance"*, arXiv:1702.04830 2017.

[69] K. Debnath, Y. Zhang, and K. Mølmer, *"Lasing in the superradiant crossover regime"*, Phys. Rev. A **98**, 063837, 2018, DOI: 10.1103/PhysRevA.98.063837.

[70] E. Jaynes and F. Cummings, *"Comparison of quantum and semiclassical radiation theories with application to the beam maser"*, Proceedings of the IEEE **51**, 89–109, 1963, DOI: 10.1109/PROC.1963.1664.

[71] K. Hepp and E. H. Lieb, *"On the superradiant phase transition for molecules in a quantized radiation field: the dicke maser model"*, Annals of Physics **76**, 360–404, 1973, ISSN: 0003-4916, DOI: https://doi.org/10.1016/0003-4916(73)90039-0.

[72] M. Tavis and F. W. Cummings, *"Exact Solution for an N-Molecule—Radiation-Field Hamiltonian"*, Phys. Rev. **170**, 379–384, 1968, DOI: 10.1103/PhysRev.170.379.

[73] M. Xu, *"Theory of steady-state superradiance"*, PhD thesis, JILA, University of Colorado, 2016.

[74] R. Kubo, *"Generalized Cumulant Expansion Method"*, Journal of the Physical Society of Japan **17**, 1100–1120, 1962, DOI: 10.1143/JPSJ.17.1100.

[75] M. M. Boyd, T. Zelevinsky, A. D. Ludlow, S. M. Foreman, S. Blatt, T. Ido, and J. Ye, *"Optical Atomic Coherence at the 1-Second Time Scale"*, Science **314**, 1430–1433, 2006, DOI: 10.1126/science.1133732.

[76] A. D. Ludlow *et al.*, *"Sr Lattice Clock at 1 × 10<sup>–16</sup> Fractional Uncertainty by Remote Optical Evaluation with a Ca Clock"*, Science **319**, 1805–1808, 2008, DOI: 10.1126/science.1153341.

[77] A. Rey, A. Gorshkov, C. Kraus, M. Martin, M. Bishof, M. Swallows, X. Zhang, C. Benko, J. Ye, N. Lemke, and A. Ludlow, *"Probing many-body interactions in an optical lattice clock"*, Annals of Physics **340**, 311–351, 2014, ISSN: 0003-4916, DOI: https://doi.org/10.1016/j.aop.2013.11.002.

[78] M. Escudero *et al.*, *"Design of continuous mHz-line clock apparatus"*, 2021, URL: https://cordis.europa.eu/project/id/820404/results.

[79] G. A. Kazakov and T. Schumm, *"Active optical frequency standard using sequential coupling of atomic ensembles"*, Phys. Rev. A **87**, 013821, 2013, DOI: 10.1103/PhysRevA.87.013821.

[80] C.-C. Chen, S. Bennetts, R. G. Escudero, B. Pasquiou, and F. Schreck, *"Continuous Guided Strontium Beam with High Phase-Space Density"*, Phys. Rev. Appl. **12**, 044014, 2019, DOI: 10.1103/PhysRevApplied.12.044014.

[81] M. B. Gray, D. A. Shaddock, C. C. Harb, and H.-A. Bachor, *"Photodetector designs for low-noise, broadband, and high-power applications"*, Review of Scientific Instruments **69**, 3755–3762, 1998, ISSN: 0034-6748, DOI: 10.1063/1.1149175.

[82] M. Bishof, M. J. Martin, M. D. Swallows, C. Benko, Y. Lin, G. Quéméner, A. M. Rey, and J. Ye, *"Inelastic collisions and density-dependent excitation suppression in a 87Sr optical lattice clock"*, Phys. Rev. A **84**, 052716, 2011, DOI: 10.1103/PhysRevA.84.052716.

[83] J. He, B. Pasquiou, R. G. Escudero, S. Zhou, M. Borkowski, and F. Schreck, *"Coherent Three-Photon Excitation of the Strontium Clock Transition"*, arXiv:2406.07530 2024.

[84] A. Traverso, R. Chakraborty, Y. N. Martinez de Escobar, P. G. Mickelson, S. B. Nagel, M. Yan, and T. C. Killian, *"Inelastic and elastic collision rates for triplet states of ultracold strontium"*, Phys. Rev. A **79**, 060702, 2009, DOI: 10.1103/PhysRevA.79.060702.

[85] P. Halder, H. Winter, and A. Hemmerich, *"Inelastic collisions of optically trapped metastable calcium atoms"*, Phys. Rev. A **88**, 063639, 2013, DOI: 10.1103/PhysRevA.88.063639.

[86] T. Hosoya, R. Inoue, T. Sato, and M. Kozuma, *"High-flux cold ytterbium atomic beam source using two-dimensional laser cooling with intercombination transition"*, Optics Communications **528**, 129048, 2023, ISSN: 0030-4018, DOI: https://doi.org/10.1016/j.optcom.2022.129048.

[87] T. Na Narong, T. Liu, N. Raghuram, and L. Hollberg, *"Stimulated slowing of Yb atoms on the narrow $^1S_0 \rightarrow {}^3P_1$ transition"*, Phys. Rev. A **104**, 053117, 2021, DOI: 10.1103/PhysRevA.104.053117.

[88] C.-C. Chen, J. L. S. Siegel, B. D. Hunt, T. Grogan, Y. S. Hassan, K. Beloy, K. Gibble, R. C. Brown, and A. D. Ludlow, *"Clock-line-mediated Sisyphus Cooling"*, arXiv:2406.13782 2024.

[89] A. Yamaguchi, M. S. Safronova, K. Gibble, and H. Katori, *"Narrow-line Cooling and Determination of the Magic Wavelength of Cd"*, Phys. Rev. Lett. **123**, 113201, 2019, DOI: 10.1103/PhysRevLett.123.113201.

[90] S. Herbers, S. Dörscher, E. Benkler, and C. Lisdat, *"Phase noise of frequency doublers in optical clock lasers"*, Opt. Express **27**, 23262–23273, 2019, DOI: 10.1364/OE.27.023262.

[91] H. Liu, *"Superradiant Atomic Beam Laser"*, PhD thesis, JILA, University of Colorado, USA, 2021.

[92] X. Zhou, X. Xu, X. Chen, and J. Chen, *"Magic wavelengths for terahertz clock transitions"*, Phys. Rev. A **81**, 012115, 2010, DOI: 10.1103/PhysRevA.81.012115.

[93] S. Bennetts *et al.*, *"Design of vacuum assembly for the compact, continuous superradiant clock"*, 2021, URL: https://cordis.europa.eu/project/id/820404/results.

[94] S. Bennetts *et al.*, *"Demonstration: Vacuum assembly for the compact, continuous superradiant clock"*, 2021, URL: https://cordis.europa.eu/project/id/820404/results.

[95] S. A. Schäfter, S. Bennetts, C. B. Silva, F. Famà, M. Tang, S. Zhou, F. Schreck, and J. H. Müller, *"Article benchmarking compact, continuous superradiant clock"*, 2023, URL: https://cordis.europa.eu/project/id/820404/results.

[96] Y. D. Chong, L. Ge, H. Cao, and A. D. Stone, *"Coherent Perfect Absorbers: Time-Reversed Lasers"*, Phys. Rev. Lett. **105**, 053901, 2010, DOI: 10.1103/PhysRevLett.105.053901.

[97] W. Wan, Y. Chong, L. Ge, H. Noh, A. D. Stone, and H. Cao, *"Time-Reversed Lasing and Interferometric Control of Absorption"*, Science **331**, 889–892, 2011, DOI: 10.1126/science.1200735.

[98] Y. D. Chong, L. Ge, H. Cao, and A. D. Stone, *"Coherent Perfect Absorbers: Time-Reversed Lasers"*, Phys. Rev. Lett. **105**, 053901, 2010, DOI: 10.1103/PhysRevLett.105.053901.

[99] A. Müllers, B. Santra, C. Baals, J. Jiang, J. Benary, R. Labouvie, D. A. Zezyulin, V. V. Konotop, and H. Ott, *"Coherent perfect absorption of nonlinear matter waves"*, Science Advances **4**, eaat6539, 2018, DOI: 10.1126/sciadv.aat6539.

[100] M. Tang, *"Superradiant Lasers Based on Strontium-88"*, PhD thesis, Niels Bohr Institute, 2022.

[101] D. J. Thompson and R. E. Scholten, *"Narrow linewidth tunable external cavity diode laser using wide bandwidth filter"*, Review of Scientific Instruments **83**, 023107, 2012, ISSN: 0034-6748, DOI: 10.1063/1.3687441.

[102] D. R. Leibrandt, M. J. Thorpe, M. Notcutt, R. E. Drullinger, T. Rosenband, and J. C. Bergquist, *"Spherical reference cavities for frequency stabilization of lasers in non-laboratory environments"*, Opt. Express **19**, 3471–3482, 2011, DOI: 10.1364/OE.19.003471.

[103] F. Vogl, *"Building a strontium clock laser"*, MA thesis, University of Innsbruck, Austria, 2013.

[104] J. Ye, L. S. Ma, and J. L. Hall, *"Ultrasensitive detections in atomic and molecular physics: demonstration in molecular overtone spectroscopy"*, J. Opt. Soc. Am. B **15**, 6–15, 1998, DOI: 10.1364/JOSAB.15.000006.

[105] E. Staub, *"Developing a High-Flux Atomic Beam Source for Experiments with Ultracold Strontium Quantum Gases"*, PhD thesis, Ludwig Maximilian University of Munich, 2019.

[106] M. Schioppo, N. Poli, M. Prevedelli, S. Falke, C. Lisdat, U. Sterr, and G. M. Tino, *"A compact and efficient strontium oven for laser-cooling experiments"*, Review of Scientific Instruments **83**, 103101, 2012, ISSN: 0034-6748, DOI: 10.1063/1.4756936.

[107] S. Stellmer, *"Degenerate quantum gases of strontium"*, PhD thesis, Institute of Experimental Physics, University of Innsbruck, Austria, 2013.

[108] M. A. Norcia, J. R. K. Cline, J. P. Bartolotta, M. J. Holland, and J. K. Thompson, *"Narrow-line laser cooling by adiabatic transfer"*, New J. Phys. **20**, 023021, 2018, DOI: 10.1088/1367-2630/aaa950.

[109] Z. X. Ye, L. Y. Xie, Z. Guo, X. B. Ma, G. R. Wang, L. You, and M. K. Tey, *"Double-degenerate Bose-Fermi mixture of strontium and lithium"*, Phys. Rev. A **102**, 033307, 2020, DOI: 10.1103/PhysRevA.102.033307.

[110] J. Huckans, W. Dubosclard, E. Maréchal, O. Gorceix, B. Laburthe-Tolra, and M. Robert-de-Saint-Vincent, *"Note on the reflectance of mirrors exposed to a strontium beam"*, 2018, arXiv: 1802.08499, URL: https://arxiv.org/abs/1802.08499.

[111] E. Peik, M. Ben Dahan, I. Bouchoule, Y. Castin, and C. Salomon, *"Bloch oscillations and an accelerator for cold atoms"*, Applied Physics B, 685, 1997, DOI: 10.1007/s003400050334.

[112] T. Akatsuka, K. Hashiguchi, T. Takahashi, N. Ohmae, M. Takamoto, and H. Katori, *"Three-stage laser cooling of Sr atoms using the* $5s5p^3P_2$ *metastable state below Doppler temperatures"*, Phys. Rev. A **103**, 023331, 2021, DOI: 10.1103/PhysRevA.103.023331.

[113] R. Hobson, W. Bowden, A. Vianello, I. R. Hill, and P. Gill, *"Midinfrared magneto-optical trap of metastable strontium for an optical lattice clock"*, Phys. Rev. A **101**, 013420, 2020, DOI: 10.1103/PhysRevA.101.013420.

[114] S. Okaba, R. Takeuchi, S. Tsuji, and H. Katori, *"Continuous generation of an ultracold atomic beam using crossed moving optical lattices"*, Phys. Rev. Appl. **21**, 034006, 2024, DOI: 10.1103/PhysRevApplied.21.034006.

[115] O. Brzobohatý, T. Čižmár, and P. Zemánek, *"High quality quasi-Bessel beam generated by round-tip axicon"*, Opt. Express **16**, 12688–12700, 2008, DOI: 10.1364/OE.16.012688.

[116] S. Dubey, G. A. Kazakov, B. Heizenreder, S. Zhou, S. Bennetts, S. A. Schäffer, A. Sitaram, and F. Schreck, *"Modeling of a continuous superradiant laser on the sub-mHz 1S0-3P0 transition in neutral strontium-88"*, arXiv:2409.06575 2024.

[117] D. D. Brown and A. Freise, *Finesse*, 2014, DOI: 10.5281/zenodo.821363, URL: http://www.gwoptics.org/finesse.

[118] M. M. Boyd, *"High Precision Spectroscopy of Strontium in an Optical Lattice: Towards a New Standard for Frequency and Time"*, PhD thesis, JILA, University of Colorado, 2007.

[119] M. A. Norcia, *"New tools for precision measurement and quantum science with narrow linewidth optical transitions"*, PhD thesis, University of Colorado Boulder, 2017.

[120] G. Kazakov, S. Dubey, F. Famà, S. Zhou, C. Silva, S. Schäfter, S. Bennetts, and F. Schreck, "Towards an Active Optical Clock using an Optical Conveyor within a Ring Cavity", *2021 Joint Conference of the European Frequency and Time Forum and IEEE International Frequency Control Symposium (EFTF/IFCS)*, 2021, pp. 1–5, DOI: 10.1109/EFTF/IFCS52194.2021.9604232.

[121] H. Katori, T. Ido, Y. Isoya, and M. Kuwata-Gonokami, *"Magneto-Optical Trapping and Cooling of Strontium Atoms down to the Photon Recoil Temperature"*, Phys. Rev. Lett. **82**, 1116–1119, 1999, DOI: 10.1103/PhysRevLett.82.1116.

[122] P. Zorabedian and W. R. Trutna, *"Interference-filter-tuned, alignment-stabilized, semiconductor external-cavity laser"*, Opt. Lett. **13**, 826–828, 1988, DOI: 10.1364/OL.13.000826.

[123] S. D. Saliba, M. Junker, L. D. Turner, and R. E. Scholten, *"Mode stability of external cavity diode lasers"*, Appl. Opt. **48**, 6692–6700, 2009, DOI: 10.1364/AO.48.006692.

[124] E. H. Chang, J. Rivera, B. Bostwick, C. Schneider, P. Yu, E. R. Hudson, and H. Collaboration, *"Low-drift-rate external cavity diode laser"*, Review of Scientific Instruments **94**, 043001, 2023, ISSN: 0034-6748, DOI: 10.1063/5.0079210.

[125] S. Subhankar, A. Restelli, Y. Wang, S. L. Rolston, and J. V. Porto, *"Microcontroller based scanning transfer cavity lock for long-term laser frequency stabilization"*, Review of Scientific Instruments **90**, 043115, 2019, ISSN: 0034-6748, DOI: 10.1063/1.5067266.

[126] M. Takamoto, Y. Tanaka, and H. Katori, *"A perspective on the future of transportable optical lattice clocks"*, Applied Physics Letters **120**, 140502, 2022, ISSN: 0003-6951, DOI: 10.1063/5.0087894.

[127] N. Ohmae *et al.*, *"Transportable Strontium Optical Lattice Clocks Operated Outside Laboratory at the Level of 10-18 Uncertainty"*, Advanced Quantum Technologies **4**, 2100015, 2021, DOI: https://doi.org/10.1002/qute.202100015.

[128] S. Vogt, S. Haefner, J. Grotti, S. Koller, A. Al-Masoudi, U. Sterr, and C. Lisdat, *"A transportable optical lattice clock"*, Journal of Physics: Conference Series **723**, 012020, 2016, DOI: 10.1088/1742-6596/723/1/012020.

[129] V. Ménoret, P. Vermeulen, N. Le Moigne, S. Bonvalot, P. Bouyer, A. Landragin, and B. Desruelle, *"Gravity measurements below 1 over 1e8 g with a transportable absolute quantum gravimeter"*, Scientific Reports **8**, 12300, 2018, DOI: 10.1038/s41598-018-30608-1.

[130] V. Ménoret, R. Geiger, G. Stern, P. Cheinet, B. Battelier, N. Zahzam, F. Pereira dos Santos, A. Bresson, A. Landragin, and P. Bouyer, "A transportable cold atom inertial sensor for space applications", *International Conference on Space Optics*, Rhodes, Greece, 2010, p. 1, DOI: 10.1117/12.2309256.

[131] C. G. Townsend, N. H. Edwards, C. J. Cooper, K. P. Zetie, C. J. Foot, A. M. Steane, P. Szriftgiser, H. Perrin, and J. Dalibard, *"Phase-space density in the magneto-optical trap"*, Phys. Rev. A **52**, 1423–1440, 1995, DOI: 10.1103/PhysRevA.52.1423.

[132] R. K. Hanley, P. Huillery, N. C. Keegan, A. D. Bounds, D. Boddy, R. Faoro, and M. P. A. Jones, *"Quantitative simulation of a magneto-optical trap operating near the photon recoil limit"*, Journal of Modern Optics **65**, 667–676, 2018, DOI: 10.1080/09500340.2017.1401679.

[133] K. Van Tilburg, N. Leefer, L. Bougas, and D. Budker, *"Search for Ultralight Scalar Dark Matter with Atomic Spectroscopy"*, Phys. Rev. Lett. **115**, 011802, 2015, DOI: 10.1103/PhysRevLett.115.011802.

[134] D. Barberena, R. J. Lewis-Swan, A. M. Rey, and J. K. Thompson, *"Ultra narrow linewidth frequency reference via measurement and feedback"*, Comptes Rendus. Physique **24**, 55–68, 2023, DOI: 10.5802/crphys.146.

[135] P. Domokos and H. Ritsch, *"Collective Cooling and Self-Organization of Atoms in a Cavity"*, Phys. Rev. Lett. **89**, 253003, 2002, DOI: 10.1103/PhysRevLett.89.253003.

[136] C. Hotter, D. Plankensteiner, L. Ostermann, and H. Ritsch, *"Superradiant cooling, trapping, and lasing of dipole-interacting clock atoms"*, Opt. Express **27**, 31193–31206, 2019, DOI: 10.1364/OE.27.031193.

[137] G. Nemova and R. Kashyap, *"Alternative technique for laser cooling with superradiance"*, Phys. Rev. A **83**, 013404, 2011, DOI: 10.1103/PhysRevA.83.013404.

[138] M. O. Scully and A. A. Svidzinsky, *"The Super of Superradiance"*, Science **325**, 1510–1511, 2009, DOI: 10.1126/science.1176695.

[139] A. Delhom, K. Guerrero, P. Calizaya Cabrera, K. Falque, A. Bramati, A. J. Brady, M. J. Jacquet, and I. Agullo, *"Entanglement from superradiance and rotating quantum fluids of light"*, Phys. Rev. D **109**, 105024, 2024, DOI: 10.1103/PhysRevD.109.105024.

[140] B. Sundar, D. Barberena, A. M. Rey, and A. P. Orioli, *"Squeezing Multilevel Atoms in Dark States via Cavity Superradiance"*, Phys. Rev. Lett. **132**, 033601, 2024, DOI: 10.1103/PhysRevLett.132.033601.

[141] K. Hayashida, T. Makihara, N. Marquez Peraca, D. Fallas Padilla, H. Pu, J. Kono, and M. Bamba, *"Perfect intrinsic squeezing at the superradiant phase transition critical point"*, Scientific Reports **13**, 2526, 2023, DOI: 10.1038/s41598-023-29202-x.

[142] S. B. Jäger, H. Liu, J. Cooper, and M. J. Holland, *"Collective emission of an atomic beam into an off-resonant cavity mode"*, Phys. Rev. A **104**, 053705, 2021, DOI: 10.1103/PhysRevA.104.053705.

[143] S. B. Jäger, H. Liu, J. Cooper, T. L. Nicholson, and M. J. Holland, *"Superradiant emission of a thermal atomic beam into an optical cavity"*, Phys. Rev. A **104**, 033711, 2021, DOI: 10.1103/PhysRevA.104.033711.

# List of publications

## •Peer-reviewed publications

**Towards an active optical clock using an optical conveyor within a ring cavity** (related to Chapter 4)

G. Kazakov, S. Dubey, F. Famà, S. Zhou, C. Beli Silva, S. A. Schäffer, S. Bennetts, and F. Schreck, 2021 Joint Conference of the European Frequency and Time Forum and IEEE International Frequency Control Symposium (EFTF/IFCS), Gainesville, FL, USA, 2021, pp. 1-5, DOI: 10.1109/EFTF/IFCS52194.2021.9604232.

Contributions: I participated in designing the experimental part, performing simulations, and discussing the results.

## •Publications submitted for peer review

**Coherent three-photon excitation of the strontium clock transition**

J. He, B. Pasquiou, R. Escudero González, S. Zhou, M. Borkowski, and F. Schreck, arXiv:2406.07530, DOI: https://arxiv.org/abs/2406.07530

Contributions: I assisted in the operation of the machine, analysis of results, design of experiments, and construction of hardware components.

**Continuous cavity-QED with an atomic beam** (related to Chapter 3)

F. Famà, S. Zhou, B. Heizenreder, M. Tang, S. Bennetts, S. B. Jäger, S. A. Schäffer, and F. Schreck, arXiv:2407.18668, DOI: https://arxiv.org/abs/2407.18668

Contributions: I participated in developing the initial experimental design, constructing the apparatus, and working on the initial debugging of the experiment.

## •Non-peer reviewed publications

**iqclock D4.3: Design of vacuum assembly for the compact, continuous superradiant clock.**

URL: https://ec.europa.eu/info/funding-tenders/opportunities/grants/docs/080166e5ddd2f307/Attachment_0.pdf

Contributions: I participated in manuscript review, design, construction, debugging, characterization and analysis. A full list of authors and their contributions is listed within the publication.

**iqclock D4.4: Demonstration: Vacuum assembly for the compact, continuous superradiant clock.**
URL: https://ec.europa.eu/info/funding-tenders/opportunities/grants/docs/080166e5ddd2fca4/Attachment_0.pdf
Contributions: I participated in manuscript review, design, construction, debugging, characterization and analysis. A full list of authors and their contributions is listed within the publication.

**iqclock D4.6: Article benchmarking compact, continuous superradiant clock.**
URL: https://ec.europa.eu/info/funding-tenders/opportunities/grants/docs/080166e5f75ee8ab/Attachment_0.pdf
Contributions: I participated in construction and design. A full list of authors and their contributions is listed within the publication.

**iqclock D5.3: Design of a superradiant optical clock on the 1S0-3P0 "mHz" transition.**
URL: https://ec.europa.eu/info/funding-tenders/opportunities/grants/docs/080166e5e53b0f27/Attachment_0.pdf
Contributions: I participated in writing, design, construction, simulation and analysis. A full list of authors and their contributions is listed within the publication.

**iqclock D5.4: Demonstration: Construction of a superradiant optical clock apparatus on the 1S0-3P0 "mHz" transition.**
URL:https://ec.europa.eu/info/funding-tenders/opportunities/grants/docs/080166e5e53a909d/Attachment_0.pdf
Contributions: I participated in design, construction, simulation and analysis. A full list of authors and their contributions is listed within the publication.

## • Journal publications in preparation

**Design of a continuous superradiant laser on the $^1S_0 - {}^3P_0$ transition in neutral strontium** (working title, related to Chapter 4)

Contributions: I participated in the design and led the construction of the experiment. I performed simulations and participated in discussions of the results. I wrote the first version of the manuscript for the experimental section.

**An improved steady-state Sr red MOT for a continuous mHz superradiant clock** (working title, based on Chapter 5)

Contributions: I led the mHz project from the start of 2022 until the start of 2024, during which the machine was built and debugged. I made significant contributions to designing, simulating, and modeling the experiment, preparing materials, building and debugging the entire system, and achieving a steady-state red MOT. Additionally, I conducted measurements and presented our work at numerous local and international conferences, including the NWO AMO meetings and IEEE-IFCS 2022.

# Acknowledgements

I would like to express my heartfelt gratitude to my wife, my parents, and other relatives. I made the decision to leave my hometown and pursue studies in a distant country, not only to acquire scientific knowledge and skills but also to experience a different culture, all in pursuit of my personal aspirations. My wife, in order to reunite our family, later resigned from her job to join me here, where we work and live together. Our parents remain in China, making it even more challenging for us to meet them than when we were still in our home country. Therefore, the support from my wife, the care and understanding from my parents, and the concern from other relatives have been the driving force behind my completion of these years of work and study.

Furthermore, I would like to extend my gratitude to my supervisor, Prof. Dr. Florian Schreck. Not only did he offer me such an interesting project and a doctoral position, but I also gained a wealth of knowledge and experience in physics through learning from him. I still remember the first thing he taught me was about the importance of balancing perfection with time efficiency. When I was aligning the laser, I spent a lot of time to make it perfect. He told me that sometimes it was not necessary to pursue perfection excessively, as it may consume too much time, and the entire experiment can still run smoothly even with minor imperfections. In our regular interactions during dinners or his daily lab visit, he also taught me how to think quickly, evaluate, and make decisions. I recall a late evening when I was working on setting up the optical cavity, and he came over to ask if I had any questions to discuss. I thought I had encountered an insurmountable problem with achieving the finesse of the cavity, but he patiently listened to my analysis and pointed out the aspects

I had overlooked in measuring the scattered light from the superpolished mirror. His wealth of experience in experiments is truly admirable and worth learning from. He is also strong in theory, capable of explaining complex physics concepts in a clear and understandable manner. During one of his lectures on STIRAP, he explained the topic very clearly and simply. After my group meeting presentations, he would also provide feedback on any inaccuracies in my presentation. It's a pity that he is always so busy, and the time available for communication with him is limited. I also want to thank Irene, Florian's wife, who occasionally came to our lab and at one time helped assemble the viewports with Florian for the mHz machine.

The person I am most grateful for during these four years is my daily supervisor, Dr. Shayne Bennetts, our postdoctoral researcher. He is an exceptionally experienced experimental physicist who excels in experimental design. Like Florian, he can quickly assess the feasibility of experiments, design them, and analyze the data obtained from experiments promptly. If the conclusions differ, he will ponder why and consider whether other experiments can be designed to corroborate certain parameters. He is proficient in mechanical design; he navigates SolidWorks as effortlessly as playing a game. Both the kHz and mHz setups were designed by him, and to my knowledge, each underwent at least eight iterations. He also understands machining methods and precision, which allows him to design things that can be directly handed over to others for machining, reducing a lot of communication costs. He is adept in optics; every time I encounter optical path problems, he patiently listens to me first and then helps me analyze them. Sometimes, because I can't explain clearly, he asks me to draw on the whiteboard, which is also his preferred method because it helps him understand more clearly. If he's unclear about something, he keeps asking questions until I explain the problem clearly and then guides me step by step to find possible solutions. He also understands circuits and has modified many circuit boards for the laboratory. What I find most impressive about him is his ability to think through such complex systems clearly before even making them, to design them, and to quickly think of solutions or alternatives when

problems arise. This can be attributed to his proficiency in MATLAB and Excel, which helps him quickly analyze many quantitative relationships. In summary, he is a very impressive physics teacher to me. When he is doing experiments, he is focused and determined; he can concentrate for long periods to solve a problem. Sometimes we work late into the night, and I'm almost too tired to continue, but he still has the energy to think. In our free time, we also chat about life, our dreams, the world, almost everything and share the differences between different cultures. This has allowed me to learn much about the culture and history here. I am very grateful to have worked with him for these past few years.

In the latter part of my doctoral journey, I would like to express my sincere gratitude to Dr. Sumit Sarkar and Dr. Sławomir Bilicki. Sumit, although a postdoctoral researcher in another project, frequently engaged in discussions with me. I was willing to share my immature physics ideas with him, such as what would happen when photons reach the edge of the universe. Instead of mocking me, he not only shared with me how he approaches such questions but also explained complex physics phenomena in simple terms and deduced new ideas. Like Shayne, he holds strong principles, sticking to what he believes is right and defending it, which I admire. Sławomir, a visiting postdoctoral researcher from Poland, spent several months with our project. As a postdoc, he not only guided me but also worked hands-on together with me on the experiment. At that time, our project required additional manpower, and his presence significantly contributed to the progress of our project. Both of them are very pragmatic individuals, honest, reliable, and trustworthy.

I would also like to extend my gratitude to Francesca Famà. At the beginning, we were very close lab partners since we came to the same project almost at the same time. We worked together to build the lasers and the kHz machine. Those moments were truly wonderful. While building together, we helped each other when problems arose, and when we were tired from assembling the setup, we would take breaks together and have a drink together. During our breaks, I never had to worry about running out


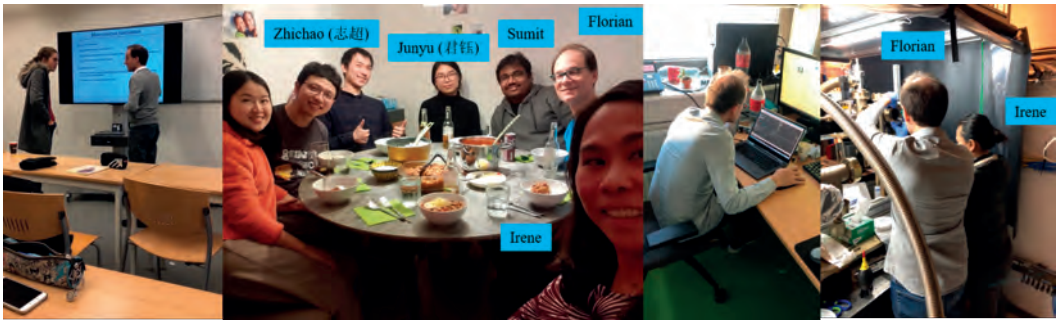


of topics to discuss because she is very talkative. I also owe a great deal of gratitude to Dr. Benjamin Pasquiou, another super-excellent postdoctoral researcher in our team. What struck me the most was his style of guidance. Whenever you ask him a question, he would in turn pose questions to you. His questions often start from the most basic known physics principles and gradually guide you to think through to answer the question you raised. When you can answer your own questions, you basically already know the answer to solving the problem. He appears very serious and often doesn't smile much, which can be intimidating. However, spending time with him, you'll find that he also tells jokes occasionally. Apart from physics, he has deep and interesting reflections on society.

I also want to express my gratitude to other members of the team, such as


FIGURE 1: Happy "workers"

another postdoctoral researcher who has since departed, Chun Chia (陈俊嘉). He often helped me with questions and clarifications. When I first joined the group, he was the only member who could chat with me in Chinese, significantly reducing communication barriers. Of course, I must also thank those who later joined me on the superradiant clock project: Ananya Sitaram, Benedikt Heizenreder, Camila Beli Silva, as well as those who have since moved on to other endeavors, such as Swadheen Dubey, Mikkel Tang, Zeyuan Zhang, and Stefan Alaric Schäffer. It was only through everyone's collective efforts that we were able to advance the implementation of the experiments.

The hot atomic beam superradiance project could be a great example of teamwork. It was a project that involved not only collaboration within our own team and the iqClock consortium but also across the world. I want to thank collaborators from other groups, especially Haonan Liu and Simon Jäger from Murray Holland's group in JILA. During the DAMOP June 2020 meeting Haonan presented the idea of using a hot atomic beam to pump a superradiant active optical clock. After the meeting, Florian, Shayne, Francesca, and I decided to try it since it seemed experimentally simple. It

offered an experimentally simple path to continuous kHz superradiance, a key goal for our iqClock consortium and a goal that now seemed impossible using the Copenhagen apparatus originally proposed. More importantly it offered a short term opportunity to get some high impact publications while we worked towards the long term goal of an active optical clock using the mHz clock transition. Haonan gave us a more detailed presentation of his work and we worked together to adapt his proposal that targeted calcium, to the 7.5 kHz $^1S_0 - ^3P_1$ transition of strontium. At the same time, our colleague Mikkel from the University of Copenhagen a partner in our iqClock consortium, cross-checked this concept with his detailed numerical simulation and proposed key parameters like the finesse of the optical cavity. I want to thank Mikkel again for his contributions and ongoing simulation support.

Experiments need dedicated effort from many people with different skills to make them come true. The experiment presented in Section 3.4 draws together so many aspects like the cooling and pumping lasers, the electronics, the vacuum system with the optical cavity, and a reference laser to name just a few. The cooling lasers with electronics (461 nm and 689 nm) were designed by Shayne, the 461 nm lasers were built by Francesca and I built the 689 nm red lasers in the first year of our PhD period. The repump lasers (679 nm, 688 nm and 707 nm) were transfer locked to an optical cavity that in turn was locked to our 689 master laser. The transfer lock cavity was reused from a former experiment. Francesca and I integrated it into a vacuum chamber under the supervision of Shayne. Then, Francesca focused on building ECDLs designed by Shayne with help from Camila on the 707 nm ECDL while I designed and built the optics and electronics for locking all the lasers to a transfer lock cavity.

We decided to focus on getting this new kHz machine going as quickly as possible. We designed and manufactured parts for the new machine in a few months. The vacuum system for the kHz superradiant clock was designed by Shayne. In particular, two key parts have been designed carefully with the advice from simulation. One part is the Sr oven with atomic flux simulations

done independently by Benjamin and Shayne. The other part is the optical cavity design supported by detailed simulations from Francesca, Mikkel and cross checked by Shayne.

Later that year three new people joined our team, Mikkel Tang, who had already helped on simulation for the project, Camila Beli, a new PhD student and Stefan Schäffer from Copenhagen who received a Danish grant to join us as a postdoc for two years. The somewhat crowded lab assembled the vacuum system (Figure 2 and 3), Mikkel worked on the finesse 100 cavity for the vacuum chamber under the supervision of Stefan and Shayne. Francesca, Camila, and I together constructed the vacuum system under supervision from Shayne with some help from Mikkel and Stefan. Meanwhile, Francesca worked on the repumper ECDLs and chamber optics, and I designed and built the repump laser locking system and later worked on the chamber optics.

Stefan and Zeyuan also focused on designing and building the reference clock laser for use as the local oscillator with help from Shayne and Camila. Camila built an 8-pass AOM for locking the cavity with help from Shayne. Francesca and Mikkel designed and built the optics around the vacuum chamber with help from all of us and later Francesca and I modified them as needed.

Just eight months after the DAMOP meeting, in the beginning of 2021, the machine construction was finished and atoms were seen in the machine, Figure 3.1(d). After that, Francesca and I worked together to debug the machine under Shayne's daily supervision and with help from other team members while Camila focused on improving the clock laser under Stefan's daily supervision. Shayne coordinated and supervised the kHz and mHz projects. By February, we had atoms in the machine and Francesca presented our work in March at DPG 2021. In April, we had frequency modulation spectroscopy signals with atoms in the cavity and I presented our work at DAMOP in June 2021. I learned a lot from the oral presentation, not only about scientific English speaking but also about physics. I especially want to thank James K. Thompson from JILA for his encouragement and


FIGURE 2: Constructing the kHz vacuum system.

openness during several interactions I was fortunate to have with him in DAMOP sessions and during the Lorentz workshop. I am grateful for his patient and clear teaching in my first encounters where he made me feel so comfortable as he explained ideas like why Doppler broadening didn't appear in the output superradiant lasing. I really appreciated his many suggestions for debugging the kHz machine after my DAMOP presentation and again his openness in discussing challenges in creating a mHz superradiant clock. Over the next few months, Francesca and I ran the machine more independently while Shayne started to focus more on the mHz machine. We measured the velocity of the atoms passing through the cavity mode and we measured a modulation. In late October, we saw the first relative "gain". A beat between the local oscillator and the resonant probe laser at the pump modulation frequency, indicating we were now able to modify

FIGURE 3: Constructing the kHz machine.

the absorption of the cavity mode as shown in Figure 4.

Since our overall objective was to build the mHz machine as well, not just the kHz machine, in October 2021 I started to spend some of my time on the mHz machine construction. In January 2022, the team was separated into the kHz project and mHz projects which I didn't expect. I had hoped that we would all continue to work together as a team on both projects but I am happy that I got to continue to work on the mHz project as that was the reason I chose this PhD project.

I led the mHz project from the start of 2022 until the start of 2024 during which the machine was built and debugged. I was the only PhD student fully working on the project with my daily supervisor Shayne. He taught me a lot about designing, simulating, and modelling the experiment. We prepared materials and built the machine. Later he moved to spend more time on another project but he continued to help along with Sumit throughout the debugging and optimizing process. Together we made the steady-state red

FIGURE 4: First "gain" from the kHz machine in October 2021, a modulation in the absorption of the cavity probe light when beat with the local oscillator.

MOT work. I also made measurements and presented our work at numerous local and international conferences, like the NWO AMO meetings and IEEE-IFCS 2022. This project was a team effort. Shayne Bennetts, Florian Schreck, and I designed the machine. Sławomir Bilicki, Shayne and Sumit Sarkar assisted with construction. The laser systems are similar to the initial version of the kHz machine, which was built by Francesca and me. Later, Benedikt, Ananya and I converted the laser system back from the kHz version and extended it to what's now used for the mHz machine. Sławomir and I built the vacuum chamber with help from Shayne and Sumit. Camila Beli helped construct some of the coils. Francesca Famà and Shayne designed the superradiant cavity and I built it with help from Benedikt Heizenreder, Camila and Shayne. Benedikt, Ananya Sitaram, and I got the blue MOT working, while Ananya and I achieved the red MOT. Shayne and I developed the smiling MOT and collected most of the data and analysis for my thesis. Benedikt and Ananya added the transverse cooling beams. We decided to delay pursuing publications to avoid undermining our ultimate goal: a continuous superradiant laser on the mHz clock transition, a significantly

more important result.

As I look back, I understand more about a Chinese phrase "三人行，必有我师焉；择其善者而从之，其不善者而改之。". I would like to thank my partners who worked so hard to make this project reality. I want to thank them for the many interesting discussions pursuing physics ideas, truth and the constant search for understanding and the optimal solution. I learned so much through this process of constant problem solving, the double checking and this really encouraged me to learn more and more. Solving problems was exciting and never failed to cheer me up even after long days and nights in the lab. When everyone worked on their sub-tasks and it all came together I felt that as a team we could achieve anything. I would also like to thank people for sharing their sometimes very different ideas as I find it interesting to try to understand and explore other cultures and viewpoints. Sometimes it was about their views on work-life balance, “don’t push yourself too much, otherwise you could end up burned out”. “If you disagree with someone or feel upset about something you should make a complaint (rather than try to discuss and resolve it)”. “Enjoying the process is more important than getting a result”. These and many other similar ideas were completely foreign to me and triggered me to think carefully about what my values should be and the way I want to do science. All of the people with their many different values and cultures within the superradiance project gave me experiences both positive and negative but certainly all those experiences gave me wisdom.

Although members of other projects in our team were not together every day, I would also like to thank Junyu He(何君钰) from the atom laser team for sharing her experience with the previous generation of the mHz machine when I was debugging it. Many times, such insights are not readily available in experimental records, but finding the right person can provide the desired information. Additionally, I want to thank Alex Urech from the optical tweezer team for his warm greetings and concerns about the progress of our experiments whenever we met, and Ivo Knottnerus for frequently sharing the progress of their experiments and teaching me some Dutch. I

am also grateful to Thies Plassmann, who once told me to cherish my time in the laboratory because it offers resources unavailable elsewhere to tackle challenging topics. Of course, I must express my gratitude to the passive clock team, including Sumit, (Batman) András Gácsbaranyi, and (superman) Scott Wolzak. Since I frequently visited their laboratory to obtain supplies, our interactions were almost daily. Whenever I fell ill and wasn't in the lab, they always noticed and warmly inquired about my well-being. Others I would like to thank include Stefano, Carla, Vincent, Sergei, Mehrdad, Anna, Jiri, Noah, Prem, Yu Chih Tseng, Digvijay, Davide, Noe, Mateusz, Simon and other teachers in our group, especially Philippe Bouyer, Klaasjan van Druten and Robert Spreeuw. I am particularly grateful to Robert; my physics foundation was not very strong, and I needed to learn a lot of knowledge for the theoretical part of my thesis. Whenever I encountered something I didn't understand during my studies, I would seek guidance from Robert. He patiently guided me to understand, and I was fortunate enough to join his quantum optics course for a more systematic learning experience. His teaching approach was very clear, and I gained a lot from each class. I would also like to thank Arghavan Safavi Naini for patiently teaching me about quantum optics and also all the people from the hybrid atom-ion group, especially Rene Gerritsma, Henrik Hirzler, Matteo Mazzanti, Zhenlin Wu, Eleanor Trimby, Ilango Maran and Liam Bond. They taught me about ions, the "other side" of atomic physics.

The people in our technology center have helped me tremendously and I deeply appreciate their knowledge and work. Whenever I need to design something mechanical, Hans Ellermeijer is the person I always turn to. He is not only experienced but also willing to share his ideas about the design, assist in drawing it, and ensure it is feasible in our mechanical workshop. Sometimes he machines the parts himself, and other times Jan Kalwij, Tristan van Klingeren, Sven Koot, or Cees Kes take on the task. They are all highly skilled mechanical engineers and craftsman. Whenever I have the opportunity to be present nearby, they are always willing to teach me how


the machines work and how to operate them. Johan Mozes from the electronic workshop has also been invaluable, helping to build many electronics projects for our machines. There are many others I would like to thank, especially Gertjan Bon, Ronald Hassing, Daan Giesen, Ronald Kortekaas and many others. I would like to thank Alix Wattjes for her management. She joined our group meetings almost every week to understand our work and our needs from the workshop, helping to communicate this information

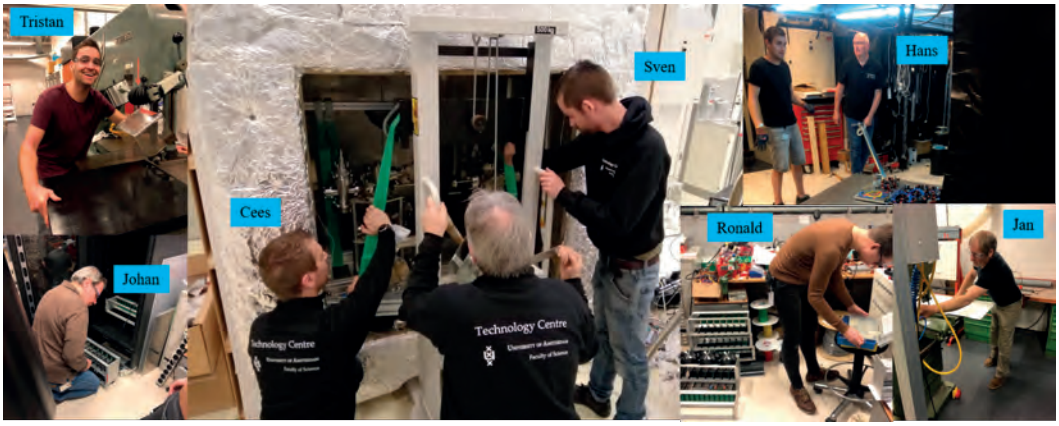


FIGURE 5: Skilled engineers

to others. Speaking of management, I would also like to thank our secretary, Jirina Salkova, who has helped me many times with documentation and administrative processes. I will also thank Rose Pham and Astrid Harryson for helping when Jirina was not there. Astrid sometimes also talks with me in Dutch helping me to learn. Talking about learning Dutch, I also want to thank my Dutch teacher Maaike. I would also like to thank Joost van Mameren for his organization for the institute. In the institute of physics, I also want to thank my independent supervisor Erik van Heumen, who gave me many suggestions when we did my evaluation.

Of course, there are many, many other wonderful people I was lucky enough to spend time with. I particularly want to thank, Panying Ji (潘应骥), a friend of 26 years who also studied at Leiden University. He arrived in the Netherlands for his PhD project earlier than I did and was a great help during my first visit to my research group. In the early days of my PhD, we spent many weekends together discussing and reflecting on the past, present, and future, sharing ideas and dreams. I also want to thank Yuan Miao (苗园) who is an outstanding theorist and DOTA player, Liang Peng (彭亮) who was my neighbour and has a sense of humor, Yufei Fu (付毓飞), who was my high school classmate, came to Amsterdam at the same time as I did and shared his experience working at Booking, Hongyun Liu (刘鸿云)

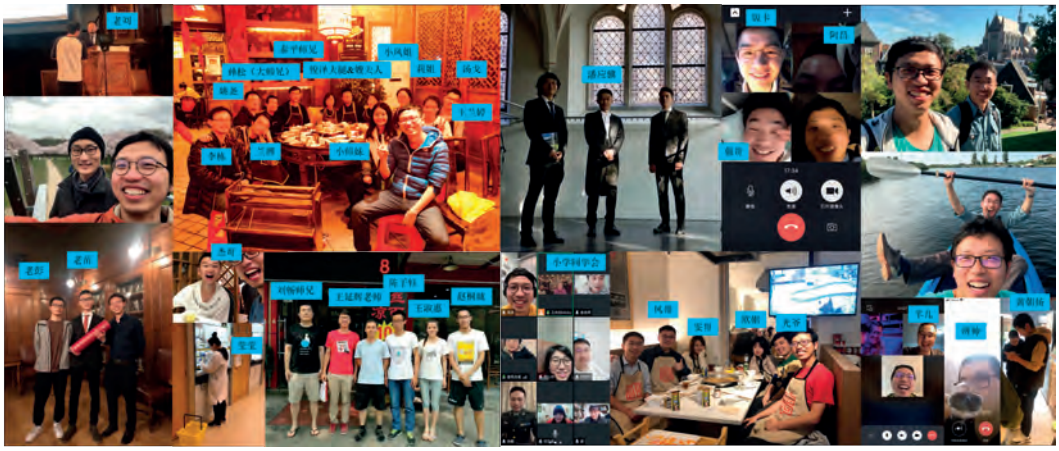

who faced similar cultural differences with his team, Zhichao Guo (郭志超) who can dedicate to work for days without sleeping, Yingying Tang (汤莹莹) who taught me some chemistry, Ziran Zhai (翟自然) who is very honest and kind, Zheng Wei (魏征) who is very talkative. My classmates (滕梓皓, 省慧, 彩霞, 江华, 李哲, 张国勇, 文熙) from the English course, Haosen Shang (商浩森) who showed me the strontium passive clock in SYRTE. I would also want to thank people from our physics institute, especially Daan Haver, WenFeng Liu (刘文峰), Xiaofei Guo (郭晓菲), Dongdong Zhou (冬冬), Starla (Qiuyu) Liu, Yao Du, Abhishek Kumar Gupta, Julie Jagielka, Kasra Farain, Dongming He (何东名), Yue Wang (小王), Ju Yuan (袁君), Fuzhen Zhou (周福珍). You have really enriched the past four years of my life. I hope that one day I can express my gratitude and repay everyone who has helped and cared for me through my actions.

# Unlocking the future of precision: continuous active optical clocks

Clocks are one of humanity's oldest and most remarkable inventions, now defining virtually our entire system of measurement. Today, optical clocks are so precise, they lose less than a second over the entire age of the universe, and performances continue to improve rapidly. All these clocks rely on ultra-stable optical cavities and highly forbidden atomic transitions to achieve their incredible accuracy.

A new approach, based on superradiance, could dramatically simplify this technology by using atoms to emit light directly and create clocks that are a million times less sensitive to external disturbances. This breakthrough could help to bring optical clocks out of the lab and enable real-world applications. Their impact could be felt from applied physics predicting earthquakes or improving GPS accuracy to expanding fundamental science, such as probing for dark matter and the universe.

In this thesis, I describe the development of two approaches aimed at demonstrating the first continuous active optical clock, each targeting different regimes. Both use strontium to achieve superradiant lasing. The first approach involves a hot atomic beam machine with a kHz-wide transition, designed for rugged industrial timekeeping. The second uses an ultra-cold atomic system with a mHz-wide transition, aiming for the ultimate active optical clock, one that will define a new state-of-the-art in precision measurement.

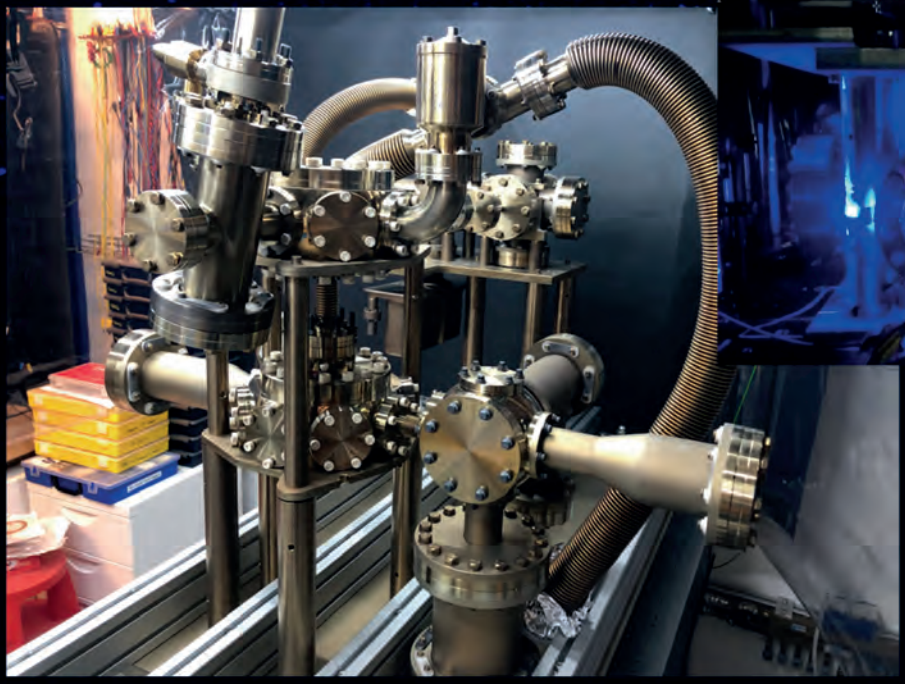

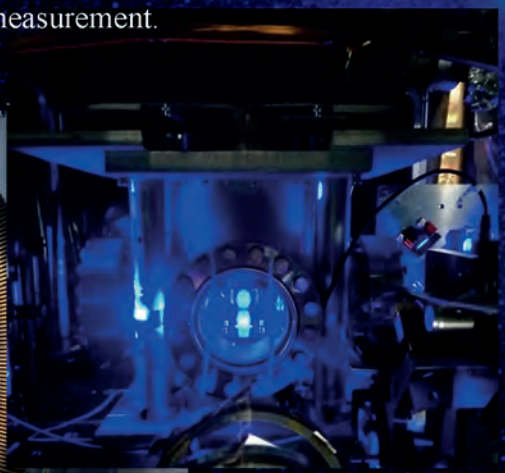

Experimental Quantum Physics

ISBN 978-94-6473-609-0

9 789464 736090